Magnetocaloric materials and first order phase transitions

Neves Bez, Henrique; Bahl, Christian; Nielsen, Kaspar Kirstein; Smith, Anders

Publication date:
2016

Document Version
Publisher's PDF, also known as Version of record

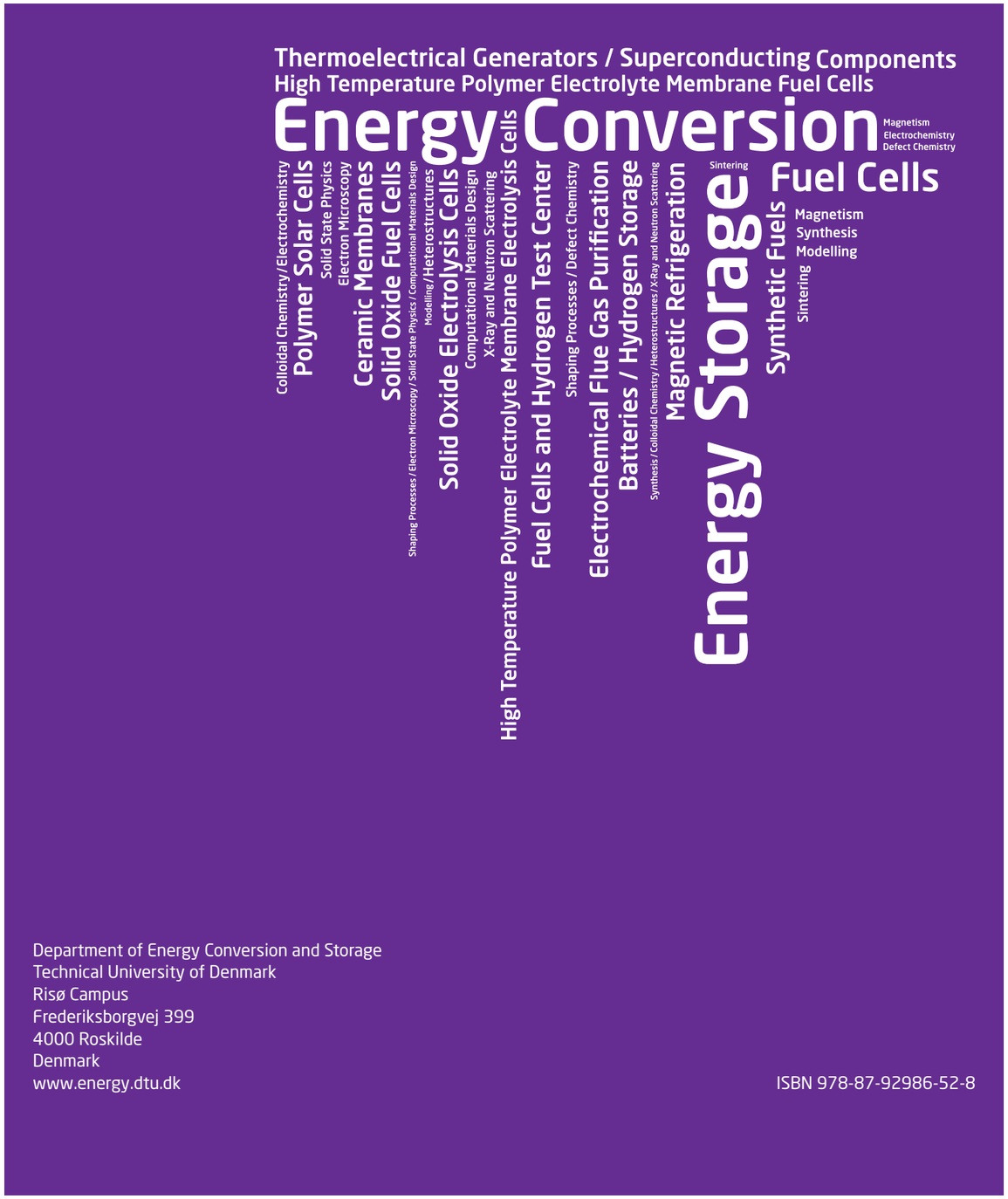

Department of Energy Conversion and Storage
Technical University of Denmark
Risø Campus
Frederiksborgvej 399
4000 Roskilde
Denmark
www.energy.dtu.dk

ISBN 978-87-92986-52-8

Magnetocaloric materials and first order phase transitions

September 2016

Technical University of Denmark

Magnetocaloric materials and first order phase transitions

Henrique Neves Bez
Department of Energy Conversion and Storage

Ph.D. Thesis, September 2016

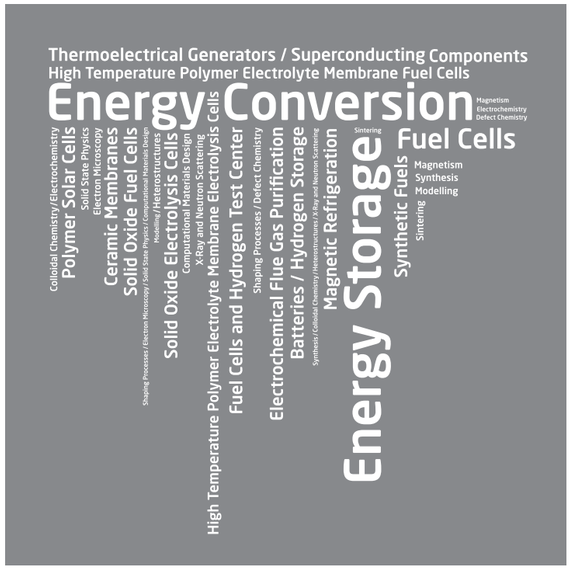

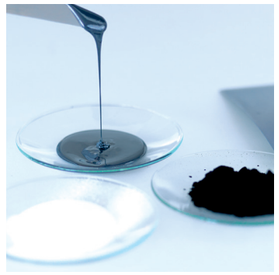

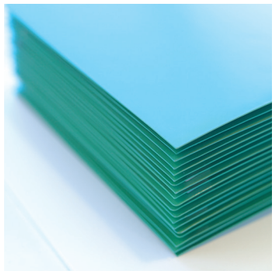

DTU Energy
Department of Energy Conversion and Storage

Technical University of Denmark

Magnetocaloric materials and first order phase transitions

PhD Thesis

Henrique Neves Bez

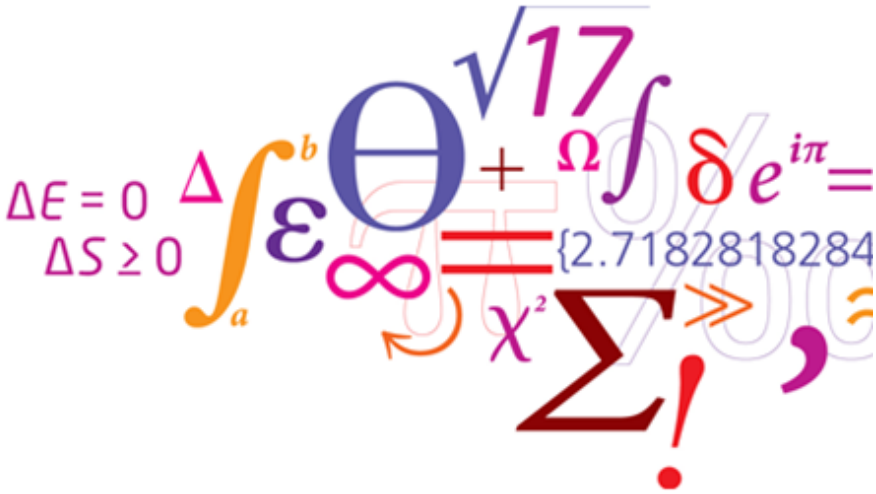

July 18th, 2016

DTU Energy
Department of Energy Conversion and Storage

Where is the life we have lost in living?
Where is the wisdom we have lost in knowledge?
Where is the knowledge we have lost in information?

THOMAS STEARNS ELLIOT

Acknowledgements

As a Brazilian coming from a small town, I have to first here thank my family. Brazil is a place with many less opportunities compared to most European countries, with a bad education system, specially in the scientific area. Without the support and struggle of my family to give me and my sister a proper education, I would never be able to even think about a PhD, like it is usually in my country.

Although I did my master in magnetocaloric materials as well, the focus shifted completely from syntheses processes to complex characterization methods and modelling. This shift would never be possible in such a short term of three years, if I did not have the guidance of great supervisors − Christian Bahl, Kaspar Nielsen and Anders Smith. These guys should be an example of professionalism to everyone. I could talk with them whenever I wanted, even about the most obvious doubts (either personal or professional) that one can have, and it was never shown anything but respect, humbleness and comprehension − the very definition of good leadership. They are people that I will always look up to, and I will be forever grateful to them.

I cannot not mention my colleague, friend and flatmate Andrea Insinga. This guy has one of the most brilliant minds I have ever seen, and perhaps the purest heart among all the people I know. Without his assistance, the quality of my work would significantly decrease. He has countlessly helped me to code on MATLAB and LaTeX, basically teaching me how to code from scratch. Moreover, his impact on me during these three years was the strongest regarding me as a person, through several philosophical discussions regarding a vast range of topics, from prejudice, to economics, politics, social duties, moral behavior and paradoxes. He will be a friend that I will always look back with nothing but admiration.

My colleagues from the Electrofunctional Materials section greatly impacted my PhD as well. The same values mentioned for Christian, Kaspar and Anders may be seen in them. The group truly understands the concept of synergy. I would like to express here my gratitude to the group, in particular to Nini Pryds, Kurt Engelbrecht, Rasmus Bjørk, Tian Lei, Kristina Navickaitė, Dan Eriksen, Stefano Soprani, Stefano Dall'Olio, Jaka Tušek, Jørgen Geyti, Li Han and Yunzhong Chen. Additionally, I would also like to thank the technicians Pernille Nielsen and Ebtisam Abdellahi for the kind assistance in the labs throughout these three years.

During my PhD I had the pleasure to work with the group of Prof. Dr. Lesley Cohen in the Imperial College London for about a month. This time spent with them has led to several discussions and measurements that greatly improved this work. I would like to thank Prof. Lesley Cohen, Jeremy Turcaud and Edmund Lovell for all the assistance and for the nice time I have spent in London. In this context I would like to thank Vacuumschmelze GmbH, in particular Alexander Barcza, for providing the material and assisting me on the understanding of the magnetocaloric behavior

of $La(Fe,Mn,Si)_{13}H_z$.

Furthermore, I would like to thank all my friends that somehow have influenced me, either by making my life more joyful or assisting me directly during this period that can be relatively overwhelming. In particular I would like to thank Salvatore Lombardo and Iason Tsiamis, my friends and flatmates. I will never forget this amazing period I had with you. Additionally, I would like to thank Gabrielle Fachinelli (chata) for putting so much color in my life and a smile on my face, even if she is 10000 km away from me. Moreover, Felipe Trombetta and Wout Hermans have greatly improved my life in Denmark and made it so much more joyful. I would like to thank also Mary, Laura, Erica, Matilde and Leonor for all the great memories I will carry on for the rest of my life.

Abstract, English

This thesis studies the first order phase transitions of the magnetocaloric materials $La_{0.67}Ca_{0.33}MnO_3$ and $La(Fe,Mn,Si)_{13}H_z$ trying to overcome challenges that these materials face when applied in active magnetic regenerators. The study is done through experimental characterization and modelling of the properties of such materials. The experimental characterization of these materials is done through various different methods, such as X-ray diffraction, magnetometry, calorimetry, direct measurements of entropy change, capacitance dilatometry, scanning electron microscopy, energy-dispersive X-ray spectrometry and magnetocaloric regenerative tests. The magnetic, thermal and structural properties obtained from such measurements are then evaluated through different models, i.e. the Curie-Weiss law, the Bean-Rodbell model, the free electron model and the Debye model.

The measured magnetocaloric properties of $La_{0.67}Ca_{0.33}MnO_3$ shows a paradoxical behavior; the material shows features of both a first order phase transition and of a second order one. Identities as shift of the heat capacity peak and an asymmetric growth of of the entropy change with magnetic field would describe this material transition as a first order one. However, the material did not present any signs of intrinsic hysteresis, a feature common in first order transitions. This is attributed to a chemical distributionin this first order phase transition material that can lead to a smearing of the transition and the hysteresis, and such effect is observed through modelling. Moreover, inverse susceptibility measurements showed what could be evidences of magnetic polarons being formed in the paramagnetic phase of the material. The origin of the first order transition seems to be due to the magneto-elastic coupling observed through isothermal magnetostriction and dilatometric measurements. Although the Bean-Rodbell model has described with a good agreement the entropy change, hysteresis, magnetization and heat capacity, it has failed to describe the isothermal magnetostriction. It is suggested that such failure could be related to different factors that might influence constructively to each other: (i) the model assumes localized magnetic moments, while this material presents a double exchange interaction; (ii) the model assumes a temperature and field independent bulk modulus, which literature has shown that is not the case; and (iii) the approximation of the cluster being temperature and field independent is exaggerated and perhaps cannot be taken.

A series of $La(Fe,Mn,Si)_{13}H_z$ with slightly changes in the composition is also evaluated here. This material may present a second order phase transition for large content of Mn and Si, which will become a first order one as the Mn and Si content decreases. The material also presents a volume change, which also increases as Mn and Si content decreases, which in return may lead to detrimental mechanical stability of the material during application. The shift of the orderness from second to

first order transition is observed through heat capacity, magnetization and entropy change measurements. By measuring bulky particles (with a particle size in the range of 500∼1000 μm) of La(Fe,Mn,Si)$_{13}$H$_z$ with first order phase transition, it was possible to observe very sharp transitions. This is not the case for finer ground particles which show a smooth transition, as if it was second order. Although this behavior has been explained in the literature as an artefact due to the inclusion of defects when grinding the material, here it is proposed a different explanation given the evidences. Firstly, it is argued that the material is brittle and insertion of defects through grinding is unlikely. Secondly, it is observed through entropy change measurements that a bulky particle has a larger entropy change. However, the particle cracks and separates into several particles due to stresses generated during the transition, which are related to the volume change. After this effect, if the entropy change is remeasured it shows very similar behavior to measurements of ground particles. Therefore, the results suggests that defects inserted through grinding is probably not the case. To explain such behavior, in this thesis it is proposed that slightly differences in the composition throughout the sample may lead to a Curie temperature distribution. This in return would lead to different regions of the sample undergoing the transition in different temperatures. However, given the polycrystallinity of the material, the crystallites with different Curie temperatures will be volumetric constrained until enough energy is given to the system and the whole bulky particle undergoes the transition. This explains why bulky particles have a sharp transition and ground particles have a smoother one; the latter is much less volumetric constrained than the former. An outcome of such behavior is observed as strain development during the phase transition; this strain was calculated applying the Williamson-Hall method. The strain development is much more significant in the ferromagnetic phase than in the paramagnetic one, which is attributed to the weakening of the magnetic interactions as the ferromagnetic phase approach the transition. This is speculated as a decrease of the bulk modulus of the ferromagnetic phase as the temperature increases. The paramagnetic phase, however, is expect to have a relatively constant bulk modulus as there is no magnetic interactions. When observing the microscopy images, they show that cracks are usually somehow connected to a minor La-rich secondary phase observed as inclusions in the grain boundaries. It is argued that this phase is the only brittle and hard phase that does not present a volume change. Therefore the decrease of this phase, however low content it is, could lead to an improvement in the mechanical stability of the material during application. Finally the Bean-Rodbell model is applied to the describe the volumetric behavior observed through X-ray measurements as a function of the temperature. The model describes with good agreement the volume discontinuity across the phase transition, and the superimposed distribution of Curie temperature can describe well the paramagnetic growth as the transition occurs. However, the model over-predicts the thermal hysteresis and under-predicts the shift of the the transition temperature with magnetic field.

Resumé, dansk

Denne afhandling studerer førsteordens-faseovergangene i de magnetokaloriske materialer $La_{0.67}Ca_{0.33}MnO_3$ og $La(Fe,Mn,Si)_{13}H_z$ for at søge at løse nogle af de udfordringer, der er for anvendelse af materialerne i aktive magnetiske regeneratorer. Studiet består i eksperimentel karakterisering i kombination med modellering af egenskaberne for disse materialer. Den eksperimentelle karakterisering er blevet foretaget med en række forskellige metoder som røntgendiffraktion, magnetometri, kalorimetri, direkte målinger af entropiændring, kapacitiv dilatometri, scanning-elektronmikroskopi, energidispersiv røntgenspektrometri og test af magnetokaloriske regeneratorer. De magnetiske, termiske og strukturelle egenskaber, der er bestemt ved sådanne målinger, er derefter blevet evalueret gennem forskellige modeller, inkl. Curie-Weiss-loven, Bean-Rodbell-modellen, frielektronmodellen og Debye-modellen.

De målte magnetokaloriske egenskaber af $La_{0.67}Ca_{0.33}MnO_3$ udviser en paradoksal opførsel: materialet udviser egenskaber der både minder om en førsteordens faseovergang og en andenordens. Træk som en forskydning af toppunktet i den specifikke varmekapacitet og en asymmetrisk øgning af entropiændringen som funktion af magnetisk felt er karakteristisk for førsteordens-overgange. På den anden side udviser materialet ikke nogen tegn på intrinsisk hysterese, hvilket ellers er almindeligt i førsteordens-overgange. Dette bliver forklaret med en distribution af den kemiske sammensætning af et førsteordens-materiale, som kan føre til en udtværing af faseovergangen og hysteresen, hvilket observeres ved modellering. Desuden viser målinger af den inverse susceptibilitet træk, der kunne tyde på at der dannes magnetiske polaroner i den paramagnetiske fase af materialet. Oprindelsen til førsteordens-overgangen synes at være den magneto-elastiske kobling, der kan observeres ved måling af isotermisk magnetostriktion samt ved dilatometri. Selv om Bean-Rodbell-modellen med god overensstemmelse kan redegøre for den observerede entropiænding, hysterese, magnetisering og specifik varmekapacitet, kan den ikke beskrive den isotermiske magnetostriktion. Det bliver foreslået at denne mangel kan relateres til samspillet mellem forskellige faktorer: (i) modellen antager lokaliserede magnetiske momenter, mens materialets vekselvirkning er af typen double exchange; (ii) modellen antager, at kompressibilitetsmodulet er uafhængigt af temperatur og felt, hvilket ifølge litteraturen ikke er tilfældet; (iii) approksimationen med at regne de magnetiske klynger for at være uafhængige af temperatur og felt er overdrevet og muligvis ugyldig.

En serie af $La(Fe,Mn,Si)_{13}H_z$ med små ændringer i sammensætningen bliver også evalueret her. Dette materiale kan have en andenordens faseovergang for stort Mn- og Si-indhold, som bliver førsteordens efterhånden som Mn- og Si-indholdet aftager. Materialet udviser også en volumenændring, der øges i takt med Mn- og Si-indholdet, hvilket kan føre til dårlig mekanisk stabilitet af materialet under an-

vendelse i en regenerator. ændringen i ordenen af materialets faseovergang fra første til anden orden kan observeres gennem målinger af den specifikke varmekapacitet, magnetiseringen og entropiændringen. Ved at måle på forholdsvis store partikler (med en partikelstørrelse på 500-1000 Îijm) var det muligt at observere en meget skarp overgang. Det er ikke tilfældet for mere finmalede partikler, der udviser en jævn overgang som om den var af anden orden. Selv om denne opførsel har været beskrevet i litteraturen som en effekt af, at der introduceres defekter, når man pulveret formales, så foreslås der her en anden forklaring baseret på de foreliggende målinger. For det første argumenteres der med, at materialet er skørt, og det derfor er usandsynligt, at der introduceres defekter i materialet ved formaling. For det andet viser målinger af entropiændringen, at en stor partikel har en større entropiændring. Imidlertid revner partiklen og separerer i flere stykker pga. indre spændinger der opstår under faseovergangen, hvilket er relateret til volumenændringen. Efter dette er sket viser genmålinger af entropiændringen en opførsel, der er meget lig målinger af formalede partikler. Dette tyder på, at opførslen ikke skyldes, at der introduceres defekter under formalingen. Som en forklaring fremsættes den hypotese, at små variationer i den kemiske sammensætning hen over prøven kan føre til den spredning i Curie-temperaturen. Dette ville føre til, at forskellige områder af prøven fasetransformerer ved forskellige temperaturer. Imidlertid vil krystallitter med forskellige Curie-temperaturer blive volumetrisk begrænset af resten af den polykrystallinske prøve, indtil der er tilført energi nok til systemet, og hele prøven transformerer. Det forklarer hvorfor store partikler har en skarp overgang og formalede partikler en mere glidende overgang: de sidstnævnte er ikke volumetrisk begrænsede i samme omfang som de første. En konsekvens af denne opførsel er, at der kan observeres en udvikling af tøjninger i prøven under faseovergangen. Disse tøjninger blev udregnet vha. Williamson-Hall-metoden. Tøjningerne er mere udtalte i den ferromagnetiske fase end i den paramagnetiske fase, hvilket forklares med svækkelsen af de magnetiske vekselvirkninger, når den ferromagnetiske fase nærmer sig faseovergangen. Det formodes også at være årsag til en reduktion i kompressibilitetsmodulet i den ferromagnetiske fase, når temperaturen øges. I den paramagnetiske fase forventes kompressibilitetsmodulet derimod at være forholdsvis konstant, da der ikke er magnetiske vekselvirkninger. På mikroskopibilleder kan det ses, at revner oftest er forbundet med en sekundær, lantan-rig fase, som kan observeres som inklusioner i korngrænserne. Der argumenteres for, at denne fase er den eneste skøre og hårde fase, som ikke udviser en volumenændring. En reduktion af denne fase kunne derfor føre til en forbedring af den mekaniske stabilitet af materialet under drift. Endelig anvendes Bean-Rodbell-modellen til at beskrive den volumetriske opførsel, der kan observeres ved røntgenmålinger som funktion af temperaturen. Modellen beskriver med god overensstemmelse diskontinuiteten i volumen hen over faseovergangen, og en fordeling af Curie-temperaturer giver en god beskrivelse af væksten i den paramagnetiske fase i takt med faseovergangens forløb. Derimod forudsiger modellen en for stor termisk hysterese og en for lille forskydning af overgangstemperaturen med magnetisk felt.

List of publications

The publications here mentioned can be found as appendices in the end of this thesis.

1. Bez, H. N., Nielsen, K. K., Norby, P., Smith, A., Bahl, C. R. H., Magneto-elastic coupling in $La(Fe,Mn,Si)_{13}H_y$ within the Bean-Rodbell model, *AIP Advances* **6** (2016) 056217.

2. Bez, H. N., Nielsen, K. K., Smith, A., Bahl, C. R. H., A detailed study of the hysteresis in $La_{0.67}Ca_{0.33}MnO_3$, *Journal of Magnetism and Magnetic materials* **416** (2016) 429-433.

3. Bez, H. N., Nielsen, K. K., Smith, A., Norby, P., Ståhl, K., Bahl, C. R. H., Strain development during phase transition of $La(Fe,Mn,Si)_{13}H_z$, *under review in Applied Physics Letters* (2016).

4. Smith, A., Nielsen, K. K., Bez, H. N., Bahl, C. R. H., Non-universal scaling of the magnetocaloric effect as an insight into spin-lattice interactions in manganites, *accepted in Physical Review B* (2016).

5. Nielsen, K. K., Bez, H. N., von Moos, L., Bjørk, R., Eriksen, D., Bahl, C. R. H., Direct measurements of magnetic entropy change, *Review of Scientific Instruments* **86** (2015) 103903.

6. Turcaud, J., Bez, H. N., Ruiz-Trejo, E., Bahl, C. R. H., Nielsen, K. K., Smith, A., Cohen, L. F., Influence of manganite powder grain size in Ag-particle coating on the magnetocaloric effect and the active magnentic regenerator performance, *Acta Materialia* **97** (2015) 413-418.

7. Tian, L., Nielsen, K. K., Engelbrecht, K., Bahl, C. R. H., Bez, H. N., Veje, C. T., Sensitivity study of multi-layer active magnetic regenerators using first order magnetocaloric material $La(Fe,Mn,Si)_{13}H_y$, *Journal of Applied Physics* **118** (2015) 014903.

8. Bahl, C. R. H., Navickaitė, K., Bez, H. N., Lei, T., Engelbrecht, K., Bjørk, R., Li, K., Li, Z., Shen, J., Dai, W., Jia, J., Wu, Y., Long, Y., Hu, F., Shen, B., Resin bonded magnetocaloric plates tested in a refrigeration device, *submitted to the International Journal of Refrigeration* (2016).

9. Bez, H. N., Navickaitė, K., Lei, T., Engelbrecht, K., Barcza, A., Bahl, C. R. H., Epoxy-bonded $La(Fe,Mn,Si)_{13}H_z$ as a multi layered active magnetic regenerator, *submitted to the* 7^{th} *International Conference on Magnetic Refrigeration at Room temperature* (2016).

Contents

Chapter 1

Introduction

The thesis presented here aims to provide clear and insightful knowledge on the phase transition of magnetocaloric materials, in particular the ones with first order phase transition (FOPT). The common feature between magnetocaloric materials is the magnetocaloric effect (MCE), which is a thermal response in magnetic materials when subjected to adiabatic magnetization or demagnetization. In general, the only prerequisite for a material to be considered magnetocaloric is to have a thermal response when its magnetic disorder is changed, which usually is done by varying an external applied magnetic field. Therefore, regarding properties of a material to be magnetocaloric, the material must have a magnetic phase at a given temperature, pressure and magnetic field, and its spin ordering must vary when the external magnetic field is varied. The latter is more evident around the magnetic phase transition of the material. In this sense, all magnetic materials present the magnetocaloric effect, given the external conditions. These materials have been studied for almost a century, specially for cooling applications, often called magnetic cooling. Still, in the late 90s the research done in magnetic cooling started to increase exponentially, thanks to the discovery of magnetocaloric materials with performance much higher than the usual, the magnetocaloric materials with first order phase transition.

FOPT magnetocaloric materials may present much better performance when compared to second order phase transition (SOPT) materials. When a FOPT material undergoes the transition, the magnetization and volume/structure change discontinuously, and latent heat is associated with the transition. Regarding their properties, the thermal response that FOPT materials present is stronger, therefore they are more attractive for cooling and heating applications. However, these materials present complications uncommon to SOPT materials. Apart from the volume/structure change, FOPT materials may present magnetic and thermal hysteresis, along with some possible time dependent issues. Moreover, the temperature range in which the magnetocaloric effect occurs is much narrower than that of SOPT materials. This short temperature range leads to some extra engineering necessary in order to apply such materials in magnetic cooling or heating; such engineering is not trivial, and a lot of effort is being made by the scientific community to optimize it. On top of that, when processing materials it is intrinsically difficult to fabricate a material chemically homogeneous in its completeness. Slight changes of concentrations of the elements are most often found from region to region in a material. This is not a feature only for magnetocaloric materials, but any given alloy.

As this PhD is a part of a larger project[1], which aims to use the FOPT magnetocaloric materials in a heat pump, the objective of this thesis is to address the challenges involved with the fabrication, characterization, modelling and application of 2 particular FOPT magnetocaloric materials − $La_{0.67}Ca_{0.33}MnO_3$ and $La(Fe,Mn,Si)_{13}H_z$ − and to suggest solutions to their phase transitions.

Aiming to deliver a clear message to the reader, this thesis is divided into seven chapters:

Chapter 1 It is the present chapter and it gives an introduction to the topic of this thesis and its objectives.

Chapter 2 The state of the art is discussed here. A historic introduction about the magnetocaloric effect and its applications is given. The thermodynamics of this effect is explained. Moreover, an introduction to the magnetocaloric materials here studied is given.

Chapter 3 Here the characterization methods are explained. The calorimeters, magnetometers, dilatometer, microscopes, diffractometers and regenerator testing device are described.

Chapter 4 In this chapter, the results concerning the fabrication, characterization and modelling of $La_{0.67}Ca_{0.33}MnO_3$ are shown and discussed.

Chapter 5 In this chapter, the results concerning the characterization and modelling of $La(Fe,Mn,Si)_{13}H_z$ are shown and discussed.

Chapter 6 The conclusions from this work are stated here.

Chapter 7 The perspectives and future challenges are discussed in this chapter.

Appendices The appendices summarize the publications related to this thesis.

[1] EnovHeat Project − one may find more information on it at www.enovheat.dk.

Chapter 2

State of the art

This chapter describes the state of the art in magnetocaloric materials and applications. It describes the history of the magnetocaloric effect, thermodynamics involved in this effect, connecting the different contributions from the lattice, electronic and magnetic properties of the material. The materials and models used in this thesis are also here explained.

2.1 History of the magnetocaloric effect

The history of the magnetocaloric effect dates to almost a century ago. Weiss and Piccard (1918) discovered that by changing the applied magnetic field close to the phase transition of Ni, one could observe a temperature change of the material. This publication delineates the discovery of the magnetocaloric effect, which can be defined as a reversible temperature change when the material is subjected to a adiabatic magnetization or demagnetization (Smith, 2013). It took 15 years from its discovery for the magnetocaloric effect be first applied – when Giauque and Macdougall (1933) used the magnetocaloric effect to reach temperatures below 1 K, fact that conceived the award of the Nobel prize in chemistry in 1949.

The first application of the magnetocaloric effect around room temperature was only done 43 years after Giauque and Macdougall (1933). Brown (1976) used Gd in a custom-built device, which used 157 g of the material in order to reach 47 K of temperature change, through thermo-magnetic regenerative cycles.

The research on magnetocalorics started to increase exponentially (Smith, 2013) when Pecharsky and Gschneidner (1997) discovered a new magnetocaloric material, $Gd_5Si_2Ge_2$. This material showed a much larger magnetocaloric effect when compared to Gd. The demand for environmentally friendly technologies and the discovery of this new alloy led to an increased interest in the magnetocaloric field.

The principle of the effect can be understood in the following way. Consider a magnetic material close to its phase transition. In this region the magnetic state will be more disordered, as shown in Figure 2.1 by the blue box. By applying a magnetic field adiabatically, one can force the magnetic state to be more ordered, therefore decreasing the magnetic contribution to the entropy. Since there is no heat transfer, the total entropy remains constant, so the magnetic entropy change is backed up by the lattice and electronic contribution. This is observed macroscopically as a temperature change.

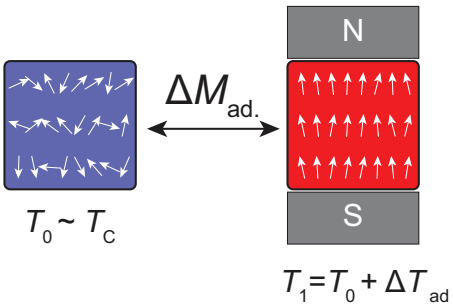

Figure 2.1: Schematic drawing of the effect of the magnetocaloric effect, showing the influence of an external magnetic field on a magnetic material around its magnetic phase transition.

In order to apply the magnetocaloric effect in any cooling or heating technology, one has to consider that the magnetic field change source plays a major role. Moreover, excluding industrial cooling or heating applications, the machine is expected to be small. Having this in mind, one solution is to use an assembly of permanent magnets, which in reasonable sizes will allow a field change of about 1.5 T. This field change in return will lead to just a few degrees of adiabatic temperature change, not enough for most of the heating or cooling applications. The solution to this challenge was already used by Barclay and Steyert (1982) – active magnetic regenerative cycles. In such approach, the magnetocaloric material is used as the active magnetic regenerator (AMR). An example of a AMR cycle is given in Figure 2.2. This cycle can be separated in 4 steps. Starting from a temperature $T_0 \sim T_C$, the magnetic field is changed from an initial value, H_i, to a bigger value, H_f, isentropically[1]. As explained before, this field change will lead a temperature change, now T_1. The heat can then be released, Q_{rel}, to a heat sink, bringing the material's temperature to T_2. The material then is isentropically demagnetized to H_i, bringing the temperature to T_3, which allows the material to absorb heat, Q_{abs}, and finishing the cycle.

2.2 Thermodynamics

In this section the thermodynamics involved on the magnetocaloric effect are discussed. The thermodynamics of this effect, however, must be considered differently, depending if the material presents a first order phase transition or a second order. Up to now, we have taken that the magnetocaloric effect is always reversible. Still, this is only true for second order phase transitions. First order phase transitions are extremely dependent in the history of the material (von Moos et al., 2015), and involve latent heat and volumetric/structural changes. The definition here used for phase transition is the one stated by Ehrenfest. He proposed to classify transitions with respect to the free energy. In his definition, a first order phase transition presents a discontinuity in the first derivative of the free energy, while a second order one would have a discontinuity in the second derivative (Jaeger, 1998).

[1] In order to a process be isentropic, it must be adiabatic *and* reversible.

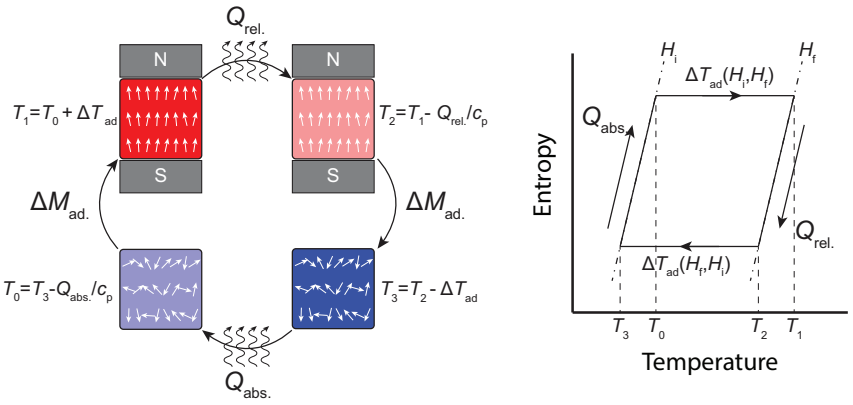

Figure 2.2: Example of an AMR cycle on the left. The graph on the right shows schematically the entropy as a function of the temperature involved in the AMR cycle.

2.2.1 Second order phase transition

The origin of the reversible magnetocaloric effect comes from the basic thermodynamic laws. Let us consider a work done isobarically and isometrically by an external magnetic field, $\mu_0 H$[2], on a magnetic material (Çengel and Boles, 2006):

$$\delta W = \mu_0 H \mathrm{d}M, \tag{2.1}$$

where M is the magnetization, μ_0 is the magnetic permeability of vacuum, and W is the work. The internal energy change, $\mathrm{d}U$, is then given by:

$$\mathrm{d}U = \delta W + \delta Q, \tag{2.2}$$

where δQ is the heat released or absorbed by the system.

Let us consider now the Gibbs free energy, G, which can be described for this system as follows:

$$G = U - sT - \mu_0 H M, \tag{2.3}$$

where s is the entropy. This equation can be expressed in the differential form as:

$$\mathrm{d}G = -s\mathrm{d}T - \mu_0 M \mathrm{d}H, \tag{2.4}$$

The partial derivatives will then give

$$M = -\mu_0 \left(\frac{\partial G}{\partial H}\right)_T, \tag{2.5}$$

and

$$s = -\left(\frac{\partial G}{\partial T}\right)_H. \tag{2.6}$$

Being G a state function, one can apply the Euler reciprocity relation to get[3]:

$$\mu_0 \left(\frac{\partial M}{\partial T}\right)_H = \left(\frac{\partial s}{\partial H}\right)_T, \tag{2.7}$$

[2] μ_0 is explicitly written here, in order to keep H with the unit Am^{-1}.

[3] This relation is usually named after Maxwell. The Maxwell relations, however, give only relations between derivatives of thermodynamic variables. The Euler reciprocity relation in other hand gives the mathematical reasoning behind Maxwell relations.

which is one of the Maxwell relations. With this relation in hand, it is straightforward to calculate the isothermal entropy changed involved in a field change,

$$\Delta s(T, \Delta H) = \mu_0 \int_{H_\mathrm{i}}^{H_\mathrm{f}} \left(\frac{\partial M(T,H)}{\partial T} \right)_H \mathrm{d}H, \tag{2.8}$$

where $\Delta H = H_\mathrm{f} - H_\mathrm{i}$. It is important to note that Δs is a function of H_f and H_i themselves, not only of ΔH. From this equation, it is clear why the magnetocaloric effect is more evident around the T_C, since this is the region with the largest $\frac{\partial M}{\partial T}$. Furthermore, one can see from this equation that by having measurements of magnetization as a function of field and temperature, one can calculate the entropy change experimentally. Given the thermodynamic cycle shown in Figure 2.2, it is clear that this is one of the major properties that characterize the magnetocaloric effect.

Another major property is the adiabatic temperature change, which is related to the entropy change by the heat capacity. Let us have that the heat capacity is

$$c_{H,P}(T, H) = T \left(\frac{\partial s}{\partial T} \right)_H, \tag{2.9}$$

where c is the heat capacity. Since entropy is a state function, its differential can be written as a function of the different contributions as

$$\mathrm{d}s = \left(\frac{\partial s}{\partial T} \right)_H \mathrm{d}T + \mu_0 \left(\frac{\partial s}{\partial H} \right)_T \mathrm{d}H. \tag{2.10}$$

Since this process is adiabatic $\mathrm{d}s = 0$ $\mathrm{Jkg^{-1}K^{-1}}$, and combining equations 2.7, 2.9 and 2.10 one can get the adiabatic temperature change,

$$\Delta T_\mathrm{ad}(T, \Delta H) = -\mu_0 \int_\gamma \frac{T}{c_{H,P}(T,H)} \left(\frac{\partial M}{\partial T} \right)_H \mathrm{d}H, \tag{2.11}$$

where γ is the relevant isentrope curve along which the integral is evaluated.

In literature, these are the four most evaluated properties: magnetization, entropy change, heat capacity and adiabatic temperature change. The latter, however, is not trivially calculated, as T is expected to vary with the field. Still, there are equipments to directly measure it (Liu et al., 2011). Although ΔT_ad is a more intuitive and palpable property, if one is already evaluating the first three properties mentioned, ΔT_ad does not give further insight on the transition. Therefore, in this thesis the evaluation of adiabatic temperature change will be set aside, and the focus will be on the study of the other properties. Figure 2.3 shows schematic plots of the behavior of a SOPT magnetocaloric material, regarding the magnetization 2.3(a), the heat capacity 2.3(b) and the entropy change 2.3(c). Note that the entropy change is given in absolute values, as most of the magnetocaloric materials present a negative entropy change when increasing the magnetic field. These plots were generated using the Bean-Rodbell model (Bean and Rodbell, 1962), which is a phenomenological approach within the mean field theory. The discussion on the model will be given in Section 2.4.

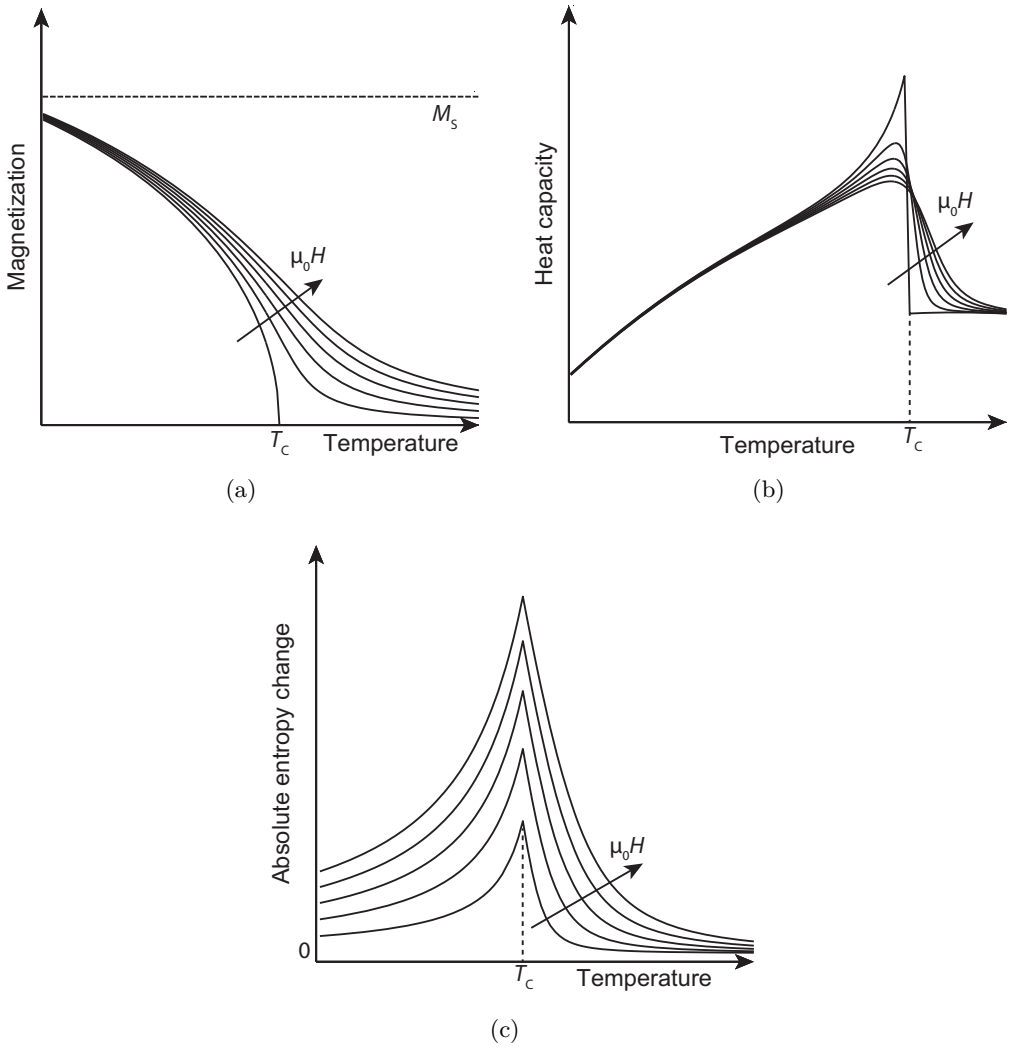

Figure 2.3: Schematic plots of second order phase transition behavior of (a) Magnetization, (b) heat capacity and (c) entropy change as a function of the temperature and magnetic field.

2.2.2 First order phase transition

One can see in both equations 2.8 and 2.11 that one major way to increase the magnetocaloric effect is to have a large change of magnetization over temperature. However, by the definition of a second order phase transition, the magnetic transition occurs continuously, not allowing a abrupt change of the magnetization. Therefore, to generate a larger magnetocaloric effect one must use first order phase transitions, i.e. discontinuous magnetic transitions.

This type of phase transition is usually accompanied by a volume or structural change. It is also associated with irreversibilities, generally observed in the form of thermal and magnetic hysteresis. Several magnetocaloric materials present such behavior, and some of them will be discussed in the next section. One can imagine

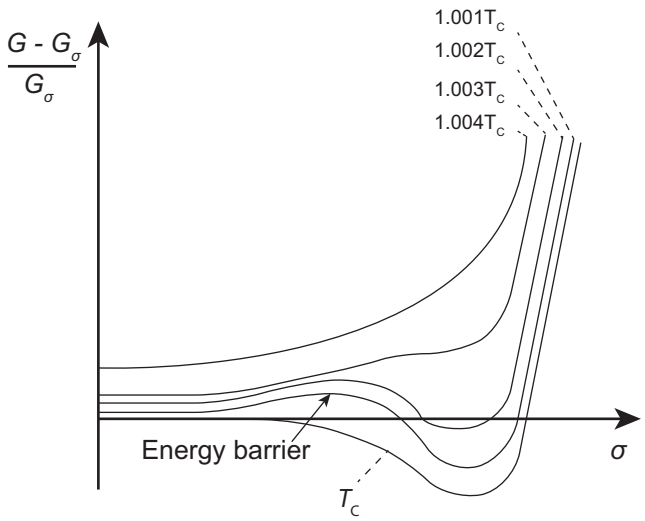

Figure 2.4: Schematic plots of the isothermals of the Gibbs free energy, as a function of the relative magnetization.

the transition region of a ferromagnetic material as shown in Figure 2.4 in terms of the Gibbs free energy (Hillert, 2008). In this figure we have schematic plots of the isotherms of the relative gibbs free energy as a function of the relative magnetization $\sigma = M/M_s$ where M_s is the saturation magnetization, or the magnetization of a perfect and infinite magnetic material at $T = 0$ K. If one is at $T >> T_C$, $\sigma = 0$. By starting cooling the material, at some point $T_C < T < 1.003T_C$[4] will be reached. At this range there are two minima of the relative free energy; however since the material is coming from a *history* where $\sigma = 0$, it will remain there unless some energy is introduced in the system to surpass the energy barrier in between the two minima. Upon Further cooling, one will reach $T \leq T_C$ where now there is only one minimum and the material will present spontaneous magnetization. Therefore, the transition temperature upon cooling is at $T = T_C$.

The same process can be imagined upon heating and starting within the ferromagnetic phase region. Upon heating, we will reach $T = T_C$, but now we are already in that minima, therefore there is no phase transition in this temperature. According to the schematic plots, the transition to paramagnetic will occur only when the high σ minima disappears, i.e. at $T = 1.003T_C$.

Figure 2.5 shows schematic plots of the behavior of a FOPT magnetocaloric material, regarding the magnetization 2.5(a), the heat capacity 2.5(b) and the entropy change 2.5(c). These plots were generated using the Bean-Rodbell model (Bean and Rodbell, 1962) as well. One can see that the transition shift towards higher temperatures when a magnetic applied field is increased, which is a feature expected for all FOPT magnetocaloric materials, feature that is not observed for pure second order phase transitions. Moreover, one may see the discontinuity on the magnetization, the classic feature of a first order magnetic phase transition. In the words of Bean and Rodbell (1962), "The situation is like that of a man who has run beyond the brink of a cliff; there is no gentle way down".

[4]The value $1.003T_C$ is an arbitrary value to ease the explanation.

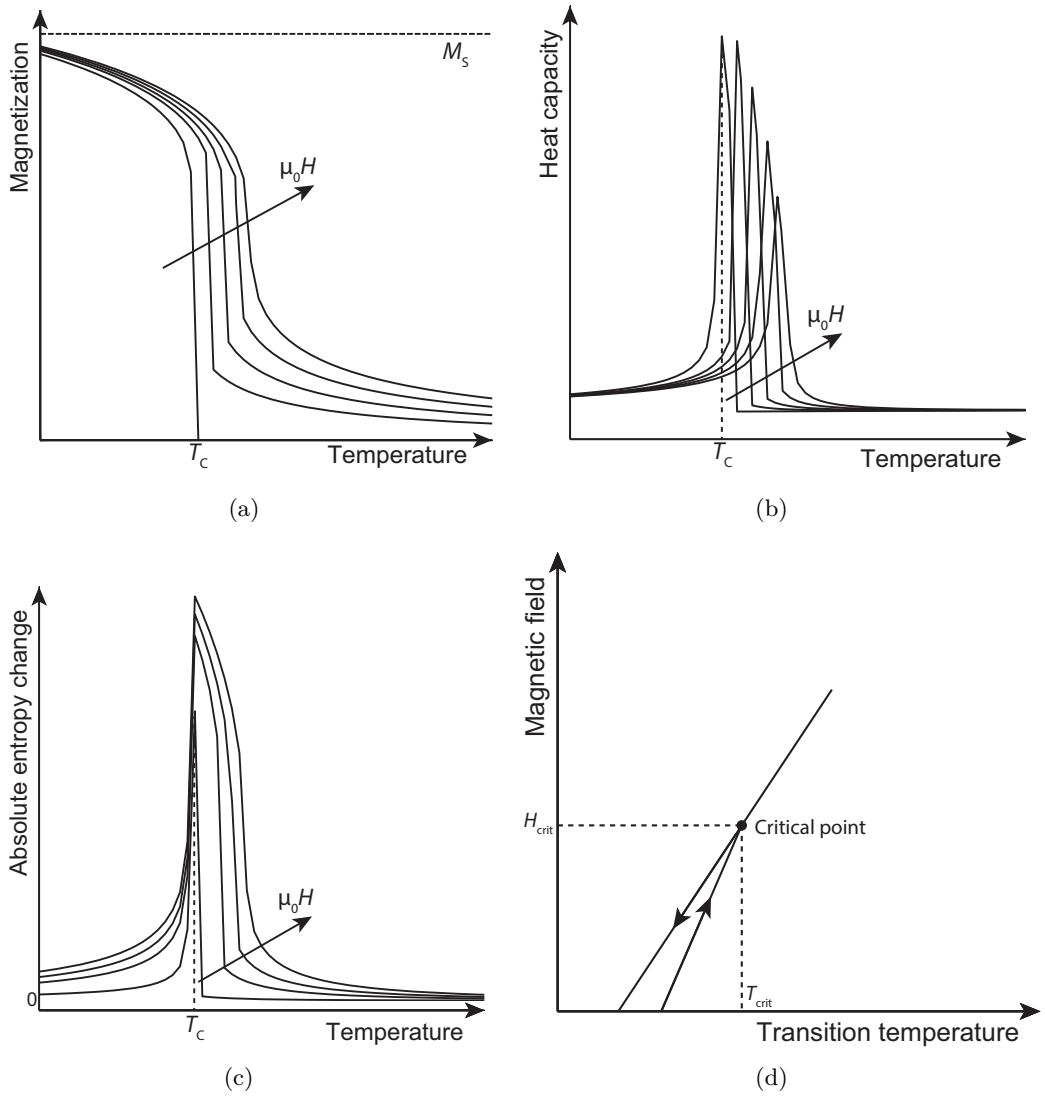

Figure 2.5: Schematic plots of first order phase transition behavior of (a) Magnetization, (b) heat capacity and (c) entropy change as a function of the temperature and magnetic field. Figure (d) shows the transition temperature as a function of the magnetic field.

The heat capacity shows a peak shift towards higher temperatures, but also a broader and smaller peak. This is related to the fact of the approximation of the transition to the critical point (Çengel and Boles, 2006). One can see in the magnetization curve 2.5(a) that with the increasing field, the transition becomes more continuous and at the critical point, as shown in Figure 2.5(d), the transition will not show any more hysteresis nor latent heat, and become completely continuous. Therefore, after the critical point the transition becomes a second order one.

2.2.3 Challenges to overcome with FOPT materials

Throughout this chapter several features of FOPT materials have been pointed out. Some features are good for AMR applications, e.g. the large entropy change. Nonetheless, many of these features are not, as described below:

1. Sharp transition: FOPT are by definition discontinuous. Although this gives rise to large magnetocaloric effect, this also means that the magnetocaloric effect will be large in a very small temperature range. This is an issue for magnetic cooling applications, as usually it aims for temperature spans above 20 K (Gschneidner and Pcharsky, 2008), since although the material has large magnetocaloric effect and a regenerative cycle is used, the low temperature range of the effect means that the AMR has to be engineered in such way to contain several layers with slightly different T_C in each of them. Such engineering is not trivial and studies are still going on how to optimize such layers (Lei et al., 2015). The observable sharpness of the transition can also be affected by extrinsic factors, e.g. thermal diffusivity and T_C distribution, making it also more complicated to characterize FOPT magnetocaloric materials.

2. Crystal structure or volume change: The volume or crystal structure change observed in most FOPT magnetocaloric materials may be also detrimental to the mechanical stability of the regenerator during application, depending on change magnitude; and the mechanical properties and microstructure of the material. This is the case for FOPT La-Fe-Si alloys (Lyubina et al., 2010); in $La_{0.67}Ca_{0.33}MnO_3$ depreciation of mechanical integrity was not reported, as far as the author of this thesis knows.

3. Hysteresis: This is a feature of FOPT transition that ultimately leads to heat losses as it is well demonstrated by LoBue et al. (2005); von Moos et al. (2015). As in item 1, the observable hysteresis (magnetic or thermal) is also affected by extrinsic factors that must be considered when characterizing the material and analyzing the results.

Other challenges are also expected, nonetheless they are not a feature only exhibited by FOPT materials, but also SOPT. For example, one has to consider the chemical distribution which ultimately will spread the T_C of the material accordingly, and therefore other properties around the transition (Bebenin et al., 2013; Turcaud et al., 2014; Bez et al., 2016a). Moreover, oxidation issues, thermal conductivity, the shapeability of the material and rare-earth content have also to be considered.

2.3 Magnetocaloric materials - their properties and challenges

There is a broad range of magneticaloric materials with a significant magnetocaloric effect. They can be in an elemental for, e.g. Gd (Griffel et al., 1954); complex intermetallic alloys, e.g. La-Fe-Si alloys (Fujieda et al., 2003; Barcza et al., 2011) and MnFe(P,Si,B) (Guillou et al., 2014); and ceramics, e.g. manganites (Phan and Yu, 2007). As previously mentioned, the classification of these materials is nowadays given by the order of the transition. Here it will be adressed the general properties

of SOPT Gd alloys, as Gd isoften used as a reference. Moreover, the materials that are the focus of this thesis are also addressed here.

2.3.1 Gd alloys

Second order magnetic phase transition materials comprehend all elemental ferromagnetic materials, i.e. Fe, Co, Ni and Gd; and other compounds and alloys. As the Curie temperature of Fe, Co and Ni is way above room temperature, these are often disregarded but let us not forget that the magnetocaloric effect was discovered in a calorimetric measurement of Ni by Weiss and Piccard (1918). Gd being the material most used for devices up to the present date (Gschneidner and Pcharsky, 2008) needs some attention, even if the focus of this thesis is FOPT materials.

Gd is often used as a comparison when evaluating the performance a magneticaloric material. Just by being an elemental magnetocaloric material, it already present an extremely important property - it is very shapeable. As explained in Figure 2.2, the magnetocaloric material will need to dump or absorb heat, therefore the heat transfer between the material and the heat sink and heat source has to be optimized. Among many different properties of the material, being shapeable plays an important role (Engelbrecht et al., 2011).

Gadolinium presents a low peak of entropy change of about 3 $\mathrm{Jkg^{-1}K^{-1}}$ at $T_\mathrm{C} \sim 294$ K and a full width at half maximum of about 30 K, when $\mu_0 \Delta H = 1.0$ T. In addition, it has a low heat capacity of about 300 $\mathrm{Jkg^{-1}K^{-1}}$, and as we know from equation 2.11 this does not necessarily means the adiabatic temperature change will be small. In fact, even compared to FOPT materials the ΔT_ad difference is not large (Pecharsky and Gschneidner, 1997). The general behavior of its thermal and magnetic properties follow the ones shown in Figure 2.3. This properties are the reason why gadolinium and SOPT Gd alloys (Foldeaki et al., 1997) are used as AMR up to nowadays (Eriksen et al., 2015) in magnetic refrigeration.

2.3.2 Mixed-valence manganites

Another important series of magnetocaloric material series to be discussed is the mixed-valence manganites, which are mixed-valence manganese oxides with a general formula $\mathrm{RE}_{1-x}\mathrm{M}_x\mathrm{MnO}_3$, where RE stands for a rare-earth element and M for a metal. Usually RE is a trivalent element, e.g. La, Nd, Gd, Tb and Sm, while M is usually a monovalent or divalent metal, therefore usually an alkali or alkaline earth cation, e.g. Sr, Ca, K, Na and Ba (Coey et al., 1999; Phan and Yu, 2007). These compounds exhibit a large range of different crystallographic, magnetic, thermal and electronic properties that can be finely tuned with compositional adjustments. Here the focus will be $\mathrm{La}_{1-x}\mathrm{Ca}_x\mathrm{MnO}_3$, as it presents one of the best magneticaloric performances among the manganites (Turcaud et al., 2015; Phan and Yu, 2007). This series will be called LCMO series in this thesis.

The LCMO series may present different structural, electronic and magnetic properties depending on the amount of Ca doping. This series should exhibit a perovskite structure ($\mathrm{CaTiO_3}$), which is a face centered cubic structure with the RE element in the corners, the oxygen in the faces and the M cation in the octahedral site in between the oxygen atoms. Nevertheless, the stability of such structure depends on the sizes of the cations. Let us consider the cubic phase of a compound $\mathrm{ABO_3}$.

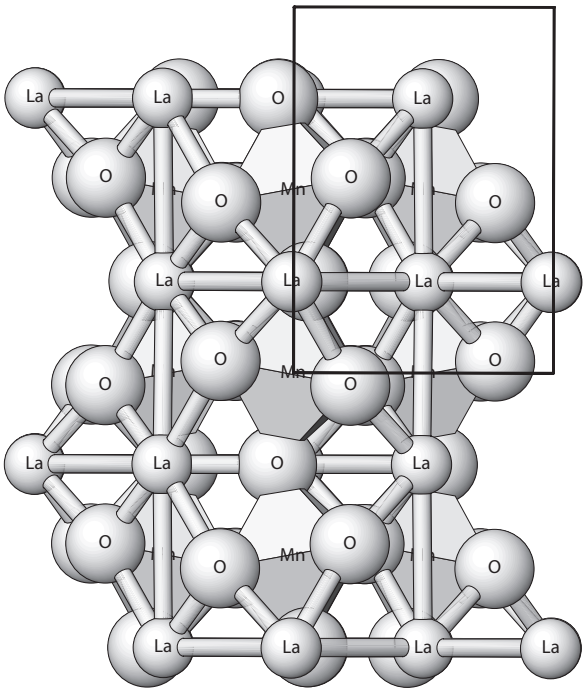

Figure 2.6: Schematic drawing of the crystal structure of $LaMnO_3$. One may observe the distortion of the MnO_6 octahedra. The black delineate rectangle represents the unit cell size.

The relationship between the size of the cations and stability of the cubic crystal structure was given by Goldschmidt (1958) as follows:

$$t' = \frac{r_A + r_O}{\sqrt{2}(r_B + r_O)}, \tag{2.12}$$

where r_A, r_B and r_O are the ionic radii of the A, B and O ions, respectively. The closer t' is to 1, the more stable will be the cubic structure. The unit will only be achieved if $r_A = r_O = 0.140$ nm, and $r_B = (2^{1/2} - 1)r_O = 0.058$ nm. The A-site cation are related to the oxygen through a twelve-fold coordination, and the B-site cation to a six-fold coordination (Goodenough, 2004).

When going away from the unit, different stable crystal structures may be found. For the parent compound of the mixed-valence manganite studied here, $LaMnO_3$, $t' \sim 0.95$. This variant of the perovskite structure has a severe distortion of the MnO_6 octahedra due to the Jahn-Teller effect, leading to the so called O'-type orthorhombic structure, where $c/\sqrt{2} < a < b$, and a, b and c are the unit cell parameters. The Jahn-Teller effect is the distortion of the octahedra site due to degenerate ground state of the Mn^{+3}, splitting the energy levels of this ion, hence lowering the energy (Coey et al., 1999). One may see a schematic drawing of the crystal structure of $LaMnO_3$ in Figure 2.6. The unit cell size is represented by the black delineate rectangle, and one may see the distortion of the MnO_6 octahedra.

Nevertheless, in the parent alloy the Mn atoms arrange themselves in a an-

tiferromagnetic structure with Néel temperature $T_N \sim 140$ K[5], where in the plane a-b the spins are coupled ferromagnetically, but the successive arrangement of the planes is antiferromagnetic (Wollan and Koehler, 1955).

In order to go for a ferromagnetic to paramagnetic phase transition, one may add solid solution given as $La_{1-x}M_xMnO_3$. Here there are several alkali and alkaline earth metals that may be added to change the magnetic ordering of the compound, which in this thesis the focus is with Ca solid solution. When calcium is added in solid substitution to the La-sites, a linear proportional part of the Mn becomes tetravalent, Mn^{+4}, due to the divalent Ca ion. The Jahn-Teller effect is less significant with the increase of Ca content, and the ferromagnetic ordering is observed for $La_{1-x}Ca_xMnO_3$ with $0.2 < x < 0.4$ (Billinge et al., 2000; Coey et al., 1999). Figure 2.7(a) shows the magnetic moments and electric conductivity as a function of x in $La_{1-x}M_xMnO_3$ at 80 K. As shown, the magnetization and the electric conductivity increase to a maximum value when $x \sim 0.3$.

Zener (1951) proposed an explanation for such behavior, which is the double exchange interaction between the 3d atoms, i.e. Mn. In his explanation, it is considered that the conductive electrons do not change their spin orientation when hopping from one atom to another, due to the strong intra-atomic Hund rule exchange energy. Furthermore, he introduced the concept of simultaneous exchange of electron from Mn^{+3} to O^{-2} and from O^{-2} to Mn^{+4}, which is called double exchange and it is always ferromagnetic.

The Curie temperature of such material varies with the Ca doping, and the transition form ferromagnetic to paramagnetic is around 255 K for $x = 0.3$ (Adams et al., 2004; Loudon and Midgley, 2006; Turcaud et al., 2015). Additionally, there have been several reports in the literature (Kumar et al., 1998; Jia et al., 2006a; Teresa et al., 1997) about the formation of magnetic polarons (clusters) in the paramagnetic phase. Magnetic polarons are formed by the exchange interaction of a carrier spin with the localized spins of magnetic atoms. This leads to a short-range alignment of spins resulting in a larger magnetic moment (Jacek Kossut, 2010).

In addition, it is observed that the Jahn-Teller distortion increases when the material undergoes the transition from ferromagnetic to paramagnetic (Billinge et al., 2000), giving a small volume change across the magnetic transition of about 0.1 % (Teresa et al., 1996) also known as spontaneous magnetostriction. This is discussed in terms of a magneto-elastic coupling (Turcaud et al., 2015). Evaluations of the bulk modulus as a function of the temperature via sound-velocity measurements (Zhu et al., 1999) on $La_{0.67}Ca_{0.33}MnO_3$ suggest that there is a softening of the lattice modes around the phase transition, as may be observed in Figure 2.7(b). One can see that the softening is much greater in the ferromagnetic phase than in the paramagnetic phase, strengthening the argument of a magneto-elastic coupling in the ferromagnetic region.

There is a debate in literature regarding if $La_{1-x}Ca_xMnO_3$ present a first-order magnetic phase transition or a second order, in particular for $x \sim 0.3$. Thermal hysteresis has been observed (Lin et al., 2006), although magnetic hysteresis has been ruled out (Morrison et al., 2011). Although no latent heat was observed during the magnetic transition as well (Morrison et al., 2011), careful modelling

[5]Néel temperature is the temperature where the material transits from an antiferromagnetic to a paramagnetic state.

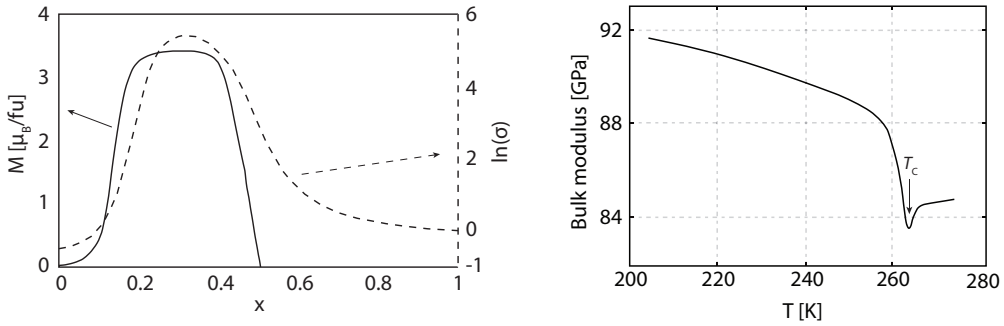

(a) (b)

Figure 2.7: (a) Ferromagnetic moment and electric conductivity of $La_{1-x}Ca_xMnO_3$ as a function of x measured at 80 K. This image is an adaptation from Coey et al. (1999), graph shown in page 172.. (b) Bulk modulus of $La_{0.67}Ca_{0.33}MnO_3$ as function of the temperature. This image is an adaptation from Zhu et al. (1999), graph shown in page 4.

of $La_{0.7}Ca_{0.3}MnO_3$ has suggested that the material presents a first-order transition (Turcaud et al., 2015). Additionally, discussions regarding the broadening of the transition due to chemical distributions residual from the fabrication methods have been reported (Bebenin et al., 2013). In Chapter 4 there is a further discussion about the nature of the order of the phase transition, thermal hysteresis, and studies related to the chemical distribution and magnetocaloric properties of $La_{0.67}Ca_{0.33}MnO_3$.

2.3.3 La-Fe-Si alloys

Regarding FOPT magnetocaloric materials, there are currently two trends for which material to use in a magnetic cooling device; Fe_2P-based materials (Tegus et al., 2002) and La-Fe-Si alloys (Krypiakewytsch et al., 1968). In this thesis, the focus will be given in La-Fe-Si alloys, particularly in the $La(Fe,Mn,Si)_{13}H_z$ family.

Buschow and Velge (1967) discovered that $LaCo_{13}$ stabilized on a $NaZn_{13}$-type crystal structure presents ferromagnetic properties. One year later Krypiakewytsch et al. (1968) showed that one could add Si as a solid solution in the transition metal site in order to stabilize the same structure, making it possible to have the transition metal Fe instead of the Co. Later Palstra et al. (1983) have shown that $La(Fe_{1-x}Si_x)_{13}$ exhibit a critical behavior in their temperature dependence of the magnetization. Additionally, the Curie temperature could be finely tuned by the Fe/Si ratio, while compromising the critical behavior of the magnetic transition with the increase of Si content. However, the T_C of this compound is in the low temperature range of $190 < T_C < 220$K, which makes it difficult to use for magnetic cooling applications around room temperature.

Fujieda et al. (2001) have shown that by interstitially inserting H, the T_C of $La(Fe,Si)_{13}H_z$ increases to the room temperature range. Moreover, by controlling the amount of H, the T_C could be tuned in the range $190 < T_C < 325$ K Fujieda et al. (2003). Nevertheless, the hydrogen when not saturated in the structure tends

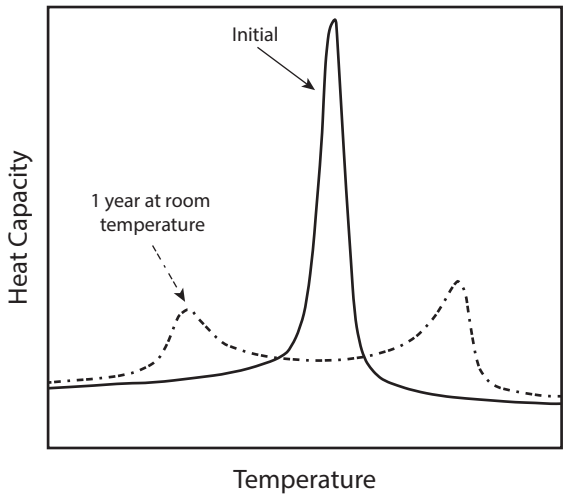

Figure 2.8: Heat capacity as a function of the temperature, showing the age splitting effect in an H unsaturated $La(Fe,Si)_{13}H_y$ sample. This image is an adaptation from Zimm and Jacobs (2013), graph shown in page 2.

to diffuse and concentrate over time in different regions of the sample, leading to a splitting of the transition temperature (Zimm and Jacobs, 2013). This is schematically shown in Figure 2.8, by the heat capacity peak split after the sample is at rest for one year at room temperature.

Barcza et al. (2011) proposed a method to overcome this challenge. The proposed solution is to substitute some of the Fe atoms by Mn, and the ratio of Fe/Mn/Si controls the T_C, while the H is always fully saturated. This allowed to overcome the instability of H, and finely tune the Curie temperature around the room temperature, whilst without much degradation of the magnetocaloric properties. Still, with increasing contents of Mn and Si, the phase transition tends to go from first order to a second order one.

The phase transition of $La(Fe,Si)_{13}H_z$ can be ascribed as a itinerant electron metamagnetism (IEM) transition, which is a first-order transition arising from the partially non-localized character of the Fe moments (Gruner et al., 2015). The IEM transition occurs from a Pauli paramagnetic[6] phase to an itinerant electron ferromagnetic phase (Fujita et al., 2001; Liu et al., 2006), and apart from being observed in Pauli exchange-enhanced paramagnets, this phenomenon is also correlated to spin fluctuations Saito et al. (2000). Additionally, these fluctuations give rise to different effects, e.g. magneto-volume effects and large electronic heat capacity coefficient (Gruner et al., 2015; Liu et al., 2006).

As Fujita et al. (2001) have shown, the $La(Fe,Si)_{13}H_z$ also presents the magneto-volume effect, i.e. spontaneous magnetostriction. It was shown that the thermally

[6]Pauli paramagnetism arises from the difference in magnetic potential energy between spin up and spin down electrons. When a magnetic field is applied in a conductive material, the magnetic potential energy of the electron is raised or lowered depending on the electron spin state. This gives to the material a larger paramagnetic susceptibility due to the electron gas, and this is known as the Pauli paramagnetism (Blundell, 2001).

induced FOPT corresponds to the IEM transition for a field $\mu_0 H = 0$ T. In addition, it was shown that the IEM transition is a conclusive evidence of the two minima picture of the Gibbs free energy, shown previously in Figure 2.4. Furthermore, as the material presents a $NaZn_{13}$-type crystal structure both in the FM and PM phase, this is a plain volume change without crystal structure change. By thorough X-ray diffraction (characterization method explained in the section 3.3), Fujita et al. (2001) have shown that the material presents a discontinuous volume change at the T_C region, with some temperatures showing a co-existence of FM and PM, which was attributed to super-cooling effects.

The $La(Fe,Mn,Si)_{13}H_z$ series has already been well characterized regarding the magnetocaloric properties, and the publication by Basso et al. (2015) summarizes them well.

2.4 Models

Several different models try to describe the thermal, magnetic and structural properties as well as the phase transition of magnetocaloric materials. In this section, the models involved in this thesis are introduced.

2.4.1 The Curie-Weiss Law

The Curie-Weiss law describes how the susceptibility of a ferromagnet behaves in the paramagnetic state as function of the temperature. At the time (prior the discovery of quantum effects), Weiss observed that some materials experience a large magnetic field even though the applied magnetic field is low. He then postulated a term to the magnetic field experienced by the material, the Weiss molecular field constant λ; the total field that the material experiences would be $H_{tot} = H_{app} + \lambda M$, where H_{app} is the applied magnetic field, and λ gives the correlation between magnetization of the material and the experienced field. From this postulation the following equation was derived:

$$\chi(T) = \frac{\rho_s g^2 \mu_B^2 [J(J+1)]}{k_B (T - T_C)}, \tag{2.13}$$

where χ is the magnetic susceptibility, ρ_s is the spin density, g is the Landé factor, μ_B is the Bohr magneton, J is the total angular momentum and k_B is the boltzmann constant. Later on Heisenberg has shown that this field originates from a quantum-mechanical exchange interaction (Buschow and de Boer, 2004) between the magnetic spins. The behavior of the susceptibility of a paramagnetic phase may lead to important information. For example, Jia et al. (2006a) have shown that by applying a modification of the Curie-Weiss law, they could calculate sizes of magnetic polarons. Still, the Curie-Weiss approach works only for paramagnetism, and the ferromagnetic behavior and the transition itself have yet to be considered, and the next subsection will describe the approach within the mean field theory (MFT).

2.4.2 Mean field theory and the Bean-Rodbell model

The mean field theory attempts to describe the behavior of complex and large statistical models by using a simpler one. What is done, basically, is to divide the large system in small components that interact with each other by an exchange field. One

can think of it as if all the spins experience an identical average exchange field, which is created by the neighbouring spins (Blundell, 2001). This field is proportional to the magnetization of the material. One of the models within MFT is the nearest neighbour Heisenberg model. It considers microscopic models of magnetic interactions. In this model the spins are considered quantum-mechanically, and in this case the dominant spin coupling mechanism may lead to a energy minima where the closest neighbouring magnetic dipoles are all aligned. From the Heisenberg model one derive the magnetization

$$M(T,H) = \frac{N}{V} g\mu_{\mathrm{B}} J B_J(x), \tag{2.14}$$

where N is the number of magnetic atoms in the volume V. $B_J(x)$ is the Brillouin function:

$$B_J(x) = \frac{2J+1}{2J}\coth\left(\frac{2J+1}{2J}x\right) - \frac{1}{2J}\coth\left(\frac{1}{2J}x\right), \tag{2.15}$$

and x is given by

$$x = \frac{g\mu_0\mu_{\mathrm{B}}(H_{app} + \lambda M(T,H))J}{k_{\mathrm{B}}T}, \tag{2.16}$$

and the magnetization can then be solved numerically. Here we see again λ, which in this case represents the exchange constant, and it can be calculated by the following equation within the Heisenberg model

$$\lambda = \frac{3T_{\mathrm{C}}k_{\mathrm{B}}}{g^2\mu_0\mu_{\mathrm{B}}^2 J(J+1)}\frac{V}{N}. \tag{2.17}$$

While this approach manages to predict second order phase transitions well, it fails to describe FOPT due to its inherent discontinuity in the transition. Bean and Rodbell (1962) reasonably proposed that the exchange constant in fact should vary with the volume of the material, since this would mean a change of the spin-spin distances. What they did was to add a term to the exchange constant which is a function of the volume change

$$\lambda = \lambda_0\left[1 + \beta\left(\frac{V - V_0}{V_0}\right)\right], \tag{2.18}$$

since we see in equation 2.17 that λ is proportional to T_{C}

$$T_{\mathrm{C}} = T_0\left[1 + \beta\left(\frac{V - V_0}{V_0}\right)\right], \tag{2.19}$$

where T_0 is the Curie temperature of the system when V is constrained to V_0, which is the volume at 0 K in the absence of strains introduced internally, e.g. by exchange interactions, or externally for example by applied stresses. The parameter β controls the spin-lattice coupling strength. In an analogous way to λ,

$$\lambda_0 = \frac{3T_0k_{\mathrm{B}}}{g^2\mu_0\mu_{\mathrm{B}}^2 J(J+1)}\frac{V_0}{N}. \tag{2.20}$$

Let us now consider the total free energy per volume of a purely ferromagnetic interaction of a material,

$$G = G_{\mathrm{magnetic}} + G_{\mathrm{pressure}} + G_{\mathrm{elastic}}, \tag{2.21}$$

where G_{magnetic} is the free energy related to the field and exchange; G_{pressure} is the pressure term and G_{elastic} is the elastic term. The total free energy per volume will be then

$$G(T,P,H;M,V) = -TS_{\text{mag}} - \mu_0 MH - \frac{1}{2}\lambda\mu_0 M^2 + \frac{1}{2\kappa}\frac{(V-V_0)^2}{V_0^2} + P\frac{V-V_0}{V_0}, \quad (2.22)$$

where κ is the compressibility, which is the reciprocal of the bulk modulus, and P is the pressure. S_{mag} is the magnetic entropy per volume and can be defined by

$$S_{\text{mag}} = k_{\text{B}}\frac{N}{V}\left[\ln\frac{\sinh(\frac{2J+1}{2J}x)}{\sinh(\frac{1}{2J}x)} - xB_j(x)\right]. \quad (2.23)$$

The electronic and lattice contributions to the entropy will be introduced later on this subsection through the free electron model and the Debye model. By minimizing the total free energy in respect to the volume, we can calculate the equilibrium volume:

$$\frac{V-V_0}{V_0} = \frac{1}{2}\lambda_0\beta\kappa\mu_0 M^2 - P\kappa. \quad (2.24)$$

The first outcome of the model can be seen in equation 2.24; the volume changes with the square of the magnetization. Moreover one may see how κ and β play an important role in this relation between volume and magnetization. Additionally, if one consider a discontinuous magnetic transition, this equation shows that the volume will change discontinuously as well.

Bean and Rodbell (1962) showed that if β is positive, one can expect negative thermal expansion around the phase transition, related to the decrease of the magnetization. This is schematically illustrated in Figure 2.9(a). It is important to note that negative thermal expansion can happen even if the transition is second order.

The equilibrium magnetization can be calculated by substituting equation 2.24 in 2.22 and minimizing it in respect to magnetization. The resulting equation has then to be solved numerically. Upon evaluating numerically two minima will be found for FOPT. The correct minimum will depend on the *hystory* of the material as explained in Figure 2.4. The details of the calculations may be found in the original paper by Bean and Rodbell (1962). In addition, one of the outcomes of the model is the η parameter. This parameter dictates the order of the transition, and can be calculated by the following:

$$\eta = 40\frac{N}{V_0}k_{\text{B}}\kappa T_0\beta^2\frac{[J(J+1)]^2}{(2J+1)^4-1}, \quad (2.25)$$

where for $\eta \leq 1$ the transition is second order and for $\eta > 1$ the transition is first order. One can see the magnetization behavior as a function of the temperature for different η values in Figure 2.9(b); $\eta = 0$ gives the behavior of the material with a SOPT, as shown in Fig. 2.3(a). For $\eta = 0$, one gets back that $\lambda = \lambda_0$ and $T_{\text{C}} = T_0$ and there is no magneto-elastic coupling. As η increases towards the unit, the transition behaves "less continuously", nonetheless still continuous. Moreover, one can see that once $\eta > 1$, the transition occurs in a temperature $T_{\text{C}} > T_0$.

In the Bean-Rodbell model some assumptions are taken, which in return give some limitations to it. First of all, the model assumes that the material is completely homogeneous. Several reports have shown that inhomogeneities may broaden

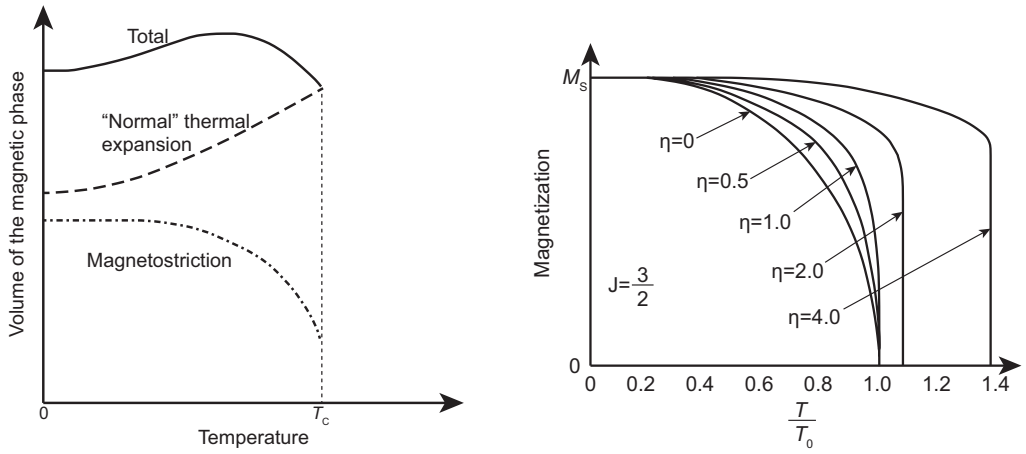

(a) (b)

Figure 2.9: (a) Volume of the magnetic phase as a function of the temperature, showing the effect of the magnetostriction in the thermal expansion. (b) Magnetization as a function of the relative temperature for different η values and $J = 3/2$. Both graphs are adapted from Bean and Rodbell (1962), pages number 109 and 112, respectively.

the transition, in a way it is no longer discontinuous overall. The solution proposed for this was to apply a normal distribution in T_0 in order to simulate the inhomogeneities, and the results showed then a good agreement with measured data (Bahl et al., 2012; Bebenin et al., 2013; Turcaud et al., 2014). Moreover, the model assumes isotropic elastic changes in the transition, although Bean and Rodbell (1962) showed that even if this assumption is not true for the analyzed material MnAs, the modelled magnetic properties were in good agreement with the measured ones. Additionally, the compressibility is considered to be constant with temperature, while we know from Figure 2.7(b) that this is not the case.

2.4.3 Heat capacity contributions

The electronic and lattice contributions to the entropy are taken into consideration through the free electron model and the Debye model. Since in this thesis most of the discussions are given in respect to the heat capacity, here these entropy contributions are shown in terms of the heat capacity. The heat capacity can be defined by its different contributions:

$$c(T, H) = c_{\text{Debye}}(T) + c_{\text{Sommerfeld}}(T) + c_{\text{magnetic}}(T, H). \tag{2.26}$$

The free electron model is used to describe the conductive electrons in a material. It was mainly developed by Arnold Sommerfeld, hence it is also known as Sommerfeld model. The electronic contribution to the heat capacity within this model can be calculated by

$$c_{\text{Sommerfeld}}(T) = \gamma_e T, \tag{2.27}$$

and,

$$\gamma_{\mathrm{e}} = \frac{\pi^2 (3\pi^2)^{-2/3} m_{\mathrm{e}} k_{\mathrm{B}}^2}{\hbar^2} \left(\frac{N_{\mathrm{c.e.}}}{V} \right)^{1/3}, \tag{2.28}$$

where γ_{e} is the Sommerfeld constant, m_{e} is the electron mass and $N_{\mathrm{c.e.}}$ is the number of conductive electrons in V.

The Debye model (Debye, 1912) estimates the contribution of the phonons to the heat capacity of the material. It uses the concept that the vibration of the lattice works as if phonons in a box. The heat capacity contribution calculated through this model gives,

$$c_{\mathrm{Debye}}(T) = 9 \frac{N_{\mathrm{atoms}}}{V} k_{\mathrm{B}} \left(\frac{T}{\Theta_D} \right)^3 \int_0^{\Theta_D/T} \frac{y^4 \mathrm{e}^y}{(\mathrm{e}^y - 1)^2} dy, \tag{2.29}$$

where N_{atoms} is the number of atoms in the volume V, and Θ_D is the Debye temperature. Although this model describes well the low temperature heat capacity, the discrepancy increases in high temperatures and for high temperatures the Einstein model of solids have a better agreement. Still, in the temperatures investigated in this thesis, the Debye model should give a good description of the lattice contribution to the heat capacity.

The magnetic contribution to the heat capacity is derived through the MFT, and is given by (Morrish, 2001)

$$c_{\mathrm{mag(T,H)}} = -\mu_0 H \left(\frac{\partial M}{\partial T} \right) - \mu_0 \lambda \left(\frac{\partial M^2}{\partial T} \right), \tag{2.30}$$

One can see in equation 2.30 that if there is a discontinuity in M for a given $\mu_0 H$, there will be an infinitely sharp peak on the heat capacity, as expected for a first order phase transition (Hillert, 2008; Çengel and Boles, 2006).

Chapter 3

Characterization methods

In this chapter, the characterization methods used in this thesis are presented. Here is shown and explained each one of the characterization methods, which includes: calorimetry, vibration sample magnetometry, capacitance dilatometry, scanning electron microscopy and regenerative testing device.

3.1 Calorimetry

As it was shown in the previous chapter, one of the many ways to qualify a magnetocaloric material is by the heat capacity, especially across the phase transition. One can infer many characteristics of the material through such measurement: transition temperature as function of magnetic field, chemical inhomogeneities and indirectly estimate the entropy as function of temperature and field (Franco et al., 2012; Smith et al., 2012). The heat capacity is usually measured by calorimetric measurements, which are, in the purest way, a measurement of heat flux inward or outward a sample. Heat capacity measurements done in scanning calorimeters are thermally dynamic, where the heat flux, $\dot{Q}$, is measured as a function of a varying temperature:

$$C_{P,H} = \left(\frac{\delta Q}{\delta T}\right) = \left(\frac{\delta Q/\delta t}{\delta T/\delta t}\right) = \left(\frac{\dot{Q}}{\dot{T}}\right), \tag{3.1}$$

where $C_{P,H}$ is the heat capacity at constant applied pressure and magnetic field, and $\dot{T}$ is the temperature rate. In this thesis, two differential scanning calorimeters (DSC) are used to characterize the materials. One is a commercial calorimeter which was used to characterize the heat capacity in a wide range of temperature. However, this DSC does not allow to conduct experiments with applied magnetic fields. Therefore, a custom-built DSC is used to characterize the heat capacity under applied magnetic fields, but in a shorter temperature range. The following two subsections will address these two DSCs and the experimental methods involved.

3.1.1 Custom-built DSC

This DSC consists basically of four parts: the Halbach magnet assembly, the sample chamber, the cold bath reservoir and the control's and data acquisition's system (Jeppesen et al., 2008). A schematic drawing of the sample chamber is shown in figure 3.1. A picture of the sample chamber may be seen in Appendix A.1.3. The

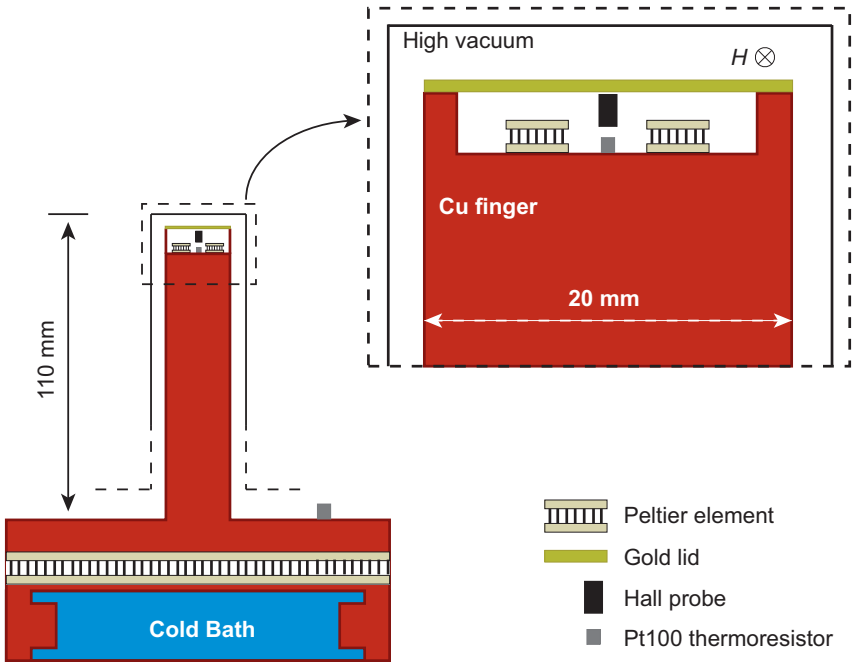

Figure 3.1: Schematic drawing of DTU's custom-built DSC.

overall temperature of the sample chamber is controlled by the cold bath reservoir temperature, which is connected to the bottom of the sample chamber. between the cold bath and the Cu finger there is a peltier element which is used for varying and controlling the temperature of the Cu finger, by using the temperature sensor Pt100 thermoresistor at the bottom of the Cu finger as a feedback. The cold bath reservoir temperature is set to 274 K and the peltier element can then control the temperature of the Cu finger from 238 K to 328 K. The lower bound is due to the limited cooling power of the peltier in this system, while the upper bound is due to the wiring and glued components.

The whole copper finger is enclosed in an Al housing in order to keep high vacuum, with pressures below 1e-5 mbar. At such low pressures the conductive and convective thermal loses are minimized (von Moos et al., 2014). A golden lid is used to avoid irradiation issues. The Cu finger is then inserted in the Halbach magnet assembly with two concentric Halbach magnets. By counter rotating the magnets with the same angular velocity magnitude, the direction of the magnetic field in the sample chamber is kept constant (see direction in figure 3.1), therefore the assembly is able to vary the magnetic field from 0 to 1.5 T with a homogeneous field, and field change rates from 0.005 to 1 T/s. A schematic drawing of the magnet assembly is shown in figure 3.2. In the lower right the graph shows a magnetic field measured by the Hall probe as a function of the angle between the magnets.

The temperature on the top of the Cu finger is measured by another Pt100 thermoresistor. Moreover, in the top of the cold finger there are two virtually identical peltier elements, and they are the main part for the heat flux measurement. Their features may be seen in Table 3.1.

Peltier elements are mainly composed by thermoelectric materials. These materials create a electrical potential when a temperature gradient is created – the

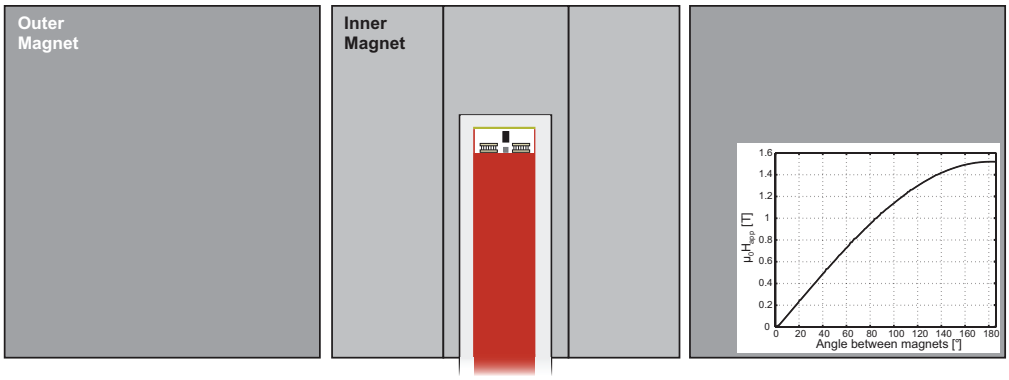

Figure 3.2: Schematic drawing of the Halbach magnet assembly. The graph on the right shows the magnetic field in the air gap as a function of the angle between magnets.

Type	Peltier OT08,11,F1,0305,11,w2.25
Dimensions	4.88x3.25x2.44 mm
$\dot{Q}_{\max}$**@** T_r	0.6 W @ 298 K
$\Delta T_{\max}$**@** T_r	67 K @ 298 K
Ohmic resistance @ T_r	1.43 Ω @ 298 K

Table 3.1: Peltier element characteristics.

so-called Seebeck effect − and it can be given as follows:

$$U = -S\Delta T \tag{3.2}$$

Where U is the electric potential difference, S is the Seebeck coefficient of the material and T is temperature. If one consider now a sample on one of the peltier elements, with a contact area A_c and mass $m_{\rm s}$, Fourier's law tells us that the heat flux through a material is given by

$$\dot{Q} = -A_c k \frac{\partial T}{\partial x}, \tag{3.3}$$

where k is the thermal conductive coefficient of the peltier. Assuming a linear temperature gradient within the peltier element:

$$\dot{q} = \frac{\dot{Q}}{m_s} = -A_c k \frac{\Delta T}{m_s L}, \tag{3.4}$$

where L is the peltier length and A_c is the contact area. Comparing now equations 3.1, 3.2 and 3.4, the following relation may be found between heat flux and potential difference

$$c(T,H)_{P,H} = \frac{A_c k}{LS} \frac{U(T,H)}{m_s \dot{T}}. \tag{3.5}$$

Now comes to play the second peltier element on the top of the Cu finger. All calorimeters use a couple of heat fluximeters, so the output U is the difference between the signal from the sample's peltier element and the second one. This is

used in order to minimize contributions to the signal due to the peltier itself, as given by the following equation

$$c(T,H)_{P,H} = \frac{A_c k}{LS}\frac{(U_\mathrm{s}(T,H) - U_{emp}(T))}{m_s \dot{T}} = \frac{A_c k}{LS}\frac{\Delta U_\mathrm{s}(T,H)}{m_s \dot{T}}, \tag{3.6}$$

where U_s and U_{emp} are the potential difference of the sample's peltier and the second peltier, respectively, and ΔU_s should have contributions from the sample itself only. However, the assumption that both peltier are identical, can be further ensured by performing a measurement where both peltiers are empty and applying it in the calculation as:

$$c(T,H)_{P,H} = \frac{A_c k}{LS}\frac{(\Delta U_s(T,H) - \Delta U_0(T))}{m_s \dot{T}}, \tag{3.7}$$

where ΔU_0 is the difference when both peltiers are emptied. During the measurements, however, one of the peltier is never truly empty. The sample's peltier always has a layer of grease add, since when the a sample measurement is run a small amount of thermal conductive grease is add to improve the signal/noise ratio.

In order to take out the peltier's parameters, a standard calibration method is used (Höhne et al., 2003). In this method a standard reference material, in this case a Cu sample (99.999 % trace metal basis), is used as a reference material, since its heat capacity is already well stablished (White and Collocott, 1984). The heat capacity of the reference will be then:

$$c(T)^{ref}_{P,H} = \frac{A_c k}{LS}\frac{(\Delta U_r(T) - \Delta U_0(T))}{m_r \dot{T}}, \tag{3.8}$$

where ΔU_r and m_r are the potential difference and the mass of the reference, respectively. Now applying the measured data, and the literature values of the heat capacity of Cu in equation 3.8 one can calculate the contribution of the peltier parameters($A_c k/LS$) as a function of the temperature, as shown in Figure 3.3 for a temperature rate of 1 K/min. By using a fitted curve, one can subtract the noises contributions to the sample's $c_{P,H}$ calculation.

Usually, other standard calibration samples are necessary, in particular for temperature calibration (Höhne et al., 2003). What is usually done is to measure a material with a first order phase transition within the temperature range of the equipment, with different temperature rates. By applying a linear regression of the transition temperatures with respect to the temperature rate, one can find out what would be the real temperature the material is observing. This was done previously using Ga as an standard material (von Moos et al., 2014). He showed by careful measurements that the temperature measured by the Pt100 sensor has an offset of about 0.9 K. Still, there are two issues on the temperature calibration which are not solved by this approach:

i The sample shape and mass. Even though there is a thermal conductive grease between the sample and peltier element, the contact area may vary from sample to sample, even if they present the same mass. Therefore, by using a standard material to calibrate the temperature one does not account for the different contact areas, which will lead to different thermal contact resistance.

ii The thermal diffusivity of the sample. The measured transition temperature will be affected by the thermal diffusivity of the respective material, therefore

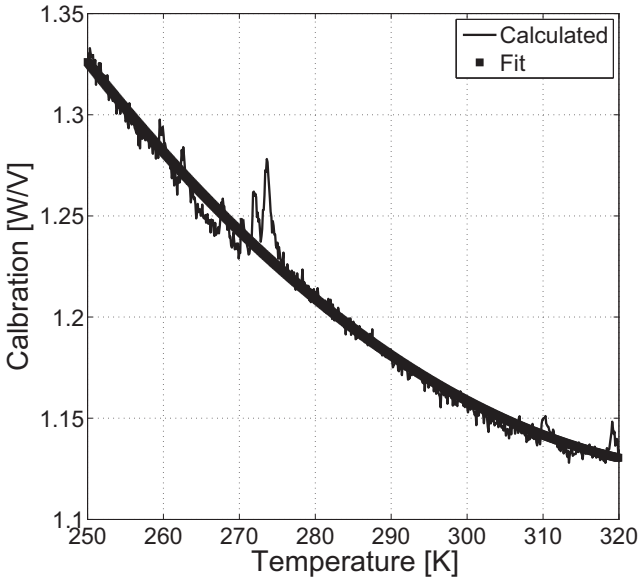

Figure 3.3: The calibration of the peltier signal, from a measurement of a pure Cu sample.

a standard material would account this feature only for materials with similar thermal conductivities.

These two issues build up on each other. Therefore, here each sample is measured in different temperature rates, and the linear regression is performed for each of them. It is important to note that using this approach the temperature will not be accurate, but it will be precise. This is particularly important for thermal hysteresis determination, as it will be shown in the next chapters of the thesis.

Direct measurement of isothermal entropy change

The option of continuously vary the magnetic field, and the low convection and irradiation losses make it possible to measure directly the isothermal entropy change. By combining equation 3.2 and 3.4:

$$\Delta s_T(T, H_i, H_f) = \frac{q}{\frac{t_i \to t_f}{T}} = \frac{A_c k}{m_s LST} \int_{t_i}^{t_f} \Delta U_s(T, t_i, t_f) dt, \tag{3.9}$$

where H_i and H_f are the initial and final applied field, t_i is the time when the field first started to vary, and t_f is the time at which the potential difference does not present significant difference to the background noise level. Figure 3.4 shows an example of a measurement of a Gd sample, with $H_i = 0.01$ and $H_f = 1.26$ T, and a field change rate of 0.1 T/s.

As the schematic drawing in figure 3.1, the sample temperature is not directly measured, but measured at the top of the cold finger. The high vacuum assures that the only possible loss mechanism is radiation, in other words:

$$\dot{Q}_{loss} = \alpha A_s (T_{amb}^4 - T_s^4), \tag{3.10}$$

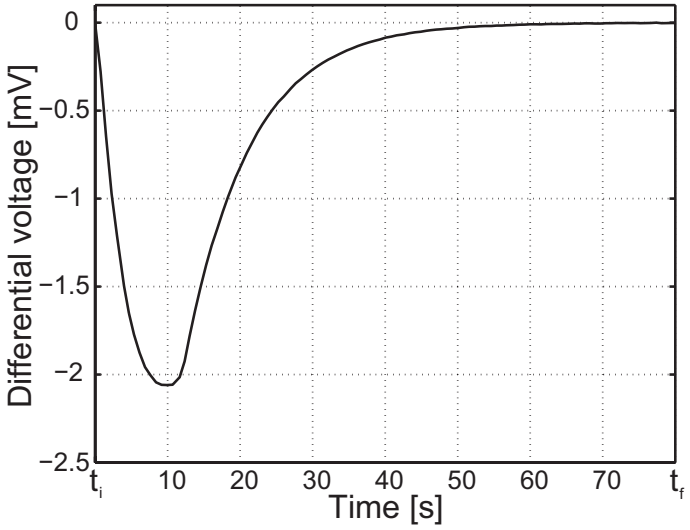

Figure 3.4: Potential difference of a Gd sample of 38.9 mg. The field change was from 0.01 T to 1.26 T with a rate of 0.1 T/s.

where α is the Stefan-Boltzmann constant, A_s is the sample's surface area, and T_{amb} a T_s are the ambient and sample temperature. The emissivity of the sample is assumed to be one. Since radiation is the only loss mechanism, and assuming steady state, the temperature difference from the sample to the top of the Cu finger is given by:

$$\Delta T_s = T_s - T_{Cu} = \dot{Q}_{loss} R, \tag{3.11}$$

Where R is the thermal resistance of the peltier and $R = \dot{Q}/\Delta T_{\max} = 112$ KW^{-1}, and T_{Cu} is the temperature in the top of the Cu finger. By combining equations 3.10 and 3.11, one gets a four order polynomial, which can be solved numerically. Figure 3.5 shows ΔT_s as a function of the measured T_{Cu}, for different T_{amb}. The results shown in this thesis are then corrected for the temperature difference here described. Additionally, the error propagation from the different possible contributions to the Δs measurement were calculated and an error of about 7% is observed. The details of the error propagation is shown in Nielsen et al. (2015), which is Appendix A.1.3 in this thesis.

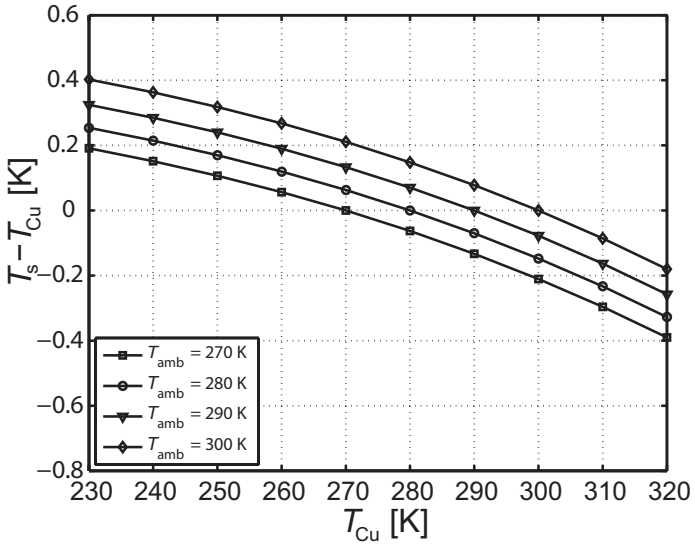

Figure 3.5: Temperature difference between the sample and and the temperature measured by the Pt100 sensor at the top of the cold finger, for different ambient temperatures.

3.1.2 Fitting procedure

In order to do modelling, it is important to have data with low noise level. Therefore, in this thesis fitting procedures were used when needed. The fitting is performed in such way to optimize the agreement in the transition region.

One could qualify the peak as an asymmetric Lorentzian distribution. So, in order to properly fit, the transition region is separated in two regions, before and after the peak temperature, T_{peak}, and the following fitting function is used:

$$c(T,H)_{P,H} = a_1(T - T_{peak}) + \begin{cases} (Y - b_{11})(\frac{d_{11}^2}{d_{11}^2 + (T - T_{peak})^2}) + b_{11}, & \text{if } T < T_{peak} \\ (Y - b_{21})(\frac{d_{21}^2}{d_{21}^2 + (T - T_{peak})^2}) + b_{21}, & \text{if } T \geq T_{peak} \end{cases}, \tag{3.12}$$

where Y is the peak value of the heat capacity, b is the background heat capacity level, d is the full width at half maximum (FWHM) and a_1 is the slope of the heat capacity for $T < (T_{peak} - 10)$. Figure 3.6 shows am example of the fitting for a magnetocaloric material. The different fitting parameters are shown, with the exception of a_1. As the graph shows, there is a good agreement between the fitting and the measurement. Therefore, the fitted curves will be used when modelling is performed, unless explicitly stated otherwise.

3.2 Vibrating sample magnetometry

In order to measure the magnetic properties of the different materials vibrating sample magnetometry (VSM) is used (Foner, 1959). The basic principle of measurement in this device is the Faraday's law, i.e. if an external magnetic field is varied on a conductive coil a current proportional to the magnetic field change rate, i.e. time derivative of the magnetic flux, is generated. In this thesis, VSMs slightly different

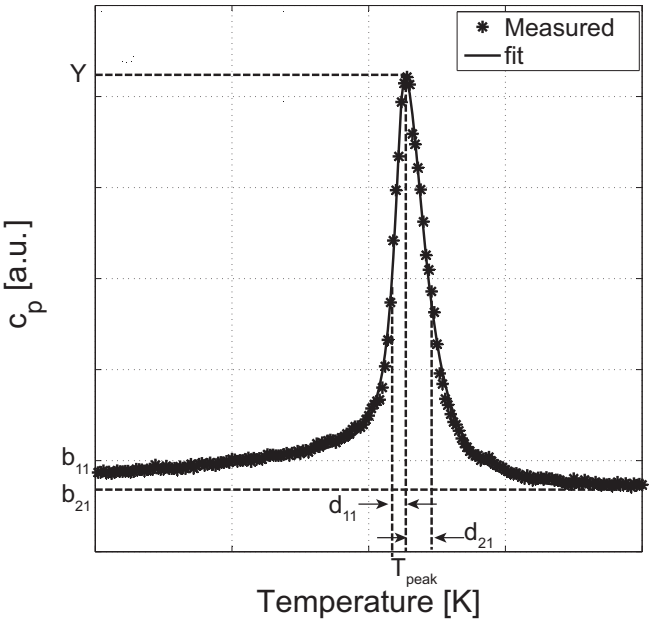

Figure 3.6: Heat capacity as a function of temperature of a magnetocaloric material. One may see the good agreement between the fitting and the measured data.

from that of Foner are used, but the measurement principle is the same. Figure 3.7 shows a schematic drawing of the VSMs used in this thesis. A sample is attached to the vibrating rod and by vibrating it vertically, in between the 2 pairs of pick up coils (the upper pair, and bottom pair), which are purposely wounded in different directions, so the signal measured by each pair of coils interferes constructively.

One of the most characterized properties of a magnetocaloric material is Δs, due to its importance and relative ease of measurement/calculation. By isothermal magnetization measurements one can calculate it using the Maxwell relation assuming equilibrium conditions, resulting in:

$$\Delta s(T, H_i; H_f) = \mu_0 \int_{H_i}^{H_f} \left(\frac{\partial M(T)}{\partial T} \right)_H dH. \tag{3.13}$$

Where H_f and H_i are the final and initial applied magnetic field, respectively; M is the magnetization, H is the applied magnetic field and T is the temperature. Using numerical methods to evaluate the derivative and integration one can find a method to quantify the magnetic entropy change by isothermal magnetization measurements:

$$\Delta s(T_n, H_0; H_k) \approx \mu_0 \sum_{k'=0}^{k} \frac{M_{n+1,k'} - M_{n-1,k'}}{T_{n+1} - T_{n-1}} (H_{n,k'+1} - H_{n,k'}). \tag{3.14}$$

Where n and k are the index labels corresponding to the isothermal measurement and applied magnetic field, respectively. This approximation facilitates the process of calculating Δs. Nevertheless, one must be careful when setting the experimental procedure of the isothermal magnetization measurements in order to assure

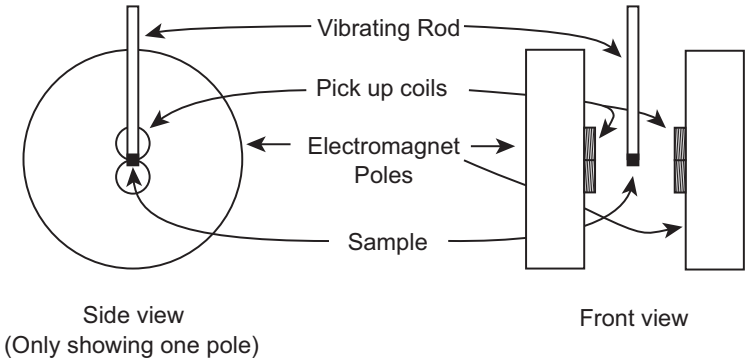

Figure 3.7: Simplistic schematic drawing of the VSMs used in this thesis.

reliable results, as many different parameters may be set differently, e.g. magnetic field and temperature sweep rates, the temperature step for the isothermal magnetization measurements, among others. Pecharsky et al. have shown that the errors related to measurement imprecisions may be built up depending on the combination of the measurement setup used (Pecharsky and Gschneidner, 1999).

The demagnetization factor of prism-shaped samples was taken into consideration using the method proposed by Aharoni (1998). Nonetheless, when measuring packed powders and irregular shaped particles, the approach proposed by Aharoni (1998) can no longer be used. In this thesis, the approach for this problem is the following. Firstly, the sample is brought to a temperature $T_0 << T_C$ where it is fully ferromagnetic and the applied field, H_{app}, is then varied from 0 T to a maximum field H_{max}. The demagnetization factor, N_d, will be the one that minimizes the internal field $H_{int} = H_{app} - \mu_0 N_d M(T_0, H_{int})$, while keeping $\mu_0 dM(T_0, H_{int})/dH_{int} > 0$. Figure 3.8 shows a magnetization curve of a $La(Fe,Mn,Si)_{13}H_z$ sample as a function of the internal magnetic field correcting for demagnetization, $N_d = 0.202$, and not correcting for it, $N_d = 0$, at $T_0 = T_C - 20$.

In this context, one of the setting parameters which has not been given sufficient importance is the temperature grid of the measurements, here called δT, where $\delta T = 1/2(T_{n+1} - T_{n-1})$. One may notice in the literature that there is not a standard or much comprehension of how much this parameter may affect the calculated Δs. Furthermore, in isothermal magnetization measurements a fine temperature grid may lead to two dependent issues: i) due to fluctuations on the temperature, noise is generated in the data and ii) therefore, the temperature stabilization process is one of the most time consuming part of the measurement. Hence, it is difficult to find papers in this topic with isothermal magnetic measurements with δT smaller than 1 K (Morrison et al., 2012; Balli et al., 2014; Pecharsky and Gschneidner, 1997). Furthermore, some of the magnetocaloric materials present thermal and magnetic hysteresis, which must be carefully characterized as the material behaviour depends on the field and thermal history (von Moos et al., 2015; Caron et al., 2009).

In order to systematically study the effect of the temperature grid in the Δs calculation, three different materials were used. $La(Fe,Mn,Si)_{13}H_y$ provided by Vacuumschmelze GmbH, commercial grade Gd and $La_{0.67}Ca_{0.33}MnO_3$ (here called LCMO) produced by solid-state method. Each of these materials have different behaviour of Δs as function of temperature and magnetic field change (Morrison et al.,

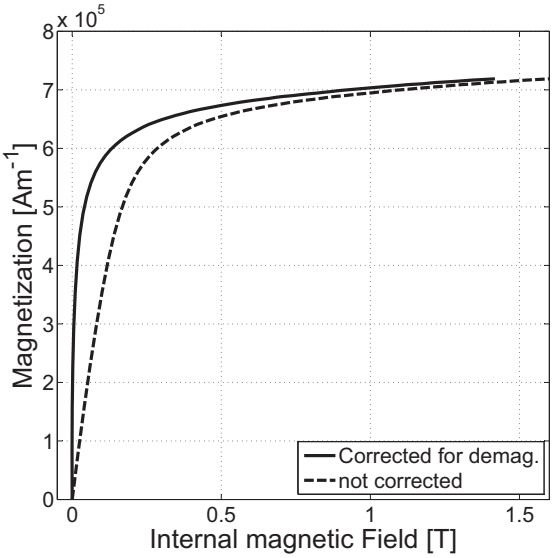

Figure 3.8: Magnetization as a function of the magnetic field with and without a correction for demagnetization effect.

2012; Pecharsky and Gschneidner, 1997; Chen et al., 2006). The materials were characterized within a relevant temperature range around their Curie temperatures, T_C. For the evaluation of the effect of δT, a relatively small $\delta T_1 = 1$ K was used throughout the whole measurement setup. The magnetic field was applied stepwise from 0 T to 1.6 T, with a field step of 0.01 T, a field rate of 1.67 mT/s and a hold time of 5 s in each field step.

The study of the temperature step effect starts with the original temperature grid. From these is possible to evaluate the effect of different temperature grids for which $\delta T_1 \rightarrow \delta T_j = j \times \delta T_1$, where j is an integer. One way to do it is to arbitrarily select a starting point and eliminating the extra data points to obtain the temperature grids, δT_j.

Figure 3.9(a) shows the magnetization of $LaFe_{11.36}Mn_{0.34}Si_{1.3}H_{1.65}$ as a function of the temperature, in different temperature steps and for an internal magnetic field of 0.05 T. One can clearly see that the effect is to broaden the transition. As equation 3.13 shows, a sharp transition results in a larger entropy change, and a broader transition leads to a smoother and smaller entropy change. That is in fact what is observed, as shown in Figure 3.9(b).

Figure 3.10 shows the normalized maximum Δs as a function the temperature step and magnetic field change for the three different materials. The normalization of the maximum Δs was done in respect to the maximum Δs at the respective field and $\mathrm{d}\,T = 1$ K. The figure shows that the effect of the temperature step is to decrease the entropy change, and the effect is larger for smaller field changes. Moreover, the effect is extremely influenced by the transition type. For a SOPT material as Gd, which does not present discontinuity, the effect is negligible. However for FOPT, such as $La(Fe,Mn,Si)_{13}H_z$ and $La_{0.67}Ca_{0.33}MnO_3$ (Bez et al., 2016a,b), the effect is much larger, and should not be neglected.

It is also clear that the entropy change should be even bigger for $\mathrm{d}T < 1$

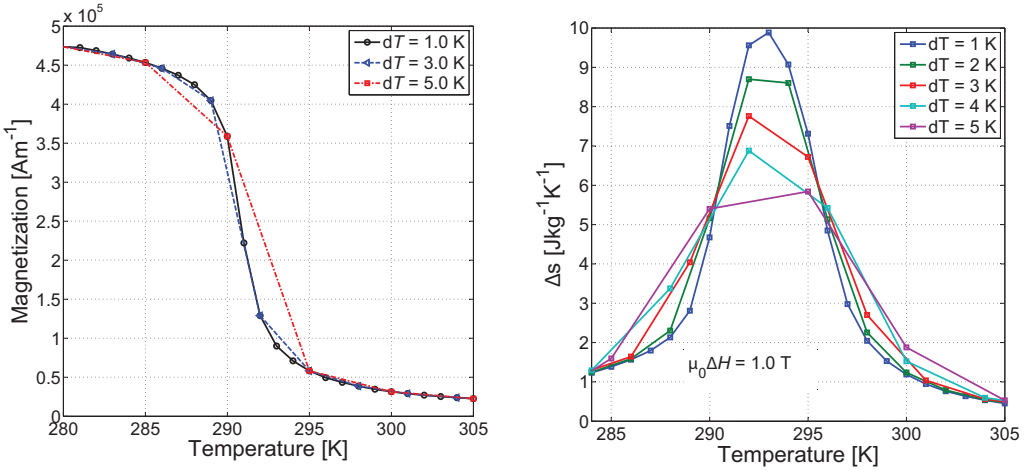

(a) (b)

Figure 3.9: (a) Magnetization as a function of the temperature of $LaFe_{11.36}Mn_{0.34}Si_{1.3}H_{1.65}$ with $\mu_0 H = 0.05$ T. (b) Entropy change for $\mu_0 \Delta H = 1.0$ T showing the effect of different temperature steps of the isothermal magnetization measurements of $LaFe_{11.36}Mn_{0.34}Si_{1.3}H_{1.65}$.

K, having its *true* value at $dT \rightarrow 0$ K. However, due to small fluctuations of the temperature, the magnetization also changes, and closer to the transition this can lead to larger variations of the magnetization. This effect together with the fact that the entropy change is calculated by a derivative in respect to the temperature, leads to errors that will be amplified by temperature steps too small. Therefore, in this thesis the magnetization measurements for entropy change calculation were always performed with temperature steps of 0.5 or 1.0 K.

Another feature normal to FOPT magnetocaloric materials is the irreversibilities observed as hysteresis. von Moos et al. (2014) have shown that in order to avoid the effect of the irreversibility, the material has to be in the initial state of the measurement in a single pure phase. So for a ferro- to paramagnetic transition, the hysteresis effect can be observed if the measurement always start purely in one of these phases, given a temperature and magnetic field. Experimentally, what can be done is to have a temperature reset in between isothermal measurements. When measuring the magnetization at a fixed field, but as a function of the temperature, there is no need to reset to a temperature since there is no field-induced transition. For isothermal magnetization measurements the transition field-induced or thermally-induced. Let us consider a hypothetical material with a Curie temperature while heating $T_C^h = 292$ K and while cooling $T_C^c = 290$ K at 0 T. To evaluate the magnetic entropy change without hysteresis losses during the heating, the procedure is as follows:

i. Decrease the temperature to the reset temperature $T_{reset}^{FM} << T_C^h$, let the sample stabilize thermally and increase to the measurement temperature T_n, and let the sample stabilize thermally again.

ii. Vary the magnetic field from H_i to H_f.

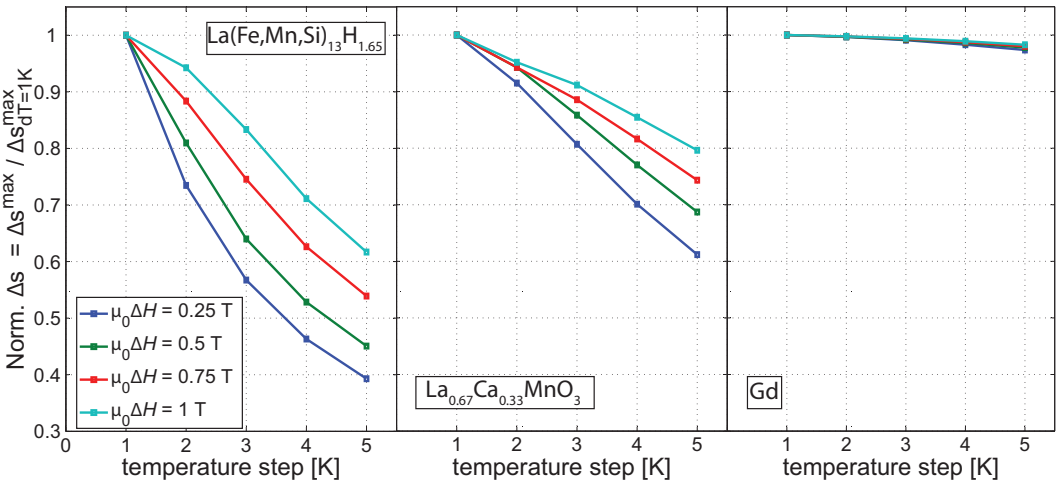

Figure 3.10: Normalized maximum entropy change as a function of the temperature step and field for three different materials.

iii. Decrease the temperature to $T_{\text{reset}}^{\text{FM}} << T_{\text{C}}^{\text{h}}$, let it stabilize and increase it to the next measurement temperature $T_{\text{n+1}}$.

iv. Vary the magnetic field from H_i to H_f.

v. Repeat from item iii until all relevant temperatures are evaluated.

In addition, it may be used in an analogous way for the cooling procedure, where the sample is reset at a temperature $T_{\text{reset}}^{\text{PM}} >> T_{\text{C}}^{\text{c}}$. Using this technique one can measure the entropy change where losses due to the thermal hysteresis are not included. This is particularly important if one is evaluating the intrinsic properties of the material. However, when using the material in a AMR it will go through cyclic processes where there is no temperature resets. Therefore, characterization for AMR simulations have to include the losses due to hysteresis.

3.3 X-ray diffraction

3.3.1 Principle

X-ray waves were discovered in 1895 by the physicist Roentgen, and its name is due to unknown nature at the time. It was not until 1912 that X-ray diffraction (XRD) was discovered, and its nature understood (Cullity, 1978). XRD is a powerful technique used to characterize the structural properties of materials. Such characterization gives qualitative and quantitative information on the crystal and microstructure.

The x-ray diffraction technique is based upon the constructive interaction of X-rays after interacting with the lattice. Let us consider the perfectly parallel and monochromatic x-ray beam in figure 3.11 shining on the surface of a crystal lattice at an angle θ and scattered in the same angle. Considering the X-rays 1 and 2 as they strike atoms B and A, respectively, they scatter in all directions. However, only in the directions 1' and 2' that they will interact constructively, since the distance travelled by both waves from the perpendicular plane W−W' to Z−Z' was the same.

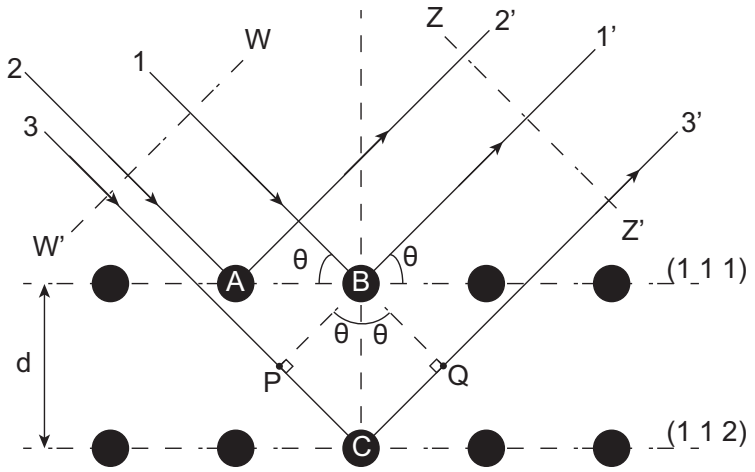

Figure 3.11: Schematic drawing of the principle behind the x-ray diffraction technique. The solid circles are atoms, the solid lines are the X-rays incident beans.

Now consider the rays 1 and 3 shining on the atoms B and C, the only way they can interact constructively is if the extra distance travelled by the wave 3, from point P to C to Q, is a multiple of the wavelength of the incident x-ray, in other words:

$$PC + CQ = d\sin(\theta) + d\sin(\theta) = 2d\sin(\theta) = n\lambda, \tag{3.15}$$

where n is an integer, λ is the wavelength of the incident beam, and d is the interplanar distance of the crystal structure. This conclusion was first made by W. L. Bragg, and it is known as Bragg's law. Therefore, x-ray diffraction is a x-ray scattering phenomenon in which atoms constructively contribute to. Bragg's law also points out that the condition for diffraction is $n\lambda \leq 2d$, since $sin(\theta) \leq 1$ (Cullity, 1978). Moreover, one may expect that for crystalline materials it will only exist a finite number of angles that diffraction is observed.

3.3.2 Rietveld Refinement

As explained before, the diffraction pattern observed in an XRD measurement will be determined by the crystal structure of a material. This means that the shape and size of a crystal structure will determine the angular positions of the peaks, and the arrangement of the atoms within the unit cell will determine the relative peaks' intensities. As the crystal structure determines the pattern, one could expect that the other way around also works, i.e. it is possible to determine the crystal structure from the diffraction pattern. Indeed it is possible, *but not in a simple manner*. Disregarding instrumental effects, temperature and absorption issues, if a crystal structure is known, one can calculate its peaks' positions and intensities in a straightforward manner. However, given the diffraction pattern it is not straightforward to find the crystal structure that fits the pattern. The procedure adopted to find the crystal structure is in its essence empirical. One has to make an educated guess of the crystal structure, calculate its diffraction pattern and compare with the observed one. In case they do not match, another guess has to be done and so it goes. Nowadays, most of the crystal structures are already known for most of

different materials one can imagine and databases can be found, easing the life of material scientists[1]. Such databases not only give the crystal structure of materials, but bundle the most different conditions of measurement, such as temperature, pressure, sample form, radiation wavelength, among others.

Rietveld (1967, 1969) has proposed a complex, but complete method for crystal structure determination and characterization from XRD. The proposed method uses the crystal structure guess as an initial input, and through several fitting parameters applies the least-square method until the difference between the calculated pattern and the measured one has reached a minimum. Within the refinement, the parameters are approximated via Taylor expansions that by itself demands a good initial guess, which in other hand explains why the initial guess of the crystal structure is important. Moreover, different local minima may be found depending on the initial guess of the parameters. The refinements in this thesis were performed using WINPOW program, developed by Prof. Kenny Ståhl at the Technical University of Denmark.

The Rietveld refinement method is based on minimizing the following equation (Pecharsky and Zavalij, 2005):

$$\Phi = \sum_{i=1}^{n} w_i \left(Y_i^{obs} - Y_i^{calc} \right)^2, \tag{3.16}$$

Where Y_i^{obs} and Y_i^{calc} are the observed and calculated intensity, respectively, at a point i on the diffraction pattern and w_i is the weight assigned to the i^{th} data point. Considering a powder diffraction data and a single incident radiation wavelength, one can calculate the intensity by:

$$Y_i^{calc} = b_i + K \sum_{j=1}^{m} I_j y_j(x_j), \tag{3.17}$$

where b_i is the background at the i^{th} data point, K is the phase scale factor, m is the number of Bragg reflections that contribute for the intensity at i^{th}, I_j is the intensity of the j^{th} Bragg reflection, $y_j(x_j)$ is the peak profile function and $x_j = 2\theta_j^{calc} - 2\theta_i$. In I_j enters many different factors which refer to polarization, structure, preferred orientation, absorption and extinction corrections.

The most commonly used peak profile function used is the so-called pseudo-voigt, which is basically a linear convolution of a Gaussian and a Lorentzian profile. The pseudo-voigt function can be ascribed as follows:

$$y(x) = \gamma \frac{2}{\beta\pi} \left(1 + \frac{4}{\beta^2} x^2 \right) + (1 - \gamma) \frac{2\sqrt{\ln 2}}{\beta\sqrt{\pi}} \mathrm{e}^{\frac{-4ln2}{\beta^2} x^2}, \tag{3.18}$$

where γ is the mixing parameter, which determines the fraction contribution of Lorentzian function; $\gamma = 0$ it is fully Gaussian and $\gamma = 1$ it is fully Lorentzian. β is the full width at half maximum (also seen as its acronym, FWHM) parameter, and it is a function of the scattering angle and is calculated as follows (Caglioti et al., 1958):

$$\beta(\theta) = \sqrt{u \tan^2 \theta + v \tan \theta + w}. \tag{3.19}$$

[1] In this thesis the Inorganic Crystal Structure Database, also known for its acronym ICSD, was used and it can be found at https://www.fiz-karlsruhe.de/en/leistungen/kristallographie/icsd.html

In this thesis it was used two different x-ray diffractometers. A Brucker D8 diffractometer, with a Cu radiation source. The powder sample is spinning throughout the measurement. The irradiated area is fixed with a diameter of 6 mm. The second diffractometer used is a Rigaku SmartLab, with a Cu radiation source. The irradiated area is fixed with a diameter of 6 mm as well. Despite of similar setup, this diffractometer has the possibility to insert a furnace chamber that can control the sample's temperature from 295 K to 1473 K. In order to avoid oxidation at high temperatures, the chamber has the option to be evacuated to high vacuum pressures. Such setup was advantageous in order to characterize the phase transition of FOPT $La(Fe,Mn,Si)_{13}H_z$.

3.4 Capacitance dilatometry

In order to measure thermal expansion and magnetostriction, a capacitance dilatometer was used (Rotter et al., 1998). These measurements were performed in the Imperial College London. Capacitance dilatometers are usually in a more compact size when compared to the usual "push-rod" dilatometers (Genossar and Steinitz, 1990). The basic principle of this measurement is that if one place a sample into a capacitive cell, where the distance of the capacitive plates is given by the length of the sample, the capacitance of the cell will be controlled therefore by the length of the sample. This allows to acquire high resolution data as shown by Turcaud et al. (2015).

This capacitive cell's longest dimension is 18 mm, and being this small allows measurements in a Physical Property measurement System (PPMS), in this case a 9−T Quantum Design. PPMS' are apparati that allows the control of pressure, temperature, magnetic field, among others. In this case, the PPMS was used to control the temperature and applied magnetic field.

As most devices, this capacitance dilatometer needs calibration. In a way, the calibration procedure is very similar way to the calibration of the heat capacity described in a previous subsection of this chapter. Further information on the dilatometer and the calibration may be found in Rotter et al. (1998).

3.5 Scanning electron microscopy

The microstructure of the materials was evaluated by scanning electron microscopy (SEM). This technique uses a focused beam of electrons to produce images of a sample. The electrons interact differently with the different atoms and topologies of the sample, giving topological and compositional information as an output.

This technique gives many different types of signal, but two main types are used to produce the images. After the interaction with the material, the electrons may be secondary electrons (SE) and backscattered electrons (BSE). The different type of electrons will come on average from different depths of the sample, where SE are mostly from the surface region and BSE may come from deeper regions.

The interaction of the electrons with the sample may be inelastic scattering − giving the SE signal; elastic scattering − giving the BSE signal; emission of radiation − which will be discussed later on this section; among other types of interactions (or lack of) that are irrelevant in this thesis. These signals can then be detected by different detectors. The secondary electrons are usually low energy electrons, which

are taken out from the k-shell of the sample through inelastic scattering. It is due to the low energy of them that they give information only of the surface of the sample. In this thesis, however, it was used only BSE for sample evaluation.

Backscattered electrons are high-energy electrons, originated from the focused beam, which are elastically scattered when interacting with the atoms from the sample. The high-energy level of this electrons are also the reason why they might come from a deeper region of the sample as well. As one may imagine, this interactions will be stronger with the increase of the the atomic number. So, if in a given situation there are more than one phase in a sample, with different compositions and/or densities in each one, the one comprising heavier elements will appear as a brighter phase and vice versa.

As mentioned before, together with the electrons, there will be some radiation originating due to the interaction of the electrons with the sample. The radiation in this case are X-rays, and they are detected by an energy-dispersive X-ray spectrometer (EDS), built-in many of the SEMs. This device allows to study the specific chemical composition of different regions of the sample. Let us consider that when the beam of electrons hit the sample, it can eject an electron from a inner shell of an atom. An electron from an outer one, which has higher energy, will then fill the hole left by the ejected electron and the energy difference will be released in the form of an X-ray. This X-rays can then be detected by spectrometer, and as each element has a characteristic energy-level spectrum, one can qualify and quantify the composition of the material.

3.6 Magnetocaloric regeneration test device

The final product of a magnetocaloric material is a magnetocaloric regenerator. At DTU there is a device that is able to evaluate the material as a regenerator itself (Bahl et al., 2008). In such tests, many different properties – of both the intrinsic material properties and the regenerator‘s ones – come to play an important role, e.g. thermal diffusivity, corrosion resistance, mechanical stability, “shapeability”, and obviously magnetic entropy change and heat capacity. Figure 3.12(a) shows part of the device, which is inside a commercial fridge. This device works as a reciprocal regeneration device, with the hot end on the top, and cold end in the bottom. In the center there is a Halbach magnet with a constant and homogeneous magnetic field in the gap of about 1.1 T. Figure 3.12(b) shows an example of a regenerator, which in this case is $La(Fe,Mn,Si)_{13}H_z$ particles with 3 wt% of epoxy in order to keep the particles together.

The device is inside a commercial fridge in order to control the ambient temperature. Additionally, in the hot end there is a heat exchanger, which consist of an Cu coil with water circulating in it. This water is kept in the temperature of the commercial refrigerator through a bath in the bottom of the refrigerator (not shown in the figure). Thus, this heat exchanger keeps the hot end at a constant temperature and, more than that, allows to control which temperature to be in the hot end by controlling the refrigerator's temperature. It is important to know that due to this fact, the hot end temperature will be equal to the device's ambient temperature.

The results concerning these measurements are shown in the paper submitted for publication in the proceedings of the 7^{th} International Conference on Magnetic

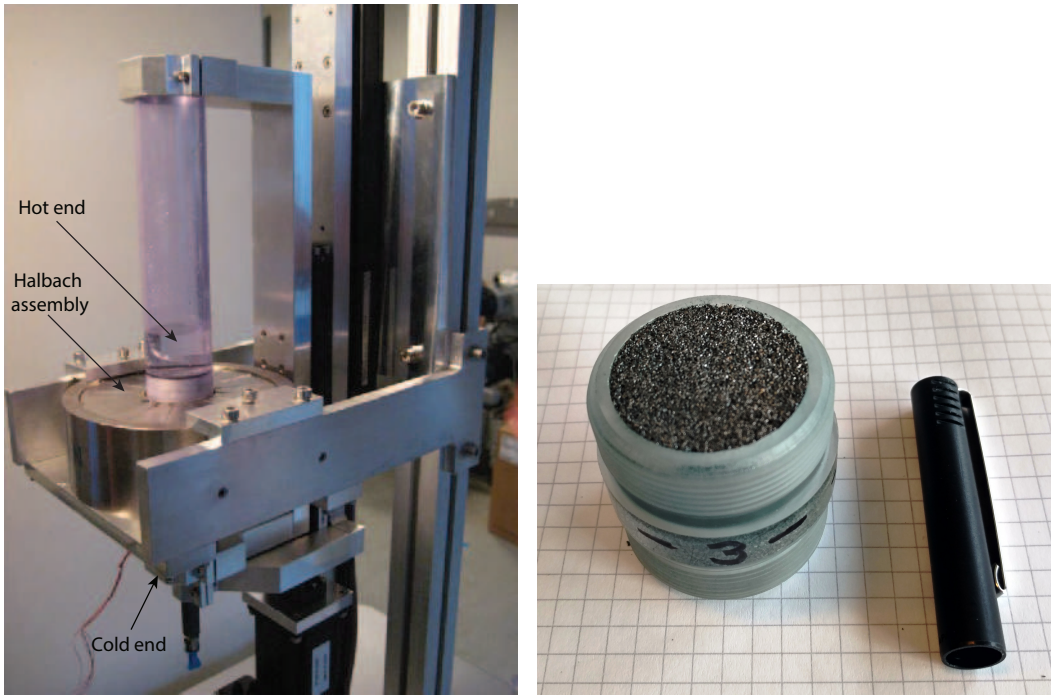

(a) (b)

Figure 3.12: (a) Picture of the magnetocaloric testing device (Nielsen et al., 2010). (b) Picture of a regenerator of epoxy-bonded $La(Fe,Mn,Si)_{13}H_z$ particles. Pen top for scale.

Refrigeration at Room Temperature, and this paper can be found in appendix A.2.1.

Chapter 4

$La_{0.67}Ca_{0.33}MnO_3$

4.1 Fabrication and quality evaluation

In order to evaluate the phase transition of $La_{0.67}Ca_{0.33}MnO_3$, bulk polycrystalline samples were synthesized by the solid state method. For more information on the effect of the process in the properties of the La-manganites, Phan and Yu (2007) has a thorough review on it. In this thesis, powders of La_2O_3 (purity 99.999% – Alfa-Aesar Reacton Lanthanum(III) oxide), MnO_2 (purity 99.997% – Alfa-Aesar Manganese(IV) oxide) and $CaCO_3$ (purity 99.95% – Alfa-Aesar Calcium Carbonate) are stoichiometrically mixed to get $La_{0.67}Ca_{0.33}MnO_3$ as a final result, considering the elimination of excess O and C. Here, the material is mixed and ground by using a rolling mill with cylindrical alumina parts of about 5 mm diameter and and 7 mm height. The proportion of cylindrical parts and powder was such to keep a mass ratio of 10:1. The powder mixture is put in a cylindrical container together with the cylindrical alumina parts and ethanol. The container is then rotated at 180 rpm for 48h.

After the mixing and roll milling, the powder was put into a becker together with the ethanol and the mixture was left to dry. Then the dried powder is transferred into an alumina crucible and the calcination process is performed. The calcination here was done at 1123 K, with a heating rate of 5 $Kmin^{-1}$, for a period of 24 hours. The powder is then left to cool slowly in the furnace.

During the calcination the powders may form agglomerates, which would be detrimental for the sintering step. To avoid aggomerates, the powder was ground softly in a agate mortar. Then the powder was uniaxially pressed to give some mechanical stability to the green parts. Then the green parts were isostatically pressed with a pressure of 2 kbar. After the pressing step the sample is then put to sinter at 1403 K, with a heating rate of 5 $Kmin^{-1}$, for 48 h.

To evaluate if the aimed stoichiometry was achieved, powder XRD, low temperature magnetization and SEM images were taken. These results are shown in Figure 4.1. The XRD measurement was done in a Brucker D8 diffractometer, and the ICSD number 82820 is used as the educated guess for the crystalline structure; This ICSD number refers to the data of a powder XRD of $La_{2/3}Ca_{1/3}MnO_3$. The following parameters were refined: temperature factor; unit cell parameters a, b and c; scale factor; the FWHM parameters u, v and w; the Lorentzian mixing parameter; and 5 background parameters, i.e. in a total 14 parameters were refined. the

angle range was $20^o < 2\theta < 100^o$, with a step of $2\theta = 0.02^o$. The resulting measurement, refinement and difference between both is shown in Figure 4.1(a). One may see a good agreement between measurement and refinement, and the errors are $R_p = 2.89$, $R_{wp} = 4.79$, $R_{Bragg} = 1.54$ and $\chi^2 = 6.68$. These results show that the material presents a single phase of $La_{0.67}Ca_{0.33}MnO_3$. Moreover, from the refinement one can extract the unit cell parameters a, b and c, and the volume, which are 5.4717(8) Å, 5.45690(1) Å, 7.7085(1) Å, and 230.163(7) $Å^3$ respectively. These results are in agreement with literature values (Morrison et al., 2011).

Figure 4.1(b) shows a magnetization measurement performed in a high field VSM (Cryogen Free Measurement System - 16 T) at 10 K from 0 to 10 T, with a rate of 0.1 T/min to find the saturation magnetization. The sample has the approximate dimensions 3.8 × 1.2 × 1.2 mm^3 and a mass of 47.4 mg. The same sample cut was used for all the magnetization and calorimetric measurements. In the image the solid line is the measured magnetization and the dashed red line is the theoretical saturation value calculated as follows:

$$M_s = g\mu_B J \rho_s. \tag{4.1}$$

where ρ_s is the magnetic spin density. The Landé factor used is 2, J is 1.835 (average on the ratio of Mn^{+3} and Mn^{+4}) and the spin density is calculated simply by the number of magnetic atoms (four) in the volume V obtained by XRD, giving a magnetic spin density of 1.7391e28 spins/m^3. These values were used to calculate the theoretical saturation magnetization. One can see that the experimental and theoretical values are in good agreement; the measured magnetization value, 3.57 μ_B per unit formula, is around 97% of the theoretical saturation magnetization value, 3.67μ_B per unit formula (Bez et al., 2016b).

Figure 4.1(c) A backscattered electron image taken in a SEM Hitachi TM3000. One may see that the material has a homogeneous phase. The inset shows in a higher magnification the finely dispersed pores in the material. The porosity was measured by the Archimedes method, and 8 % of the volume of the part is pores.

As it was discussed in the subsection 2.3.2, there has been some reports of the existence of magnetic polarons (or clusters) in this material (Teresa et al., 1996; Souza et al., 2008; Turcaud et al., 2014). To investigated that, the inverse susceptibility was measured at different fields. The inverse susceptibility, χ^{-1}, can be fitted using a modification to the Curie-Weiss law:

$$\chi = \frac{\rho_s}{C} \frac{\mu_{eff}^2}{\kappa_B (T - T_C)}, \tag{4.2}$$

where the effective magnetic momment is $\mu_{eff} = g\mu_B \sqrt{CJ(CJ+1)}$ and T_C is the Curie temperature. Comparing equations 2.13 and 4.2, one may see that an extra term C was added, which is the term that dictates the cluster size. The cluster size is added in the calculation of χ in equation 4.2 dividing ρ_s and in μ_{eff} multiplying J. By using such approach in the calculation of the theoretical saturation magnetization, there is no need to consider clusters as both ρ_s and J enter linearly.

Fig. 4.2 shows the measured inverse susceptibility as a function of the temperature for different internal magnetic fields. One can observe a deviation from the Curie-Weiss law around 274 K. This behavior is related to the presence of the magnetic clusters (Turcaud et al., 2014). Additionally, the fields investigated show that

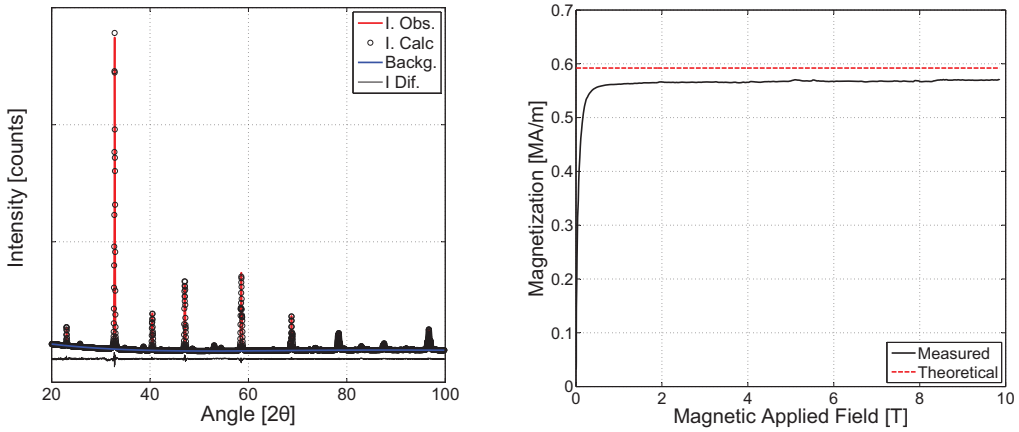

(a) (b)

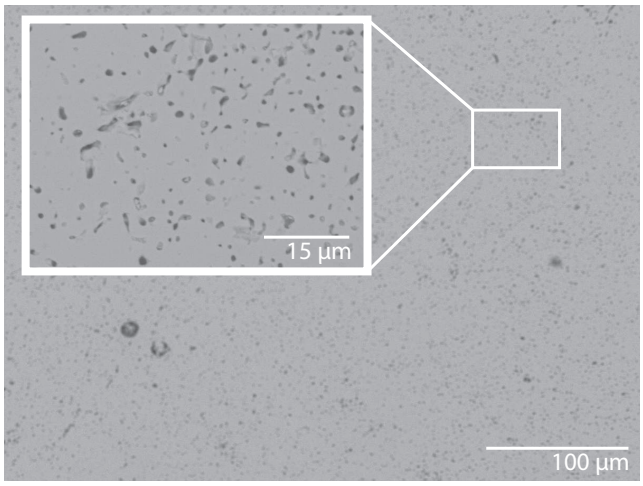

(c)

Figure 4.1: (a) XRD pattern and Rietveld refinement of the perovskite showing the desired single phase structure. (b) Magnetization measurement at 10 K, from 0 T to 10 T at a rate of 0.1 T/min. The solid line represents the measurement, and the dashed red line is the theoretical value of the saturation magnetization. (c) Shows a backscattered electron image of the prepared material. The inset shows the pores in a higher magnification.

the inverse susceptibility is field independent in the paramagnetic phase. One can use the Curie-Weiss law in this region in order to calculate the cluster size (Jia et al., 2006a). Using the least-square method for a the field of 10 mT and for $280 < T < 350$ K, it was found that the best fit is with $C = 2.80$ and $T_C = 263.6$ K, showing a good agreement with the measured data. The image also shows how should be the behavior if there was no cluster and if $T_C = 264$ K. In addition, the cluster size is in agreement with the literature, where it was shown that for increasing content of Ca in $La_{1-x}Ca_xMnO_3$ the cluster size decreases from 4.5 for $x = 0.2$ to 2.9 for $x = 0.3$ (Turcaud et al., 2015).

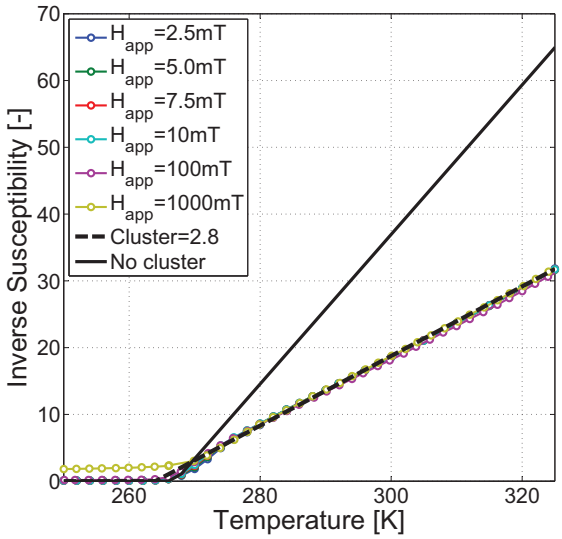

Figure 4.2: Inverse magnetic susceptibility around the phase transition temperature, for an applied field of 10 mT.

4.2 Thermal hysteresis

The thermal hysteresis evaluation of this material starts with heat capacity measurements. These measurements were done as described in the subsection 3.1.1. Figure 4.3(a) shows the heat capacity, c_p, as a function of the temperature for different rates. The peak values and positions are in agreement with the literature (Lin et al., 2006; Morrison et al., 2011). The peak temperatures (T_{peak}) of the c_p curves were fitted as a function of rate in order to exclude the apparent hysteresis, as shown in Fig. 4.3(b). The apparent hysteresis decreases with decreasing temperature rates, and for the extrapolated 0 Kmin^{-1}rate the intrinsic hysteresis is 0.08 $\pm$0.2 K, therefore zero considering the fitting and extrapolation uncertainties. Lin et al. (2006) who have measured the heat capacity at 5 Kmin^{-1}, have observed a thermal hysteresis of about 5 K, which is the expected hysteresis at 5 Kmin^{-1} from the fitting curves in Figure 4.3(b).

The aparent hysteresis under different temperature rates is related to the thermal diffusivity of the material. $La_{0.67}Ca_{0.33}MnO_3$ has a large specific heat and a relatively low thermal conductivity, $\kappa_c \sim$ 1-3 $\text{Wm}^{-1}\text{K}^{-1}$ (Turcaud et al., 2013), which then leads to a low thermal diffusivity. Considering the base level of $c_p = 550$ $\text{Jkg}^{-1}\text{K}^{-1}$, the density obtained from the XRD measurement $\rho = 6034$ kgm^{-3} and assuming a value of κ_c =2 $\text{Wm}^{-1}\text{K}^{-1}$, the thermal diffusivity can be calculated by

$$D = \frac{\kappa_c}{c_p \rho}, \tag{4.3}$$

and for $La_{0.67}Ca_{0.33}MnO_3$ it is $6{\cdot}10^{-7}$ m^2s^{-1}. This is approximately five times smaller than other common magnetocaloric materials such as $La(Fe_{0.88}Si_{0.12})_{13}H_{1.0}$ where it is $\sim 2.7{\times}10^{-6}$ m^2s^{-1}, very similar to the diffusivity of Gd (Fujieda et al., 2004). Therefore, the temperature rate is much more influential on the position of the peaks of $La_{0.67}Ca_{0.33}MnO_3$ compared to other magnetocaloric materials.

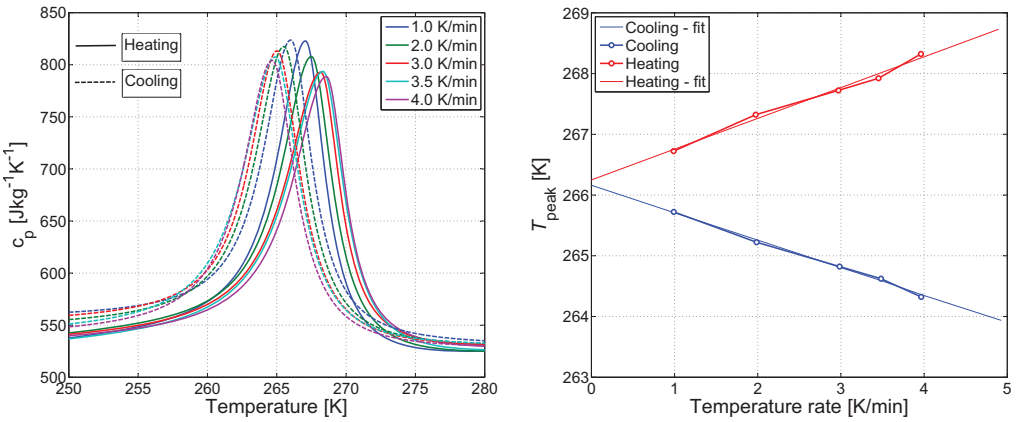

(a) (b)

Figure 4.3: (a)Specific heat as a function of temperature for different temperature rates at 0 T. (b) Heat capacity peak temperature, T_{peak}, as a function of temperature rates for both heating and cooling. At finite heating and cooling rates extrinsic hysteresis is apparent. However, the intrinsic hysteresis, corresponding to the extrapolated temperature rate 0 Kmin^{-1}, vanishes.

Specific heat measurements under different applied fields were performed to further investigate the thermal hysteresis. Figure 4.4(a) shows the heat capacity during the cooling procedure with $\dot{T} = -1.0$ Kmin^{-1}, under different applied fields. As the graph shows, the heat capacity peak is shifting towards higher temperatures for increasing values of $\mu_0 H$. This indicates a behaviour similar to that of a first order phase transition (Smith et al., 2012). Figure 4.4(b) shows T_{peak} as a function of field, for both heating and cooling procedures, with $|\dot{T}| = 1.0$ Kmin^{-1}. The linear fits show a slope of 6.2 $\pm$0.9 KT^{-1} for both the heating and cooling procedures. Furthermore, when extrapolating to a rate of 0 Kmin^{-1}as in Figure 4.3(b), the lines collapse showing the absence of hysteresis. In contrast, for materials with intrinsic hysteresis the amount of hysteresis decreases linearly with field, until a critical field is reached at which the transition becomes continuous and there is no more hysteresis,as schematically shown in Figure 2.5(d).

Figure 4.5(a) shows indirect measurements of Δs as a function of temperature for different values of ΔH. One may see the asymmetric behaviour of the peak with increase in field; a behaviour related to first order transitions (Smith et al., 2012). Additionally, the peak is in agreement with literature values (Lin et al., 2006; Turcaud et al., 2015). A slight hysteretic behaviour around the T_{peak} is observed, with a ΔT_{hyst} of approximately 0.7 K in the full-width half maximum (FWHM). On the other hand, direct measurements of Δs (see Figure 4.5(b)) show no observable difference between the peak positions and, therefore, no significant thermal hysteresis was observed. Figure 4.5(b)shows four curves of Δs. The curves represent four equilibrium conditions of measurements explained in the subsection 3.2. The reset temperatures of this measurements were $T_{\text{C}}^{\text{h}} = 240$ K and $T_{\text{C}}^{\text{c}} = 290$ K for heating and cooling respectively. The difference between the two types of measurements arises from the uncertainties related to the measurements. As Pecharsky and Gschneid-

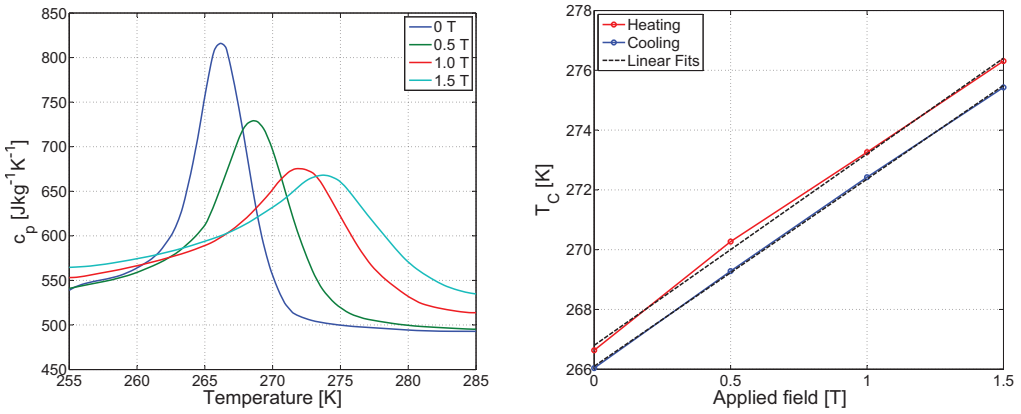

(a) (b)

Figure 4.4: (a) Specific heat as a function of temperature and under different applied field, with $\dot{T} = -1.0$ Kmin^{-1}. (b) The specific heat peak temperature, T_{peak}, as a function of applied magnetic fields for both heating and cooling heat capacity measurements, with $|\dot{T}| = 1.0$ Kmin^{-1}. The dashed lines are linear fits.

ner (1999) have shown, Δs derived from magnetization measurements may have an uncertainty of up to 20%, making it challenging to try to extract reliable values of a small hysteresis, if there is any. It is important to note that the direct measurement of Δs, is done with a high precision instrument with a temperature uncertainty of $\pm$ 10mK (Nielsen et al., 2015). Furthermore, each point is measured individually, avoiding the smoothing effect observed when finite difference approximation is used to calculate Δs from magnetization derivatives, as shown in the subsection 3.2.

It is found no discernible *intrinsic* hysteresis in these LCMO samples, as shown above through the measurements of heat capacity and calorimetric measurements of entropy change. This is consistent with previous reports using an AC calorimetric method Morrison et al. (2011). On the other hand the observed behaviour of the specific heat and isothermal entropy change is characteristic of a FOPT. These observations can be reconciled if we consider the spread in critical temperature which is caused by compositional variations and the tendency to formation of magnetically inhomogeneous states in the manganites (Bebenin et al., 2013). For weakly first-order materials even a small spread in critical temperatures may be enough to smooth out the transition and make the hysteresis decrease or disappear. By using the Bean-Rodbell mode, it was found that indeed $La_{0.67}Ca_{0.33}MnO_3$ is weakly first order, with an $\eta = 1.25$. The model details are shown in the last section of this chapter.

Figure 4.6 shows the modelled behaviour of the entropy curve under both heating and cooling, with a standard deviation on the Gaussian distribution ΔT_0 = 2.6 K, and without any distribution. It is clear that the weak hysteresis present when there is no compositional distribution, i.e. $\Delta T_0 = 0$ K, tends to vanish when the spread is taken into consideration, i.e. $\Delta T_0 = 2.6$ K. It is also important to notice that the entropy curve shown here is in zero field. Previous works (Smith et al., 2012; Basso et al., 2015) have shown that the thermal hysteresis decreases with the increase of magnetic field, making it the largest at zero field.

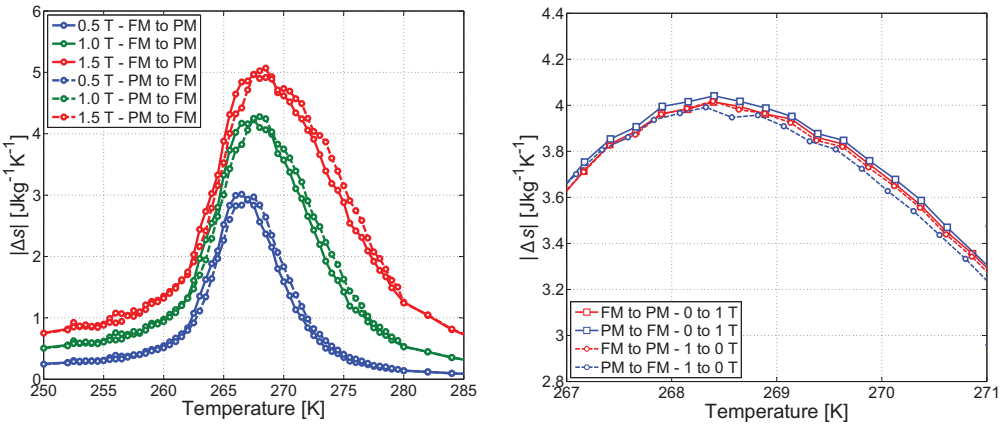

(a) (b)

Figure 4.5: (a) Entropy change calculated from magnetization measurements under equilibrium conditions from 0 T to 0.5, 1.0 and 1.5 T. (b) Entropy change measured directly in the DSC for $\Delta H = 1.0$ T, around the transition temperature with a temperature step of 0.25 K.

4.3 Magneto-volume coupling evaluation

As seen in the previous section, the LCMO samples studied in this thesis exhibit FOPT features, while not presenting thermal hysteresis. The first order phase transition of magnetocaloric materials have been highly correlated with changes in the volume and/or crystalline structure (Pecharsky and Gschneidner, 1997; Fujita et al., 2001; Guillou et al., 2014). In this subsection the magneto-elastic coupling of $La_{0.67}Ca_{0.33}MnO_3$ is evaluated through dilatometric measurements, performed in the Imperial College London. The characterization method is explained in the previous chapter.

The thermal expansion was evaluated unidimensionally as a function of the temperature, with a temperature rate of $|\dot{T}| = 0.33$ Kmin^{-1}. Figure 4.7 shows the linear thermal expansion as a function of the temperature without any applied magnetic field. One can see a change in the linear expansion around the Curie temperature. Firstly, this is an evidence that the material presents magneto-elastic coupling, as previously observed in $La_{0.67}Ca_{0.33}MnO_3$ (Ewe et al., 2008). Secondly, there is an apparent hysteresis of about 0.3 K. Nonetheless, the same argument of thermal diffusivity given in the previous section can be used here to explain the observed hysteresis in the measurement.

Figure 4.8(a) shows the isothermal magnetostriction as a function of the temperature for internal magnetic field changes, $\Delta H_{\text{int}} = 0.5$, 1.0 and 1.5 T. One may see the peak grows asymmetrically towards higher temperatures with increasing field. Similar values and behavior were observed in similar perovskites. A relationship between the entropy change and the magnetostriction is found, where $\Delta s(T, \Delta H) = 1.45e4\omega(T, \Delta H)$. This behavior has been reported in the literature (Turcaud et al., 2015), although no direct and simple relation between both has been found for the La-Ca-manganite series. In fact, the trend observed by Turcaud et al. (2015) is ob-

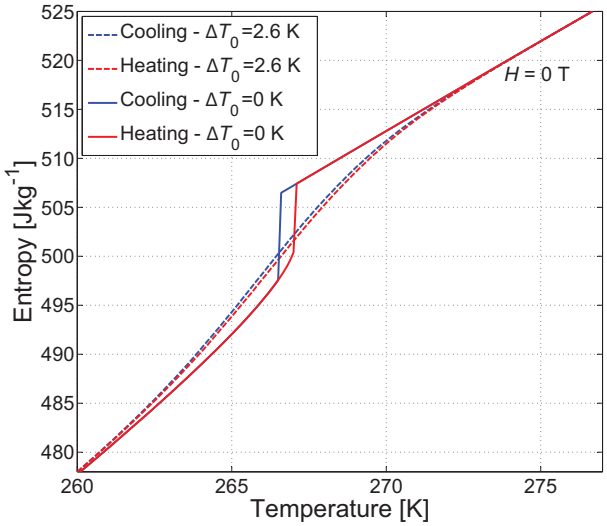

Figure 4.6: Entropy as function of the temperature, for heating and cooling procedures, and $H = 0$ T. One may see the vanishing impact of the distribution ΔT_0 on the hysteresis.

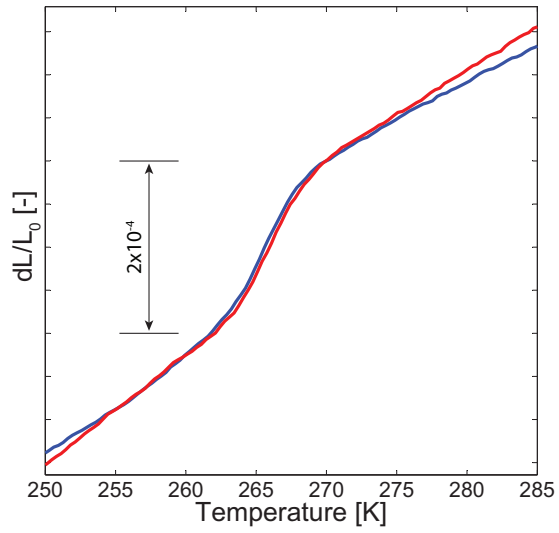

Figure 4.7: Linear thermal expansion as a function of the temperature without applied field.

served here as well, i.e. the factor continues to increase with the increasing content of calcium. Figure 4.8(b) shows a combination of the factors observed there[1] and the one observed here. The fit function allows a phenomenological relation between Δs and ω for La-Ca-manganites in field changes below 1.5 T, and the relation is giving by the following equation

$$\Delta s(T, \Delta H, x) = \left(\mathrm{a}x^2 - \mathrm{b}x + \mathrm{c}\right) \times \omega(T, \Delta H, x) \tag{4.4}$$

where x is the Ca content in $La_{1-x}Ca_xMnO_3$ and a, b and c are the fitting coefficients with values $53(\pm 20)\times 10^4$, $-21(\pm 10)\times 10^4$ and $3(\pm 3)\times 10^4$ $\mathrm{Jkg^{-1}K^{-1}}$, respectively. This fit describes with good agreement the relation between Δs and ω, however it does not mean it would work with La-Ca-manganites out of the range investigated, although the author of this thesis suspects that such approach could be used for the whole ferromagnetic series of $La_{1-x}Ca_xMnO_3$; therefore, equation 4.4 is advised to be used only for $0.2 < x < 0.33$ in $La_{0.67}Ca_{0.33}MnO_3$ and only for fields lower than 1.5 T, i.e. the fields investigated in this thesis. Although equation 4.4 works fine around the transition, it was not checked if this relationship would work well in other temperature regions.

Additionally, one can see that an interesting effect in this material is that the isothermal magnetostriction is negative, i.e. the volume decreases with the magnetic field. The increase of the factor shown in Figure 4.8(b) could be related to two points: (i) the decrease of the Jahn-Teller distortion with the increase of Ca content in $La_{1-x}Ca_xMnO_3$ (Coey et al., 1999), due to the overall increase of Mn tetravalent, which, unlike the trivalent, does not tend to distort its octahedral site; and (ii) that the Jahn-Teller distortion decreases signficantly when going from the paramagnetic state to the ferromagnetic one (Billinge et al., 2000; Belevtsev et al., 2006). Moreover, the trend observed in the factor can shed some light on the origin of the entropy change of this material. The fact that the factor increases with Ca content suggest that the lattice contribution to the entropy change decreases with increasing Ca content.

4.4 Magneto-elastic coupling within the Bean-Rodbell framework

The Bean-Rodbell framework was used to model the magneto-elastic coupling of $La_{0.67}Ca_{0.33}MnO_3$. The model is described in details in the subsection 2.4.2. This model has already been used to investigate manganites as shown in (Turcaud et al., 2015; Amaral et al., 2003), showing good agreement between measured data and the model.

Throughout this chapter, several measurements were shown and many of them are used as an input parameter for the modelling. The total angular momentum for example is taken to be 97% of the theoretical value, due to the low temperature magnetization measurement shown in Figure 4.1(b), and because M_s goes linearly with J. Moreover, the constrained volume, V_0, is set to be the one of the paramagnetic phase measured at room temperature by XRD, and the volume change is evaluated only in respect to the magnetic contribution. The density is taken from the XRD

[1] The material there was prepared by the solid state method as well.

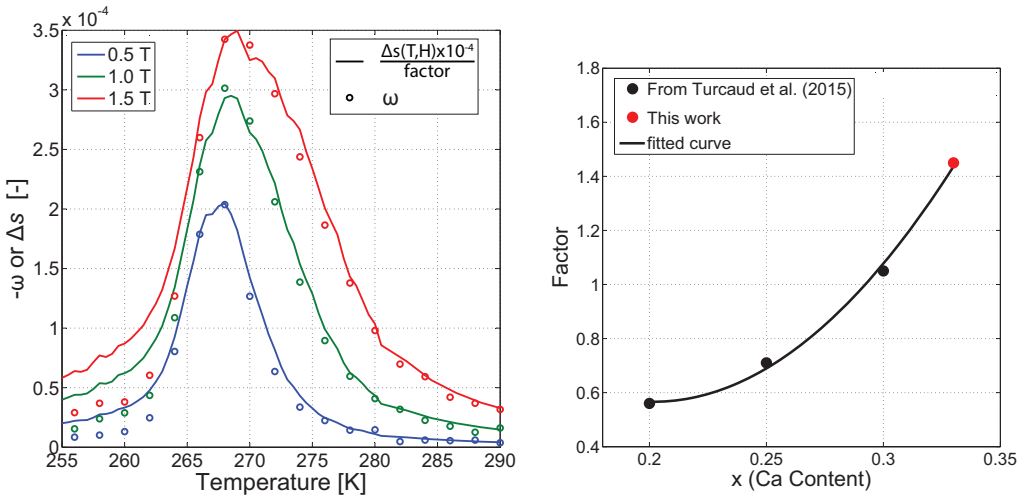

(a) (b)

Figure 4.8: . (a) Isothermal magnetostriction as a function of temperature and magnetic field. The solid lines represent the measured entropy change divided by a factor, for the same temperature and field change. (b) The factor from (a) as a function of Ca content. The black dots are from the reference (Turcaud et al., 2015), and the solid curve is a fit.

measurements as well. The spin density is calculated as explained in subsection 4.1. The cluster size contribution to the paramagnetic phase calculated in the section 4.1 are also used as an input in the model, by simply multiplying J and dividing ρ_s by it (Turcaud et al., 2014).

The electronic contribution to heat capacity is calculated using the free electron model, while the Sommerfeld constant γ_e is calculated through equation 2.28, where V is set to be equal V_0 and the number of conductive electrons will be $4{\times}0.67{\times}1$ since there are four unit formulas in the volume V_0, and the fraction of Mn^{+3}/Mn^{+4} is 0.67 and Mn^{+3} has only one e_g mobile electron, while Mn^{+4} has none. The lattice contribution is calculated through equation 2.29, where Θ_D is used as a fitting parameter. The compressibility was taken from literature. The remaining parameters T_0 and η are varied to fit the measurement. Moreover, the effect of possible Curie temperature distribution is taken in consideration by applying a normal distribution to T_0 (Bebenin et al., 2013; Turcaud et al., 2014), and its standard deviation, ΔT_0, is used as a fitting parameter, giving in total 4 fitting parameters related to magneto-elastic coupling and one fitting parameter related to the lattice contribution to the heat capacity. The parameters used for the thermal and magnetic modelling are listed[2] in Table 4.1.The parameters η and ΔT_0 are slightly different from the previous subsection because in this stance it was tried to plug in the effect of the clusters in the model. In the subsection dealing with the thermal hysteresis, the clusters were not yet considered in the model. The clusters, however, did not influence the thermal hysteresis, which remained in the range of 0.15 K, just as shown in Figure 4.6.

[2]note that here the spin density is in kg^{-1}, while in section 4.1 is in m^{-3}.

Parameter	Value	reference
κ	$\sim$ 7e-12 [Nm^{-2}]	(Ewe et al., 2008)
V_0	230.16e-30 [m^3]	This work
J	1.77	This work
ρ	6034 [kgm^{-3}]	This work
ρ_s	2.88e24 [kg^{-1}]	Calculated
γ_e	0.0061 [JK^{-2}kg^{-1}]	Calculated
T_0	263.0 [K]	Varied parameter
ΔT_0	2.0 [K]	Varied parameter
C	2.80	Varied parameter
Θ_D	525 [K]	Varied parameter
η	1.29	Varied parameter
β	-58	Linked to η

Table 4.1: Parameters used in the Bean-Rodbell, Debye and Free electron models.

The agreement between model and measured data is done by evaluating the magnetization of the material through the least-square method. This was performed for fields in the range $0.2 < \mu_0 H < 1.5$ T. The lower bound of the range was used to minimize the influence of the domain effects in the low field region. The parameters are similar to those shown in literature (Turcaud et al., 2014, 2015) for similar stoichiometries. One may also observe that β is negative, which is not usually obeserved within this model. However, as we have seen in Figure 4.7, the ferromagnetic phase is smaller than the paramagnetic phase, as there is a significant decrease of the Jahn-Teller distortion when going from paramagnetic phase to the ferromagnetic one (Billinge et al., 2000; Belevtsev et al., 2006). Moreover, the same is observed when the transition is magnetically induced, as shown in Figure 4.8(a).

Figure 4.9(a) shows a comparison between the measured magnetization and the modelled one, where a good agreement is observed. It is also important to have in mind that this agreement is only achieved if the cluster size is taken in consideration. It plays a major role in the paramagnetic phase behavior. Here the cluster size was considered temperature and field independent for modelling simplification. However, there has been evidence that it may vary slightly with field for other perovskites (Jia et al., 2006a). Moreover, it is important to note that the clusters have been ascribed only to the paramagnetic phase, while in this thesis, as in literature (Turcaud et al., 2014, 2015), it was considered overall. Additionally, literature suggests that rather than a ferro- to paramagnetic transition, LCMO presents a ferromagnetic to polaronic phase transition (Souza et al., 2008).

Figure 4.9(b) shows the measured entropy change and the modelled one as a function of temperature and field, where again both are in good agreement. This could be expected already since the magnetization data was well fit. However, it is shown here in order to illustrate that the agreement is not lost when considering the magnetization data with $H < 0.2$ T for the Δs calculation, even though the magnetization best fit was evaluated only for $H > 0.2$ T.

Figure 4.10 shows the heat capacity as a function of the temperature for the appoximated internal magnetic fields of 0, 0.3, 0.8 and 1.3 T. The field applied during this measurement had to be applied normally in comparison to the one ap-

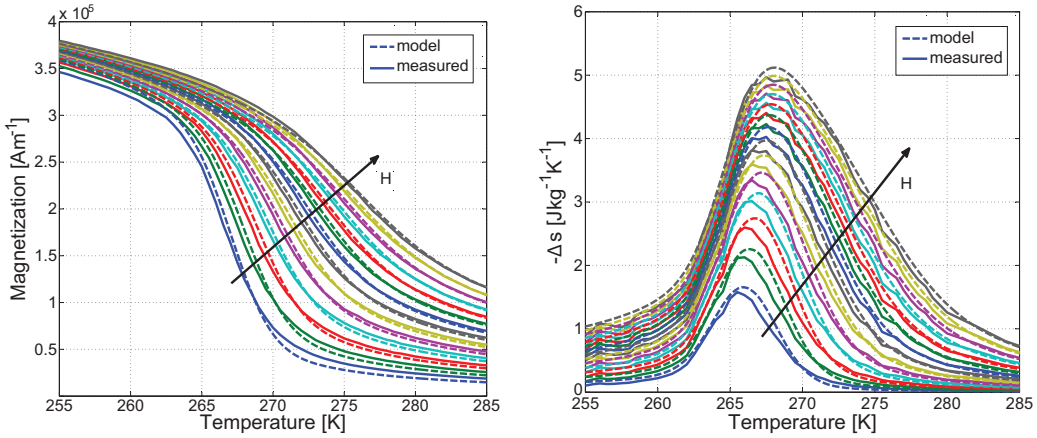

(a) (b)

Figure 4.9: (a) Magnetization as a function of temperature and internal magnetic field. The field varies from 0.2 to 1.5 T in steps of 0.1 T. (b) Entropy change as a function of temperature and internal magnetic field change. The field was changed from 0 to 0.2, 0.3, 0.4 ... 1.5 T.

plied in the magnetization measurements, due to incompatibility of sample size and the c_p measurement setup, which then led to higher demagnetization factors. One may see how the model reproduces the general behavior of the heat capacity as a function of field and temperature, considering the uncertainties of the measurement and approximations. The noise observed in the zero-field modelled data is due to nature of first order transition coupled with the T_0 distribution, it would require an unnecessary computational time to completely avoid it. The effect of the ΔT_0 has been shown previously in Figure 4.6 by the entropy curves as a function of the temperature. These curves were calculated by simple integration of the total heat capacity, which contains the magnetic, electronic and lattice contributions as shown in equation 2.26. The basic effect is to smear out the sharp transition and therefore the properties of the material related to temperature and field derivatives. The *smearing out* effect will be further discussed on the next Chapter.

One may see the parameter $\eta = 1.29$ in Table 4.1. This parameter evaluates the order of the transition and is defined by:

$$\eta = 40\frac{\rho_s}{C}\kappa_B\kappa T_0\beta^2\frac{[CJ(CJ+1)]^2}{(2CJ+1)^4-1}, \tag{4.5}$$

note that here the clusters are also included, while in the State of the Art Chapter it was not. It was derived by Bean and Rodbell (1962) that for $\eta > 1$, the material undergoes a first order phase transition. Indeed, several first order-like behavior may be observe, e.g. the asymmetric growth of the magnetic entropy change in Figure 4.9(b), and heat capacity peak shifting with fields in Figure 4.10.

Figure 4.11(a) shows the relative spontaneous magnetostriction as a function of temperature for the different fields (dashed lines) as predicted by the model, whereas the solid lines are calculated by $\frac{1}{2}\lambda_0\beta\kappa\mu_0 M^2_{\text{meas.}}$, where $M_{\text{meas.}}$ is the measured magnetization. This relation between the relative volume change at fixed field is shown

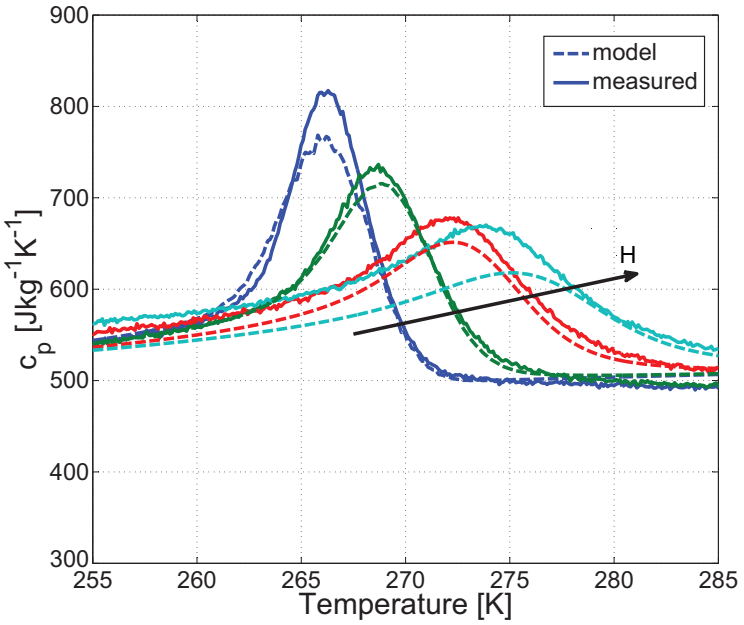

Figure 4.10: Heat capacity as a function of the temperature for the approximated internal magnetic fields of 0, 0.3, 0.8 and 1.3 T, during the cooling procedure.

in Equation 2.24. As expected there is a good agreement, which is reasonable as we have seen the good agreement between the magnetizations as well, and the modelled spontaneous magnetostriction is basically a function of the magnetization.

The investigation of the volume change is further evaluated by the isothermal magnetostriction, $\omega(T, \Delta H)$. This property is chosen instead of the volume itself, because the model here does not take into consideration thermal expansion, and isothermal magnetostriction measurements are at hand. In order to calculate the isothermal magnetostriction from the Bean-Rodbell model, one starts with equation 2.24 to get:

$$\omega(T, \Delta H) = \frac{V(T, H_f) - V(T, H_i)}{V(T, H_i)} = \frac{M(T, H_f)^2 - M(T, H_i)^2}{M(T, H_i)^2 + 2(\lambda_0 \beta \kappa \mu_0)^{-1}} \tag{4.6}$$

One may see that if $T > T_C$ and $H_i = 0$ T that equation 4.6 returns equation 2.24 for $P = 0$ MPa. Figure 4.11(b) shows the comparison between the isothermal magnetostriction of the model (dashed lines) and measured data (solid lines). As one can see, here is where the model fails to describe the material's behaviour. The measured ω is about 9 times smaller then the modelled one. The volume change over prediction may be intricate to the very basic assumptions of the model itself. Bean and Rodbell have shown that this model works for MnAs, which also presents anisotropic elastic properties. Moreover, the magnetic properties of MnAs arise from direct exchange interactions. Concerning what was shown up to this point the model may have failed to represent the magnetostriction due to two possibilities. Firstly the perovskite here studied presents anisotropic elastic properties. Although Bean and Rodbell (1962) have shown that the model correctly predicts the magnetic behavior, transition shift with field and hysteresis for an anisotropic elastic material, it has not evaluated the isothermal magnetostrictive behavior. In fact, up to

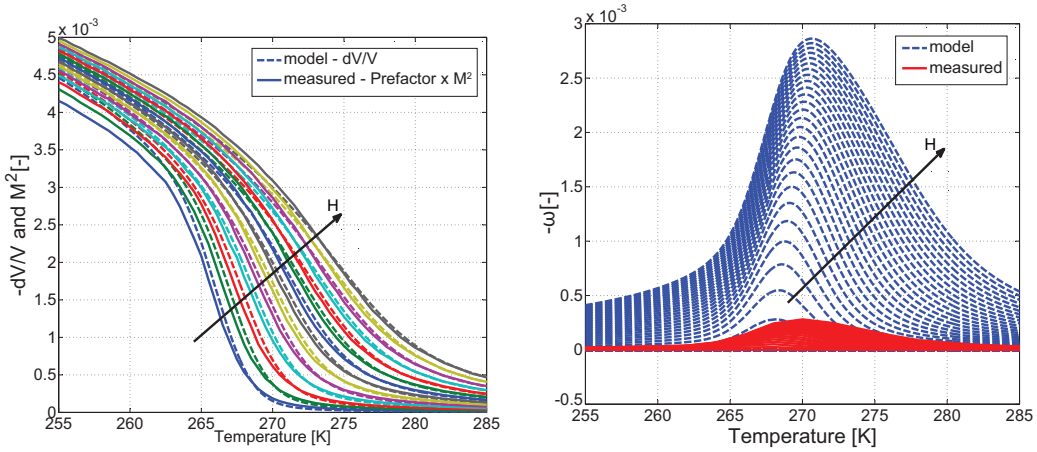

Figure 4.11: (a) the spontaneous magnetostriction as a function of temperature and different fields (dashed lines) as predicted by the model, whereas the solid lines are a pre-factor ($\frac{1}{2}\lambda_0\beta\kappa\mu_0$) times the squared measured magnetization as a function of temperature and field. (b) Magnetostriction as a function of temperature and field for the model and measured data. The field was changed from 0.2 to 0.3, 0.4, 0.5 ... 1.5 T.

the author's knowledge, there has not yet been a published study of the isothermal magnetostrictive behavior through Bean-Rodbell model. Secondly, studies have shown that the T_C is influenced by the angle between Mn-O, and thus the Jahn-Teller distortion (Bridges et al., 2010), rather than the volume itself (Coey et al., 1999).

Unfortunately, it was not found any reference to compare the isothermal magnetostriction model results. Still, the model describes with good agreement the thermal and magnetic behavior of the material. Perhaps if the model is modified to take in consideration the features here mentioned, the volume change could also be predicted.

4.5 Summary

In this chapter a detailed study of the phase transition of $La_{0.67}Ca_{0.33}MnO_3$ was presented. Different characterization methods and models were used in order to deliver a better understanding of the transition. The following conclusions may be taken from the results showed here:

(a) Evidences of magnetic polarons or clusters were observed through a deviation of the Curie-Weiss inverse susceptibility. The size of these clusters was not influenced by external magnetic field, for fields up to 1.0 T.

(b) Heat capacity measurements at different temperature rates and fields showed that any observed hysteresis in this material is an artefact of extrinsic factors related to thermal diffusivity and thermal contact resistance. While direct

entropy change measurements in equilibrium conditions showed no discernible hysteresis.

(c) Still, the material present FOPT features, even though no hysteresis is observed; The transition temperature shifts with magnetic field, as observed in the heat capacity measurements, and the entropy change consequently grows asymmetrically towards higher temperature, as the entropy change measurement shows.

(d) The link between the lack of hysteresis, and FOPT features can be given by a distribution on the Curie temperature. If the material presents defects, e.g. chemical distribution or strain, it may lead to a T_C distribution. By using the Bean-Rodbell model with a imposed normal distribution to the fitting parameter T_0, it was observed that the thermal hysteresis decreases significantly with the T_C distribution. Therefore, a perfect single crystal of $La_{0.67}Ca_{0.33}MnO_3$ should present thermal hysteresis, and the observable thermal hysteresis should decrease with the increase of defects.

(e) Additionally, the material showed magneto-elastic coupling through expansion when going from a ferro- to a paramagnetic state. In isotherm terms, the magnetostriction showed a contraction with increasing magnetic field.

(f) It is observed that the isothermal magnetostrictive behavior is very similar to the isothermal entropy changes. In fact, a relation between both is proposed for varying content of Ca in $La_{1-x}Ca_xMnO_3$, within the ferromagnetic region ($0.2 < x < 0.33$), and for $\Delta H \leq 1.5$ T.

(g) The magneto-elastic coupling was further investigated with the Bean-Rodbell model. It showed good agreement to the measured magnetization and entropy change when considering the clusters. However, when calculating the isothermal magnetostrictive behavior, the model failed to predict the property. The shape of the curves were very similar, nonetheless the magnitude was around 9 times smaller in the measurement than the in the model.

(h) Although this material has been highly characterized and modelled in the literature. The author does not find modelled results of isothermal magnetostrictive behaviors. At this point the author can on speculate about the reasons behind it. Firstly the polaronic effect was considered to be magnetically and thermally independent which is incorrect. However, if this was the only issue, the modelled results should at least show a better agreement in the paramagnetic magnetostrictive behavior, which was not the case. Despite this fact, the magnetic properties were well predict using the cluster size similar to the one calculated from the inverse susceptibility.

(i) The second point is that the model considers the compressibility to be constant in respect to temperature and field, hence the bulk modulus as well. Nevertheless, literature has shown that this is not the case. This could also be the influence behind the lack of agreement of the magnetostriction model.

Chapter 5

$La(Fe,Mn,Si)_{13}H_{1.65}$

In this chapter it is presented and discussed the results concerning the characterization and modelling of $La(Fe,Mn,Si)_{13}H_{1.65}$. The characterization methods used to characterize the materials are described in Chapter 3. The materials used in this chapter are provided by Vacuumschmelze GmbH, and have been characterized in detail by other research groups (Lovell et al., 2015; Basso et al., 2015). This material is provided in powder form, since there is not yet an industrial process to fully hydrogenate La-Fe-Si alloys in the bulk form, as described in the subsection 2.3.3. The powder particles are irregular shaped, with sharp corners and in the range of 500 μm of size.

This chapter consists of different sections. Firstly the general properties of this material will be discussed in terms of heat capacity, magnetization and magnetic entropy change. Since such properties have been in general analyzed in the literature (Basso et al., 2015), this is used just to qualify the different compositions and see if the properties are in agreement with the literature. The following section discusses the effect of a distribution of T_C in the material properties. Then, a deeper analysis of the volumetric behavior during the transition of FOPT compositions is done through XRD measurements, the Williamson-Hall method and the Bean-Rodbell model. Finally a summary of the results will be given by the end of the chapter.

5.1 General properties

The general properties of $LaFe_{13-x-y}Mn_xSi_yH_{1.65}$ were evaluated as a function of Fe/Mn/Si content. This material was produced (Barcza et al., 2011) and provided by Vacuumschmelze GmmbH & Co. Kg, which is also a part of the Enovheat project. Heat capacity measurements are used to acquire information on the transition temperature, transition sharpness and thermal hysteresis. In order to be able to measure this property, the particles are first ground to finer particles ($< 100\mu$m). This assures a better thermal contact between particle and grease. Then the particles are wrapped in an Al foil with a thin layer of grease, and this is put on the peltier for the measurement. The Al foil piece was usually 10 times lighter than the sample, so its contribution to the measured heat capacity is little. Still, the foil was considered and a calibration measurement is performed to take out its contribution.

In order to extract extrinsic contributions to the heat capacity measurement, in

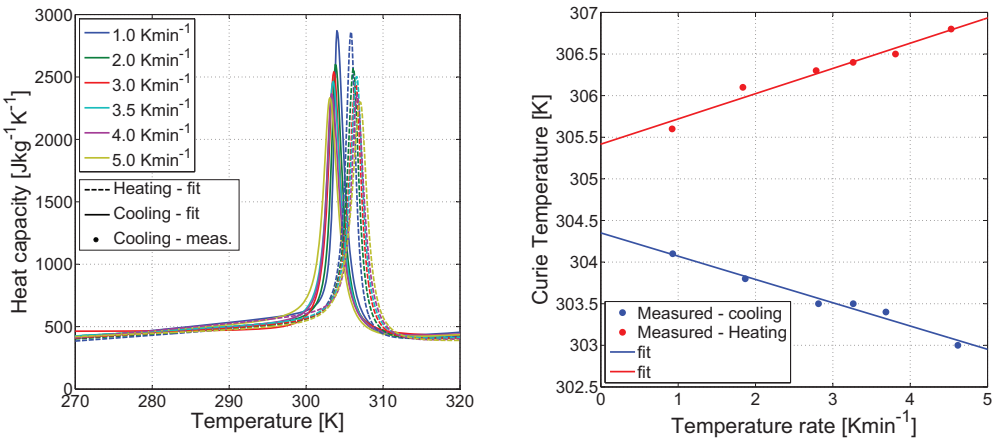

(a) (b)

Figure 5.1: (a)Heat capacity as a function of temperature and temperature rate at 0 T of $LaFe_{11.47}Mn_{0.25}Si_{1.28}H_{1.65}$. (b) The peak temperature as a function of temperature rate. The hysteresis is calculated from the linear regression temperature difference at 0 Kmin^{-1}.

x	y	**Material ID**	T_C	$\Delta T_{hyst.}$
0.46	1.32	VAC-4	270.7±0.2 K	0.2±0.3 K
0.37	1.30	VAC10	286.5±0.1 K	0.4±0.2 K
0.30	1.29	VAC21	292.1±0.2 K	0.5±0.4 K
0.25	1.28	VAC30	305.4±0.2 K	1.0±0.5 K
0.22	1.23	VAC42	315.7±0.3 K	1.0±0.5 K
0.06	1.18	VAC70	339.6±0.4 K*	2.2±0.7 K*

Table 5.1: The Curie temperature during the heating procedure, thermal hysteresis and the different sample IDs that are used in this thesis for the different Mn and Si content in $LaFe_{13-x-y}Mn_xSi_yH_{1.65}$. (*)This data is from the commercial DSC, since the T_C of this material is out of the temperature range of the custom-built one.

particular to investigate the hysteresis. As previously stated in the $La_{0.67}Ca_{0.33}MnO_3$ chapter, the hysteresis is the largest at 0 T. So the investigation as a function of temperature and temperature rates is performed at 0 T. Figure 5.1(a) shows an example of heat capacity measurement as a function of temperature and temperature rate at 0 T of $LaFe_{11.47}Mn_{0.25}Si_{1.28}H_{1.65}$. Moreover, Figure 5.1(b) shows the transition temperature as a function of temperature rate. The same behavior as in the $La_{0.67}Ca_{0.33}MnO_3$ is observed in this case, i.e. the temperature rate tends to shift the peak position, giving some extrinsic contribution to the measured T_C. Again, the same argument of diffusivity issues are the reason for this effect. Using the same procedure, the different compositions of $La(Fe,Mn,Si)_{13}H_z$ were investigated. In Table 5.1 the T_C during the heating procedure and thermal hysteresis and ΔT_{hyst} are shown for the different compositions. Additionally, in this table the material ID that will be used throughout this chapter is provided.

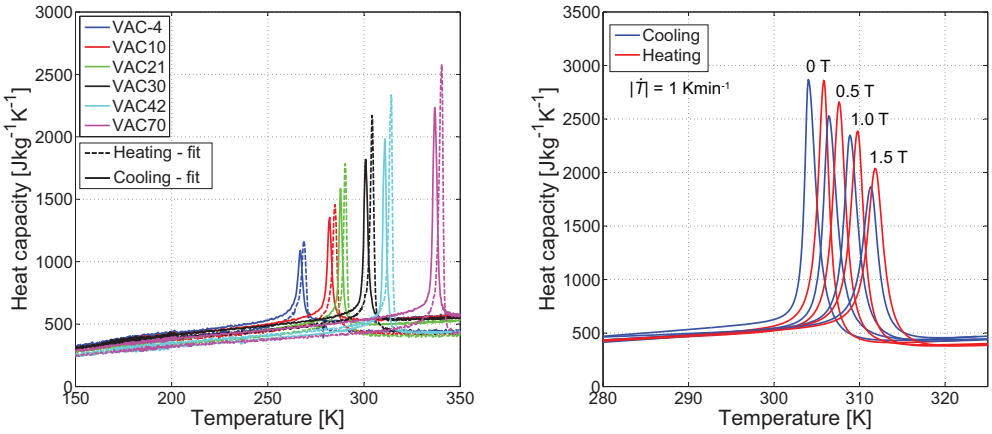

(a) (b)

Figure 5.2: (a) Heat capacity as a function of temperature for the different compositions measured at a commercial DSC and with $|\dot{T}| = \pm 2.0$ Kmin^{-1}. (b) The heat capacity as a function of applied field for VAC30 for $|\dot{T}| = \pm 1.0$ Kmin^{-1}.

The heat capacity was also evaluated as a function of temperature in a commercial DSC at a rate of ± 2 Kmin^{-1}, and the result is shown in Figure 5.2(a). One may see again the hysteresis increasing with the decrease of Mn and Si content, confirming what is observed in table 5.1. Moreover, for the material VAC70 the measurement was also performed as a function of temperature rate (not shown in the image). This is because the T_C of this material falls out of the temperature range of the custom-built DSC. Therefore, the thermal hysteresis shown in Table 5.1 for VAC70 is a result of the measurement in the commercial DSC, while the other results shown in the table are from measurements in the custom-built calorimeter. In addition, from Figure 5.2(a) one may see that the material presents very similar behavior, where the difference is just the peak sharpness, the T_C and the hysteresis. Due to number of materials here studied, some of the results in this chapter are shown for just one material, although all the materials were characterized, in order to ease for the reader and do not overpopulate the thesis with unnecessary graphs.

The heat capacity as a function of temperature and field was also investigated for the materials VAC-4, VAC10, VAC21, VAC30 and VAC42. The material VAC70 is left out because the commercial DSC does not present an apparatus for changing the field. Figure 5.2(b) shows the heat capacity as a function of field and temperature for VAC30. All these materials showed the same behavior: the heat capacity peak decreases with increasing fields while shifting towards higher temperatures. These features are normally related to first order transitions as previously discussed.

Still, a clear difference can be observed between Figure 5.2(b) and the heat capacity measurement as a function of field of $La_{0.67}Ca_{0.33}MnO_3$ (see Figure 4.4): the observed hysteresis decreases with field. This is a clear indication that VAC30 indeed presents thermal hysteresis. In order to evaluate the thermal hysteresis as a function of applied magnetic field, the T_C as a function of field for each of the materials was computed. These measurements were done at 1 Kmin^{-1}, and the contribution given

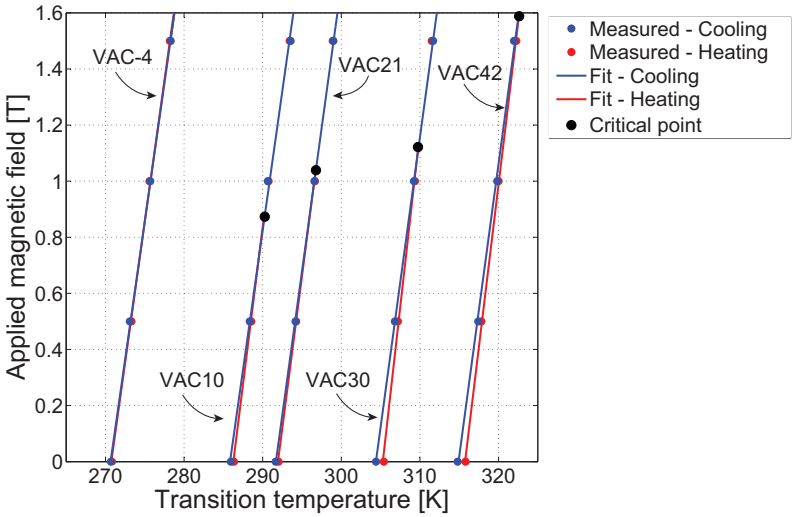

Figure 5.3: The transition temperature as a function of applied magnetic field for the different compositions of La(Fe,Mn,Si)$_{13}$H$_z$.

by the temperature rate was taken into consideration. One may see in Figure 5.3 that the transition temperature increases with magnetic field for all the materials. However, one of the materials does not present hysteresis – VAC-4. This is the material with the highest content of Mn and Si, which leads to SOPT (Barcza et al., 2011; Basso et al., 2015). Basso et al. (2015) however, also did not observed significant thermal hysteresis in VAC10 while in this work we observe hysteresis in this material. As we may expected from Table 5.1 the thermal hysteresis with decreasing Mn and Si content increases, here also we observe that the critical point increases for increasing T_C, which supports the idea that the transition becomes more first order-like with decreasing content of Mn and Si[1].

Additionally, one may observe in Table 5.2 that the shift of the transition with respect to the applied field, dT_t/dH, is constant for the cooling procedure with the decrease of Mn/Si content, while for the heating procedure dT_t/dH decreases with the decrease of Mn/Si content. Moreover the critical field is increasing with the decrease of Mn and Si content.

Figure 5.4(a) shows the magnetization as a function of temperature for a field of 0.1 T for different compositions of La(Fe,Mn,Si)$_{13}$H$_z$[2]. This field was chosen in order to evaluate the transition with minimum domain effects. We may observe once again, the sharpness of the transition increasing with the Mn/Si content. Additionally, Figure 5.4(b) shows the cyclic behavior of the entropy change calculated through the approximation of the Maxwell relation as explained in section 3.2. The

[1]The idea of a transition being more first order than others might be misleading. The author of this thesis would like to make it clear that a transition is first order or it is not – there is no magnitude to it. However, some measurable identities, e.g. latent heat and hysteresis, do change for different FOPT materials. This is what is meant by a "more" first order transition, and the reader is advised to keep it in mind.

[2]VAC70 was not included in this study, as the main purpose of the cyclic study was to provide data for numerical modelling of AMR for the EnovHeat project heat pump, which will operate at temperatures below 320 K. Nonetheless, the results were fruitful and therefore a discussion about them is here added.

Material	dT_t/dH (heating)	dT_t/dH (cooling)
VAC-4	4.8±0.3 KT^{-1}	4.9±0.3 KT^{-1}
VAC10	4.6±0.2 KT^{-1}	5.0±0.5 KT^{-1}
VAC21	4.6±0.2 KT^{-1}	4.9±0.2 KT^{-1}
VAC30	4.3±0.5 KT^{-1}	4.8±0.1 KT^{-1}
VAC42	4.3±0.2 KT^{-1}	4.8±0.5 KT^{-1}

Table 5.2: The shift of the transition temperature T_t with the applied magnetic field for the different materials during heating and cooling.

cyclic process is the one where the losses due to hysteresis are taken into account in the entropy calculation as discussed in section 3.2 and in the literature (Basso et al., 2015; von Moos et al., 2015). Firstly, Figure 5.4(b) shows that all the materials present an asymmetric increase of the Δs towards higher temperatures, feature of a first order phase transition as previously discussed.

Secondly, these values of entropy change are slightly smaller than the ones shown by Basso et al. (2015). In their measurements the Δs was measured isothermally in a calorimeter, much similarly to the characterization method explained in the subsection 3.1.1. In this thesis the approach was the approximation of the Maxwell relation. As explained in the section 3.2, this approximation leads to a decrease and broadening of the calculated entropy change, due to the discretization of the magnetization measurements with respect to the temperature. On the other hand, the isothermal calorimetric approach does not have issues regarding discretization, which certainly leads to larger values of Δs. Another point is that here the demagnetization field is taken in consideration, while there it is not mentioned if it is considered. When the demagnetization field is considered in order to correct for the internal field, the effect is to decrease the entropy change (Bahl and Nielsen, 2009). Therefore, it is not straightforward to compare both results of entropy change, although the general behavior as a function of Mn/Si content and magnetic field change remains the same.

The microstructure was investigated through SEM backscattered electron images. Figure 5.5 shows two images of the microstructure of VAC70. One may see in Figure 5.5(b) that there are three phase: the La-rich phase, which is the observed as the white spots; the α-Fe, which is represented by the dark gray area. The remaining phase is the main one, $La(Fe,Mn,Si)_{13}H_z$. Additionally, the grain sizes are in the range of 15-30 μm. Furthermore, the α-Fe grains are within the main phase grains, while the La-rich phase are mostly in small island in the grain boundaries of the main phase. As it will be pointed out in the section 5.3, this microstructure may play an important role on the mechanical stability of the material.

The material was also evaluated as an active magnetic regenerator. The investigation shows a comparison between using multi-layer regenerator and a single layer one, as well as the effect of epoxy bonding the $La(Fe,Mn,Si)_{13}H_z$ particles. The results of this investigation are summarized in the Appendix A.2.1.

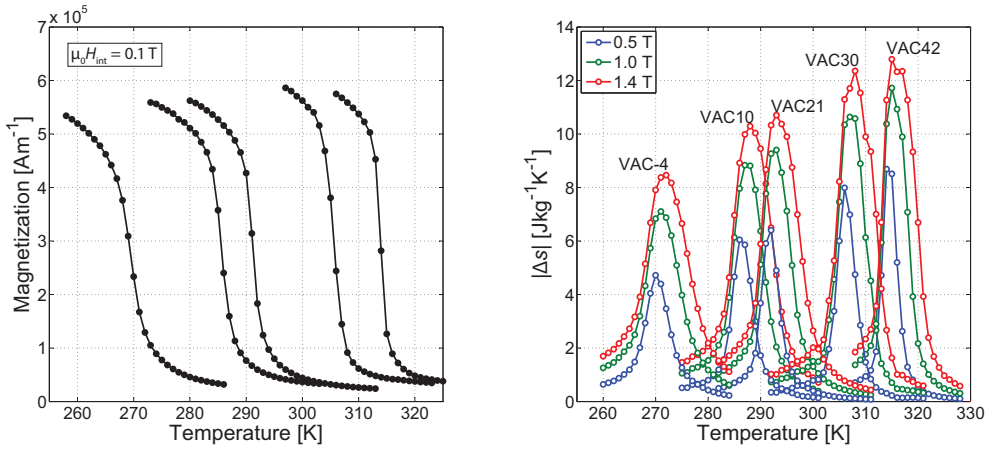

(a) (b)

Figure 5.4: (a) The magnetization as a function of temperature at an internal field of 0.1 T and (b) the cyclic entropy change as a function of temperature for different internal field changes and for different compositions of La(Fe,Mn,Si)$_{13}$H$_z$.

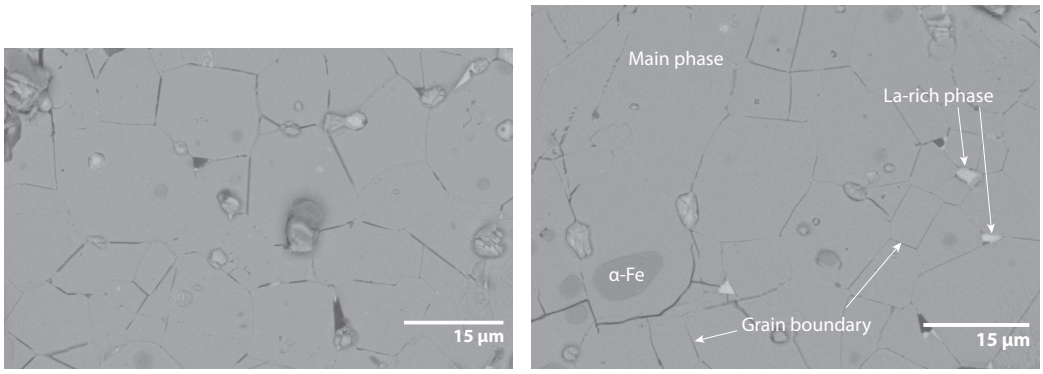

(a) (b)

Figure 5.5: (a) and (b) show micrographs of La(Fe,Mn,Si)$_{13}$H$_z$. In (b) the different phases and features are pointed out.

5.2 The Curie temperature distribution

It has been suggested in literature that Curie temperature distributions tend to form in magnetocaloric materials, due to compositional distributions or other defects[3]. The distribution was studied in terms of the heat capacity, magnetization and entropy change.

The study of the effect of the distribution starts with magnetization measurements at a fixed applied field. These measurements were performed in three types of samples: (i) Single particles, (ii) multiple single particles, and (iii) multiple ground

[3]The compositional distribution itself may be considered as a defect

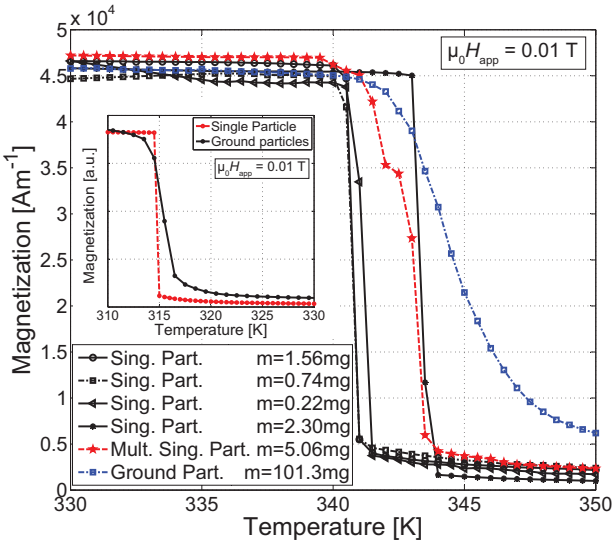

Figure 5.6: Magnetization as a function of temperature in an applied field of 0.01 T, for the different types of sample for VAC70. The inset shows a comparison between single particle and ground particles for VAC42.

particles. For the types (i) and (ii) of samples the particles were glued to a rod inside an area of 16 mm^2, and for the type (iii) the powder was pressed inside a cylindrical container and attached to the rod of the VSM. Moreover, the single particles have a particle size of about 500 μm, while the ground particles were ground to a particle size $< 60\mu$m. The temperature stability was $T \pm 0.2$ K. As observed in Figure 3.10, first order phase transitions are more susceptible to broadening effects. Therefore, for this study VAC70 is used, as the literature (Basso et al., 2015) has shown it is most likely the strongest FOPT material in the $La(Fe,Mn,Si)_{13}H_z$ series here analyzed, which is also backed up by the heat capacity measurements shown in Figure 5.2(a).

Figure 5.6 shows the magnetization as a function of temperature for the different sample types of VAC70. Firstly it is clear that single particles present a extremely sharp transition. Secondly, the Curie temperature is dependent on the particle that was taken to be measured, which proves the distribution of Curie temperature. Moreover, when adding multiple single particles (dashed red line) – in a range of 10 to 15 particles, the effect was such that the transition becomes stepwise with respect to temperature. This effect is attributed to the different T_C that each particle may present. Once the particles are ground the material shows a continuous transition, even though it is expected to be a first order phase transition, i.e. discontinuous. The inset shows the magnetization as a function of temperature for an applied magnetic of 0.01 T for VAC42, confirming the effect observed in VAC70.

A previous work on the effect of particle size of $LaFe_{11.6}Si_{1.4}$ argues that the transition becomes SOPT with the decrease of the particle size due to the extreme stresses that the particles undergo when milling them to smaller sizes (Liu et al., 2012). Nevertheless, up to the knowledge of the author of this thesis there has not been a publication studying the mechanical properties of $La(Fe,Si)_{13}$ alloys and their hydrides. On the other hand, there has been several studies showing that the material presents brittle behavior (Lyubina et al., 2010; Waske et al., 2015; Liu et al., 2012).

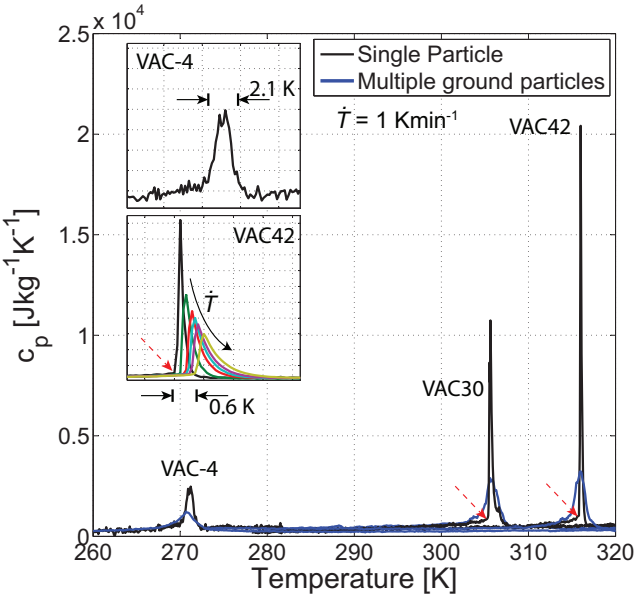

Figure 5.7: The heat capacity as a function of temperature at zero field during the heating procedure for single particles and multiple ground particles. The top inset show a zoom on the transition of VAC-4. The bottom inset shows a zoom of the transition of VAC42 for different rates, where the black arrow indicates the direction of increasing rate. The red dashed arrows are pointing the a kink where the transition occurs. The data may have been artificially shifted in the temperature axis by ±1.0 K to match peak positions and ease comparison.

When materials present a brittle behavior, mechanisms to generate defects are extremely limited. Usually these defects can be separated in three major groups: dislocations, stacking faults and surface formation (cracks and grain boundaries); where the first one is one-dimensional and the other two are two-dimensional defects (Callister, 2007). In brittle materials, the nucleation, and the movement of dislocation (i.e. plastic deformation) are extremely unlikely. The stacking fault is not deeply studied in this thesis. Still, as the material presents a face-centered cubic structure it should present a higher stacking fault energy, nonetheless signals of their presence were not observed in the microstructure of the material through SEM imaging. Cahn and Haasen (1996) have shown that even in low magnifications, one could observe wavy features in a (polished) grain of Al that has undergone severe plastic deformation, and these features are related to the high stacking fault energy of Al[4]. These wavy features have not been observed in the micrographs of this work, although the optimal way to observe such features would be by secondary electron images instead of backscattered. In addition La(Fe,Mn,Si)$_{13}$H$_z$ presents brittle behavior, which basically does not allow plastic deformation. The last major defect is the well known grain boundary. However, in order to insert enough inhomogeneity through surface formation for properties modification, the particle size has to decrease significantly to nanometric scales, which is not the case of this study.

Therefore, the T_C distribution in this thesis is interrelated to compositional

[4]One may see the image in the page 1920 of the Volume 3 of the book.

distribution and the polycrystallinity of the material. This means that slight concentration variations are assumed to be present throughout the material. This effect is backed up by heat capacity measurements. These measurements were performed with different temperature rates at 0 T and at $|\dot{T}| = 1.0$ Kmin^{-1}. The thermal hysteresis did not show significant differences from the ones stated in Table 5.1. Figure 5.7 shows the heat capacity of VAC-4, VAC30 and VAC42 as a function of temperature for a temperature rate of $\dot{T} = 1$ Kmin^{-1} and at 0 T for single particles and multiple ground particles. This data is the original measured one and it was not fited according to subsection 3.1.2. The first thing to notice is that the data becomes much noisier for single particles, which is due to the relative low mass of these samples (∼1mg) in comparison to the multiple particles (∼10mg).

A clear feature in this graph is the difference of the sharpness between multiple particles, in particular for VAC30 and VAC42. As the dashed red arrows point out, there is a kink in both materials just below the transition. The bottom inset of the figure shows a zoom of the transition of VAC42 for different temperature rates, and for each of them the kink is present. This leads to the conclusion that this observed kink is not due to noise effects, but an intrinsic behavior of the material. Additionally, one may see that the magnitude of the peak increases with the decrease with the Mn/Si content for both single and multiple particles, as expected from the previous measurements. Such sharp peaks lead to the conclusion that the transition of these materials are indeed discontinuous, i.e. a first order transition. On the other hand, VAC-4 did not present any kink for the single particle and the peak is relatively wider than the other materials, which again may mean that its transition is second order.

In addition, it is observed that the relative difference of the magnitude of the peak increases with the decrease of Mn and Si content. Nevertheless, if VAC30 and VAC42 do present a FOPT (and they do, as later in this thesis it will be pointed out), one should not evaluate the magnitude of the peak as an indication of how much is the "orderness" of the transition. This is because a FOPT would lead to a delta function, and the difference between the peak magnitude of VAC30 and VAC42 single particles is just due to measurement uncertainties or possibly small T_C distributions within the particle itself. Moreover, the area under the peak was also calculated for both materials and for both type of samples. VAC42 showed an area[5] of 5.3±0.3 and 5.4±0.2 kJkg^{-1} for the multiple particles and single particle, respectively, while VAC30 showed an area of 5.5±0.3 kJkg^{-1} for both types of sample. Usually the area under the peak in the heat capacity represents the latent heat involved in the transformation. This result shows that despite of both VAC30 and VAC42 present a different magnitude of the heat capacity peak, the energy involved in the transformation is the same. In section 5.3 it is shown that indeed the volume change that both materials present is virtually the same, which is an indication that both VAC30 and VAC42 should present similar latent heat.

The reason for the difference of single particle and multiple ground particles is related with the T_C distribution. This, however, does not necessarily mean that the single particle does not have a T_C distribution. As discussed in chapter 2, this material presents a volume change when changing its magnetic state. Moreover, we observed through SEM images that the particles are polycrystalline. Let us assume

[5]The mean and standard deviation are calculated from the different temperature rates.

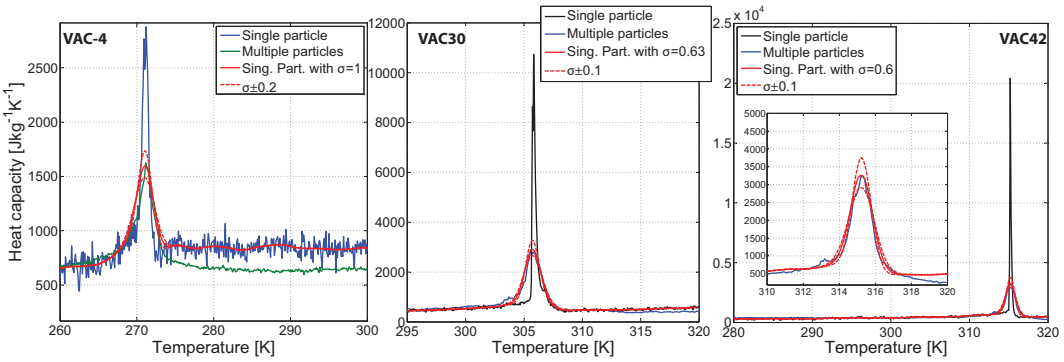

Figure 5.8: Heat capacity as a function of temperature of VAC-4, VAC30 and VAC42 for single and multiple particles. The effect of superimposing a normal distribution to the single particle data is also shown, and the inset of the graph on the left shows the a closer look on the effect of different σ. The data may have been artificially shifted in the temperature axis by ± 1.0 K to ease comparison.

that each grain inside the particles might have a slightly different T_C from its surrounding grains. This means that the grains within the particle are mechanically locked in between themselves (Waske et al., 2015; Liu et al., 2012) and the volume change is limited and, therefore, the transition of each single grain can be altered by such limitation, so the transition is held back until a specific temperature where the energy is sufficient to overcome the limitation. On the other hand, when the particles are crushed to finer particles, the grains will be less constrained, giving a broadening to the transition.

To simulate the effect of the distribution on the heat capacity measurement, a normal distribution is superimposed on the single particle measurements and a best fit to the multiple particles is taken. The fit was done through the least-square method. Figure 5.8 shows again the heat capacity as a function of temperature of VAC-4, VAC30 and VAC42 for both single and multiple ground particles, however now it is also shown the effect of applying a normal distribution to the single particle data. The results show that a standard deviation in the region of $0.6 < \sigma < 1$ reproduces with good agreement the multiple particles behavior[6].

These results support the idea that decreasing the particle size, the transition is *observably* more continuous. However, the latent heat involved in the transition is the same, regardless of the particle size (with the probable exception of nano-particles). Moreover, we observe that just by applying a normal distribution to the single particle data, it was possible to reproduce the multiple ground particles behavior. These two results indicate that the transition of the material does not become that of a SOPT, however its properties is smeared out due to T_C distribution, giving *the impression* that it is second order.

In addition to heat capacity measurements, the study of the effect of T_C distribution is also performed through magnetization measurements for Δs calculation of the material VAC70, as it exhibits the sharpest transition and as figures 5.8 and

[6]Kaspar K. Nielen has performed a deconvolution in the measured data of the multiple particles, which led also to reproduction of the single particle data. The result is not shown here as it was not a production from the author of this thesis.

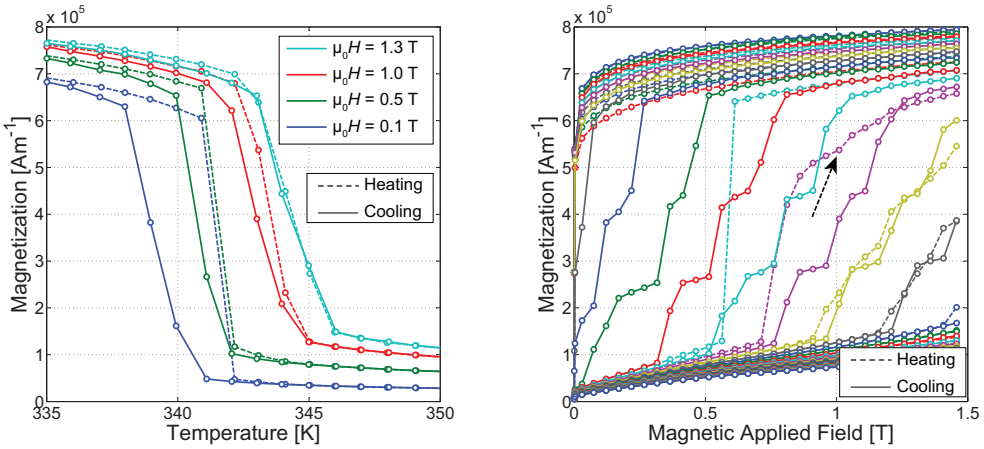

(a) (b)

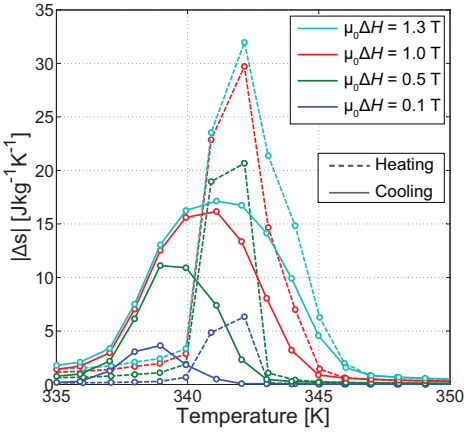

(c)

Figure 5.9: Single Particle results of VAC70; Magnetization as function of (a) temperature and (b) internal magnetic field. (c) The entropy change as a function of temperature. All figures show the properties for both heating and cooling procedures.

5.6 show, it is heavily influenced by the particle sizes. These magnetization measurements were performed in two sample types for each stoichiometry: (i) Single particle and (ii) multiple ground particles. The multiple ground particle mass is in the range of 70 mg, while the single particle is in the range of 1mg. We start the analyses with Figure 5.9 summarizing the magnetic properties. The results shown in Figures 5.9(a) and 5.9(b) are those of the single particle of a material in the equilibrium state. Figure 5.9(a) shows the magnetization as a function of temperature for different fields and for the cooling and heating procedure. It is important to note here that the measurements were performed first during heating, then during cooling. The results show again a very sharp transition even for an internal magnetic field as high as 1.3 T, which is not observed in multiple particles as shown in Figure 5.6. The hysteresis decreases with the increase of field, as previously it was

shown for the other La(Fe,Mn,Si)$_{13}$H$_z$ materials. Moreover, Figure 5.9(b) shows a very sharp magnetically induced transition. In addition, the magnetization shows a very different behavior during heating and cooling. Figure 5.9(c) shows the entropy change for both heating and cooling. One may see that the heating branch of the Δs curve is much larger than the cooling one − roughly twice the amount.

These measurements were performed once more on the same particle to understand if this is the intrinsic magnetic properties of the material or this difference between heating and cooling is due to some extrinsic feature. Figure (a), (b) and (c) summarize the results of the second run of magnetization measurements in the same single particle of VAC70. These measurements were also done in equilibrium conditions, where the results shown are the first cooling, and the second heating run. One may see that the behaviours of the heating and cooling curves are in general very similar, not showing any longer the difference seen in Figure 5.9. Additionally, Figure 5.10(d) shows a comparison of all the different Δs measured for VAC70. One can see that in the first heating behavior is anomalous compared to the other ones, where the multiple particles and single particle show very similar behavior.

When extracting the sample out of the VSM after the second run of magnetization measurements, it was observed that the single particle has broken apart. The author of this thesis could count four pieces, although the mass of the broken particles did not sum up to the original single particle. The reasoning behind this anomolous behavior of the magnetization curves can be attributed to the cracking of the particle. It is believed that the particle broke in the first transition from PM to FM phase. The arrow in Figure 5.9(b) shows in which isothermal measurement it is believed the sample broke a part. After this curve all the isothermal measurements showed similar behavior. Nevertheless, it is possible to see that before this the transition was much sharper, which led to a larger entropy change. Once the single particle has broken the transition become much broader, and the Δs become very similar to the one observed for multiple particles.

The same study was performed in VAC30 and VAC42. The single particle of these materials, however, did not break a part during measurement, and the magnetic behavior as a function of temperature and field is very similar to the one shown for the first run of VAC70 (Figure 5.10).

5.3 The lattice across the transition

In this section, the lattice of La(Fe,Mn,Si)$_{13}$H$_z$ is evaluated through XRD isothermal measurements during the magnetic transition. These measurements were performed Rigaku SmartLab diffractometer, with a furnace that allows a stable temperature control for temperatures above room temperature. The measurement is done stepwise in temperature, where the minimum step the device allows is 1 K, which is the temperature step used. All the XRD isothermal measurements are performed once it is ensured that the temperature is stable. Additionally, the temperature rate in between measurements was 1 Kmin^{-1}, which also ensured no temperature overshoot. The materials evaluated in this section are VAC30, VAC42 and VAC70, since the furnace allows temperature control only above room temperature. Additionally the powders were ground into very fine particles (the majority of them with sizes below 60 μm) to ensure the quality of data.

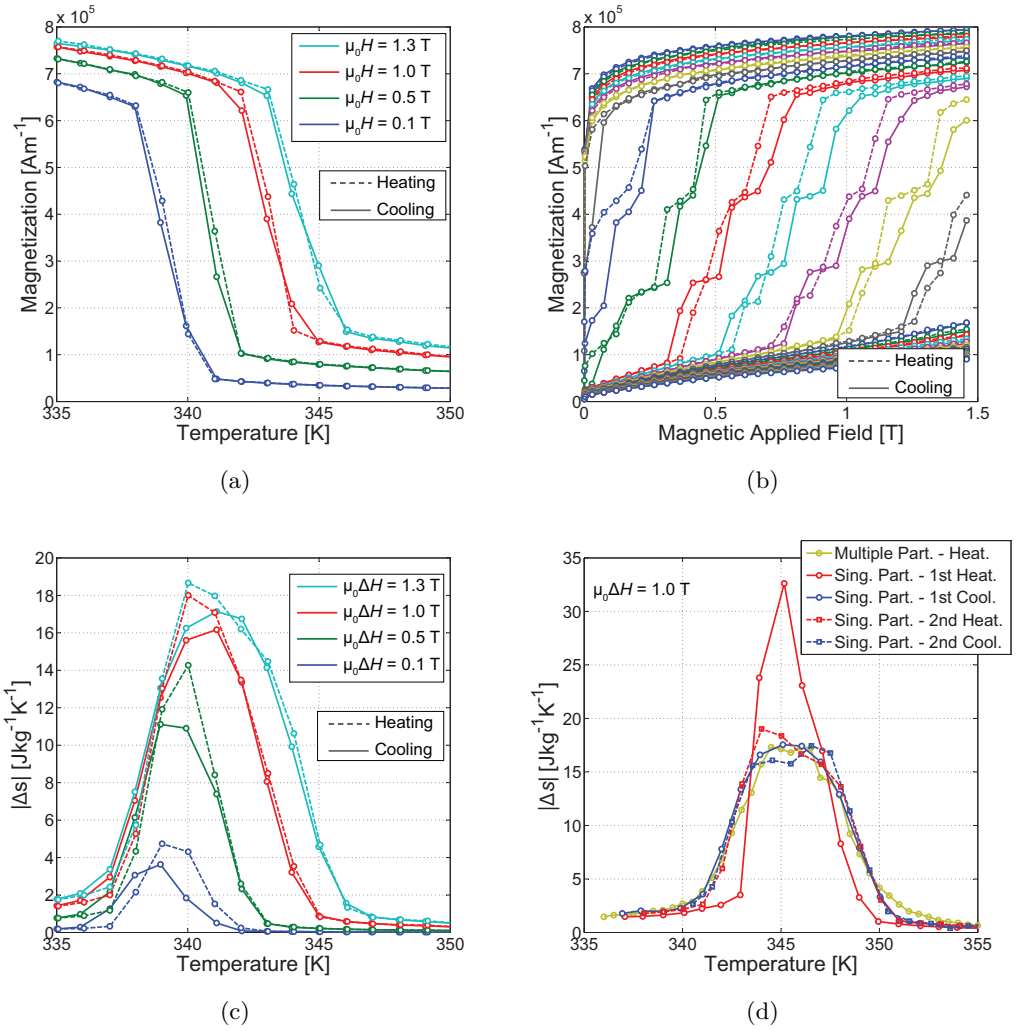

Figure 5.10: Single Particle results; Magnetization as function of the (a) temperature and (b) internal magnetic field. (c) shows the entropy change as a function of temperature. In (a), (b) and (c) The curves are the ones of the first cooling run, and the second heating run. (d) Entropy change as a function of temperature comparing the result of multiple particles, and the first and second run of the single particle. In (d) temperature may have been artificially shifted by ±1.0 K to ease comparison.

The XRD patterns are refined using the Rietveld refinement as explained in subsection 3.3.2. The following parameters are refined in order to have a good agreement between the measured pattern and the refined one: temperature factor; unit cell parameter a[7]; scale factor; the FWHM parameters u, v and w; the asymmetry parameter; the Lorentzian mixing parameter; and 6 background parameters, i.e. in a total 14 parameters were refined. The educated guess was done using the ICSD number 161853 for the $La(Fe,Mn,Si)_{13}H_z$ crystalline structure and ICSD number 53802 for the α-Fe structure.

[7]The unit cell is that of a face-centered cubic structure, therefore a=b=c.

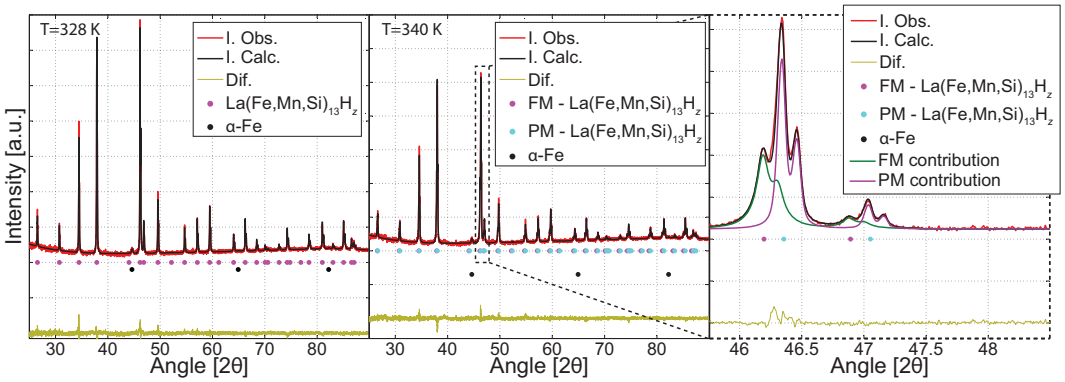

Figure 5.11: XRD patterns of VAC70 in two different temperatures, 328 (left) and 340 K (middle). The right hand graph shows a zoom in the main peak at 340 K.

Figure 5.11 shows the XRD patterns at two different temperatures $T = 328$ and 340 K of VAC70, where the material is in the ferromagnetic (FM) phase and during the transition, respectively. Moreover, the dashed graph shows a zoom in the main peak in $T = 340$ K. The graphs show a good agreement between the refinement and measured XRD patterns, both in the pure phases region and the transition region. As we can see, during the phase transition both the contributions of the ferromagnetic and paramagnetic (PM) phases have to be taken into account in order to correctly refine. Moreover, during the phase transition, due to the co-existence of the FM and PM phases it is intrinsically difficult to refine the structure due to the peak overlap between the $K_{\alpha 2}$ peak of the FM phase and the $K_{\alpha 1}$ of the PM phase. Additionally, it will be later shown that in the PM pure phase region investigated, the paramagnetic phase exhibits a constant unit cell volume. Therefore, to facilitate the refinement, the paramagnetic phase lattice parameter is fixed during the transition to the one at $T > T_C$. As the dashed graph shows, the PM contribution is agreeing with the measured peak position even if the PM lattice parameter is fixed and not refined during the transition, which leads to the conclusion that it is indeed constant in the temperature range investigated since the peak position is only controlled by the lattice parameters.

In Figure 5.12(a) a zoom at a peak in the XRD patterns of VAC70 is shown. Each curve from the graph is at a different temperature, where in the top it is the highest temperature, and the bottom it is the lowest investigated. It is interesting to observe that in the middle of the temperature range, we observe again that the peaks overlap, indicating the region of the transition. Figure 5.12(b) shows the unit cell volume of the La(Fe,Mn,Si)$_{13}$H$_z$ as a function of temperature. The graph shows that the paramagnetic unit cell volume increases with the amount of Mn and Si. In addition, the ferromagnetic unit cell volume is larger than the one of the paramagnetic phase, also expected as it was previously shown the same for La(Fe,Si)$_{13}$ (Fujieda et al., 2001; Waske et al., 2015). Additionally, in this graph one can see the negative thermal expansion of the ferromagnetic phase, and it is related to the loss of magnetization. As it is pointed out in chapter 2, Bean and Rodbell (1962) showed that a material with a positive β should present volume decrease with the loss of magnetization, and therefore it is bound to present negative thermal expansion. The next section will discuss about volume change of La(Fe,Mn,Si)$_{13}$H$_z$

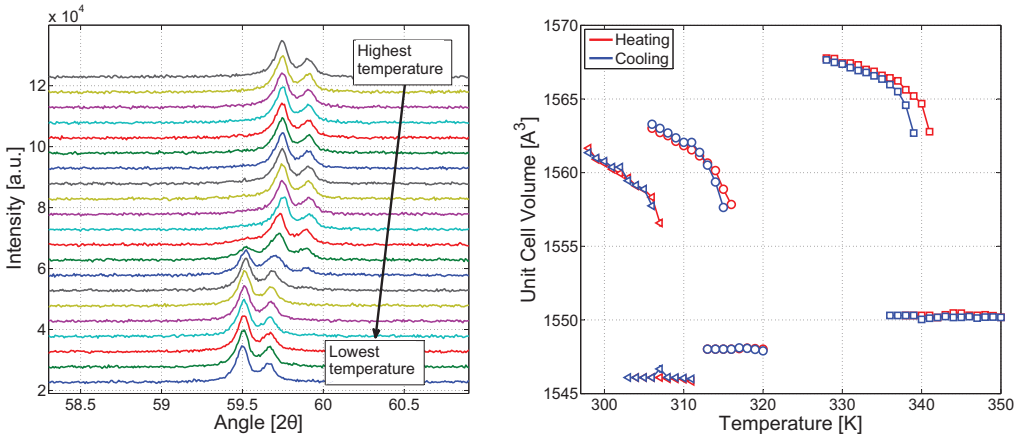

(a) (b)

Figure 5.12: (a) A zoom in the XRD patterns during the cooling procedure of VAC70. The reflection shown is for the peak (6 4 2). (b) Unit cell volume as a function of temperature for the three different materials during the cooling and heating procedures. The error bars when not observed are within the symbol sizes.

in terms of the Bean-Rodbell model.

Another outcome from the Rietveld refinement is the phase fractions. In all the three materials about 2 wt.% of α-Fe was found. The remaining phase observed in the refinements was the main phase, $La(Fe,Mn,Si)_{13}H_z$. The La-rich phase observed in the SEM images was not observed in the XRD patterns, which means that its fraction is at least lower than the one of α-Fe. In Figure 5.13 it is shown the ferromagnetic fraction of VAC30, VAC42 and VAC70 as a function of temperature during the heating and cooling procedures. It is clear from the graph that the materials exhibit some hysteresis of about 1-2 K, confirming the previous results regarding hysteresis. Additionally, the graph shows that the temperature transition occurs within a span of about 5-6 K, depending in the material. This again leads to the conclusion that there is T_C distribution.

In the dashed graph in Figure 5.11 we can see the ferromagnetic and paramagnetic contributions to the measured peak. From this image it is clear that the peak of the ferromagnetic phase is relatively broader then the peak of the paramagnetic phase. Williamson and Hall (1953) have shown that the broadening of the peak is related to the particle size and non-uniform strain, and the following equivalence was derived:

$$\beta(\theta)\cos\theta = \frac{k\lambda}{D} + 4\epsilon\sin\theta, \tag{5.1}$$

where $\beta(\theta)$ is the FWHM as function of the scattering angle, k is the Scherrer constant, λ is the wavelength of the incident radiation[8] D is the crystallite (i.e. grain) size and ϵ is the non-uniform strain. The particle size is not of interest here, as this term of the equation is usually only for particle sizes $< 1\mu$m (Cullity, 1978). If one considers an XRD measurement of a strain-free material ($\epsilon = 0$) with grain

[8]Keep in mind that the Bean-Rodbell model presents constants labelled with the same symbol, nevertheless they represent different things.

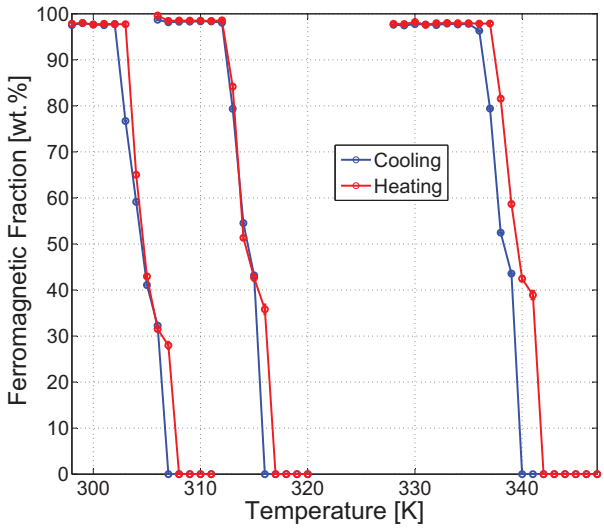

Figure 5.13: Ferromagnetic phase fraction as a function of temperature for VAC30, VAC42 and VAC70 during the heating and cooling procedures. The error bars when not observed are within the symbol sizes.

size of 1 μm, $k = 0.94$, and the wavelength of $K_{\alpha 1}$ of Cu 1.540510 Å, it is clear that the contribution of the crystallite size to the broadening falling out of the angular resolution that most diffractometers present.

As mentioned, ϵ is the non-uniform strain. Indeed there are two ways to modify the lattice through strain, uniformly and non-uniformly. Uniform strain is, for example, what the interstitial H does. It is inserted interstitially and homogeneously in the lattice, applying a "chemical" pressure and an uniform strain in the lattice is the consequence. Figure 5.14 shows a schematic drawing of the effect of strains in the peaks in the XRD pattern. Since the ultimate effect of an uniform strain is to modify the lattice parameter equally everywhere, this leads to a shift of the peak to larger angles (negative or compressive strain) or lower angles (positive or tensile strain). In the other hand, if the strain is non-uniform then the effect is to broaden the peak as shown in the schematic drawing. However, in the drawing the non-uniform strain is such that does not change the unit cell volume mean value; nevertheless it is still possible to have a non-uniform strain that also shifts the peak, a part from broadening it.

In order to use the Williamson-Hall method to evaluate the strain during the phase transition of the material, one has to account for instrumental effects in the broadening of the peak. For that a standard strain-free material, in this case LaB_6, is measured in the same measurement settings and the broadening can then be corrected through a Gaussian summation of the two contributions:

$$\beta(\theta)^2 = \beta(\theta)^2_{\text{LaFeSi}} - \beta(\theta)^2_{\text{instrumental}}, \tag{5.2}$$

where $\beta(\theta)_{\text{LaFeSi}}$ is the calculated broadening for the La(Fe,Mn,Si)$_{13}$H$_z$ phase and $\beta(\theta)_{\text{instrumental}}$ is the one of LaB_6. This equation also shows that the strain calculated through the Williamson-Hall method will always be positive, even if it is compressive strain, since $\beta(\theta)$ must be positive.

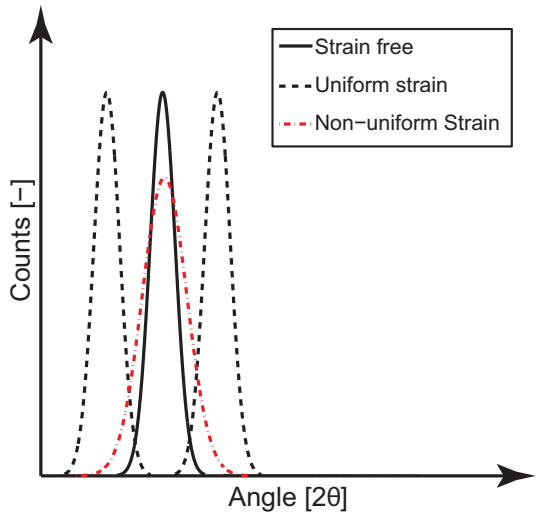

Figure 5.14: Schematic drawing of the effect of different types of strain in the peaks of an XRD pattern.

Usually the β is calculated by fitting individually each peak. Nevertheless, as we have observed in Figure 5.12(a) there is an overlap of the peaks which limits of such approach. Due to that, in this thesis the full width at half maximum is calculated from the Rietveld refinement FWHM parameters as given by the Caglioti equation (Caglioti et al., 1958):

$$\beta(\theta) = (u\tan^2\theta + v\tan\theta + w)^{1/2} \tag{5.3}$$

where u,v and w are the Rietveld FWHM parameters. Williamson-Hall plots of the ferromagnetic phase of VAC70 for $335 \leq T \leq 341$ K are shown in Figure 5.15. As equation 5.1 shows, the slopes of this curves are the non-uniform strain. Additionally, the slopes are all positive as it was previously mentioned to expect. The implicit principle of broadening as an outcome of strain is related non-uniform lattice parameters, and both a compressive or a tensile non-uniform strain will give a broadening of the peak. Therefore, the different effects and trends in the whole temperature range of measurements have to be considered in order to decide whether the strain is in reality positive or negative.

The panel (i) of Figure 5.16(a) shows the strain as a function of temperature of VAC70 for both heating and cooling procedure, while (ii) shows the unit cell volume. The error bars are calculated considering the error propagation from the different fittings – Rietveld refinement fitting of the $La(Fe,Mn,Si)_{13}H_z$ phase, the refinement of the standard material LaB_6 and the linear fitting in Figure 5.15. All the calculated strain was positive, however it was imposed during the transition that the material should present a negative slope, which will be explained in the following paragraphs. Additionally, as one may see, the pure phases present some degree of non-uniform strain. This is expected as the material is not perfect – it presents dislocation concentration, grain boundaries, vacancies, etc. Additionally, as the previous section has described, the material presents some T_C distribution that might be associated with a chemical distribution. This chemical distribution in itself could lead to some non-uniform strain.

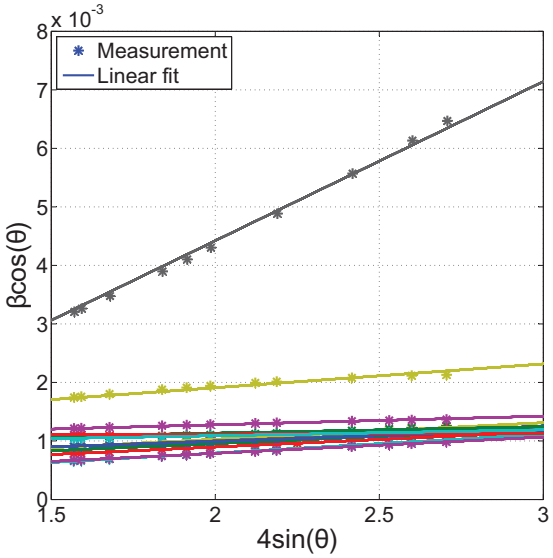

Figure 5.15: Williamson-Hall plot of the ferromagnetic phase of VAC70 for different temperatures.

To evaluate the effect of H in the non-uniform strain, a sample of VAC70 was dehydrogenated. The dehydrogenation procedure was performed in a furnace at 773 K, where the temperature was increased with a temperature rate of 5 Kmin^{-1}. The powder is held at this temperature for one hour and then it is allowed to slowly cool to room temperature inside the furnace. This whole procedure was performed under high vacuum, with the pressure in the range of 10^{-5} mbar to avoid oxidation. The XRD measurement was performed at room temperature in the same settings as the other measurements, to be able to extract the instrumental contribution to the broadening. No extra peak was observed in the XRD, which means no other phase was formed. Furthermore, the α-Fe content did not change. Moreover, once the H is desorbed, the material becomes paramagnetic at room temperature (Barcza et al., 2011) due to the shorter spin-spin distances.

In the panel (i) of Figure 5.16(a) one may see the square symbol represents the strain of the H-desorbed sample. The symbol was put purposely in a higher temperature than it was measured, to keep the paramagnetic results all together and ease the comprehension of the image. The results show that the H-desorbed sample exhibits half of the strain of the hydrogenated sample. Since the H enters interstitially in the structure to result in an increase of the unit cell volume and T_C, it is expected to generate positive strain on the pure phases, i.e. a tensile strain. Therefore, the pure phases temperature regions the strain remains positive.

The strain in the ferromagnetic phase decreases to zero just below the T_C. This can be caused by the softening of the lattice induced by the magnetic interactions closer to the transition (Gruner et al., 2015). The FM phase strain is fixed to negative, since we observe in the panel (ii) of the Figure 5.16(a) that the ferromagnetic unit cell volume decreases with temperature. Therefore, the most likely is that compressive strain is being developed during the transition. Figure 5.16(b) shows the strain as a function of temperature for VAC30 and VAC42, with similar

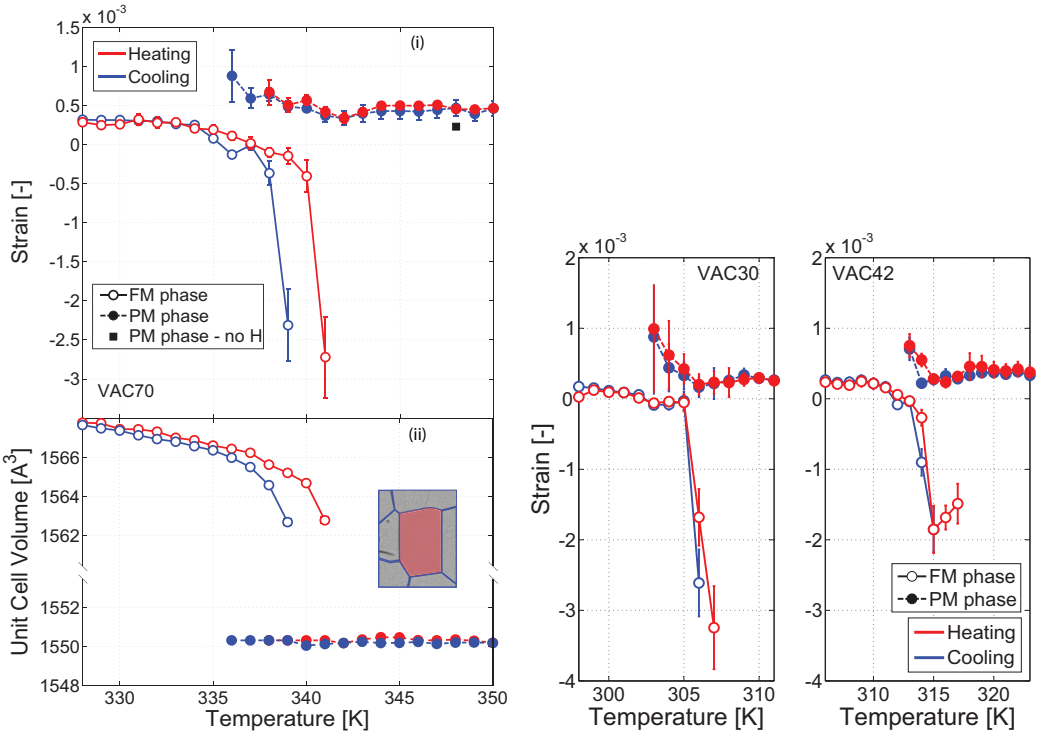

Figure 5.16: (a) (i) Strain and (ii) volume as a function of temperature for VAC70. The inset shows an schematic micrograph of a crystallite of the material for explanation of the strain development. This crystallite is the dashed one in Figure 5.17(b). (b) Strain as a function of temperature for VAC30 and VAC42 during the heating and cooling procedures.

behavior to the one observed in VAC70. The strain of VAC42 during heating shows a feature in the two last temperatures, 316 and 317 K; The strain stopped increasing and remained equal to the the strain at 315 K (considering the error bars). The author of this thesis does not have a fully understood explanation for this behavior, however one of the possibilities is that some of the particles during the XRD measurement cracked, therefore decreasing the strain and releasing some of strain energy into surface energy.

The ferromagnetic and paramagnetic phases exhibit different strain behavior. This can be related to a difference in the bulk modulus of each phase, as observed for other magnetocaloric materials with a volume change at T_C (Zhu et al., 1999) (see, e.g., Figure 2.7(b)). A schematic drawing of the expected behavior of the bulk moduli accros the transition is shown in Figure 5.17(a). As Gruner et al. (2015) have shown, close to the transition there is a softening of the lattice induced by the magnetic interactions. Additionally, the larger volume of the FM phase is attributed to the magneto-elastic coupling that this material exhibits. However, the softening is not expected for the PM phase, where the magnetic moments are not coupled; hence, the bulk modulus of this phase will remain more or less constant close to the transition, as schematically shown in Figure 5.17(a). In this schematic behavior of the bulk moduli the PM phase bulk moduli was put above the one of the FM, since

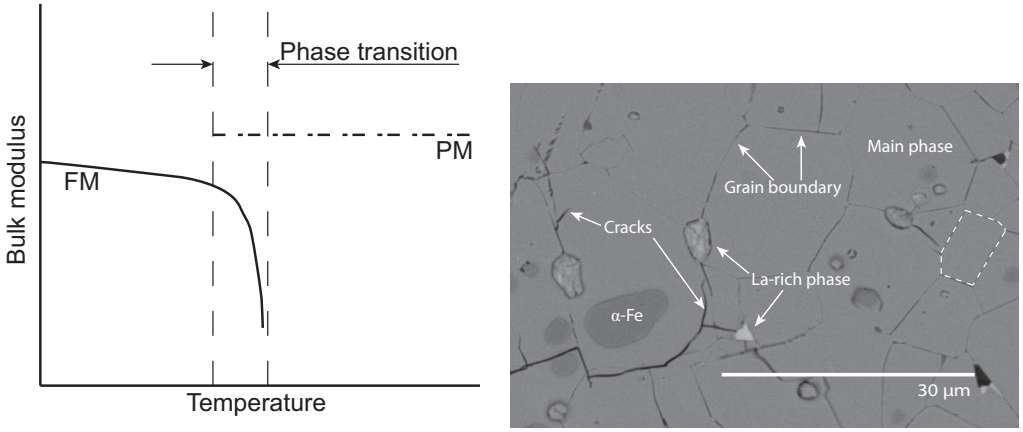

(a) (b)

Figure 5.17: (a) Schematic drawing of the expected bulk modulus behavior across the transitions. (b) A zoom in a crack shown in Figure 5.5(b).

this phase presents a larger density with the same crystal structure (André Meyers and Chawla, 2009).

The *apparently* gradual transition as a function of temperature can be explained in terms of a compositional distribution. Let us again imagine a situation where a grain of La(Fe,Mn,Si)$_{13}$H$_z$, which each of its surrounding grains has slightly different and higher transition temperature. As the temperature increases, more and more FM grains become isolated and completely surrounded by the PM phase, and as the PM phase is smaller, it will compress the FM phase (see the schematic micrograph in the inset of Figure 5.16(a)). This can be thought in analogy with a hollow sphere. When the temperature of the sphere decreases, the inner volume will decrease. If we put a material with a smaller thermal expansion coefficient filling the sphere, this material will then be compressed by the surrounding sphere. The same would occur with the FM crystallites that were once surrounded by FM crystallites, but as the transition goes the smaller volume of the PM phase will compress the FM phase. In this scenario, if the argument of change of bulk moduli is right, this will allow the FM phase to be more susceptible to the compressive forces and it will respond with a large strain development.

As a material consisting of three phases, the cracking mechanism is highly dependent on the microstructure. It has been reported (Liu et al., 2011), and observed in this study, that the α-Fe grains are embedded within the grains of the main phase, while the La-rich phase is mostly located at the grain boundaries of the main phase. This La-rich phase, however in a small fraction, may play an important role in the mechanical stability of the material. We may think in an analogous way to the hydrogen-decrepitation observed in several rare-earth alloys (Harris et al., 1985; Ragg et al., 1997; Bez et al., 2013). The decrepitation process consists of hydrogen diffusing firstly in the rare-earth rich phase, expanding it and cracking it due to the brittleness of such materials. By continuing the hydrogenation, the hydrogen also diffuses in the main phase, which also cracks. One may see that the whole mechanism of hydrogen-decrepitation is based on the volume expansion of multi-phase material.

SampleID	VAC30	VAC42	VAC70
T_0 [K]	290	300	320
β	36	35	35
η	1.8	1.75	1.9
ΔT_0 [K]	1.0	1.0	0.8
V_0 [Å^3]	1546	1548	1550.3
ρ_s [kg^{-1}]	8.45e24	8.45e24	8.63e24
κ [Nm^{-2}]	3e-12	3e-12	3e-12
J	0.92	0.92	0.92
ρ [kgm^{-3}]	7000	7000	7000
ΔV [%]	0.82	0.83	1.04

Table 5.3: Table of parameters used in the Bean-Rodbell model. The varied parameters were η, T_0 and ΔT_0. It is also shown the volume change from the measured data.

In the investigation done in this thesis, we can indeed think in an analogous way, where instead of the volume expansion being chemically driven, it is thermally or magnetically driven. Still as here it is propose that the FM phase is much more susceptible to deformation, and the La-rich phase is the only hard and brittle phase, it seems that the crack must nucleate in the sharp corners of the grain boundaries where the La-rich phase is situated as shown in Figure 5.17(b).

5.4 La(Fe,Mn,Si)$_{13}$H$_z$ magneto-elastic coupling

As $La_{0.67}Ca_{0.33}MnO_3$, the magneto-elastic coupling in La(Fe,Mn,Si)$_{13}$H$_z$ is evaluated within the Bean-Rodbell model. This model is described in more details in the subsection 2.4.2. This model has already been used to describe the magneto-elastic coupling of La-Fe-Si alloys (Jia et al., 2006b). The magneto-elastic coupling is evaluated for VAC30, VAC42 and VAC70.

Many of the parameters used for the modelling were measured. For example, J was calculated by measuring the isothermal magnetization at 10 K, from 0 to 10 T, and then equation 4.1 is used to find $J = 0.9182$. Moreover, the constrained volume, V_0, is set to be the one of the paramagnetic phase measured at high temperature by XRD, and the volume change is evaluated only with respect to the magnetic contribution. The density is taken from the XRD measurements as well. The spin density is calculated as explained in subsection 4.1. The varied parameters in this study to find a good agreement between model and data were: (i) T_0 to shift the transition to the right region; (ii) η to evaluate the "orderness" of the transition; and (iii) ΔT_0 to reproduce the T_C distribution. Since $\beta \propto \sqrt{\eta/T_0}$ as shown by equation 4.5, β is also indirectly varied. The agreement between model and measurement was evaluated with respect to the volume measured data, and parameters were found visually comparing the modelled and the measured results.

Table 5.3 shows the parameters used in the modelling of the three different materials. Figures 5.18(a), 5.18(b) and 5.18(c) show the agreement between the model and measured data; where it is observed a good agreement. It is possible to observe that the ferromagnetic phase at the end of the transition usually presents

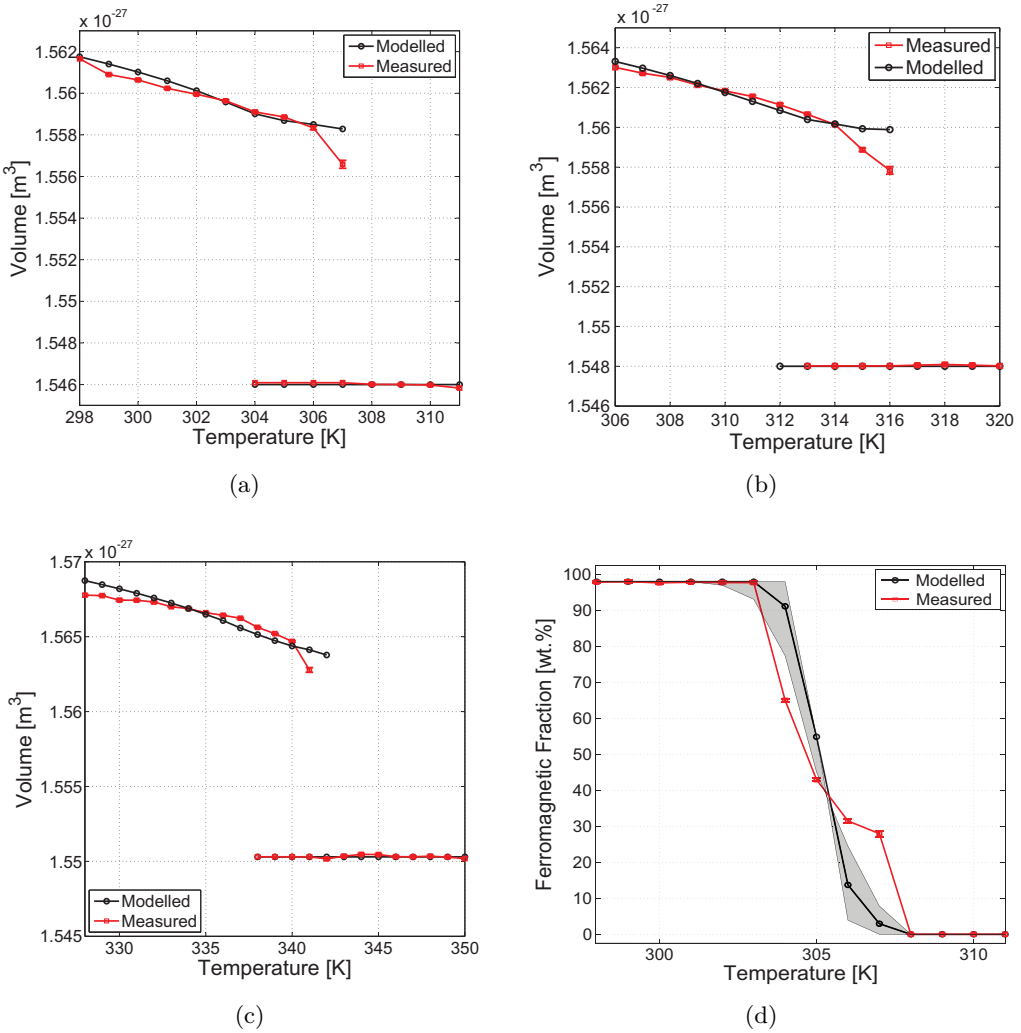

Figure 5.18: Unit cell volume as a function of temperature during the heating procedure for (a) VAC30, (b) VAC42 and (c) VAC70. (d) shows the ferromagnetic fraction as a function of temperature for VAC30, and the shaded area represents $\Delta T_0 \pm 0.5$ K.

a kink downwards, which could be related to the strain development explained in the previous chapter. The model, nonetheless, did not reproduce this effect as it does not include crystallite mechanical constrictions. The magnitude of the volume change is well reproduced by the model and it is basically affected by the η value. Additionally the distribution is well represented by the used ΔT_0 as shown in the three images. Moreover, Figure 5.18(d) shows the ferromagnetic fraction as a function of temperature for VAC30, again demonstrating the good agreement given by the superimposed distribution.

Figure 5.19 shows the entropy change as a function of temperature for a field change of 1.0 T and for the three materials analysed through modelling. Figure 5.19(a) shows the Δs for 3 different measurements: multiple particles out of equilibrium (squared symbols); multiple particles in equilibrium (circles); and single

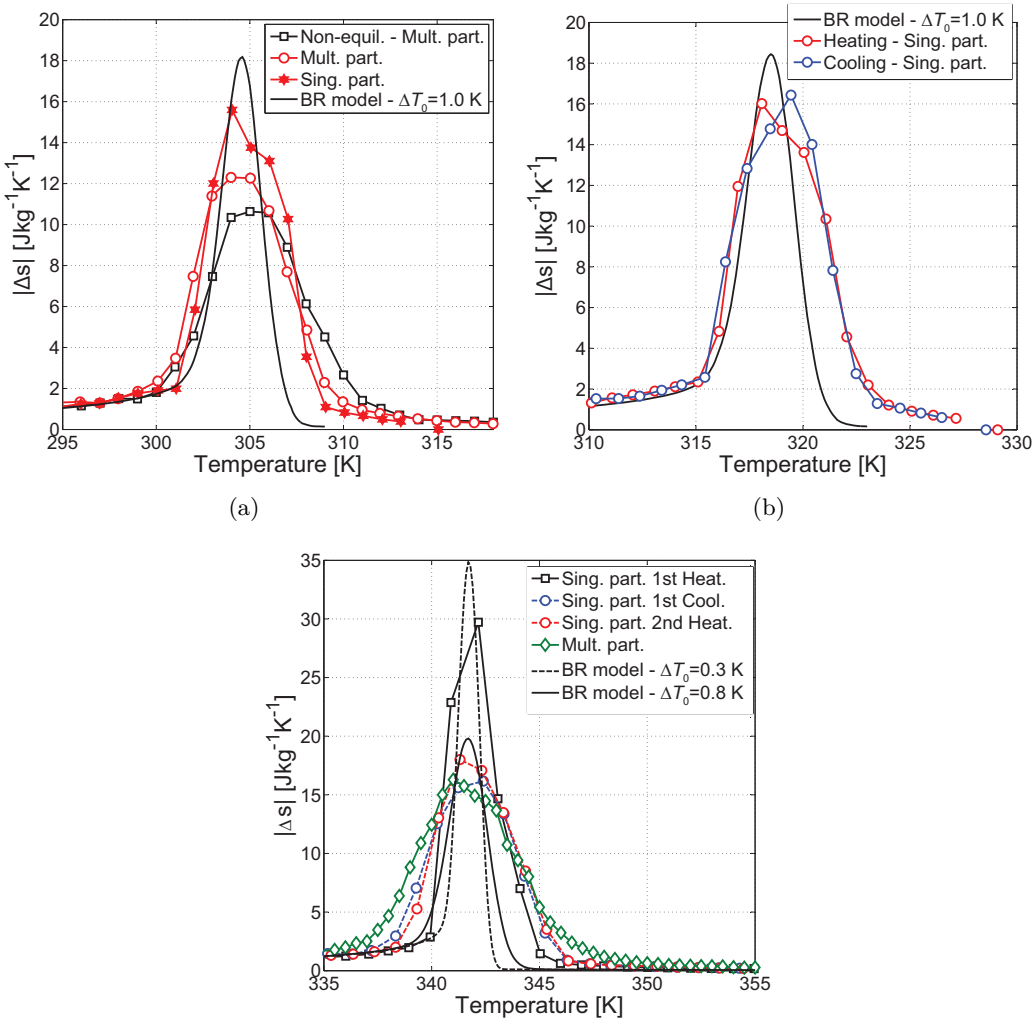

Figure 5.19: Entropy change as a function of temperature for the three materials analyzed through Bean-Rodbell model and for a field change of 1.0 T. In (a) and (c) the data may have been artificially shifted in the temperature axis by ±1.0 K to ease comparison.

particle in equilibrium (stars). The full black line is the Δs from the model using the parameters from the best fit in the volume change (see Figure 5.18), showing a relatively good agreement. The result shows an increase and relative sharpening of the peak, which is already expected from the previous measurements done (see section 5.2). Figure 5.19(b) shows the entropy change for VAC42 single particle sample during heating and cooling, as well as the entropy change during heating for the model result. Again, we may observe a relatively good agreement between data and measurement, although both models (for VAC30 and VAC42) showed a slightly sharper peak.

Figure 5.19(c) shows the entropy change for different samples and modelling parameters of VAC70. The measured results are the ones already shown in Fig-

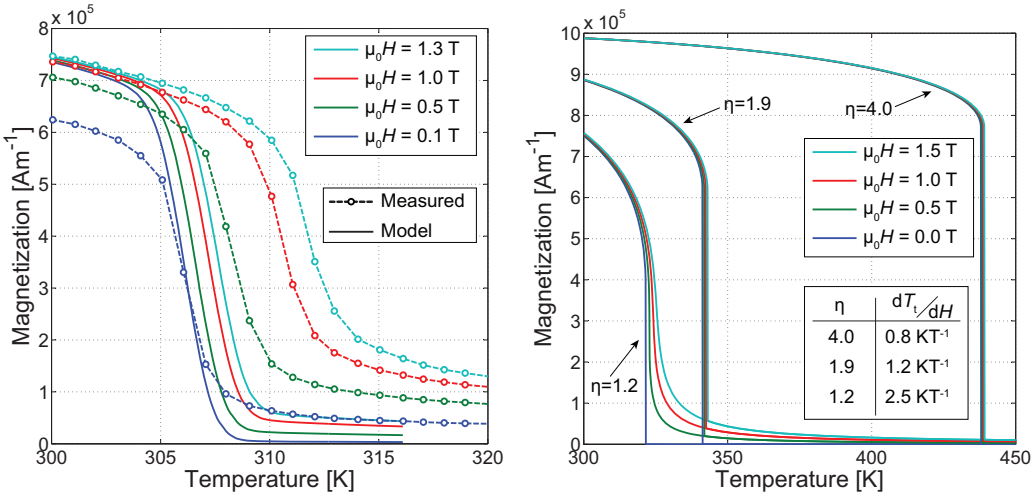

Figure 5.20: (a) Magnetization as a function of temperature in different fields for the model with the best fit parameters (see Table 5.3) and the measured magnetization of multiple particles of VAC30 in equilibrium. (b) shows the effect of η on the magnetization with a $\Delta T_0 = 0$ K.

ure 5.10(d); the new results in this plot are curves of the modelling results. One may see that the peak of $\Delta T_0 = 0.3$ K is significantly larger than the one for $\Delta T_0 = 0.8$ K, and just an increase of 0.5 K in ΔT_0 led to a decrease of ∼42% of the maximum value, very similar to the effect of the particle breaking apart − a decrease of ∼45%. Still, again the FWHM of the peak of the modelled data is relatively smaller than the measured one. To investigate why, the magnetization is also evaluated as a function of temperature[9].

As one may see from Figure 5.20(a), the model does not describe properly the magnetization. One may see that the main issue on the model result is that the magnetization does not shift much with magnetic field. In Figure 5.20(b) the modelling results are evaluated with respect to the variation of η while all the other parameters are fixed. Additionally, ΔT_0 is fixed to 0 K to ease the evaluation. It is observed that for increasing values of η (for $eta > 1$) the $\mathrm{d}T_\mathrm{t}/\mathrm{d}H$ decreases. Finally, the discontinuity in the magnetization is larger for larger η values; which was already expected from equation 2.24, since we observed larger volume changes for increasing T_C. The hysteresis (not shown) grows with η as expected. Nevertheless, for the values of η obtained from the best fit in the volume change, the modelled hysteresis at 0 T is about 4.5 K, about ∼2 K larger than the measured one. In table 5.2 we observed that indeed the heating branch of $\mathrm{d}T_\mathrm{t}/\mathrm{d}H$ is decreasing with the orderness, which together with the increase of ΔT_hyst, led to a larger critical field. All of this is observed in the modelling in this section: the increase of η is decreasing $\mathrm{d}T_\mathrm{t}/\mathrm{d}H$, while it is increasing the hysteresis. Additionally, from the Clapeyron equation[10] one

[9]This investigation of the magnetization was performed after acceptance of the paper in the Appendix A.1.2.

[10]The Clapeyron equation gives the entropy change involved in a purely first order phase transi-

can extract the first-order contribution to the entropy change (Planes et al., 2009):

$$\Delta s(T) = -\Delta M \mu_0 \frac{\mathrm{d}H}{\mathrm{d}T_\mathrm{t}} \tag{5.4}$$

where ΔM is the difference due to the discontinuity of the magnetization of the paramagnetic phase and the ferromagnetic phase at the isotherm T. One may see that the bigger the difference of magnetization, the larger the entropy change. More importantly, this equation shows that Δs from a purely FOPT is inversely proportional to $\mathrm{d}T_\mathrm{t}/\mathrm{d}H$. In this thesis, the largest $\mathrm{d}T_\mathrm{t}/\mathrm{d}H$ observed was for $\eta = 1.01$, where $\mathrm{d}T_\mathrm{t}/\mathrm{d}H \sim 3\ \mathrm{KT}^{-1}$, i.e. still not the ones observed through measurements. Fujieda et al. (2008) argue that the Bean-Rodbell model based on localized moment model seems to be invalid for discussion of the contribution of magnetism to volume in $\mathrm{La(Fe,Mn,Si)_{13}H}_z$, i.e. the approximation to a localized electron system should not work. Still, recently (Piazzi et al., 2015) literature has shown again that the model describing with a good agreement the heat capacity and entropy change, although no T_0 distribution was considered. Still, the thermal hysteresis was also over predicted in that work.

On top of the argument of Fujieda, there is also the fact that again the bulk modulus is considered constant, while it was showed this is not the case for other magnetocaloric materials with volume change in the transition. It indeed seems like the Bean-Rodbell model has to be used with more awareness of its limitations. Additionally, it is a model that considers localized moments, while literature has shown that the material presents itinerant electron magnetism.

5.5 Summary

In this chapter the phase transition of $\mathrm{La(Fe,Mn,Si)_{13}H}_z$ was studied in detailed. Different characterization methods and the Bean-Rodbell model were used in an attempt to deliver a better understanding of its transitions. The influence of the composition was also evaluated. The following points are the main ones that may be taken from the results shown:

(a) In general it was observed that the transition becomes more and more first order-like when decreasing the Mn and Si content: the thermal hysteresis increases, the critical field increases, heat capacities peaks are sharper and entropy changes are larger.

(b) The values of entropy change (cyclic) are slightly smaller than those shown in the literature (Basso et al., 2015), although it is argued that this difference can be a combination of the effect of the numerical approximation to the Maxwell relation (discussed in the section 3.2) used in this thesis and demagnetization effects.

(c) From characterizations in single particle and multiple ground particles, the effect of a distribution in the transition temperature is evaluated. Isofield magnetization measurements in single particles showed that depending on the particle (with the same nominal composition) the transition temperature could vary.

tion.

Additionally, it is virtually discontinuous for the single particle, and rather continuous for the ground ones.

(d) From heat capacity measurements in single and multiple ground particles, it is observed that those in the low end of Mn and Si content, when measured in the single particle mode, shows what resembles a delta function, with a extremely large and sharp peak. The multiple ground particles shows in the other hand the usual behavior observed in measurements of c_p ofs FOPT magnetocaloric materials. Nonetheless, the area under the peak, which should give the heat involved in the transformation, shows the same value for both samples of single and multiple ground particles. Additionally, the multiple ground particles heat capacity was reproduced by applying normal distributions to the single particle data.

(e) Through XRD measurements the lattice was evaluated across the transition. Three FOPT La(Fe,Mn,Si)$_{13}$H$_z$ compositions were used. It was observed volume changes between 0.8 and 1.0%, where the volume change increases with the decrease of Mn and Si content. Additionally, it was observed the coexistence of the ferromagnetic and paramagnetic phase across the transition, in a temperature range of about 5 K.

(f) Using the Williamson-Hall method, non-uniform strain is observed across the transition. The strain, however, observed in the ferromagnetic phase is more significant. This is attributed to the polycrystallinity and to a distribution of T_C throughout the material, due to a compositional distribution. As the material goes from the ferromagnetic to the paramagnetic region, crystallites that present a smaller T_C will tend to change volume in a lower temperature. As the transition continues, the remaining ferromagnetic crystallites are likely to be surround now by smaller grains, therefore compressing it and generating some non-uniform strain, since the ferromagnetic phase is expected to have a decrease of its bulk modulus as it approaches the transition.

(g) A smoother transition in ground particles is usually attributed to development of defects in the lattice of the material. Nevertheless, La(Fe,Mn,Si)$_{13}$H$_z$ is a brittle material, which does not allow much, if any, plastic deformation. Moreover, if strain is the reason behind the smoother transition in ground particles, then strain should also have been developed in the single particle measurements, as explained in the previous item, and therefore the single particle measurements should have had a more distributed transition. However, in the single particle it is observed a discontinuous transition. Therefore, the evidences suggest that the smoother transition of ground particles is due to a compositional distribution in the material that in the ground state the particles may change volume with less constrictions.

(h) It is observed that several cracks seems to originate from the La-rich phase (usually in the grain boundaries), despite its small fraction. Additionally, this is the only brittle and hard phase that does no have a volume change accompaining the transition, therefore it is expected that these brittle and hard grains will generate some stress in its surroundings across the transition as the volume of the grains around it change. Hence, it is expected that if there were

less of this secondary phase, the mechanical integrity of the material would increase.

(i) Using the Bean-Rodbell model with a normal distribution in T_0, the volume change and the phase fraction were well reproduced. Additionally, the entropy change was relatively well reproduced, though it was slightly sharper than the measured ones.

(j) However, by evaluating the magnetization using the best-fit parameters in the volume change, it was observed that $\mathrm{d}T_\mathrm{t}/\mathrm{d}H$ is very low in comparison to the ones measured. This explains why the Δs peaks of the model were slightly sharper than the measured ones.

(k) It was observed that $\mathrm{d}T_\mathrm{t}/\mathrm{d}H$ increases by decreasing the value of η from values above 1 towards the unit, which at first was a surprise. One could imagine that since η increasing up to 1.0 the $\mathrm{d}T_\mathrm{t}/\mathrm{d}H$ is also increasing, with increasing η above 1 (in the FOPT region) the $\mathrm{d}T_\mathrm{t}/\mathrm{d}H$ would also increase. But it is not the case, it seems that the maximum of $\mathrm{d}T_\mathrm{t}/\mathrm{d}H$ is at η approaching the unit from larger values. Still, this goes in accordance with the Clapeyron equation, which shows that the FOPT contribution to the entropy change is linearly proportional to the magnetization change, and inversely proportional to $\mathrm{d}T_\mathrm{t}/\mathrm{d}H$; both contributions are maximized with increasing η in the FOPT regime.

(l) Finally, it seems that the Bean-Rodbell fails to fully describe the properties of $\mathrm{La(Fe,Mn,Si)_{13}H}_z$. Some possibilities may be speculated on why it fails. First it is a model that considers localized moments, while literature has shown that the material presents itinerant electron magnetism. Secondly, the bulk modulus is assumed to be constant, which as in the LCMO it is not expected to be.

Chapter 6

Conclusion

In this thesis, the nature of the magnetic transition of two particular magnetocaloric materials, $La_{0.67}Ca_{0.33}MnO_3$ and $La(Fe,Mn,Si)_{13}H_z$, was studied through experimental characterization and modelling. This study led to results of thermal, magnetic and structural properties of both materials. In general the conclusions taken for the results concerning each material can be found in the Summary of their respective chapters. Nevertheless, here they are shortly stated again, and a further analysis is given now with results of both materials in hand.

6.1 $La_{0.67}Ca_{0.33}MnO_3$

Single phase polycrystalline $La_{0.67}Ca_{0.33}MnO_3$ was fabricated by the solid state method. The material showed a T_C around 265 K, where there is a volume change as well. Evidence for cluster formation above T_C was observed through a deviation of the inverse susceptibility in respect to that one expected for a Curie-Weiss paramagnet; The cluster size calculated from the inverse susceptibility measurement is 2.8, in agreement to what is expected from literature. Additionally, the measurements suggest that the observed thermal hysteresis are due to experimental effects and the low thermal diffusivity of the material. The material presents FOPT features as the transition temperature shifts with magnetic field, and the asymmetric growth of the entropy change. By using the Bean-Rodbell model with a superimposed distribution on the transition temperature it was shown that the effect of the distribution is to smear out the transition, decreasing significantly the observable thermal hysteresis. Although if the material was perfect it should present a thermal hysteresis of about 0.7 K and a discontinuity in its magnetization.

From isothermal magnetostriction measurements, it was observed experimentally the magneto-elastic coupling of the material: the volume decreases with increasing magnetic field. Additionally, it is observed a remarkable resemblance between the isothermal entropy change and the isothermal magnetostriction. Using literature values, it is proposed an equation to calculate one from the other as a function of Ca content in $La_{1-x}Ca_xMnO_3$. This function, however, should be used with caution given the boundaries. The Bean-Rodbell model, coupled with the free electron model and the Debye model reproduced well the magnetization, entropy change and heat capacity of the material. Despite of that, using the same parameters the model failed to describe the isothermal magnetostriction, over predicting it by about 9 times.

6.2 $La(Fe,Mn,Si)_{13}H_z$

$La(Fe,Mn,Si)_{13}H_z$ irregular shaped particles with sizes of about 500 μm and different T_C were provided by Vacuumschmelze GmbH. The T_C is controlled by the Fe, Mn and Si content, where low Mn and Si content leads to higher T_C. It was observed by heat capacity measurements that the decrease of Mn and Si content leads to a more first order-like transition, where the thermal hysteresis increases, the entropy change increases, the transition becomes sharper and the critical field increases. It is observed that the effect of grinding the particles to finer ones leads to a smoother transition, while a single particle has an extremely sharp transition showing a quasi delta function in the heat capacity. Nevertheless, it was observed no significant difference in the heat involved in the ferro- to paramagnetic transformation. Additionally, during magnetization measurements of single particles it was observed the material breaking apart and the magnetic properties changing drastically. As an intact single particle the entropy change was very large and sharp, but once the particle was broken the entropy change resembles the one of ground particles − smaller and smoother.

The XRD measurements as a function of temperature showed a discontinuous volume change across the magnetic transition of three different compositions of FOPT $La(Fe,Mn,Si)_{13}H_z$. The transition however showed the co-existence of ferro- and paramagnetic phase in a temperature range of 5 K. All samples presented about 2 wt.% of α-Fe. The volume change increases with the decrease of Mn and Si content. The Williamson-hall method showed the development of non-uniform strain in the ferromagnetic phase due to a decrease of the bulk modulus and a compositional distribution, hence a T_C distribution. Evidences suggests that if one decrease the brittle and hard La-rich phase in the grain boundaries, the mechanical integrity could be increased. This is because this is the only brittle and hard phase that does not change phase across the transition and therefore could generate some internal stresses in its surroundings. The Bean-Rodbell model reproduced well the volume change observed through XRD measurements. Additionally it showed a good agreement with the measured Δs, although slitghly sharper. The magnetization showed why it was sharper: the model did not reproduced well $\mathrm{d}T_t/\mathrm{d}H$. By varying η it was observed that $\mathrm{d}T_t/\mathrm{d}H$ decreases with the increase of η above the unit.

6.3 Final remarks

As it was shown, the Bean-Rodbell model was able to partially describe the properties of $La_{0.67}Ca_{0.33}MnO_3$ and $La(Fe,Mn,Si)_{13}H_z$. Nevertheless, one common feature in the modelling of both materials is that the model could not reproduce both the volumetric and magnetic behavior. In one hand, the model described well the magnetic properties of $La_{0.67}Ca_{0.33}MnO_3$ but failed in the volumetric properties with the same parameters, and vice versa for $La(Fe,Mn,Si)_{13}H_z$. Although this model has been highly used in the literature to describe magnetocaloric materials, up to the knowledge of the author there is no publication which addresses measurements of volumetric *and* magnetic properties, and the Bean-Rodbell model of such properties in the same publication.

For $La_{0.67}Ca_{0.33}MnO_3$, one could argue that the temperature and field inde-

pendence of the cluster is the reason. Another point is that literature has shown that compressibility varies with temperature, while in the model it is considered temperature independent. In addition, this material magnetism comes from double exchange interactions, rather than localized electrons. For $La(Fe,Mn,Si)_{13}H_z$ the compressibility is an issue for the same reasons as $La_{0.67}Ca_{0.33}MnO_3$ – it is expected to decrease towards the transition, while in the model is constant. Additionally, this material presents itinerant electron magnetism.

Chapter 7

Perspectives and future challenges

The application of $La_{0.67}Ca_{0.33}MnO_3$, or for that matter $La_xCa_{1-x}MnO_3$, as a possible magnetocaloric material for cooling or heating applications is limited. Although $La_{0.67}Ca_{0.33}MnO_3$ has high resistance to weathering and it is highly shapeable, its thermal properties lead to lower heat transfer properties and to relatively small temperature spans when used as an AMR. In order to improve its performance, firstly the thermal diffusivity of the material should increase significantly. This perhaps could be done by pulverizing the material and embedding the powder in a matrix of a highly thermal diffusive material and then shape it into cylinders, plates, etc. However, this could lead to a relatively large volume fraction of passive material (the thermal diffusive one) in the AMR, which is detrimental to the performance. The manganites have been highly studied in the literature and further investigations on compositional variations are not very like to show a larger magnetocaloric effect.

On the other hand $La(Fe,Mn,Si)_{13}H_z$ has promising magnetocaloric properties. It has low thermal hysteresis, good thermal properties and large magnetocaloric effect. Its Curie temperature can be easily tuned by the Fe, Mn and Si content. However, due to the large volume change, its microstructure and secondary phases, this material has been reported repeatedly for cracking during operation. We have observed that the La-rich phase may play an important role in the crack formation. Therefore, it would be extremely interesting to evaluate the mechanical integrity of a La-Fe-Si FOPT alloy without La-rich phase.

Additionally to have a better understanding of the volumetric properties of the material, it would be interesting to perform XRD measurements as a function of temperature *and* pressure. This would be useful to evaluate the bulk modulus across the transition and observe if it changes as proposed in this thesis. In addition, micro vickers hardness measurements could be performed in the different phases of the provided material to evaluate the hardness of both materials. Moreover, it would be very interesting to evaluate the stress-strain curve of such material, both in the ferromagnetic and paramagnetic phase.

Finally, this thesis leave it clear that it is necessary to take caution when using the Bean-Rodbell model to describe the magneto-elastic coupling of the material. The Bean-Rodbell did not manage to fully describe the volumetric *and* magnetic behavior of both materials. Firstly, it would be interesting if the model is modified

to allow asymmetric volume expansion (for $La_{0.67}Ca_{0.33}MnO_3$). Secondly, the model should be modified to consider the compressibility to be temperature and field dependent. At last, it is believed that the model would describe better the properties of $La_{0.67}Ca_{0.33}MnO_3$ and $La(Fe,Mn,Si)_{13}H_z$ if it was modified to allow modelling with materials with double exchange interactions and itinerant electron magnetism, respectively.

References

Adams, C. P., Lynn, J. W., Smolyaninova, V. N., Biswas, A., Greene, R. L., Ratcliff, W., Cheong, S.-W., Mukovskii, Y. M., and Shulyatev, D. A. (2004). First-order nature of the ferromagnetic phase transition in (La-Ca)MnO_3 near optimal doping. *Physical Review B*, 70:134414.

Aharoni, A. (1998). Demagnetizing factors for rectangular ferromagnetic prisms. *Jounal of Applied Physics*, 83(6):3432–3434.

Amaral, J. S., Das, S., and Amaral, V. S. (2003). The Mean-Field Theory in the Study of Ferromagnets and the Magnetocaloric Effect. In Moreno-Piraján, J. C., editor, *Thermodynamics - Systems in Equilibrium and Non-Equilibrium*, volume 2, pages 173–198. InTech.

André Meyers, M. and Chawla, K. K. (2009). *Mechanical Behavior of Materials*. Cambridge University Press, second edition.

Bahl, C., Bjørk, R., Smith, A., and Nielsen, K. (2012). Properties of magnetocaloric materials with a distribution of Curie temperatures. *Journal of Magnetism and Magnetic Materials*, 324:564–568.

Bahl, C. R. H. and Nielsen, K. K. (2009). The effect of demagnetization on the magnetocaloric properties of gadolinium. *Journal of Applied Physics*, 105:013916.

Bahl, C. R. H., Petersen, T. F., Pryds, N., and Smith, A. (2008). A versatile magnetic refrigeration test device. *The Review of scientific instruments*, 79(9):093906.

Balli, M., Jandl, S., Fournier, P., and Gospodinov, M. M. (2014). Anisotropy-enhanced giant reversible rotating magnetocaloric effect in $HoMn_2O_5$ single crystals. *Applied Physics Letters*, 104(23):232402.

Barclay, J. and Steyert, W. (1982). Active magnetic regenerator. US Patent 4,332,135.

Barcza, A., Katter, M., Zellmann, V., Russek, S., Jacobs, S., and Zimm, C. (2011). Stability and Magnetocaloric Properties of Sintered La(Fe, Mn, $Si)_{13}H_z$ Alloys. *IEEE Transactions on Magnetics*, 47(10):3391–3394.

Basso, V., Küpferling, M., Curcio, C., Bennati, C., Barzca, A., Katter, M., Bratko, M., Lovell, E., Turcaud, J., and Cohen, L. F. (2015). Specific heat and entropy change at the first order phase transition of La(Fe-Mn-Si)13-H compounds. *Journal of Applied Physics*, 118(5):053907.

Bean, C. P. and Rodbell, D. S. (1962). Magnetic Disorder a a first-order phase transformation. *Physics Reviews*, 126(1):104–115.

Bebenin, N. G., Zainullina, R. I., and Ustinov, V. V. (2013). Magnetocaloric effect in inhomogeneous ferromagnets. *Journal of Applied Physics*, 113:073907.

Belevtsev, B. I., Zvyagina, G. A., Zhekov, K. R., Kolobov, I. G., Beliayev, E. Y., Panfilov, A. S., Galtsov, N. N., Prokhvatilov, A. I., and Fink-Finowicki, J. (2006). Influence of magnetic field on the paramagnetic-ferromagnetic transition in a $La_{1-x}Ca_xMnO_3$ ($x \sim 0.25$) crystal: Ultrasonic and transport studies. *Physical Review B*, 74(5):054427.

Bez, H. N., Nielsen, K. K., Norby, P., Smith, A., and Bahl, C. R. H. (2016a). Magneto-Elastic coupling in $La(Fe,Mn,Si)_{13}H_y$ within the Bean-Rodbell model. *AIP Advances*, 6(5):056217.

Bez, H. N., Nielsen, K. K., Smith, A., and Bahl, C. R. H. (2016b). A detailed study of the hysteresis in $La_{0.67}Ca_{0.33}MnO_3$. *Accepted in Journal of Magnetism and Magnetic Materials*.

Bez, H. N., Teixeira, C. S., Eggert, B. G. F., Lozano, J. a., Capovilla, M. S., Barbosa, J. R., and Wendhausen, P. a. P. (2013). Synthesis of Room-Temperature Magnetic Refrigerants Based on La-Fe-Si by a Novel Process. *IEEE Transactions on Magnetics*, 49(8):4626–4629.

Billinge, S. J. L., Proffen, T., Petkov, V., Sarrao, J. L., and Kycia, S. (2000). Evidence for charge localization in the ferromagnetic phase of $La_{1-x}Ca_xMnO_3$ from high real-space-resolution x-ray diffraction. *Physical Review B*, 62(2):1203–1211.

Blundell, S. (2001). *Magnetism in Condensed Matter*. Oxford University Press.

Bridges, F., Downward, L., Neumeier, J. J., and Tyson, T. A. (2010). Detailed relationship between local structure, polarons, and magnetization for $La_{1-x}Ca_xMnO_3$ ($0.21 \leq x \leq 0.45$). *Physical Review B*, 81(18):184401.

Brown, G. V. (1976). Magnetic heat pumping near room temperature. *Journal of Applied Physics*, 47(8):3673.

Buschow, K. H. J. and de Boer, F. R. (2004). *Physics of Magnetism and Magnetic Materials*. Kluwer Academic Publishers.

Buschow, K. H. J. and Velge, W. A. J. J. (1967). Phase relations and intermetallic compounds in the lanthanum-cobalt system. *Journal of the Less-Common Metals*, 13:11–17.

Caglioti, G., Paoletti, A., and Ricci, F. P. (1958). Choice of collimators for a crystal spectrometer for neutron diffraction. *Nucl. Instrum. Methods*, 3:223.

Cahn, R. W. and Haasen, P. (1996). *Physical Metallurgy*, volume 3. Elsevier B.V., 4th edition edition.

Callister, W. D. J. (2007). *Materials Science and Engineering - An Introduction*. John Willey and Sons, 7th edition.

Caron, L., Ou, Z., Nguyen, T., Cam Thanh, D., Tegus, O., and Brück, E. (2009). On the determination of the magnetic entropy change in materials with first-order transitions. *Journal of Magnetism and Magnetic Materials*, 321(21):3559–3566.

Çengel, Y. A. and Boles, M. A. (2006). *Thermodynamics - An Engineering Approach*. McGraw-Hill College.

Chen, W., Nie, L. Y., Zhao, X., Zhong, W., Tang, G. D., Li, A. J., Hu, J. J., and Tian, Y. (2006). Effect of Mn-site vacancies on the magnetic entropy change and the curie temperature of $la_{0.67}ca_{0.33}Mn_{1-x}O_3$ perovskite. *Solid State Communications*, 138:165–168.

Coey, J. M. D., Viret, M., and von Molnár, S. (1999). Mixed-valence manganites. *Advances in Physics*, 48:167–293.

Cullity, B. D. (1978). *Elements of X-ray Diffraction*. Addison-Wesley Publishing Company, Inc., second edition.

Debye, P. (1912). Zur Theorie der spezifischen Warmen. *Annalen der Physik*, 344(14):789–839.

Engelbrecht, K., Nielsen, K., and Pryds, N. (2011). An experimental study of passive regenerator geometries. *International Journal of Refrigeration*, 34:1817–1822.

Eriksen, D., Engelbrecht, K., Bahl, C. R. H., Bjørk, R., Nielsen, K. K., Insinga, A. R., and Pryds, N. (2015). Design and experimental tests of a rotary active magnetic regenerator prototype. *International Journal of Refrigeration*, 58:14–21.

Ewe, L., Hamadneh, I., Salama, H. A., and Abd-Shukor, R. (2008). Sound velocity in perovskite manganites $La_{0.67}Ca_{0.33}MnO_3$ with different grain sizes. *Physica B: Condensed Matter*, 403:2394–2398.

Foldeaki, M., Schnelle, W., Gmelin, E., Benard, P., Koszegi, B., Giguere, A., Chahine, R., and Bose, T. K. (1997). Comparison of magnetocaloric properties from magnetic and thermal measurements. *Journal of Applied Physics*, 82(1):309–316.

Foner, S. (1959). Versatile and Sensitive Vibration-Sample Magnetometer. *The Review of Scientific Instruments*, 30(7):548–557.

Franco, V., Blázquez, J., Ingale, B., and Conde, A. (2012). The Magnetocaloric Effect and Magnetic Refrigeration Near Room Temperature: Materials and Models. *Annual Review of Materials Research*, 42(1):305–342.

Fujieda, S., Fujita, a., and Fukamichi, K. (2003). Large magnetocaloric effects in $NaZn_{13}$-type $La(Fe_xSi_{1\hat{a}\acute{L}\check{S}x})_{13}$ compounds and their hydrides composed of icosahedral clusters. *Science and Technology of Advanced Materials*, 4(4):339–346.

Fujieda, S., Fujita, A., Fukamichi, K., Yamaguchi, Y., and Ohoyama, K. (2008). Neutron Diffraction and Isotropic Volume Expansion Caused by Deuterium Absorption into $La(Fe_{0.88}Si_{0.12})_{13}$. *Journal of the Physical Society of Japan*, 77(7):074722.

Fujieda, S., Fujita, A., Fukamichi, K., Yamazaki, Y., and Iijima, Y. (2001). Giant isotropic magnetostriction of itinerant-electron metamagnetic $La(Fe_{0.88}Si_{0.12})_{13}H_y$ compounds. *Applied Physics Letters*, 79(5):653.

Fujieda, S., Hasegawa, Y., Fujita, A., and Fukamichi, K. (2004). Thermal transport properties of magnetic refrigerants $La(Fe_xSi_{1-x})_{13}$ and their hydrides, and $Gd_5Si_2Ge_2$ and MnAs. *Journal of Applied Physics*, 95:2429.

Fujita, a., Fujieda, S., Fukamichi, K., Mitamura, H., and Goto, T. (2001). Itinerant-electron metamagnetic transition and large magnetovolume effects in $La(Fe_xSi_{1-x})_{13}$ compounds. *Physical Review B*, 65(1):1–6.

Genossar, J. and Steinitz, M. (1990). A tilted-plate capacitance displacement sensor. *Review of Scientific Instruments*, 61:2469.

Giauque, W. and Macdougall, D. (1933). Attainment of Temperatures Below 1 ^oK Absolute by Demagnetization of $Gd_2(SO_4)_38H_2O$. *Physical Reviews*, 43(9):768–768.

Goldschmidt, V. (1958). *Geochemistry*. Oxford University Press, second edition.

Goodenough, J. B. (2004). Electronic and ionic transport properties and other physical aspects of perovskites. *Reports on Progress in Physics*, 67:1915–1993.

Griffel, M., Skochdopole, E. R., and Spedding, F. H. (1954). The heat capacity of Gadolinium from 35 to 355 K. *Physical Review*, 93(4):657–661.

Gruner, M. E., Keune, W., Roldan Cuenya, B., Weis, C., Landers, J., Makarov, S. I., Klar, D., Hu, M. Y., Alp, E. E., Zhao, J., Krautz, M., Gutfleisch, O., and Wende, H. (2015). Element-resolved thermodynamics of magnetocaloric $LaFe_{(13-x)}Si_x$. *Physical review letters*, 114(5):057202.

Gschneidner, Jr., K. A. and Pcharsky, V. K. (2008). Thirty years of near room temperature magnetic cooling: Where we are today and future prospects. *International Journal of Refrigeration*, 31:945–961.

Guillou, F., Yibole, H., Van Dijk, N. H., Zhang, L., Hardy, V., and Brück, E. (2014). About the mechanical stability of MnFe(P,Si,B) giant-magnetocaloric materials. *Journal of Alloys and Compounds*, 617:569–574.

Harris, I. R., Noble, C., and Bailey, T. (1985). The hydrogen decrepitation of an $Nd_{15}Fe_{77}B_8$ magnetic alloy. *J. Less-Common Met.*, 106:L1–L4.

Hillert, M. (2008). *Phase Equilibria, Phase Diagrams and Phase Transformations - Their Thermodynamics basics*, volume 24. Cambridge University Press, 2nd edition.

Höhne, G., Hemminger, W., and Flammersheim, H.-J. (2003). *Differential Scanning Calorimetry*. Springer.

Jacek Kossut, J. A. G., editor (2010). *Introduction to the Physics of Diluted Magnetic Semiconductors*. Springer Berlin Heidelberg.

Jaeger, G. (1998). The ehrenfest classification of phase transitions: Introduction and evolution. *Archive for History of Exact Sciences*, 53(1):51–81.

Jeppesen, S., Linderoth, S., Pryds, N., Kuhn, L. T., and Jensen, J. B. (2008). Indirect measurement of the magnetocaloric effect using a novel differential scanning calorimeter with magnetic field. *The Review of scientific instruments*, 79(8):083901.

Jia, L., Liu, G. J., Wang, J. Z., Sun, J. R., Zhang, H. W., and Shen, B. G. (2006a). Field-induced entropy change in the manganite with significant short-range magnetic order. *Applied Physics Letters*, 89(12):122515.

Jia, L., Sun, J. R., Zhang, H. W., Hu, F. X., Dong, C., and Shen, B. G. (2006b). Magnetovolume effect in intermetallics $LaFe_{13-x}Si_x$. *Journal of Physics: Condensed Matter*, 18(44):9999–10007.

Krypiakewytsch, V. P. I., Zaretschniuk, O. S., Hladyschewskyj, E. I., and Rodak, O. I. (1968). Ternäre Verbindungen vom $NaZn_{13}$-typ. *Zeitschrift für Anorganische und Allgemeine Chemie*, 259:90–96.

Kumar, P. S. A., Joy, P. A., and Date, S. K. (1998). Evidence for Jahn-Teller polaron formation and spin-cluster-assisted variable-range-hopping conduction in $La_{0.7}Ca_{0.3}MnO_3$. *Journal of Physics: Condensed Matter*, 10:L269–L275.

Lei, T., Nielsen, K. K., Engelbrecht, K., Bahl, C. R. H., Neves Bez, H., and Veje, C. T. (2015). Sensitivity study of multi-layer active magnetic regenerators using first order magnetocaloric material $La(Fe,Mn,Si)_{13}H_y$. *Journal of Applied Physics*, 118(1):014903.

Lin, G., Wei, Q., and Zhang, J. (2006). Direct measurement of the magnetocaloric effect in $La_{0.67}Ca_{0.33}MnO_3$. *Journal of Magnetism and Magnetic Materials*, 300(2):392–396.

Liu, J., Krautz, M., Skokov, K., Woodcock, T. G., and Gutfleisch, O. (2011). Systematic study of the microstructure, entropy change and adiabatic temperature change in optimized La-Fe-Si alloys. *Acta Materialia*, 59:3602–3611.

Liu, J., Moore, J., Skokov, K., Krautz, M., Löwe, K., Barcza, a., Katter, M., and Gutfleisch, O. (2012). Exploring $La(Fe,Si)_{13}$-based magnetic refrigerants towards application. *Scripta Materialia*, 67(6):584–589.

Liu, Y., Sellmyer, D. J., and Shindo, D., editors (2006). *Handbook of Advanced Magnetic Materials*. Springer.

LoBue, M., Basso, V., Sasso, C. P., and Bertotti, G. (2005). Entropy and entropy production in magnetic systems with hysteresis. *Journal of Applied Physics*, 97(10).

Loudon, J. C. and Midgley, P. A. (2006). Micromagnetic Imaging to Determine the Nature of the Ferromagnetic Phase Transition in $La_{0.7}Ca_{0.3}MnO_3$. *Physical Review Letters*, 027214:1–4.

Lovell, E., Pereira, A. M., Caplin, a. D., Lyubina, J., and Cohen, L. F. (2015). Dynamics of the First-Order Metamagnetic Transition in Magnetocaloric $La(Fe,Si)_{13}$: Reducing Hysteresis. *Advanced Energy Materials*, 5(6):1401639.

Lyubina, J., Schäfer, R., Martin, N., Schultz, L., and Gutfleisch, O. (2010). Novel design of $La(Fe,Si)_{13}$ alloys towards high magnetic refrigeration performance. *Advanced materials*, 22(33):3735–9.

Morrish, A. H. (2001). Ferromagnetism. In *The Physical Principles of Magnetism*, pages 259–331. IEEE Press.

Morrison, K., Berenov, A., and Cohen, L. F. (2011). Origin of hysteresis in $La_{0.67}Ca_{0.33}MnO_3$. In *Mater. Res. Soc. Proc.*, volume 1310.

Morrison, K., Bratko, M., Turcaud, J., Berenov, A., Caplin, A. D., and Cohen, L. F. (2012). A calorimetric method to detect a weak or distributed latent heat contribution at first order magnetic transitions. *Review of Scientific Instruments*, 83:033901.

Nielsen, K., Hattel, J., Pryds, N., Bahl, C., and Smith, A. (2010). *Numerical modeling and analysis of the active magnetic regenerator*. PhD thesis.

Nielsen, K. K., Bez, H. N., von Moos, L., Bjørk, R., Eriksen, D., and Bahl, C. R. H. (2015). Direct measurements of the magnetic entropy change. *Review of Scientific Instruments*, 86(10):103903.

Palstra, T. T. M., Mydosh, J. A., Nieuwenhuys, G. J., van der Kraan, A. M., and Buschow, K. H. J. (1983). Study of the critical behaviour of the magnetization and electrical resistivity in cubic $La(Fe, Si)_{13}$ compounds. *Journal of Magnetism and Magnetic Materials*, 36:290–296.

Pecharsky, V. K. and Gschneidner, K. A. (1999). Magnetocaloric effect from indirect measurements: Magnetization and heat capacity. *Journal of Applied Physics*, 86(1):565.

Pecharsky, V. K. and Gschneidner, Jr., K. A. (1997). Giant Magnetocaloric Effect in $Gd_5Si_2Ge_2$. *Physical Reviews Letters*, 78(3):4494–4497.

Pecharsky, V. K. and Zavalij, P. Y. (2005). *Fundamentals of Powder Diffraction and Structural Characterization of Materials*. Springer, first edition.

Phan, M.-H. and Yu, S.-C. (2007). Review of the magnetocaloric effect in manganite materials. *Journal of Magnetism and Magnetic Materials*, 308(2):325–340.

Piazzi, M., Bennati, C., Curcio, C., Kuepferling, M., and Basso, V. (2015). Modeling specific heat and entropy change in La(FeâĂŞMnâĂŞSi)13âĂŞH compounds. *Journal of Magnetism and Magnetic Materials*, 400:349–355.

Planes, A., Mañosa, L., and Acet, M. (2009). Magnetocaloric effect and its relation to shape-memory properties in ferromagnetic heusler alloys. *Journal of Physics: Condensed Matter*, 21(23):233201.

Ragg, M., Keegan, G., Nagel, H., and Harris, I. R. (1997). The HD and HDDR process in the production of Nd-Fe-B Permanent Magnets. *International Journal of Hydrogen Energy*, 22(2/3):333–342.

Rietveld, H. M. (1967). Line profiles of neutron powder-diffraction peaks for structure refinement. *Acta Crystallographica*, 22(1):151–152.

Rietveld, H. M. (1969). A profile refinement method for nuclear and magnetic structures. *Journal of Applied Crystallography*, 2(2):65–71.

Rotter, M., Müller, H., Gratz, E., Doerr, M., and Loewenhaupt, M. (1998). A miniature capacitance dilatometer for thermal expansion and magnetostriction. *Review of Scientific Instruments*, 69(7):2742–2746.

Saito, H., Yokoyama, T., Terada, Y., Fukamichi, K., Mitamura, H., and Goto, T. (2000). Universal linear relation between the critical field and the inverse susceptibility for Co-based Laves-phase metamagnets. *Solid State Communications*, 113:447–450.

Smith, A. (2013). Who discovered the magnetocaloric effect? Warburg, Weiss, and the connection between magnetism and heat. *The European Physical Journal H*, 38(4):507–517.

Smith, A., Bahl, C. R. H., Bjørk, R., Engelbrecht, K., Nielsen, K. K., and Pryds, N. (2012). Materials Challenges for High Performance Magnetocaloric Refrigeration Devices. *Advanced Energy Materials*, 2:1288–1318.

Souza, J. a., Neumeier, J. J., and Yu, Y.-K. (2008). Magnetic signatures of ferromagnetic polarons in La 0.7 Ca 0.3 MnO 3 : Colossal magnetoresistance is not a Griffiths singularity. *Physical Review B*, 78:014436.

Tegus, O., Brück, E., Buschow, K. H. J., and de Boer, F. R. (2002). Transition-metal-based magnetic refrigerants for room-temperature applications. *Nature*, 415:150–152.

Teresa, J. M. D., Ibarra, M. R., Algarabel, P. A., Ritter, C., Marquina, C., Blasco, J., García, J., del Moral, A., and Arnold, Z. (1997). Evidence for magnetic polarons in the magnetoresistive perovskites. *Nature*, 386:256–259.

Teresa, J. M. D., Ibarra, M. R., Blasco, J., García, J., Marquina, C., and Algarabel, P. A. (1996). Spontaneous behavior and magnetic field and pressure effects on $La_{2/3}Ca_{1/3}MnO_3$ perovskite. *Physical Review B*, 54(2):1187–1193.

Turcaud, J., Morrison, K., Berenov, A., Alford, N. M., Sandeman, K., and Cohen, L. (2013). Microstructural control and tuning of thermal conductivity in $La_{0.67}Ca_{0.33}MnO_{3\pm\delta}$. *Scripta Materialia*, 68(7):510–513.

Turcaud, J. A., Pereira, A. M., and Cohen, L. F. (2015). Quantifying the deleterious role of strong correlations in $La_{1-x}Ca_xMnO_3$ at the magnetocaloric transition. *Physical Review B*, 91(13):134410.

Turcaud, J. A., Pereira, A. M., Sandeman, K. G., Amaral, J. S., Morrison, K., Berenov, A., Daoud-Aladine, A., and Cohen, L. F. (2014). Spontaneous magnetization above T_C in polycrystalline $La_{0.7}Ca_{0.3}MnO_3$ and $La_{0.7}Ba_{0.3}MnO_3$. *Physical Review B*, 90(2):024410.

von Moos, L., Bahl, C., Nielsen, K., and Engelbrecht, K. (2014). *Hysteresis in Magnetocaloric Materials: An experimental and modelling approach*. PhD thesis, DTU Energy.

von Moos, L., Bahl, C. R. H., Nielsen, K. K., and Engelbrecht, K. (2015). The influence of hysteresis on the determination of the magnetocaloric effect in $Gd_5Si_2Ge_2$. *Journal of Physics D: Applied Physics*, 48:025005.

Waske, A., Giebeler, L., Weise, B., Funk, A., Hinterstein, M., Herklotz, M., Skokov, K., Fähler, S., Gutfleisch, O., and Eckert, J. (2015). Asymmetric first-order transition and interlocked particle state in magnetocaloric $La(Fe,Si)_{13}$. *physica status solidi (RRL) - Rapid Research Letters*, 9(2):136–140.

Weiss, P. and Piccard, A. (1918). Sur un nouveau phénomene magnétocalorique. *Comptes Rendus*, pages 352–354.

White, G. K. and Collocott, S. J. (1984). Heat Capacity of Reference Materials: Cu and W. *Journal of Physical and Chemical Reference Data*, 13(4):1401639.

Williamson, G. K. and Hall, W. H. (1953). X-Ray Line Broadening from Filed Aluminium and Wolfram. *Acta Metallurgica*, 1:22–31.

Wollan, E. O. and Koehler, W. C. (1955). Neutron Diffraction Study of the Magnetic Properties of the Series of Perovskite-Type Compounds [(1-x)La, xCa]MnO_3. *Physical Review*, 100(2):545–563.

Zener, C. (1951). Interaction between the d shells in the transition metals. *Physical Review*, 81(4):440–444.

Zhu, C., Zheng, R., Su, J., and He, J. (1999). Ultrasonic anomalies in $La_{0.67}Ca_{0.33}MnO_3$ near the Curie temperature. *Applied Physics Letters*, 74(23):3504–3506.

Zimm, C. B. and Jacobs, S. A. (2013). Age splitting of the $La(Fe_{1-x}Si_x)_{13}H_y$ first order magnetocaloric transition and its thermal restoration. *Journal of Applied Physics*, 113(17):111–114.

Appendix A

Publications

A.1 Publications in peer-reviewed international scientific journals

A.1.1 A detailed study of the hysteresis in $La_{0.67}Ca_{0.33}MnO_3$

Journal of Magnetism and Magnetic Materials 416 (2016) 429–433

Contents lists available at ScienceDirect

Journal of Magnetism and Magnetic Materials

journal homepage: www.elsevier.com/locate/jmmm

A detailed study of the hysteresis in $La_{0.67}Ca_{0.33}MnO_3$

Henrique N. Bez *, Kaspar K. Nielsen, Anders Smith, Christian R.H. Bahl

Department for Energy Conversion and Storage, Technical University of Denmark, Risø Campus, Frederiksborgvej 399, DK-4000 Roskilde, Denmark

ARTICLE INFO

Article history:
Received 7 February 2016
Received in revised form
5 April 2016
Accepted 3 May 2016
Available online 7 May 2016

Keywords:
Magnetocaloric effect
Hysteresis
Phase transition
Manganites

ABSTRACT

We report a thorough study of the thermal hysteretic behaviour of a single phase sample of the magnetocaloric material $La_{0.67}Ca_{0.33}MnO_3$. Previous reports in the literature have variously found hysteretic and non-hysteretic behaviour. We show the importance of measuring under carefully defined heating and cooling procedures. Careful analysis of the specific heat, measured at five different temperature ramp rates, and the magnetic entropy change indicates that there is no observable hysteresis, even though the behaviour of both quantities is consistent with a first-order phase transition. We discuss the reasons for this and for the differing results previously found.

1. Introduction

A broad range of materials display the magnetocaloric effect. An interesting example is the La-manganites, in particular $La_{0.67}Ca_{0.33}MnO_3$ which has been investigated for several years as a possible material for magnetocaloric applications [1–3]. Of particular interest is whether the phase transition is of first order or of second order. As a general rule, materials with a first-order phase transition (FOPT) can exhibit a larger magnetocaloric effect than materials with a second-order phase transition (SOPT). On the other hand thermal hysteresis, which gives rise to losses when the materials are applied in thermodynamic cycles, is associated with FOPT. This makes it of both theoretical and practical importance to investigate the hysteresis of magnetocaloric materials.

$La_{0.67}Ca_{0.33}MnO_3$ has been the subject of much research over the past decades due to its many interesting properties. Even so, it remains a much debated question whether the material undergoes a FOPT or a SOPT [4,5]. Furthermore, thermal hysteresis has been studied in this material with contradicting results [1,5–7]. One complication is that different processing routes may lead to different properties [8], e.g., the reported Curie temperatures vary between 250 and 270 K. Furthermore, care has to be taken when investigating thermal hysteresis in FOPT to avoid sampling metastable mixed states in the transition region between the paramagnetic and ferromagnetic states. It has previously been shown that for observation of the true thermal hysteresis it is necessary to 'reset' the sample between measurements by cooling or heating to a temperature where only one phase is present [9,10].

One of the models used to shed some light on the magnetic phase transition of materials is the Bean–Rodbell model [11]. Bean and Rodbell have proposed that the exchange constant, and therefore T_C, varies linearly with the lattice spacing as $T_C = T_0[1 + \beta\frac{V-V_0}{V_0}]$, where V is the unit cell volume, T is the temperature, and T_0 and V_0 are temperature and unit cell volume in the absence of exchange interaction, respectively. The parameter denoted by β controls the strength of the spin-lattice coupling. Moreover, one of the implications of this model is the introduction of possible irreversibilities, such as hysteresis. One of the parameters of the model, η, can control whether the transition is first order, $\eta > 1$, or second order, $\eta \leq 1$. This model has been used in good agreement with measured properties of some compositions of $La_{1-x}Ca_xMnO_3$, where η values above 1 [12] were observed, i.e. first order phase transition. Furthermore, the literature has shown that by superimposing a Gaussian distribution in the Curie temperature, one can simulate the effect of chemical inhomogeneities on the properties [13].

Here we use measurements of c_p and both indirect and direct measurements of the isothermal entropy change Δs to evaluate the phase transition of $La_{0.67}Ca_{0.33}MnO_3$. The indirect measurement is done by measuring the magnetisation as a function of field and temperature and subsequently using a numerical integration of the maxwell relation $\Delta s = \mu_0 \int (\partial m/\partial t)dh$, while the direct measurement uses calorimetry [14–16]. The latter avoids the approximations arising from the numerical integration and provides a very stable temperature for the measurements. Below we report studies of the thermal hysteretic and FOPT behaviour by means of measurements of Δs and c_p, and by the implementation of Bean–

* Corresponding author.
E-mail address: hnbe@dtu.dk (H.N. Bez).

http://dx.doi.org/10.1016/j.jmmm.2016.05.011
0304-8853/

Rodbell model of $La_{0.67}Ca_{0.33}MnO_3$ produced by solid-state reaction.

2. Experimental procedure

$La_{0.67}Ca_{0.33}MnO_3$ polycrystalline material was synthesised by solid-state reaction. La_2O_3, $CaCO_3$ and MnO_2 in powder form were ground and mixed stoichiometrically by roll milling during 48 h with a rotation speed of 180 rpm. The powder was then calcinated at 1123 K for 24 h. Subsequently, the powder was isostatically pressed into pellets and sintered at 1403 K for 48 h. Both calcination and sintering were performed in air. X-ray diffraction (XRD) measurements were performed in a Brucker D8 X-ray diffractometer at ambient temperature and pressure, under Cu radiation. The specific heat, c_p, was measured at different temperature rates in a custom-built differential scanning calorimeter (DSC) [17] under several applied fields. The isothermal entropy change was measured for every 0.25 K in the same device, by keeping the temperature fixed and varying the applied magnetic field. We used four different measurement protocols around the transition temperature to avoid the appearance of mixed states when characterizing the entropy change:

(i) From the ferromagnetic state (FM) towards paramagnetic state (PM) with a reset temperature at 240 K and going from 0 T to 1.0 T.
(ii) From FM towards PM with a reset temperature at 240 K and going from 1.0 T to 0 T.
(iii) From PM towards FM with a reset temperature at 290 K and going from 0 T to 1.0 T.
(iv) From PM towards FM with a reset temperature at 290 K and going from 1.0 T to 0 T.

When resetting, the sample is taken to the chosen reset temperature and allowed to thermally equilibrate. Low temperature magnetisation was measured in a high field VSM (Cryogen Free Measurement System – 16 T) at 10 K from 0 to 10 T, with a rate of 0.1 T/min to find the saturation magnetisation. Moreover, a Lake-Shore VSM, model 7407, was used to measure isothermal magnetisation around the transition temperature in order to calculate Δs, and compare with the direct measurements in the calorimeter. These Δs measurements were done from 0 T to 1.6 T and for every 0.5 K. The demagnetisation effects were taken into account when processing the data, assuming a prism shaped sample [18]. The sample has the approximate dimensions $3.8 \times 1.2 \times 1.2$ mm^3. The field orientation in the isothermal magnetisation measurements was along the long axis to minimise demagnetisation, while in the DSC the field was along the short axis, due to size incompatibility.

3. Results

LCMO has an O-type orthorhombic structure, with a distortion of the MnO_6 octahedra due to the Jahn–Teller effect [19]. Fig. 1 shows the XRD pattern and Rietveld refinement of the polycrystalline $La_{0.67}Ca_{0.33}MnO_3$. From the Rietveld refinement one may observe the single phase pattern of $La_{0.67}Ca_{0.33}MnO_3$ where the unit cell parameters a, b and c were calculated to be 5.47154(7) Å, 5.45690(1) Å and 7.7086(1) Å, respectively, resulting in a unit cell with a volume of 230.162(7) Å^3, which is in agreement with the literature [4]. Furthermore, Fig. 2 shows the magnetisation measurement at 10 K, where the solid line is the measurement and the dashed red line is the theoretical saturation value calculated as follows:

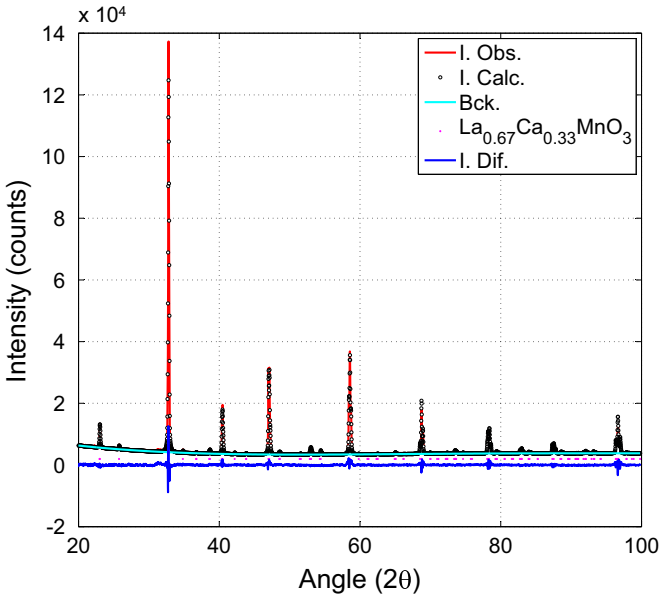

Fig. 1. XRD pattern and Rietveld refinement of the perovskite showing the desired single phase structure.

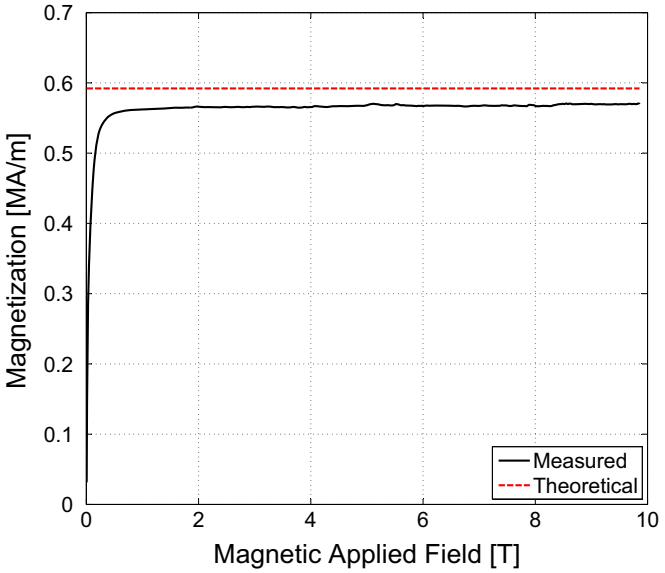

Fig. 2. Magnetisation measurement at 10 K, from 0 T to 10 T at a rate of 0.1 T/min. The solid line represents the measurement, and the dashed red line is the theoretical value of the saturation magnetisation. (For interpretation of the references to colour in this figure caption, the reader is referred to the web version of this paper.)

$$M_s = g\mu_B J\rho_s. \quad (1)$$

Here, g is the Landé factor, μ_B is the Bohr magneton, J is the total quantum angular momentum and ρ_s is the magnetic spin density. The Landé factor used is 2, J is 1.835 (average on the ratio of Mn^{+3} and Mn^{+4}) and the spin density is calculated simply by the number of magnetic atoms (four) in the volume V obtained by XRD, giving a magnetic spin density of 1.7391e28 spins/m^3. These values were used to calculate the theoretical saturation magnetisation. One can see that the experimental and theoretical values are in good agreement; the measured magnetisation value, 3.57 μ_B per unit formula, is around 97% of the theoretical saturation magnetisation value, 3.67 μ_B per unit formula.

In order to evaluate the specific heat under heating and cooling conditions, it was measured for different temperature rates, Fig. 3.

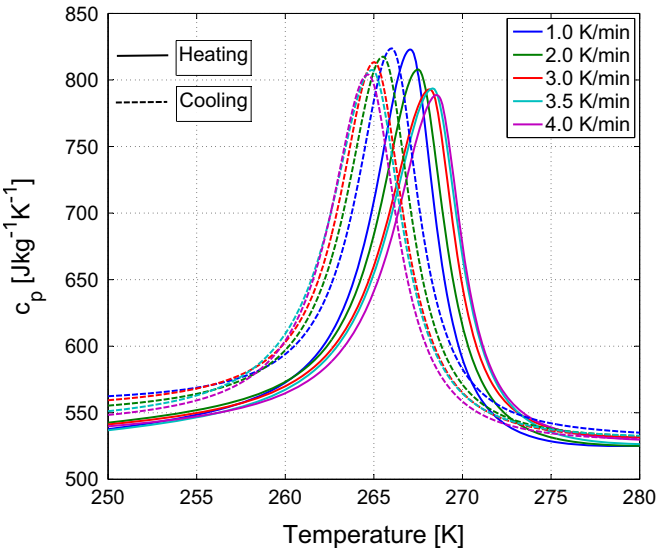

Fig. 3. Specific heat as a function of temperature for different temperature rates at 0 T.

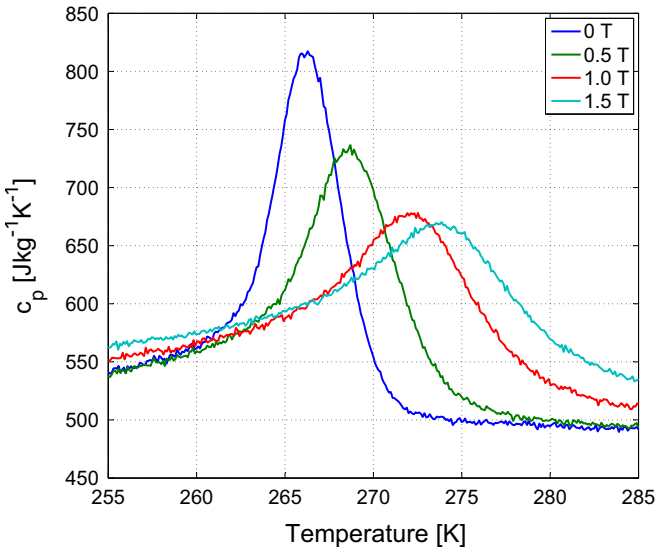

Fig. 5. Specific heat as a function of temperature and under different applied field, with $\dot{T} = -1.0$ K/min.

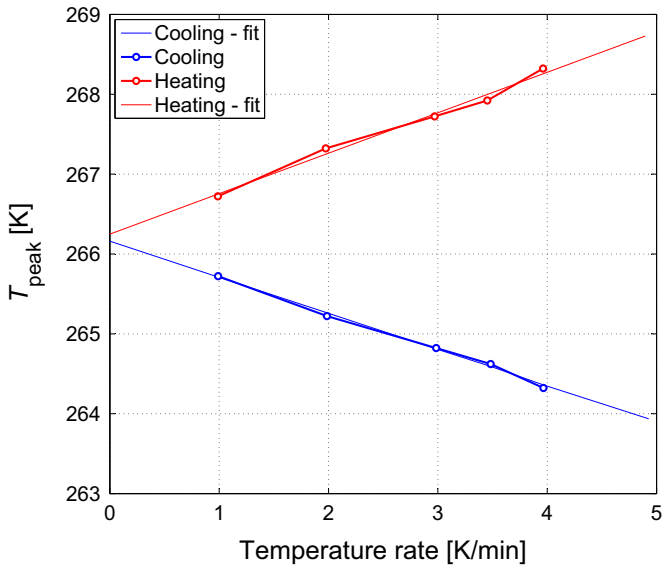

Fig. 4. Heat capacity peak temperature, T_{peak}, as a function of temperature rates for both heating and cooling. At finite heating and cooling rates extrinsic hysteresis is apparent. However, the intrinsic hysteresis, corresponding to the extrapolated temperature rate 0 K/min, vanishes.

The peak values and positions are in agreement with the literature [1,5]. The peak temperatures (T_{peak}) of the c_p curves were fitted as a function of rate in order to exclude the extrinsic hysteresis, as shown in Fig. 4. The observed hysteresis decreases with decreasing temperature rates, and for the extrapolated 0 K/min rate, the intrinsic hysteresis is 0.08 K, virtually zero considering the fitting and extrapolation uncertainties, ±0.2 K. It is interesting to notice that the expected ΔT_{hyst} for a rate of 5 K/min is the same as the one reported elsewhere [1].

The extrinsic hysteresis under different temperature rates is related to the thermal diffusivity of the material. $La_{0.67}Ca_{0.33}MnO_3$ has a large specific heat and a relatively low thermal conductivity, 1–3 W m^{-1} K^{-1} [20], which then leads to a low thermal diffusivity. Considering the base level of $c_p = 550$ J kg^{-1}K^{-1}, the density obtained from the XRD measurement $\rho = 6034$ kg m^{-3} and assuming a value of $\kappa = 2$ W m^{-1} K^{-1}, the thermal diffusivity can be calculated by $D = \kappa/c_p\rho$ and for $La_{0.67}Ca_{0.33}MnO_3$ it is $6{\cdot}10^{-7}$ m^2 s^{-1}. This is approximately five times smaller than other common magnetocaloric materials such as $La(Fe_{0.88}Si_{0.12})_{13}H_{1.0}$ where it is $\sim 2.7 \times 10^{-6}$ m^2 s^{-1}, very similar to the diffusivity of Gd [21]. Therefore, the temperature rate is much more influential on the position of the peaks of $La_{0.67}Ca_{0.33}MnO_3$ compared to other magnetocaloric materials.

To further investigate the thermal hysteresis, specific heat measurements under different applied fields were performed. Fig. 5 shows the heat capacity during the cooling procedure with $\dot{T} = -1.0$ K/min, under different applied fields. As the graph shows, the heat capacity peak is shifting towards higher temperatures for increasing values of H. This indicates a behaviour similar to that of a first order phase transition [22]. Fig. 6 shows T_{peak} as a function of field, for both heating and cooling procedures, with $|\dot{T}| = 1.0$ K/min. The linear fits show a slope of 6.2 ± 0.9 K/T for both the heating and cooling procedures. Furthermore, when extrapolating to a rate of 0 K/min as in Fig. 4, the lines collapse

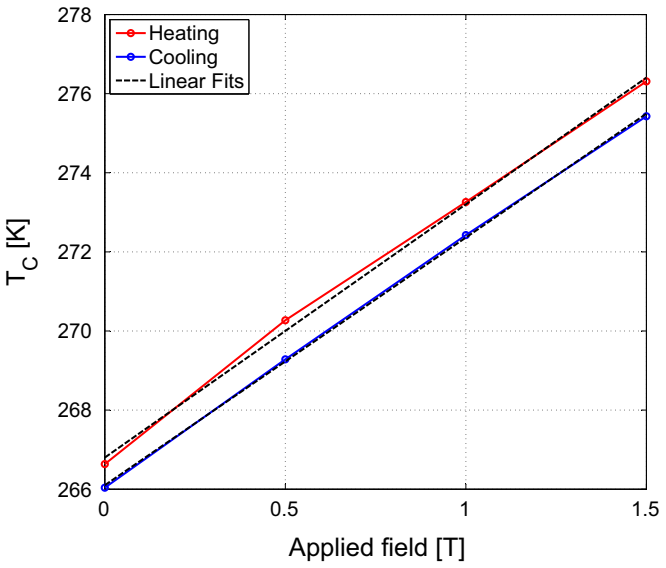

Fig. 6. The specific heat peak temperature, T_{peak}, as a function of applied magnetic fields for both heating and cooling heat capacity measurements, with $|\dot{T}| = 1.0$ K/min. The dashed lines are linear fits.

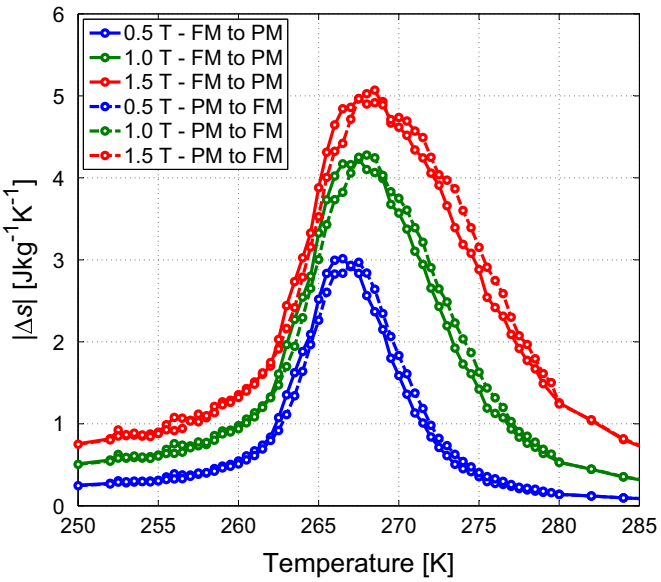

Fig. 7. Entropy change calculated from magnetisation measurements from the VSM, using methods (i) and (iii), from 0 T to 0.5, 1.0 and 1.5 T.

showing the absence of hysteresis. In contrast, for materials with intrinsic hysteresis the amount of hysteresis decreases linearly with field, until a critical field is reached at which the transition becomes continuous and there is no more hysteresis.

Fig. 7 shows indirect measurements of Δs as a function of temperature for different values of ΔH. One may see the asymmetric behaviour of the peak with increase in field; a behaviour related to first order transitions [22]. A slight hysteretic behaviour around the T_{peak} is observed, with a ΔT_{hyst} of approximately 0.7 K in the full-width half maximum (FWHM). On the other hand, direct measurements of Δs (see Fig. 8) show no observable difference between the peak positions and, therefore, no significant thermal hysteresis was observed. The peak value is in agreement with literature values [5]. The difference between the two types of measurements arises from the uncertainties related to the measurements. As Pecharsky and Gschneidner [23] have shown, Δs derived from magnetisation measurements may have an uncertainty of up to 20%, making it challenging to try to extract

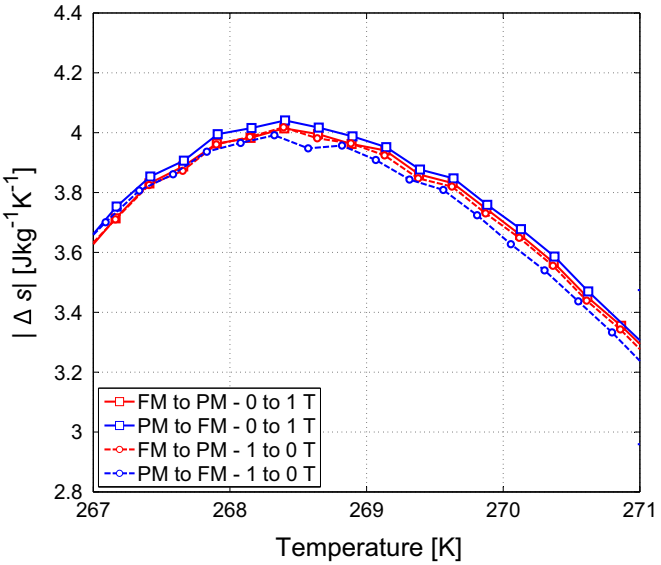

Fig. 8. Entropy change measured directly in the DSC, around the transition temperature with a temperature step of 0.25 K.

reliable values of a small or non-existent hysteresis. It is important to note that the direct measurement of Δs is done with a high precision instrument with a temperature uncertainty of ± 10 mK [16]. Furthermore, each point is measured individually, avoiding the smoothing effect observed when finite difference approximation is used to calculate Δs from magnetisation derivatives.

4. Discussion

We find no discernible *apparent* hysteresis in LCMO, as shown above through the measurements of heat capacity and calorimetric measurements of entropy change. This is consistent with previous reports using an AC calorimetric method [5]. On the other hand the observed behaviour of the specific heat and isothermal entropy change is characteristic of a FOPT. These observations can be reconciled if we consider the spread in critical temperature which is caused by compositional variations and the tendency to formation of magnetically inhomogeneous states in the manganites [13]. For weakly first-order materials even a small spread in critical temperatures may be enough to smooth out the transition and make the hysteresis disappear. Recently we showed, using detailed determination of the field dependence of Δs at T_c in combination with a fit to the Bean–Rodbell model that it is possible to determine the order of the phase transition and the spread in critical temperature [24]. We find indeed that $La_{0.67}Ca_{0.33}MnO_3$ is weakly first order, with an $\eta = 1.25$. In Fig. 9 we show the modelled behaviour of the entropy curve under both heating and cooling, with a standard deviation on the Gaussian distribution $\sigma(T_0) = 2.6$ K, and without any distribution. It is clear that the weak hysteresis present when there is no compositional inhomogeneity, i.e. $\sigma(T_0) = 0$ K tends to vanish when the spread is taken into consideration, i.e. $\sigma(T_0) = 2.6$ K. It is also important to notice that the entropy curve shown here is in zero field. Previous works [22,25] have shown that the thermal hysteresis decreases with the increase of magnetic field, making it the largest at zero field. Moreover, the inset shows the entropy change under heating and cooling procedures, for both distributions and a magnetic field change of 1 T. One may see the great impact that the spread causes the entropy change, making the peak wider and smaller. We have

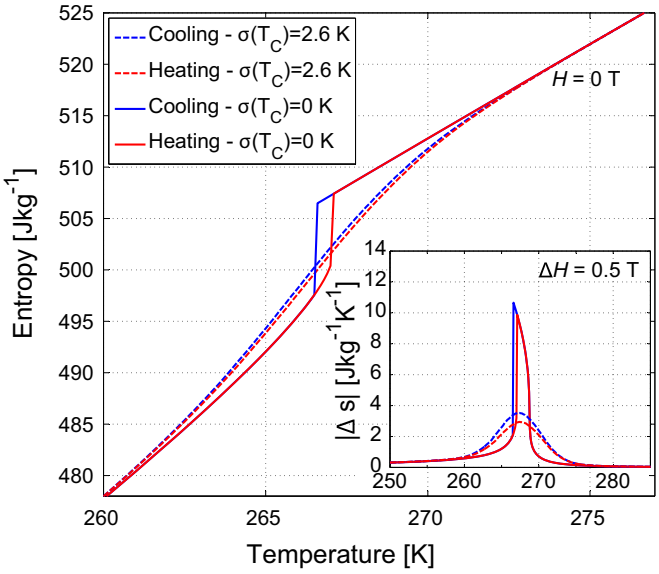

Fig. 9. Entropy as a function of the temperature, for heating and cooling procedures, and $H = 0$ T. One may see the vanishing impact of the distribution $\sigma(T_C)$ on the hysteresis. The inset shows the modelled isothermal entropy change for $\Delta H = 0.5$ T, during heating and cooling procedures.

seen the same behaviour recently [26] in $La(Fe,Mn,Si)_{13}H_{1.0}$. We believe that such behaviour is due to the chemical inhomogeneity. If a material with mass m has a single T_C, all its mass will undergo the transition at that temperature, concentrating all the entropy change at it. However, if the material has a distribution in T_C due to, e.g., chemical inhomogeneity, different parts of the material will change from FM to PM at different temperatures, so the entropy change will be distributed according to the distribution of T_C.

5. Conclusions

We have studied the thermal hysteretic behaviour of $La_{0.67}Ca_{0.33}MnO_3$ by means of several measurements and modelling. Direct Δs measurements with 0.25 K step, measured in 4 different setups have shown no temperature difference. Heat capacity measured under 0 T and different temperature rates have shown no hysteresis when done the extrapolation to equilibrium state. Observed hysteresis does not decrease with field, pointing to the absence of intrinsic hysteresis. Still, FOPT behaviour was observed as c_p shifting with field and the asymmetric growth of Δs with increasing field changes. FOPT modelled with Bean-Rodbell model and with a superimposed Gaussian distribution on the T_C have shown that the spread in T_C can decrease significantly, or even vanish the hysteresis.

Acknowledgements

This work was financed by the ENOVHEAT project which is funded by Innovation Fund Denmark (contract no. 12-132673).

References

[1] G. Lin, Q. Wei, J. Zhang, J. Magn. Magn. Mater. 300 (2) (2006) 392–396.
[2] Z.B. Guo, Y.W. Du, J.S. Zhu, H. Huang, W.P. Ding, D. Feng, Phys. Rev. B 78 (6) (1997) 1142–1145.
[3] H. Huang, Z.B. Guo, D.H. Wang, Y.W. Du, J. Magn. Magn. Mater. 173 (1997) 302–304.
[4] J.A. Turcaud, A.M. Pereira, K.G. Sandeman, J.S. Amaral, K. Morrison, A. Berenov, A. Daoud-Aladine, L.F. Cohen, Phys. Rev. B 90 (2) (2014) 024410.
[5] K. Morrison, A. Berenov, L.F. Cohen, in: Materials Research Society Proceedings, vol. 1310, 2011.
[6] L. Ewe, I. Hamadneh, H.a. Salama, R. Abd-Shukor, Physica B 403 (13–16) (2008) 2394–2398.
[7] C.L. Canedy, K.B. Ibsen, G. Xiao, J.Z. Sun, A. Gupta, W.J. Gallagher, J. Appl. Phys. 79 (8) (1996) 4546.
[8] M.-H. Phan, S.-C. Yu, J. Magn. Magn. Mater. 308 (2) (2007) 325–340.
[9] L. Caron, Z. Ou, T. Nguyen, D. Cam Thanh, O. Tegus, E. Brück, J. Magn. Magn. Mater. 321 (21) (2009) 3559–3566.
[10] L. von Moos, C.R.H. Bahl, K.K. Nielsen, K. Engelbrecht, J. Phys. D: Appl. Phys. 48 (2015) 025005.
[11] C.P. Bean, D.S. Rodbell, Phys. Rev. 126 (1) (1962) 104–115.
[12] J.A. Turcaud, A.M. Pereira, L.F. Cohen, Phys. Rev. B 91 (13) (2015) 134410.
[13] N.G. Bebenin, R.I. Zainullina, V.V. Ustinov, J. Appl. Phys. 113 (2013) 073907.
[14] M. Kuepferling, C.P. Sasso, V. Basso, L. Giudici, IEEE Trans. Magn. 43 (6) (2007) 2764–2766.
[15] V. Basso, C.P. Sasso, M. Küpferling, Rev. Sci. Instrum. 81 (11) (2010) 113904.
[16] K.K. Nielsen, H.N. Bez, L. von Moos, R. Bjørk, D. Eriksen, C.R.H. Bahl, Rev. Sci. Instrum. 86 (10) (2015) 103903.
[17] S. Jeppesen, S. Linderoth, N. Pryds, L.T. Kuhn, J.B. Jensen, Rev. Sci. Instrum. 79 (8) (2008) 083901.
[18] A. Aharoni, J. Appl. Phys. 83 (6) (1998) 3432–3434.
[19] J.M.D. Coey, M. Viret, S. von Molnár, Adv. Phys. 48 (1999) 167–293.
[20] J. Turcaud, K. Morrison, A. Berenov, N. Alford, K. Sandeman, L. Cohen, Scr. Mater. 68 (7) (2013) 510–513.
[21] S. Fujieda, J. Appl. Phys. 95 (5) (2004) 2429.
[22] A. Smith, C.R.H. Bahl, R. Bjørk, K. Engelbrecht, K.K. Nielsen, N. Pryds, Adv. Energy Mater. 2 (2012) 1288–1318.
[23] V.K. Pecharsky, K.A. Gschneidner, J. Appl. Phys. 86 (1) (1999) 565.
[24] A. Smith, K.K. Nielsen, H.N. Bez, C.R.H. Bahl, Phys. Rev. B (2016), submitted for publication.
[25] V. Basso, M. Küpferling, C. Curcio, C. Bennati, A. Barzca, M. Katter, M. Bratko, E. Lovell, J. Turcaud, L.F. Cohen, J. Appl. Phys. 118 (5) (2015) 053907.
[26] H.N. Bez, K.K. Nielsen, P. Norby, A. Smith, C.R.H. Bahl, AIP Adv. (2016), http://dx.doi.org/10.1063/1.4944400, in press.

A.1.2 Magneto-elastic coupling in La(Fe,Mn,Si)$_{13}$H$_y$ within the Bean-Rodbell model

Magneto-elastic coupling in La(Fe, Mn, Si)$_{13}$H$_y$ within the Bean-Rodbell model

Henrique N. Bez,[a] Kaspar K. Nielsen, Poul Norby, Anders Smith, and Christian R. H. Bahl
Department of Energy Conversion and Storage, Technical University of Denmark - Frederiksborgvej 399, DK-4000 Roskilde - Denmark

(Presented 12 January 2016; received 6 November 2015; accepted 12 January 2016; published online 14 March 2016)

First order magnetic phase transition materials present a large magnetocaloric effect around the transition temperature, where these materials usually undergo a large volume or structural change. This may lead to some challenges for applications, as the material may break apart during field change, due to high internal stresses. A promising magnetocaloric material is La(Fe,Mn,Si)$_{13}$H$_y$, where the transition temperature can be controlled through the Mn amount. In this work we use XRD measurements to evaluate the temperature dependence of the unit cell volume with a varying Mn amount. The system is modelled using the Bean-Rodbell model, which is based on the assumption that the spin-lattice coupling depends linearly on the unit cell volume. This coupling is defined by the model parameter η, where for $\eta > 1$ the material undergoes a first order transition and for $\eta \leq 1$ a second order transition. We superimpose a Gaussian distribution of the transition temperature with a standard deviation $\sigma(T_0)$, in order to model the chemical inhomogeneity. Good agreement is obtained between measurements and model with values of $\eta \sim 1.8$ and $\sigma(T_0) = 1.0$ K. [http://dx.doi.org/10.1063/1.4944400]

I. INTRODUCTION

The magnetocaloric effect (MCE) is a thermal response of a material when subjected to an applied magnetic field change.[1] Some materials may undergo a first order phase transition (FOPT) while others a second order (SOPT).[2] One of the FOPT materials series is the La-Fe-Si based alloys.[3] This alloy presents excellent MCE,[4] high thermal conductivity[5] and low thermal hysteresis[4] when compared to other FOPT magnetocaloric materials. Still, even with promising magnetocaloric performance, this family of materials presents some issues which have yet to be fully understood. During the phase transition the material has a volume change[6] that may break the sample apart.[7,8] Moreover, this material may present virgin behavior,[8] which is related to the microstructure of the material and the volume change.

The magnetoelastic modelling of such materials is of interest in order to predict and understand the behavior of them when cycled thermally and magnetically. Literature has shown[9] that the Bean-Rodbell model[10] can be applied for isotropic crystal structures such as NaZn$_{13}$. In this model the exchange constant, and therefore the Curie temperature, T_C, is in fact varied linearly with the lattice spacing as $T_C = T_0\left[1 + \beta\frac{V-V_0}{V_0}\right]$, where V is the unit cell volume, and T_0 is the Curie temperature of the system when V is constrained to V_0, which is the volume at 0 K in the absence of strains introduced internally, e.g. by exchange interactions, or externally e.g. applied stresses. β is a parameter that controls the spin-lattice coupling strength. From the model, another important parameter that may be extracted is η. This parameter determines the order of the transition and is given by:

[a]hnbe@dtu.dk

$$\eta = 40\rho_s \kappa T_0 k_B \beta^2 \frac{(J(J+1))^2}{(2J+1)^4 - 1}. \quad (1)$$

Here ρ_s is the density of spins in the volume V, κ is the compressibility, k_B is the Boltzmann constant and J is the total angular momentum. η relates to the order of transition so that when $\eta \leq 1$ the material undergoes a SOPT and $\eta > 1$ a FOPT. Moreover the model predicts the following relationship between volume and magnetization $\frac{V-V_0}{V_0} = \rho_s \kappa k_B T_0 \beta \sigma^2/2 - P\kappa$, where σ is the normalized magnetization in respect to the saturation and P is the external applied pressure.

We here evaluate the volume change that the FOPT $La(Fe,Mn,Si)_{13}H_y$ presents by means of X-ray diffraction (XRD) at different temperatures. We also evaluate the nature of the phase transition by isofield magnetization measurements of single particles and multiple particles of the material, observing the effect that collective versus singular properties has. Finally, we use the Bean-Rodbell model to investigate the magnetoelastic coupling of these materials.

II. EXPERIMENTAL PROCEDURE

Three different compositions of $LaFe_{13-x-y}Mn_xSi_yH_{1.65}$ alloys were provided by Vacuumschmelze GmbH, with $x = 0.25$, 0.22 and 0.06; $y = 1.28$, 1.23 and 1.18, respectively. The materials as received are in the form of irregular shaped particles with a mean diameter of 560 ± 200 μm. From calorimetric measurements, not shown here, T_C was found to be 304.1, 314.1 and 340.3 K in the three samples, respectively. The different materials were analysed in a Rigaku Smartlab XRD as a function of temperature during heating and cooling procedures, under Cu radiation and in powder form. The measurements were done every 1 K, at stable temperature and without overshooting. Using the WINPOW software, Rietveld refinement[13] was performed to calculate the lattice parameters and phase fractions in each temperature for each material.

A LakeShore VSM, model 7407, was used to measure isofield magnetizations around the transition temperature (possible ~0.15 K overshooting). Low temperature magnetization was measured in a high field VSM (Cryogen Free Measurement System - 16 T) at 10 K from 0 to 10 T, with a rate of 1.7 mT/s. This measurement was used to calculate the total angular momentum, J. Isothermal entropy change, Δs, measurements were carried out in a custom-built DSC, using the temperature reset to account for hysteresis, described elsewhere.[12] Finally, the Bean-Rodbell model was applied with a normal distribution $\sigma(T_0)$ in order to take into account the chemical inhomogeneities.

III. RESULTS AND DISCUSSION

A. Experimental Results

XRD measurements were performed on three samples of $La(Fe,Mn,Si)_{13}H_y$, with slightly different concentrations of Mn, and therefore also Fe, Si and H. In order to properly refine the measured XRD, the ICSD-161853 was used for the $NaZn_{13}$-type crystal structure of $La(Fe,Mn,Si)_{13}H_y$ and for $\alpha-$Fe we used ICSD-53802. The refinement was performed in the range $20° < 2\theta < 90°$, and all the present peaks were refined including the $\alpha-$Fe ones. Due to the peak overlap around the phase transition, the PM phase was first refined at a temperature 2 K above the transition. Then, during the transition the obtained PM lattice parameter was fixed to that value. The refined patterns presented an average value of $R_p \sim 1.2$, $R_{wp} \sim 1.8$ and $\chi^2 \sim 9.2$. Figure 1 shows the XRD patterns for all the different measured temperatures during the cooling procedure for $x = 0.06$. The paramagnetic (PM) phase of this material family presents the same crystal structure as the ferromagnetic (FM) phase,[6] only the volume is changed by about 1% at the phase transition.[9] This means that the peaks measured in the XRD most probably overlap as observed in Fig. 1. Furthermore, the presence of both pairs of peaks (from FM and PM phase, respectively) means that there is a mixed state where some of the powder particles are in the FM state and others are still in the PM state.

From the refinements one can obtain the phase volumes and fractions. The materials had approximately 2 wt.% of $\alpha-$Fe as a secondary phase. Figure 2 shows the unit cell volume as a function of the temperature for the three different materials. The first feature to notice is the volume

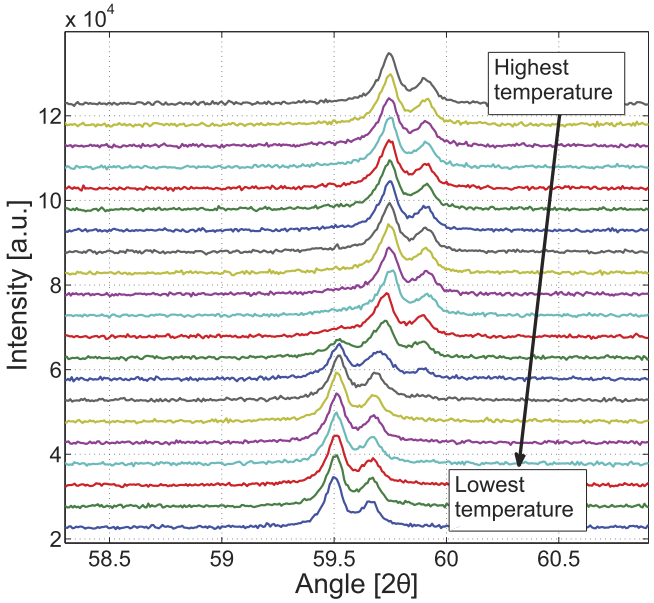

FIG. 1. XRD patterns for different fixed temperatures during the cooling procedure for $LaFe_{13-x-y}Mn_xSi_yH_{1.65}$ with $x = 0.06$. The reflection shown is for the peak (6 4 2).

change at T_C, explained in the introduction. One may also notice that for each sample there are temperatures where two unit cell volumes are plotted. These temperatures were the ones where FM and PM peaks overlapped as shown in Figure 1. Table I shows the volume change values for each material.

Figure 3 shows the FM fraction determined by Rietveld refinement as a function of the temperature for the three different materials studied. The error bars are mostly within the symbol size. The transitions seems to exhibit some thermal hysteresis, ΔT_{hyst}, but rather small. Furthermore, the transition occurs during a temperature span of about 6 K, rather than discontinuously.

To understand the transition of the material and any microstructural effects, magnetization measurements were carried out on three different particle distributions: (i) single particle, (ii) multiple single particles, and (iii) multiple ground particles (particle sizes of ~25 μm). In case (i) and

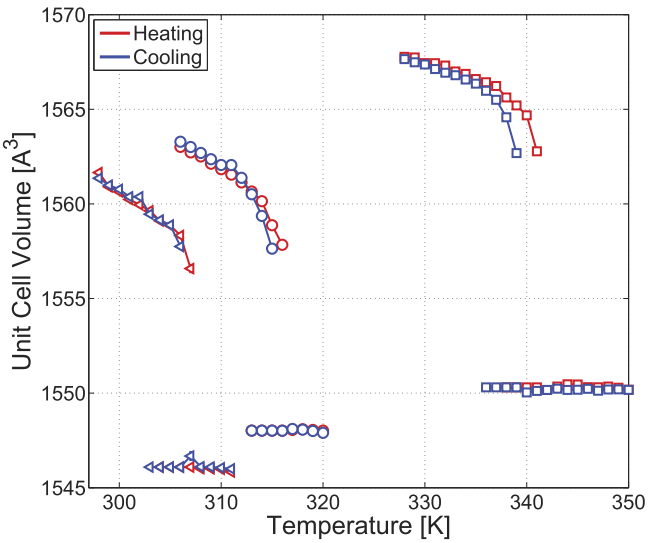

FIG. 2. Unit cell volume versus temperature for the three different materials during the cooling and heating procedures. The error bars are smaller than the symbol size.

TABLE I. Bean-Rodbell parameters and measured volume change. The parameters were found visually comparing modelled data and measured data.

x	0.25	0.22	0.06
T_0 [K]	290	300	320
$\sigma(T_0)$ [K]	1.0	1.0	0.8
η [-]	1.80	1.75	1.90
β [-]	35.93	34.81	34.83
V_0 [m^3]	$1.5460 \cdot 10^{-27}$	$1.5481 \cdot 10^{-27}$	$1.550 \cdot 10^{-27}$
ΔV [%]	0.82	0.83	1.04

(ii) the particles were glued to a rod inside an area of 4 by 4 mm, while in case (iii) the powder was put inside a cylindrical container. Figure 4 shows the magnetization measurements for $x = 0.06$, during the heating procedure. The different level of magnetization on the FM side is related to fluctuations of iron inside such small particles, and small differences in internal fields as the different particles have different demagnetization factors. Moreover, the virgin effect described elsewhere[8,11] was observed, and the samples were heated to above T_C prior to the measurements in order to avoid the virgin effect. As one may see, different single particles have different T_C, and when multiple raw particles (red dashed line) are measured the discrete behavior of the transition of single particles is observed as a plurality of sharp transitions within a few degrees. However, when the particles are ground to fine powder (blue line) with a mass of 101.3 mg, the properties change significantly, which is related to the microstructure as reported elsewhere.[14] When the powder is finely ground each single particle is, mostly, one single crystal. If one considers the presence of stoichiometry inhomogeneities, which virtually all materials possess, each single particle may have its own T_C, giving them a distribution of T_C as a whole. Oxidation was ruled out as the XRD patterns (particle size of $\sim 25 \mu$m) have not shown any peaks related to oxides.

B. Modelling Results

The Bean-Rodbell model considers the exchange constant to vary linearly with the unit cell volume, as described in the introduction. The total angular momentum, J, was calculated from saturation magnetization, M_s, measurements at 10 K up to 10 T, where $M_s = \rho_s g \mu_B J$. We have let

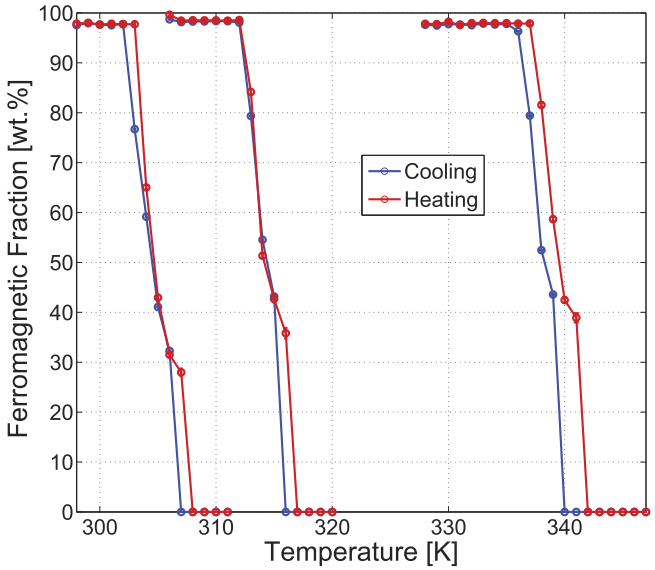

FIG. 3. FM fraction as a function of temperature determined from Rietveld refinement for the three different materials during the cooling and heating procedures.

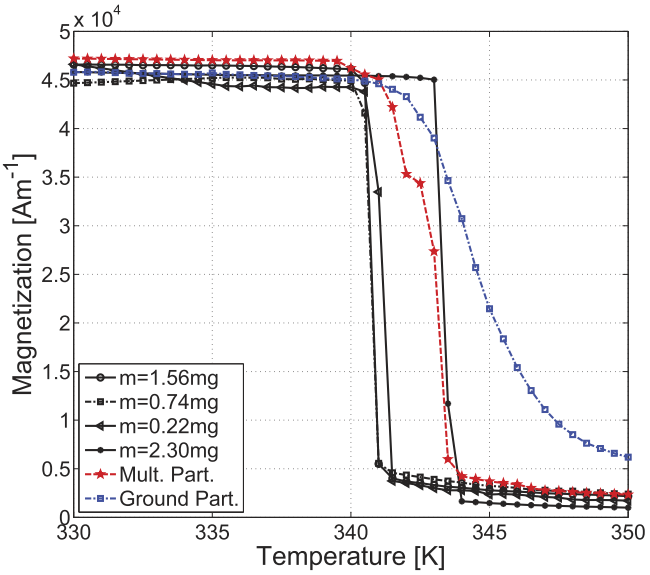

FIG. 4. Single particles and multiple particles isofield ($H_{app} = 0.01$ T) magnetization measurements, during the heating procedure.

three parameters vary: η, T_0 and $\sigma(T_0)$, where $\sigma(T_0)$ is the standard deviation of a normal distribution superimposed on T_0 to account for stoichiometric inhomogeneities.[15] Furthermore, from this normal distribution we can then calculate the FM fractions as the transition occurs. Moreover, the PM volume is constant neglecting the small thermal expansion in this temperature range. The fixed parameters were κ, J, ρ and ρ_s, with values of $3 \cdot 10^{-12}$ Pa^{-1}, 0.92, 7000 kgm^{-3} and $8.44 \cdot 10^{24}$ kg^{-1}, respectively.[9]

Figure 5 shows the unit cell volume as a function of the temperature for both the modelled and experimental results of the sample with $x = 0.25$. One may see the good agreement between the modelled and the measured data. The other compositions present as good agreement as the one shown here, and the obtained parameters are shown in Table I. One may see that the parameters are quite similar, and all materials have $\eta > 1$ i.e. they undergo a FOPT. The standard deviations are very similar as well, which is expected for a standardized materials processing technique.[16]

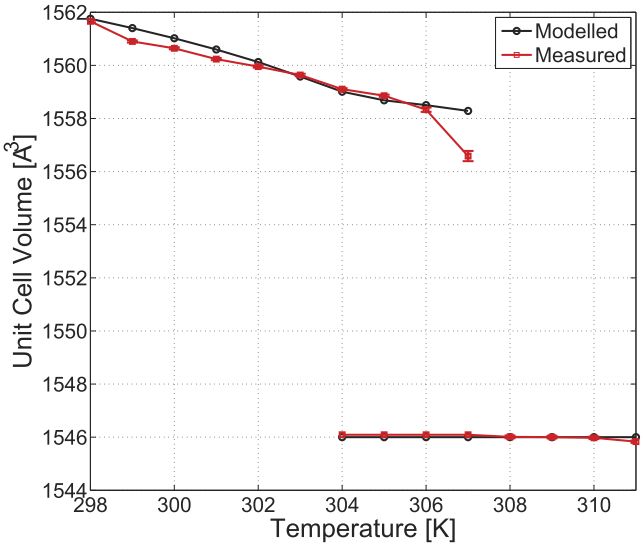

FIG. 5. Experimental and model results of volume as a function of temperature for the heating procedure of the material with $x = 0.25$.

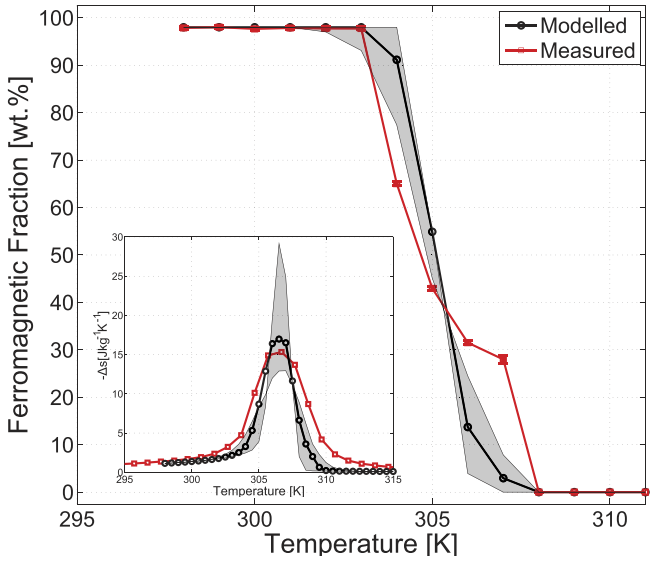

FIG. 6. Experimental and model results of FM fraction as a function of temperature for the heating procedure of the material with $x = 0.25$. The inset shows the Δs for $\mu_0 \Delta H = 1.0$ T. The shaded area in both graphs represents the region for $\sigma(T_0) \pm 0.5$ K.

Figure 6 shows the FM fraction for the composition with $x = 0.25$ during the heating procedure, comparing measurements with the modelled data. The shaded area represents a region with $\sigma(T_0) \pm 0.5$ K. The modelled results are as expected for a normally distributed function, however the measured data shows a more complex transition. Waske et al.[8] have shown that the volume change combined with microstructural features (grain boundaries arrangement) may play an important role in the transition itself. As the material transits from FM to PM, the stoichiometry distribution may lead to different T_C and therefore different parts of the sample have the transition at different temperatures. Morever the inset shows the Δs as function of the temperature for a field change of $\mu_0 \Delta H = 1.0$ T. The demagnetization factor was not considered in this case. The figure shows a good agreement between measurement and modelled data. More importantly, the results clearly shows that the distribution of T_0 has a major influence in the peak value of Δs.

IV. CONCLUSIONS

The phase transition of $La(Fe, Mn, Si)_{13}H_y$ for different compositions was evaluated by means of XRD. The results showed an increase of the unit volume volume change with decrease of x in $LaFe_{13-x-y}Mn_xSi_yH_{1.65}$. During the transition it was observed the presence of both FM and PM phases in a range of 6 K around each T_C. Magnetization measurements in single particles showed different T_C, another indication of stoichiometric distribution. Fitting the experimental data with Bean-Rodbell model indicates that all the three compositions studied presented FOPT as $\eta > 1$ for all of them.

ACKNOWLEDGMENTS

This work was financed by the ENOVHEAT project which is funded by Innovation Fund Denmark (contract no 12-132673). The authors are grateful to Vacuumschmelze GmbH for providing the samples.

[1] A. Smith, Eur. Phys. J. H **38**, 507 (2013).
[2] A. Smith, C. R. H. Bahl, R. Bjørk, K. Engelbrecht, K. K. Nielsen, and N. Pryds, Adv. Energy Mater. **2**, 1288 (2012).
[3] J. D. Moore, K. Morrison, K. G. Sandeman, M. Katter, and L. F. Cohen, Appl. Phys. Lett. **95**, 252504 (2009).

[4] V. Basso, M. Kuepferling, C. Curcio, C. Bennati, A. Barzca, M. Katter, M. Bratko, E. Lovell, J. Turcaud, and L. F. Cohen, J. Appl. Phys. **118**, 053907 (2015).
[5] K. K. Nielsen and K. Engelbrecht, J. Phys. D: Appl. Phys. **45**, 145001 (2012).
[6] A. Fujita, S. Fujieda, K. Fukamichi, H. Mitamura, and T. Goto, Phys. Rev. B **65**, 014410 (2001).
[7] J. Lyubina, R. Schäfer, N. Martin, L. Schultz, and O. Gutfleisch, Advanced Mat. **22**, 3735 (2010).
[8] A. Waske, L. Giebeler, B. Weise, A. Funk, M. Hinterstein, M. Herklotz, K. Skokov, S. Fähler, O. Gutfleisch, and J. Eckert, Phys. Status Solidi RRL **9**, 136 (2015).
[9] L. Jia, J. R. Sun, H. W. Zhang, F. X. Hu, C. Dong, and B. G. Shen, J. Phys.: Condens. Matter **18**, 9999 (2006).
[10] C. P. Bean and D. S. Rodbell, Phys. Rev. **126**, 104 (1962).
[11] D. T. Cam Thanh, E. Brück, O. Tegus, J. C. P. Klaasse, T. J. Gortenmulder, and K. H. J. Buschow, J. Appl. Phys. **99**, 08Q107 (2006).
[12] K. K. Nielsen, H. N. Bez, L. von Moos, R. Bjørk, D. Eriksen, and C. R. H. Bahl, Rev. Sci. Instrum. **86**, 103903 (2015).
[13] H. M. Rietveld, J. Appl. Cryst. **2**, 65-71 (1969).
[14] J. Liu, J. Moore, K. Skokov, M. Krautz, K. Löwe, A. Barcza, M. Katter, and O. Gutfleisch, Scr. Mater. **67**, 584 (2012).
[15] N. G. Bebenin, R. I. Zainullina, and V. V. Ustinov, J. Appl. Phys. **113**, 073907 (2013).
[16] A. Barcza, M. Katter, V. Zellmann, S. Russek, S. Jacobs, and C. Zimm, IEEE Trans. Magn. **47**, 3391 (2011).

A.1.3 Direct measurements of magnetic entropy change

Direct measurements of the magnetic entropy change

K. K. Nielsen,[a] H. N. Bez, L. von Moos, R. Bjørk, D. Eriksen, and C. R. H. Bahl
DTU Energy Conversion and Storage, Technical University of Denmark, Frederiksborgvej 399, DK-4000 Roskilde, Denmark

(Received 1 July 2015; accepted 19 September 2015; published online 6 October 2015)

An experimental device that can accurately measure the magnetic entropy change, Δs, as a function of temperature, T, and magnetic field, H, is presented. The magnetic field source is in this case a set of counter-rotating concentric Halbach-type magnets, which produce a highly homogeneous applied field with constant orientation. The field may be varied from 0 to 1.5 T in a continuous way. The temperature stability of the system is controlled to within ±10 mK and the standard range for the current setup is from 230 K to 330 K. The device is under high vacuum and we show that thermal losses to the ambient are negligible in terms of the calorimetric determination of the magnetic entropy change, while the losses cannot be ignored when correcting for the actual sample temperature. We apply the device to two different types of samples; one is commercial grade Gd, i.e., a pure second-order phase transition material, while the other is $Gd_5Si_2Ge_2$, a first order magnetic phase transition material. We demonstrate the device's ability to fully capture the thermal hysteresis of the latter sample by following appropriate thermal resetting scheme and magnetic resetting scheme. © *2015 AIP Publishing LLC.* [http://dx.doi.org/10.1063/1.4932308]

I. INTRODUCTION

Reliable experimental determination of the magnetocaloric effect (MCE) is crucial for understanding magnetocaloric materials (MCMs), evaluating their possible performance as active refrigerants in a magnetic cooling/heating device and for accurate numerical modeling of active magnetic regenerators (AMR).[1] The key properties associated with the MCE are the absolute entropy, $s(T,H)$, and magnetization, $M(T,H)$, both as a function of temperature, T, and magnetic field, H. From the absolute entropy, it is possible to derive the specific heat $c(T,H) = T\,\frac{\partial s}{\partial T}\big|_H$. Obtaining $s(T,H)$ may be done by integrating specific heat measured as a function of T and H or by combining $c(T,H=0)$ with the magnetic entropy change, $\Delta s(T,H)$.

The magnetic entropy change may be found indirectly by applying a Maxwell relation $\partial s/\partial H = \mu_0 \partial M/\partial T$ where μ_0 is the vacuum permeability. It is, however, also possible to measure $\Delta s(T,H)$ in a direct manner using calorimetry.[2,3] This is advantageous as magnetization data usually have low thermal resolution, which will result in a smearing of data when numerical differentiation is performed. Temperature control is usually also more stable in the direct measurement as opposed to in a Vibrating Sample Magnetometer (VSM) where inevitably the gas temperature has to be adjusted continuously thus leading to fluctuations. In the direct measurement equipment, a relatively large thermal reservoir dampens fluctuations to a small level.

In this paper, we describe an experimental setup that has been realized at the Technical University of Denmark for direct measurements of Δs, which is applied to measure a MCM with a first order magnetic phase transition ($Gd_5Si_2Ge_2$) and one with a second order transition (Gd). Through appropriate thermal and magnetic resettings of the sample, we demonstrate the ability of the device to probe and capture the hysteretic behavior of $Gd_5Si_2Ge_2$. Our device resembles that of Ref. 2 with the addition that our device has a fully automated systematic resetting capability (both thermal and magnetic resets). Our magnetic field source is furthermore made of permanent magnets rather than an electromagnet and the field change from zero to max (1.5 T) field can be achieved in a continuous way.

II. EXPERIMENTAL SETUP

A schematic of the experimental setup is shown in Fig. 1. The sample is placed on one of two small (3.25×4.88 mm^2) identical Peltier-cells (Optotec OT08), which are glued to a cold finger made of copper. A larger Peltier cell (TEC1-12714S) is located at the bottom of the cold finger. On one side it is connected with thermal grease to the cold finger and on the other side to a heat exchanger, which in turn has a continuous flow of a chilled fluid from an external temperature control bath (Julabo CF40 Cryo-Compact Circulator). By regulating the magnitude and direction of the current through the large Peltier cell, as well as the temperature of the chiller fluid, it is possible to control the temperature of the cold finger. Copper was chosen for its excellent thermal properties (high conductivity and large thermal mass) and because it is diamagnetic.

The temperature range of the system is from 230 K to 330 K. The temperature of the system is measured in two places by Pt-100 resistance thermometers. One at the bottom of the cold finger and one in the top (number 4 in Fig. 1) very close to the Peltier cells. Here, a Hall-probe (Arepoc HHP-NU), number 3 in Fig. 1, for measuring the magnetic field is also installed.

[a]kaki@dtu.dk

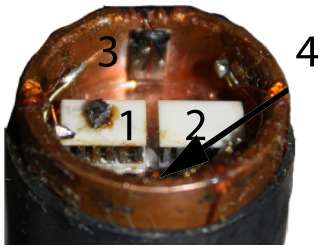

FIG. 1. Picture of the top of the cold finger. The numbers indicate the various components: 1 and 2 are the Peltier elements, 3 is the Hall probe magnetic field sensor, and 4 is the Pt-100 thermo-element. The diameter of the disk is 20 mm.

The cold-finger is situated in a vacuum chamber connected to a turbo-pump, giving a typical operational pressure of approximately 3×10^{-6} mbar. The larger heater Peltier cell is controlled via a power supply unit controlled by a PC. A PID control program implemented in LabView and using the temperature measured by the bottom temperature sensor as the process parameter, controls the current delivered to the Peltier cell and thus the temperature of the cold-finger. The voltage measurements are done using a Keithley 2700 Digital MultiMeter with a 20 channel Keithley 7700 board except for the Hall-probe, which is measured with a USB2AD DAQ module from Arepoc.[4]

The magnetic field applied to the setup is provided by a rotating Halbach cylinder permanent magnet configuration. This exact permanent magnet assembly is described in detail elsewhere.[5] The generated magnetic field is controlled by counter-rotating two concentric Halbach cylinders with equal angular velocity magnitude. Consequently, the direction of the field in the sample chamber is constant. The two Halbach cylinders are mechanically counter-rotated by the setup shown in Figure 2(a). A Powerpac stepper motor (N33HRLJ-LNK-NS-00) with a Technosoft controller (IDM240-5EI) is used for turning a pinion connected with two bevel gears of equal diameters, one fixed to the inner magnet, the other to the outer magnet. The gears and thus the magnets are supported on the outside by HEPCO bearings. The field as a function of the angle between the magnets is shown in Fig. 2(b). As can clearly be seen from the figure, the field can be adjusted from 0 to 1.5 T continuously.

Normally, the field is varied at 0.05 T/s. Tests were done using an aluminum dummy sample to detect any eddy current induced, but within the noise of the signal nothing was observed.

A. Measurement of magnetic entropy change

A temperature difference, ΔT, between the top and bottom of one of the Peltier cells on the cold finger will result in a voltage signal, U, due to the Seebeck effect,

$$U = -S\Delta T, \tag{1}$$

with the Seebeck coefficient, S, being specific for the Peltier cells and generally varying as a function of temperature. The heat flux corresponding to the temperature difference is

$$\dot{Q} = \kappa\Delta T = -\frac{\kappa}{S}\Delta U, \tag{2}$$

with the conductance of the Peltier cell $\kappa = 1/R$. R is found as $R = \Delta T_{\max}/\dot{Q}_{\max} = 67\ \text{K}/0.6\ \text{W} = 112\ \text{KW}^{-1}$. This is, however, merely stated at room temperature. Here, the differential signal is used, i.e., the difference in signal between the Peltier cell with a sample on it and the empty Peltier cell ($\Delta U = U_{\text{sample}} - U_{\text{empty}}$).

For measurements of the magnetic entropy change the system is at a fixed temperature and the applied magnetic field is varied from a starting value, H_0, to a final value, H_1. The response of the difference in voltage signal of the two Peltier cells (see Fig. 3(a), for an example) is then integrated in time, which yields

$$\Delta s(T, H_0, H_1) = \frac{q}{T} = \frac{Q}{Tm_s} = \frac{\kappa}{STm_s}\int_{t_0}^{t_1} \Delta U \mathrm{d}t, \tag{3}$$

where the mass of the sample is denoted m_s. The voltage signal is integrated in time, t, from the start of the signal t_0 to the time t_1 where the voltage difference has returned to zero. The change in heat per mass is q while the total change in heat of the sample is Q. The value $\Delta s(T, H_0, H_1)$ is thus the magnetic entropy change upon the field change from H_0 to H_1 at the temperature T.

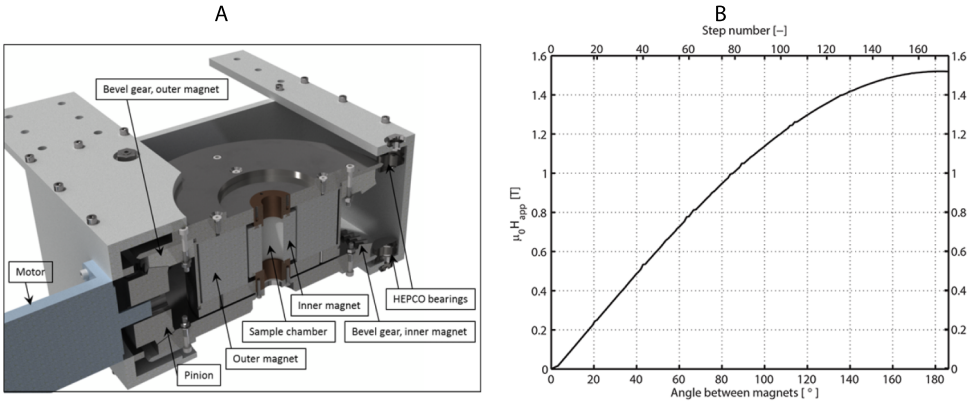

FIG. 2. (a) Cross-sectional view of the mechanical setup for support and counter-rotation of the concentric Halbach magnets. (b) The generated magnetic field as a function of the angle of rotation between the two concentric Halbach cylinders. Note that when the angle between the magnets is changed from zero to 180° this corresponds to a rotation of each magnet of 90°.

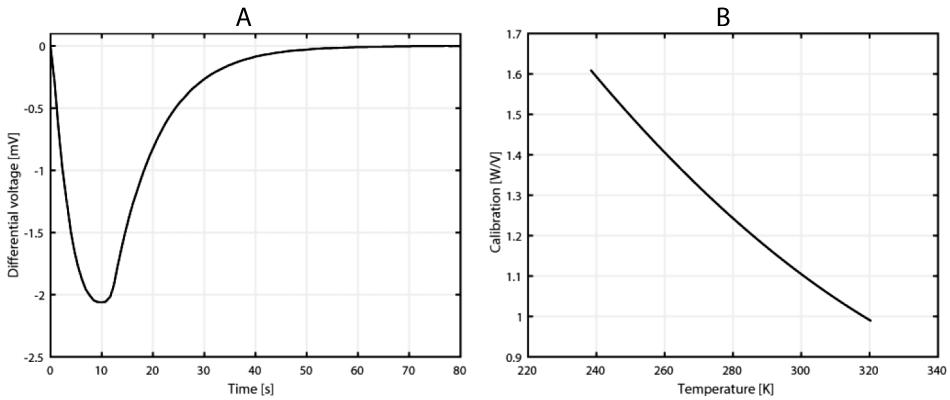

FIG. 3. (a) The differential voltage signal as a function of time of a 38.9 mg sample of commercial grade Gd. The applied field is changed from 0.01 T to 1.26 T with a ramp rate of 0.1 T/s. The time axis is zero at the time t_0. (b) The calibration of the Peltier signal (κ/S in Eq. (4)) from a measurement of a pure Cu sample.

B. Calibration

In order to obtain a proper conversion from the Peltier voltage signal to a heat flux, the signals must be calibrated. One method for calibrating the system is to use a sample with a known heat capacity, e.g., pure Cu.[6] For temperature values outside the range given in Ref. 6, i.e., from 300 K to 320 K, the values are linearly extrapolated. Assuming a constant temperature rate $\dot{T}$ (i.e., the system is set to ramp the temperature), one obtains

$$\begin{aligned} \dot{Q} &= c_{\text{ref}} m_{\text{ref}} \dot{T} \Rightarrow \\ \frac{\kappa}{S} &= -\frac{c_{\text{ref}} m_{\text{ref}} \dot{T}}{\Delta U}, \end{aligned} \tag{4}$$

where the mass of the reference Cu sample is denoted m_{ref} and the specific heat of the reference sample is c_{ref}. The calibration is plotted in Fig. 3(b).

As the sample temperature is not directly measured it is necessary to estimate the temperature difference between the sample on top of the Peltier cell and the Pt-100 element below it. It is assumed that the thermal resistance of the Cu is negligible and that it is $R = 112\ \text{KW}^{-1}$ for the measurement Peltier cell, as found above. Furthermore, the high-vacuum effectively means that the only mechanism for losses from the sample to the ambient is through radiation, i.e.,

$$\dot{Q}_{\text{loss}} = \alpha A_s \left(T_{\text{amb}}^4 - T_s^4\right), \tag{5}$$

where α is Stefan-Boltzmann's constant, A_s the radiating surface area of the sample, T_{amb} the ambient temperature, and T_s the sample temperature. Here, the emissivity of the sample is assumed to be 1. In steady-state the heat loss from the sample must be matched by the temperature difference between the sample and the top of the Cu cold finger, i.e.,

$$\Delta T_s = T_s - T_{\text{Cu}} = \dot{Q}_{\text{loss}} R. \tag{6}$$

Combining Eqs. (5) and (6) results in a fourth order polynomial in T_s, where the roots are easily found numerically.

Since the system is not completely symmetric, the temperature difference between sample and the Cu cold finger was also found through a 3D model in Comsol multiphysics with radiation losses enabled. Figure 4 shows the difference in temperature between the sample and the cold finger as a function of the cold finger temperature for various ambient temperatures. The simple model, represented by Eqs. (5)-(6), is seen to adequately catch the temperature difference compared to the more detailed Comsol model within 0.2 K. It is thus straight-forward to adjust for the thermal resistance between the Pt-100 element and the sample in order to obtain the correct sample temperature.

C. Measurement uncertainties

In order to evaluate the total measurement error the following assumptions are made:

1. Uncertainties in measurement of the magnetic field and time are negligible.
2. Possible co-variance is ignored.

The total error in the magnetic entropy change can be found by considering Equation (3). This equation can be split into two parts: the integral part, $\Delta U(t)$, and the calibration part, $(C = \kappa/(STm_s))$. The total error is given by

$$\left(\frac{\sigma(\Delta s)}{|(\Delta s)|}\right)^2 = \left(\frac{\sigma(C)}{|C|}\right)^2 + \left(\frac{\sigma(A)}{|A|}\right)^2, \tag{7}$$

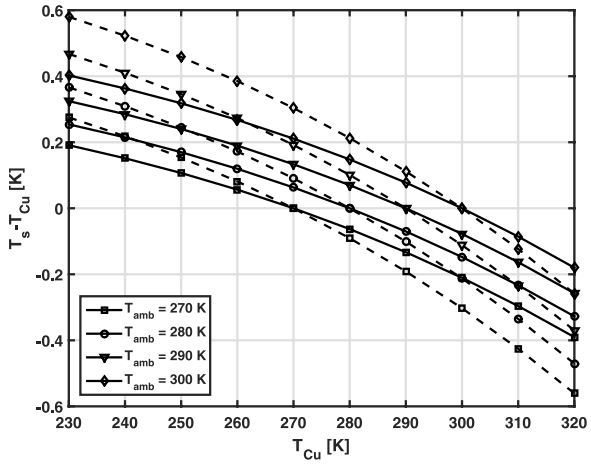

FIG. 4. Temperature difference between sample and Cu cold finger as a function of the cold finger temperature for different ambient temperatures. Solid lines are based on Eq. (6) while dashed lines are based on a detailed 3D model of the system solved using Comsol Multiphysics. The sample area is assumed equal to the Peltier surface area, $A_s = 15.86\ \text{mm}^2$.

where the first term on the right hand side is the relative error of the calibration term, while the second term is the relative error of the integral part.

The relative error sum for the calibration term is given by

$$\frac{\sigma(C)}{|C|} = \sqrt{\left(\frac{\sigma(c_{\mathrm{ref}})}{|c_{\mathrm{ref}}|}\right)^2 + \left(\frac{\sigma(m_{\mathrm{ref}})}{|m_{\mathrm{ref}}|}\right)^2 + \left(\frac{\sigma(\dot{T})}{|\dot{T}|}\right)^2 + \left(\frac{\sigma(T)}{|T|}\right)^2 + \left(\frac{\sigma(m_{\mathrm{s}})}{|m_{\mathrm{s}}|}\right)^2}. \tag{8}$$

The standard deviation of the voltage difference ($\sigma(\Delta U)$) was calculated based on the steady-state voltage difference signal. Over the applicable temperature range the standard deviation of the voltage difference was found not to be a function of temperature. The standard deviation of the integral $A(T,t) = \int \Delta U dt$ is found through

$$\sigma(A(T)) = \left(\sum_{n=1}^{N}\left[(\Delta t_n)^2(\sigma(\Delta U(T)))^2\right]\right)^{1/2}, \tag{9}$$

where the sum is over N datapoints and Δt_n is the difference in time between two adjacent datapoints. Figure 5 shows the two main relative uncertainties that comprise the uncertainty of Δs. It is observed that the relative error in the integral part (Fig. 5(a)) is small compared to the calibration part (Fig. 5(b)). Furthermore, it is seen that for $T \gg T_{\mathrm{C}}$ and $T \ll T_{\mathrm{C}}$ the error of the integral term increases. This behaviour is due to the fact that at T_{C} the area of $\Delta U(t)$ peak is relatively bigger than at other temperatures. Finally, the relative error of the calibration term decreases as the temperature increases due to the increasing voltage difference with temperature. Figure 6 shows the magnetic entropy change of Gd as a function of temperature for an applied field change of 1.0 T with the associated errorbars calculated from Eq. (7).

Pecharsky and Gschneidner Jr.[7] systematically calculated the error propagation on Δs based on c_p and magnetization data. It was shown that for Gd the errors at 5 T can be between 20%-30% for both methods, which is significantly higher than the 7.5% (with a $\mu_0 \Delta H = 1.0\,\mathrm{T}$) in the equipment presented here. It is noted that this error will decrease further as the field change is increased.

III. EXAMPLES OF ENTROPY MEASUREMENTS

A polycrystalline commercial grade Gd sample (38.9 mg, $0.9 \times 2.3 \times 2.9$ mm^3) was mounted on the measurement Peltier cell and measured in the temperature range from 275 K to 315 K. At each temperature the sample was measured in 5 different applied fields, in the range from 0.18 T to 1.50 T, by applying the first field, removing it again and then applying the second field, etc. For each field application, a signal similar to that in Fig. 3(a) is measured and integrated to give the magnetic entropy change for the current temperature and field change, using Eq. (3). The results of the measurements are shown in Fig. 7, where they are compared to measurements done on the same sample, using a LakeShore 7407 VSM to obtain the magnetic entropy change indirectly through the Maxwell relation.[8] The same orientation of the sample in the two measurements with respect to the applied field was prohibited by the sample geometry. In order to make a proper correction for the differing demagnetizing fields in the two cases the following procedure was followed: The average internal field in the sample while measuring in the VSM, H_{VSM}, was found as a function of temperature and applied field using the appropriate demagnetization factor ($N_{\mathrm{VSM}} = 0.18$, assuming a rectangular sample[9]), i.e., through the direct calculation $H_{\mathrm{VSM}} = H_{\mathrm{app,VSM}} - N_{\mathrm{VSM}}M$. This directly gives the average magnetization, M, of the sample as a function of temperature and internal field. In order to find the internal field in the calorimetric measurements, $H_{\Delta s}$, the average demagnetization factor $N_{\Delta s} = 0.26$ (again assuming a rectangular prism[9]) was used in $H_{\Delta s} = H_{\mathrm{app},\Delta s} - N_{\Delta s}M$, which is solved iteratively using M from the VSM measurements. For each applied field in the calorimeter the internal field in the sample is thus found as a function of temperature. Finally, this field is used to

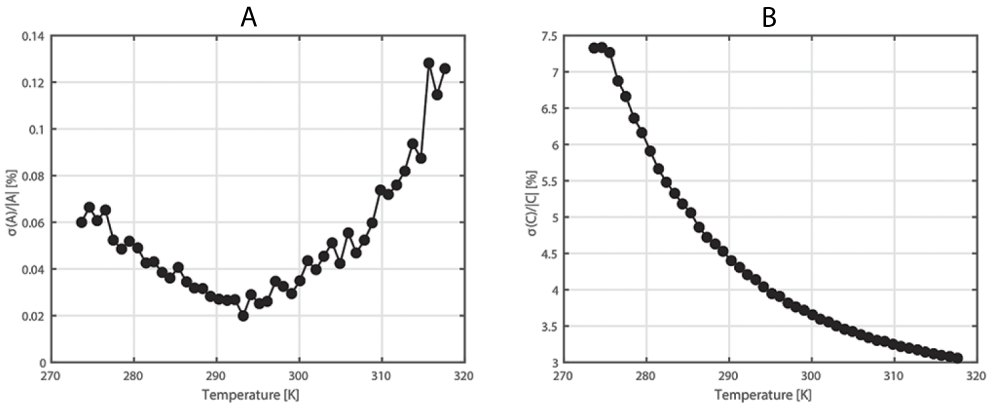

FIG. 5. (a) The relative standard deviation of the integral term. (b) The calibration term as a function of temperature. A minimum in $\sigma(A)/|A|$ at $T_{\mathrm{C}} \approx 292$ K region is seen.

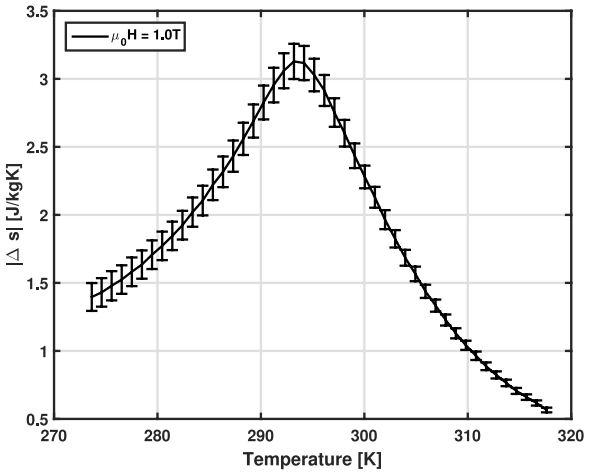

FIG. 6. Magnetic entropy change of Gd, for $\mu_0 \Delta H_{app} = 1.0$ T, as a function of temperature and the associated error of the measurement. Note that the field considered is the applied magnetic field.

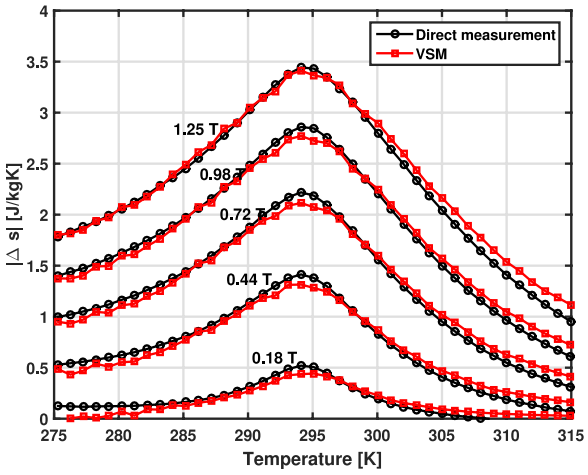

FIG. 7. The magnetic entropy change of Gd found using the appropriate Maxwell relation on VSM magnetization data and through the direct calorimetric approach described in this paper. The applied magnetic fields of the direct measurements are indicated in the figure. The VSM data have been interpolated in order to correct for demagnetization according to the method described in the text. The mass of the sample was 38.9 mg.

interpolate in the calculated entropy change data from the VSM measurements. The magnetic entropy change is given as a function of temperature for various applied fields (in the calorimeter) while the VSM data have been interpolated as described above so that the two sets of measurements have the same internal field in each data point. The direct method for measuring the entropy change agrees quite well with the results from the indirect conventional approach, although with a slight tendency for the direct measurements to produce a sharper peak. This may in part be explained from the fact that the VSM-based entropy change data is calculated through the temperature-derivative of the magnetization, which in turn will tend to round the peak slightly. Still, both results are inside each others uncertainties.

A. Thermal resetting and hysteresis measurements

Both thermal and magnetic hystereses are present to some degree in MCMs with a first order transition. In order to measure this accurately it is crucial to be able to accurately control the state and history of the sample. One way to do this is to reset the sample between each measurement. This means that after temperature equilibration and subsequent magnetization the sample is cooled or heated to a temperature outside the hysteresis region. The excellent temperature and magnetic field control offered by the experimental setup described here enables hysteresis measurements to be done in an automated, efficient, and accurate way. Specifically it is important to note that the instrument does not overshoot when changing the temperature or field. Such overshooting is quite common in measurement devices, such as VSMs, and will make the characterisation and interpretation of hysteresis difficult. The average thermal equilibrium time for stabilizing at a given temperature is approximately four minutes.

The experiment can be set to automatically do a thermal reset by going sufficiently above or below T_C between each measurement. If the sample is not reset it may enter a metastable state.[10] A polycrystalline bulk sample of the well known and highly hysteretic magnetocaloric material $Gd_5Si_2Ge_2$, with T_C around 272 K, provided by Ames Laboratory, was measured in five different protocols applied to each temperature point:

1. No reset and field change from 0 to 1.5 T (called "Non-equilibrium" in Fig. 8).

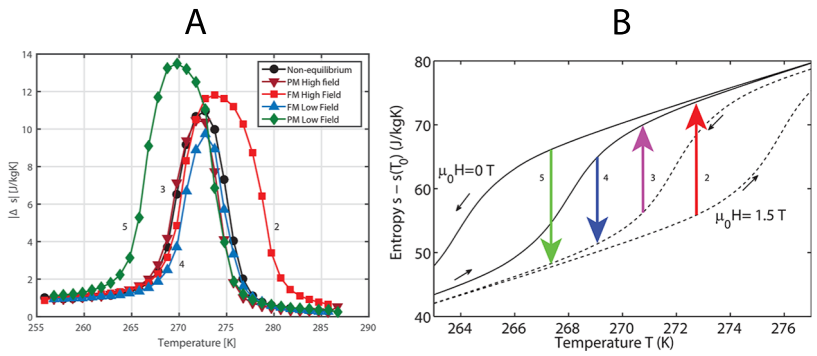

FIG. 8. (a) The magnetic entropy change as a function of temperature for the polycrystalline sample $Gd_5Si_2Ge_2$ under an applied field change from zero to 1.5 T. The sample was measured under five different conditions as described in the text. (b) The entropy diagram derived from specific heat data (see Ref. 11). The arrows indicate the different experiment modes (at random temperatures). The curves/arrows in the two figures are numbered according to the definitions in the text. The mass of the sample was 10.2 mg.

2. Ferromagnetic reset (at $T = 233$ K) and field change from 1.5 to 0 T (called "FM High Field" in Fig. 8).
3. Paramagnetic reset (at $T = 293$ K) and field change from 1.5 to 0 T (called "PM High Field" in Fig. 8).
4. Ferromagnetic reset (at $T = 233$ K) and field change from 0 to 1.5 T (called "FM Low Field" in Fig. 8).
5. Paramagnetic reset (at $T = 293$ K) and field change from 0 to 1.5 T (called "PM Low Field" in Fig. 8).

The non-equilibrium, ferromagnetic low to high field and paramagnetic high to low field data align fairly well, while the ferromagnetic high to low field and paramagnetic low to high field are significantly different. This is expected due to the hysteresis of the sample (see, e.g., Ref. 11 for details). Figure 8(b) conceptually shows how the different curves appear. Once a magnetization has been done the sample is considered in a non-equilibrium state and in order to accurately predict the outcome of successive magnetizations / demagnetizations without a thermal reset, modeling is needed.[11] It is debatable whether the first measurement after a given resetting procedure results in the magnetic entropy change only. As we have shown, subsequent (de-) magnetizations result in self-consistent data. However, the external driving mechanism for the experiment is a change in applied magnetic field and from that perspective the resulting measurement is the magnetic entropy change.

IV. CONCLUSION

A custom device for direct measurement of the magnetic entropy change was presented and examples of measurements of two different types of samples were shown. The measurements agree well with data obtained through conventional magnetization measurements. Also, the thermal hysteresis in materials with a first order transition can be full characterized due to the feature of thermal resetting available in the device. The high accuracy with which the temperature and applied field can be controlled and the fact that losses to the ambient are virtually negligible (in terms of the calorimetry; they have to be taken into account when determining the sample temperature) enables high resolution and accuracy measurements.

ACKNOWLEDGMENTS

This work was in part financed by the ENOVHEAT project which is funded by Innovation Fund Denmark (Contract No. 12-132673). We also thank Professor K. A. Gschneidner, Jr. and Professor V. Pecharsky from Ames Laboratory for providing the $Gd_5Si_2Ge_2$ sample.

[1]K. K. Nielsen, J. Tusek, K. Engelbrecht, S. Schopfer, A. Kitanovski, C. R. H. Bahl, A. Smith, N. Pryds, and A. Poredos, "Review on numerical modeling of active magnetic regenerators for room temperature applications," Int. J. Refrig. **34**, 603–616 (2011).

[2]V. Basso, C. P. Sasso, and M. Küpferling, "A Peltier cells differential calorimeter with kinetic correction for the measurement of c(p)(H, T) and Delta s(H, T) of magnetocaloric materials," Rev. Sci. Instrum. **81**, 113904 (2010).

[3]M. Kuepferling, C. P. Sasso, V. Basso, and L. Giudici, "An isothermal Peltier cell calorimeter for measuring the magnetocaloric effect," IEEE Trans. Magn. **43**, 2764–2766 (2007).

[4]See www.arepoc.sk for Arepoc s.r.o., Bratislava, Slovakia.

[5]R. Bjørk, C. R. H. Bahl, A. Smith, and N. Pryds, "Comparison of adjustable permanent magnetic field sources," J. Magn. Magn. Mater. **322**, 3664–3671 (2010).

[6]G. T. Furukawa, W. G. Saba, and M. L. Reilly, "Critical analysis of the heat capacity data of the literature and evaluation of thermodynamic properties of copper, silver and gold from 0 to 300 k," NIST Technical Report No. 18, 1968.

[7]V. K. Pecharsky and K. A. Gschneidner, Jr., "Magnetocaloric effect from indirect measurements: Magnetization and heat capacity," J. Appl. Phys. **86**, 565–575 (1999).

[8]R. Bjørk, C. R. H. Bahl, and M. Katter, "Magnetocaloric properties of $LaFe_{13-x-y}Co_xSi_y$ and commercial grade Gd," J. Magn. Magn. Mater. **322**, 3882–3888 (2010).

[9]A. Aharoni, "Demagnetizing factors for rectangular ferromagnetic prisms," J. Appl. Phys. **83**, 3432–3434 (1998).

[10]L. Caron, Z. Q. Ou, T. T. Nguyen, D. T. C. Thanh, O. Tegus, and E. Brück, "On the determination of the magnetic entropy change in materials with first-order transitions," J. Magn. Magn. Mater. **321**, 3559–3566 (2009).

[11]L. von Moos, C. Bahl, K. Nielsen, and K. Engelbrecht, "The influence of hysteresis on the determination of the magnetocaloric effect in $Gd_5Si_2Ge_2$," J. Phys. D: Appl. Phys. **48**(2), 025005 (2015).

A.1.4 Influence of manganite powder grain size and Ag-particle coating on the magnetocaloric effect and the active magnetic regenerator performance

Acta Materialia 97 (2015) 413–418

Contents lists available at ScienceDirect

Acta Materialia

journal homepage: www.elsevier.com/locate/actamat

Influence of manganite powder grain size and Ag-particle coating on the magnetocaloric effect and the active magnetic regenerator performance

J.A. Turcaud [a,*], H.N. Bez [b], E. Ruiz-Trejo [c], C.R.H. Bahl [b], K.K. Nielsen [b], A. Smith [b], L.F. Cohen [a]

[a] Department of Physics, Blackett Laboratory, Imperial College London, SW7 2AZ London, UK
[b] Department of Energy Conversion and Storage, Technical University of Denmark, Frederiksborgvej 399, DK-4000 Roskilde, Denmark
[c] Department of Earth Science and Engineering, Imperial College London, SW7 2AZ London, UK

ARTICLE INFO

Article history:
Received 28 April 2015
Revised 24 June 2015
Accepted 26 June 2015
Available online 16 July 2015

Keywords:
Magnetocalorics
Active magnetic regenerators
SEM
XRD
Microstructuring
Nanostructuring

ABSTRACT

The magnetocaloric performance of $La_{0.67}Ca_{0.27}Sr_{0.06}Mn_{1.05}O_3$ is investigated as a function of the powder grain size and also as a function of decoration of grains with highly conductive silver particulates as a coating layer. We demonstrate that the thermal and electrical conductivities can be significantly modified by the Ag-particle coating when the material is examined in sintered pellet form and we compare results with a second manganite composition $La_{0.67}Ca_{0.33}MnO_3$ with significantly smaller grain size. However, we find that this microstructural engineering does not improve the performance of the active magnetic regenerator cycle using the silver decorated material in powder form. The regenerator performance is improved by the reduction of the powder grain size of the refrigerant which we attribute to improved thermal management due to increased surface to volume ratio.

1. Introduction

Magnetic refrigeration has been considered to be a candidate mechanism for efficient and environmentally friendly solid state cooling for almost 40 years [1]. It relies on the magnetocaloric effect (MCE), defined as the adiabatic change in temperature ΔT_{ad} of a material caused by application of a magnetic field. Material advances over the last 15 years have brought this technology closer to realisation [2,3], principally through the discovery of materials with large changes of entropy at a first order magnetic phase transition, the temperature of which can be sufficiently manipulated by an applied magnetic field [4].

The construction of a magnetic cooling engine requires that the refrigerant exchanges heat efficiently using a fluid blow upon magnetisation and demagnetisation. The availability of at least four magnetic refrigerant families (Gd-, Fe_2P-, La(Fe, Si)$_{13}$- and manganite-based) for prototype cooling engines has driven a recent increase in the study of refrigerant properties beyond the more-usually studied adiabatic temperature change and field-induced entropy change [5,6]. The properties studied include: magnetic hysteresis [7], corrosion resistance [8] and thermal conductivity (κ) [9].

Thermal conductivity plays an important role in the cooling efficiency of the active magnetic regenerator (AMR) cycle. A recent simulation suggested optimal values of κ, between 7 and 10 W m^{-1} K^{-1}, depending on the working frequency and the geometry of the AMR [10].

The present study is driven primarily by the need to improve the understanding of the influence of microstructure and thermal conductivity on performance of magnetocaloric materials in operating conditions. This study is also motivated to reduce the extrinsic magnetic [11] and thermal [12,13] hysteresis that can arise due to low κ and/or large parasitic thermal resistance during laboratory scale measurement and indeed during operation in the AMR cycle. Material processing, such as in powder compaction into pellets, can lead to reduction of thermal conductivity relative to bulk values, especially in metallic materials. Control over κ is desirable and as the magnetocaloric topic matures, κ is a property of increasing importance.

In La(Fe, Si)$_{13}$-based alloys, where if anything κ is on the high side because they are intermetallic alloys, it has been shown that κ of a compressed powder sample can be about 5 times smaller than the bulk material. This reduced value can be subsequently

* Corresponding author.
E-mail address: jeremy.turcaud08@imperial.ac.uk (J.A. Turcaud).

http://dx.doi.org/10.1016/j.actamat.2015.06.058
1359-6454/

enhanced up to a factor of three by the introduction of a secondary copper phase, electrodeposited on the grains [14].

Previously we have pioneered the engineering of κ in $La_{0.67}Ca_{0.33}MnO_{3\pm\delta}$ (LCMO) by impregnation of silver through open pores in low density sintered pellets. Silver was introduced by placing the pellets into a melt of $AgNO_3$ at 573 K for a fixed amount of time, followed by the annealing at 773 K in air for 10 h to decompose silver nitrate into metallic silver. The results were compelling, showing a threefold increase in κ using this route to produce silver impregnation [9]. However the method is reliant upon the distribution of open pores, which varies from sample to sample and on the production of porous samples containing closed pores which then simply represent a wasted volume. Hence we were motivated to find more reliable routes to achieve similar properties.

Recently a method based on the Tollens' reaction [15] was reported and used successfully to produce a dense and low-metal content composite of silver and Sm doped ceria. As well as exploration of this new method for improvements of grain boundary properties in sintered pellets, we also wanted to establish whether silver coating was of benefit to the AMR cycle when the samples were in powder form.

$La_{0.67}(Ca_xSr_{0.33-x})Mn_{1+\chi}O_{3\pm\delta}$ is one of the manganite material families considered for application as a magnetic refrigerant at room temperature [24,25] At $x = 0.33$, it exhibits what is generally believed to be a first order transition from a paramagnetic insulator to a ferromagnetic metal, with a Curie temperature, T_C, close to 267 K. Although the isothermal entropy change and ΔT_{ad} found so far are modest [4], the material has some advantageous features, principally its low cost, ease of processing, and manufacturability. As shown in Table 1, the reported thermal conductivity of virgin manganites is rather low, ranging between 1 W m^{-1} K^{-1} [9] and 2 W m^{-1} K^{-1} [9,20], in comparison with other magnetocaloric materials. Here we examine the influence on κ when adding a highly conductive phase to the interior of $La_{0.67}Ca_{0.27}Sr_{0.06}Mn_{1.05}O_3$ (LCSMO) pellets.

We have previously evaluated a LCSMO graded parallel plate regenerator in a reciprocal AMR device [26]. In this device [27], it is possible to quantitatively evaluate how the material would perform as a refrigerant. It was shown that, despite exhibiting modest magnetocaloric properties, a temperature span of 9.3 K was obtained between the hot and cold reservoirs for this LCSMO regenerator. Considering that the technology benchmark material, Gd, obtained a 10.2 K temperature span in the same device [27], the LCSMO family might compete evenly with Gd, especially if one manages to increase the thermal conductivity of it.

In the present study we compare the magnetocaloric performance of LCSMO particles that have been coated with silver against virgin ones using the device of Ref. [27].

Table 1
Reported values of thermal conductivity at room temperature for different types of magnetocaloric materials.

Material	Reported κ (W m^{-1} K^{-1})	References
$La_{0.7}Sr_{0.3-x}Ag_xMnO_3$	0.9–1.2	[16]
$La_{1-x}Ag_xMnO_3$	1–1.3	[17]
$Pr_{0.55}Na_{0.05}Sr_{0.4}MnO_3$	1.5	[18]
$Pr_{0.6}Sr_{0.4}MnO_3$	1.75	[18]
$La_{0.67}Ca_{0.33}MnO_{3\pm\delta}$	1–2	[9,19,21]
MnAs alloys	2	[21]
LCMO Ag-impregnated	2.5	[9]
$Ce_5Ni_2Si_3$	3.6	[22]
$Gd_5Si_2Ge_2$	5	[21]
La $(Fe_{0.88}Si_{0.12})_{13}$	9	[21]
$Gd_{0.18}Dy_{0.82}$	~10	[23]
Gd	10–11	[21,23]

2. Experimental details

$La_{0.67}Ca_{0.27}Sr_{0.06}Mn_{1.05}O_3$ powders were prepared by spray pyrolysis. Each of these powders was calcined at 1273 K for 2 h and suspended in a slurry before being tape casted into flat plates, as described by Bulatova et al. [28] The plates were crushed down to polycrystalline particles which were sieved into two batches of different particle size, 200–300 μm (small) and 300–500 μm (large). We also compare the properties with a second composition $La_{0.67}Ca_{0.33}MnO_3$ (LCMO) where powders were synthesized by glycine nitrate process (GNP) with small and uniform resulting particle size (~1 μm).

A portion of large particle LCSMO sample and the LCMO were coated with Ag. The technique used here is based on the Tollens' reaction which was recently used to manufacture metal ceramic composites [15,29]. The manganite particles were suspended in a solution of $AgNO_3$ and concentrated KOH that was subsequently cleared with a few drops of NH_4OH. Silver precipitated and coated any available surface, in particular the surface of the manganite particles, after introducing dropwise a diluted solution of a reducing agent (dextrose). The precipitate was then rinsed. All remaining salts were removed from the mixture by passing it through centrifugation at 4000 rounds per minute for 15 min, and removing the basic liquid, replacing it with deionized water. This purification step was repeated 5 times to ensure that no aqueous ammonia was present in the solution. Remaining water was finally evaporated.

Structural and phase purity was determined by XRD using a Bruker D2 diffractometer. A FEG-SEM Gemini 1525 scanning electron microscope (SEM) was used to image the samples.

Then cylindrical test pellets of 3 mm thickness and 7 mm diameter were pressed at 100 MPa for 1 min and sintered at 1573 K for 2 h. These sintering conditions are commonly used to get pellets ready for magnetisation and thermal transport measurements. It thus gave us a comparative study between virgin, small and large particle size, and Ag particle coated pellets. Achieved densities were 68%, 70%, 68%, 77% and 85% for LCSMO small, LCSMO large, LCSMO Ag-particle coated, LCMO virgin and LCMO Ag-particle coated pellets, respectively. Original particle shape and size were still clearly visible by eye at the pellet surfaces after sintering, for LCSMO sample only. Grain sizes inside the pellets are of the same order as the size of the particles they are made of.

Magnetization was measured using a 9 T Quantum Design Physical Property Measurement System (PPMS) fitted with a Vibrating Sample Magnetometer (VSM) option. Thermal conductivity and resistivity were continuously measured under a 0.5 K min^{-1} cooling rate using a Thermal Transport Option (TTO) mounted on the PPMS.

The regenerator performances of LCSMO small, LCSMO large and LCSMO Ag-particle coated were evaluated in a reciprocal AMR device. LCMO particles were too fine-grained to be used here, therefore they were not tested. The particles were placed inside a powder bed. The regenerator was taken into and out of a 1.1 T static magnetic field while deionized water was pushed in and out of the regenerator by a piston. The ambient temperature was controlled by placing the device inside a commercial refrigerator, and the hot end temperature, T_{hot}, was fixed at the controlled refrigerator's ambient temperature by a heat exchanger. After typically several hundred cycles, a steady state was reached and temperatures stabilized at both ends. The temperature was measured at both the cold and hot ends of the regenerator, allowing us to determine the temperature span, ΔT_{span}, as the difference between the hot and cold end. The total mass of each regenerator was about 43 gm. Their average bulk porosities were 65–67% and the regenerators were 33 mm long with a diameter of 28 mm.

3. Bulk properties

A single phase orthorhombic perovskite structure (space group: *Pnma*) with the lattice parameters $a = 5.461(1)$ Å, $b = 7.731(1)$ Å, $c = 5.485(1)$ Å was revealed by Rietveld refinement of XRD data in the two types of virgin pellets. The Ag-particle coated sample shows peaks (Fig. 1) from the cubic closed-packed silver phase (space group: *Fm-3m*) with cell parameter $a = 4.087(1)$ Å, consistent with that of bulk Ag and particles larger than 17 nm [30].

Fig. 2 shows SEM images of LCMO Ag-particle coated powder (a) and a cross section of a pellet (b). We can see how the Ag particulates decorate the manganite particle. We also see in Fig. 2b that using this decorated powder in a sintered pellet, silver ends inside the pores. It may also form short, non-percolating pathways at grain boundaries, as shown by tomography by Ruiz-Trejo et al. [15].

Fig. 3 shows the field cooled magnetization of three LCSMO pellets made using virgin small and large particles and Ag-coated particles, respectively. At low field, 3 mT, and high field, 1 T, we observe a systematic lowering of the magnetization for the Ag-particle coated sample. This is due to the addition of the non-magnetic Ag to the sample. The reduction is consistent with the amount of Ag added (about 10% in mass), see inset of Fig. 4. In there, we see a lower magnetisation, about 10% in mass, for Ag-particle coated sample as expected. The theoretical magnetisation saturation of LCSMO is 3.8535 μ_B per F.U. This translates to a theoretical magnetisation of 100.13 A m^2 kg^{-1}. Most importantly, there is no other noticeable change between the three samples in $M(T)$, and especially not in the sharpness of the paramagnetic to ferromagnetic transition under either high or small field.

Fig. 4 shows the absolute value of the isothermal entropy change, ΔS, of LCSMO pellets, under 1 T field application, calculated using the following Maxwell relation on set of isothermal magnetisation $M(H)$ curves taken at different temperatures, T_1, T_2, …, T_j:

$$\Delta S\left(\left(\frac{T_{j+1}+T_j}{2}\right),\ \Delta H\right) = \mu_0 \sum_i \frac{M(T_{j+1},\ H_i) - M(T_j,\ H_i)}{T_{j+1} - T_j}\Delta H_i. \qquad (1)$$

We see a lower isothermal entropy change, with a reduction of about 9% at the peak value, for Ag-particle coated LCSMO sample in comparison with virgin pellets. We indeed observe identical entropy changes of the two virgin pellets. The small difference in saturation magnetisation (~2%) between large and small particle as seen in the inset of Fig. 4 does not show up on the entropy plot.

Fig. 5a shows the thermal conductivity of the sintered pellets made up of small grain, large grain and silver coated large grain particle of LCSMO. The trends are similar to our previous reports showing that in pellet form, large grain samples have higher κ [9] because of fewer grain boundaries, and grain boundary resistance (electrical and thermal) is greatly diminished by the introduction of silver [9,15,29].

The measured electrical resistivity (assuming full cross sectional area of the sample for the calculation), Fig. 5b, is similar for the two virgin samples. We see a substantial decrease in the resistivity by introduction of the Ag-particle coating, and we notice

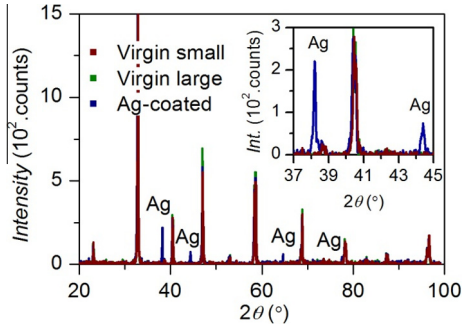

Fig. 1. XRD patterns of virgin, small and large particle, and of Ag-particle coated pellets. Inset shows two extra peaks from the silver phase.

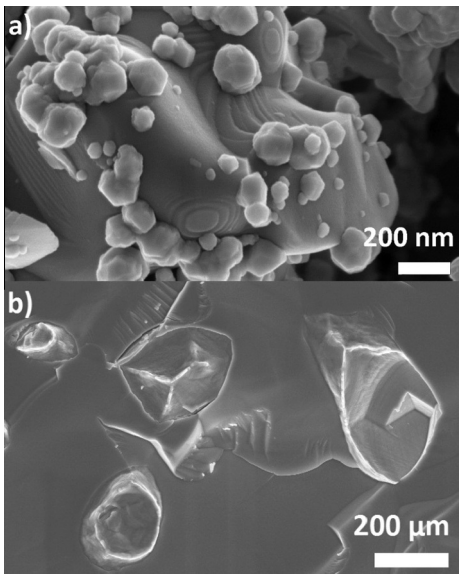

Fig. 2. (a) SEM image of silver particulates decorating a manganite grain in LCMO powders. (b) SEM image of the cross section of Ag-particle coated LCMO pellet.

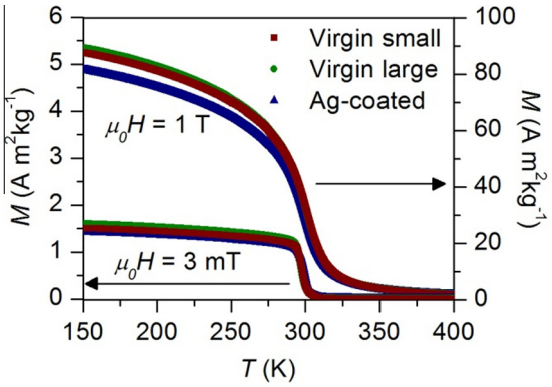

Fig. 3. Field cooled magnetization as a function of temperature, $M(T)$, of three pellet made under the application of small, 3 mT, and large magnetic fields, 1 T.

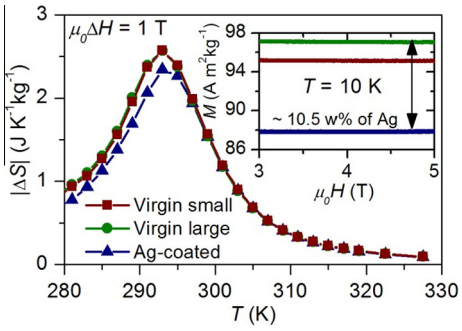

Fig. 4. Isothermal entropy change under a 1 T field application for the virgin and Ag-particle coated LCSMO pellets. Inset is the saturation magnetisation recorded at 10 K.

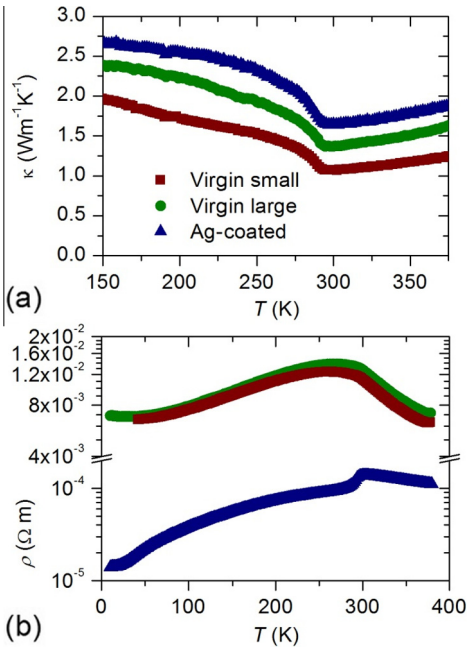

Fig. 5. Thermal conductivity (a) and resistivity (b) as a function of the temperature of LCSMO pellets made of virgin small and large grains and Ag-coated large grains.

a recovery of the intragrain behaviour, as seen by a sharper bump at the insulator–metal transition (as we have reported previously [9]). We have thus improved the grain boundary conductance and removed parasitic intergrain resistivity.

Results are more significant in pellets with smaller grains as shown by the results for the LCMO sample in Fig.6; κ is low in the virgin state because of the increased density of grain boundaries. The thermal conductivity is greatly increased over our previous reports for the same amount of silvered infiltrated into the pellet (~10%), demonstrating that grains can be coated much more efficiently using this method compared to the infiltration route [9].

For both LCSMO and LCMO pellets, a slight reduction of the extrinsic magnetic hysteresis measured during isothermal magnetisation was noticed through the width decrease of $M-H$ loop (not shown here) in comparison with virgin materials.

4. Magnetocaloric performances

Magnetocaloric performances of the samples in particle form were investigated using a test device [27] based on the AMR cycle. Fig. 7 shows the temperature span, ΔT_{span}, reached for the three types of regenerators for a utilisation of 0.76 and 0.8 for large virgin and Ag-coated particles, and small virgin particles, respectively. Utilisation is defined as the ratio between the thermal mass of the heat transfer fluid moved during one AMR cycle and the thermal mass of the regenerator [31],

$$U = \frac{\dot{m}_f T_p c_f}{m_{LSCMO} c_{LSCMO}}, \quad (2)$$

where $\dot{m}_f$, c_f, m_{LSCMO}, c_{LSCMO}, and T_p are the mass flow rate and specific heat capacity of the fluid (here water), the mass and specific heat capacity of the LCSMO particles, and the period of fluid movement, respectively. The specific heat capacities c_f and c_{LSCMO} were taken as being the accepted 4186 and 650 J K^{-1} kg^{-1} value for water and LCSMO (not shown here but measured and in agreement with Dinesen et al. [25]), respectively.

In Fig. 7, we do not see any noticeable difference in the achieved temperature span between Ag particle coated and virgin large powders for this utilisation ratio conditions. However, we do see a noticeable improvement when the particle size is smaller.

Keeping the ambient temperature constant at 297 K ensured that the hot end temperature remained close to the peak temperature of Fig. 7 for the three regenerators. The influence of utilisation was then investigated under these conditions. This is shown in Fig. 8.

It seems that optimal utilisation ratio was similar for the three regenerators with a value of around 0.6. As for the general influence on the magnetocaloric performances, we observe a remarkable improvement approaching Gd performances of 10.2 K temperature span, when the particle size is reduced. This can be explained by the fact that as the diameter of the particles decreases the heat transfer coefficient and specific surface area responsible for the heat exchange with the fluid, here water, increase. Overall, the performance of the AMR is enhanced. The available magnetic entropy change is utilized more effectively in the case with smaller particles. However, as the operating frequency is increased it is expected that the smaller particles will decrease in performance due to the significantly increased flow resistance.

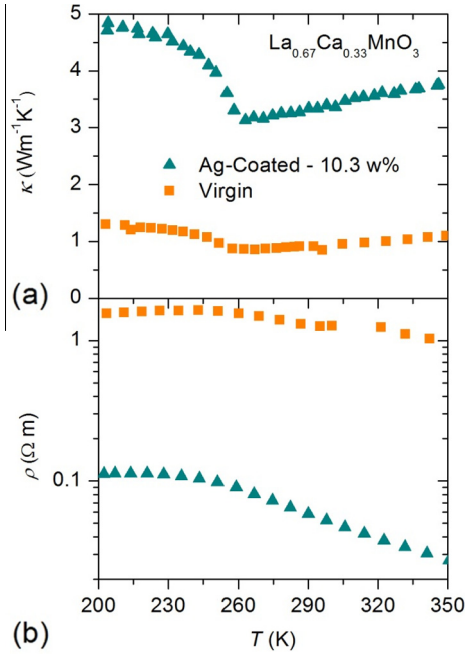

Fig. 6. Thermal conductivity (a) and resistivity (b) as a function of the temperature of $La_{0.67}Ca_{0.33}MnO_3$ virgin and Ag-particle coated pellets made of powders synthesized by GNP.

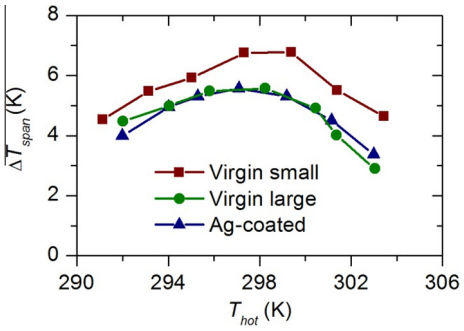

Fig. 7. Temperature span as a function of the hot end temperature of regenerators made of LCSMO virgin small and large particles, and Ag-coated particles.

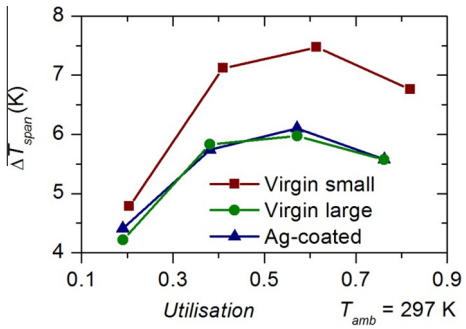

Fig. 8. Temperature span as a function of the utilisation ratio of regenerators made of LCSMO virgin small and large particles, and Ag-coated particles. The ambient temperature, T_{amb}, was kept at 297 K.

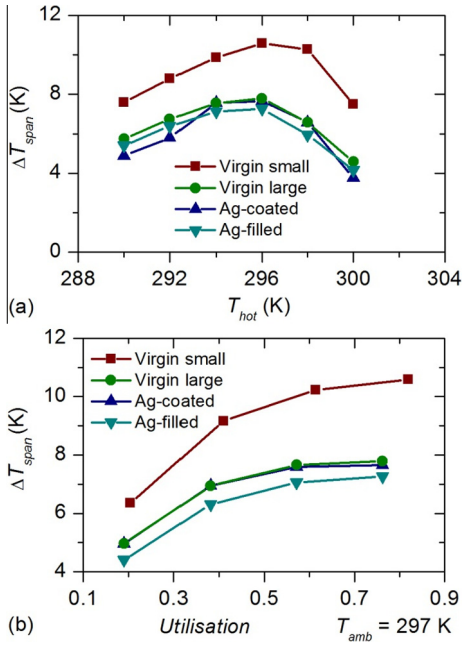

Fig. 9. Model results of simulating the experiments. (a) The zero load temperature span as a function of hot side temperature. (b) Temperature span as a function of thermal utilization as defined in Eq. (2).

For the experiments presented in this paper this was not an issue as the operating frequency of the device was well below 1 Hz.

Ag-coating of the particles did not improve heat transfer between LCSMO particles and water either.

5. Modeling the experiments

A numerical AMR model [31] was used to simulate the experiments. Four cases were considered: the two virgin sets (small and large particles, respectively) and two sets with large particles with different Ag-based property sets: one with the overall thermal conductivity of the particles to be equal to that of the Ag-coated particles (Fig. 6), the other, Ag-filled, merely with the silver acting as a parasitic passive material, *i.e.* reducing the effective magnetic entropy change by 10%. The particles were assumed spherical with diameters 0.3 mm (small) and 0.5 mm (large). The full spatial magnetic field profile and the time-dependent demagnetizing field were taken into account. The results clearly show the same trend as the experiment; the regenerator with the small particles produces a larger temperature span than the three cases with large particles (Fig. 9). The Ag-coated, *i.e.* the regenerator modelled as having a larger effective thermal conductivity, generally produces the smallest temperature span. As the AMR cycles considered here are at a very low operating frequency (about 0.14 Hz) thermal conduction in the axial direction comprises a significant loss mechanism. At higher frequencies this is much less significant whereas conduction from the particles to the fluid will benefit from a larger thermal conductivity of the solid due to the increase in Biot number at higher operating frequencies.

Overall, the model temperature spans are higher than the corresponding experimental ones. This is due to heat losses to the ambient in the experimental setup, which are not included in the model.

6. Conclusions

Magnetocaloric $La_{0.67}Ca_{0.27}Sr_{0.06}Mn_{1.05}O_3$ and $La_{0.67}Ca_{0.33}MnO_3$ particles were subjected to a new silver decoration technique that has proved to be more reliable and more successful than previous reports for engineering the thermal and electrical resistance at the grain boundaries of pellets. Powder beds were made from the particles and tested as active magnetic regenerators. We found that at the low cycle frequencies investigated here, silver decoration on the outside of particles does not increase the refrigeration performance as measured by the achievable temperature span across the regenerator. On the other hand, the regenerator performance was remarkably improved by particle size reduction.

Acknowledgements

This work was supported by the UK EPSRC Grant EP/G060940/1 entitled Nanostructured Functional Materials for Energy Efficient Refrigeration, Energy Harvesting and Production of Hydrogen from Water, and by the ENOVHEAT project which is funded by Innovation Fund Denmark (contract No 12-132673). J.A.T. acknowledges the help of Dr. Andrey Berenov, Imperial College London, for the making of the LCMO samples.

References

[1] G.V. Brown, Magnetic heat pumping near room temperature, J. Appl. Phys. 47 (8) (1976) 3673.
[2] K.A. Gschneidner Jr., V.K. Pecharsky, Thirty years of near room temperature magnetic cooling: where we are today and future prospects, Int. J. Refrig. 31 (6) (2008) 945.
[3] L. Theil Kuhn, N. Pryds, C.R.H. Bahl, A. Smith, Magnetic refrigeration at room temperature – from magnetocaloric materials to a prototype, J. Phys. Conf. Ser. 303 (1) (2011) 012082.
[4] K.G. Sandeman, Magnetocaloric materials: the search for new systems, Scr. Mater. 67 (6) (2012) 566.
[5] E. Brück, Developments in magnetocaloric refrigeration, J. Phys. D Appl. Phys. 38 (23) (2005) R381.
[6] Y.I. Spichkin, A.M. Tishin, The magnetocaloric effect and its applications, Mater. Today 6 (11) (2003) 51.
[7] V. Basso, C.P. Sasso, K.P. Skokov, O. Gutfleisch, V.V. Khovaylo, Hysteresis and magnetocaloric effect at the magnetostructural phase transition of Ni–Mn–Ga and Ni–Mn–Co–Sn Heusler alloys, Phys. Rev. B 85 (1) (2012) 014430.
[8] M. Zhang, Y. Long, R.-C. Ye, Y.-Q. Chang, Corrosion behavior of magnetic refrigeration material La–Fe–Co–Si in distilled water, J. Alloys Compd. 509 (8) (2011) 3627.
[9] J.A. Turcaud, K. Morrison, A. Berenov, N.McN. Alford, K.G. Sandeman, L.F. Cohen, Microstructural control and tuning of thermal conductivity in $La_{0.67}Ca_{0.33}MnO_{3\pm\delta}$, Scr. Mater. 68 (7) (2013) 510.
[10] K.K. Nielsen, K. Engelbrecht, The influence of the solid thermal conductivity on active magnetic regenerator, J. Phys. D Appl. Phys. 45 (2012).
[11] J.D. Moore, K. Morrison, K.G. Sandeman, M. Katter, L.F. Cohen, Reducing extrinsic hysteresis in first-order La(Fe Co, Si)$_{13}$ magnetocaloric systems, Appl. Phys. Lett. 95 (25) (2009) 252504.
[12] V. Basso, C. Beatrice, M. LoBue, P. Tiberto, G. Bertotti, Connection between hysteresis and thermal relaxation in magnetic materials, Phys. Rev. B 61 (2) (2000) 1278.
[13] V. Basso, C.P. Sasso, M. LoBue, Thermodynamic aspects of first-order phase transformations with hysteresis in magnetic materials, J. Magn. Magn. Mater. 316 (2) (2007) 262.

[14] J. Lyubina, U. Hannemann, M.P. Ryan, L.F. Cohen, Electrolytic hydriding of $LaFe_{13-x}Si_x$ alloys for energy efficient magnetic cooling, Adv. Mater. 24 (15) (2012) 2042.
[15] E. Ruiz-Trejo, P. Boldrin, A. Lubin, F. Tariq, S. Fearn, R. Chater, S.N. Cook, A. Atkinson, R.I. Gruar, C.J. Tighe, J. Darr, N.P. Brandon, Novel composite cermet for low-metal-content oxygen separation membranes, Chem. Mater. 26 (13) (2014) 3887.
[16] M. Battabyal, T.K. Dey, Thermal and electronic transport in $La_{0.7}Sr_{0.3-x}Ag_xMnO_3$ compounds between 50 and 450 K, Physica B 373 (1) (2006) 46.
[17] M. Battabyal, T.K. Dey, Thermal conductivity of silver doped lanthanum manganites between 10 and 300 K, J. Phys. Chem. Solids 65 (11) (2004) 1895.
[18] R. Thaljaoui, W. Boujelben, M. Pękała, K. Pękała, J. Mucha, A. Cheikhrouhou, Structural, magnetic and transport study of monovalent Na-doped manganite $Pr_{0.55}Na_{0.05}Sr_{0.4}MnO_3$, J. Alloys Compd. 558 (2013) 236.
[19] J.L. Cohn, J.J. Neumeier, C.P. Popoviciu, K.J. McClellan, Th. Leventouri, Local lattice distortions and thermal transport in perovskite manganites, Phys. Rev. B 56 (14) (1997) 8495.
[20] D.W. Visser, A.P. Ramirez, M.A. Subramanian, Thermal conductivity of manganite perovskites: colossal magnetoresistance as a lattice-dynamics transition, Phys. Rev. Lett. 78 (20) (1997) 3947.
[21] S. Fujieda, Y. Hasegawa, A. Fujita, K. Fukamichi, Thermal transport properties of magnetic refrigerants $La(Fe_xSi_{1-x})_{13}$ and their hydrides, and $Gd_5Si_2Ge_2$ and MnAs, J. Appl. Phys. 95 (5) (2004) 2429.
[22] A. Kowalczyk, M. Falkowski, T. Toliński, Magnetic, transport and thermodynamic properties of $Ce_5Ni_2Si_3$ compound, Solid State Sci. 14 (10) (2012) 1496.
[23] K. Kamiya, T. Numazawa, T. Koen, T. Okano, K. Matsumoto, S. Nimori, Thermal property of magnetic materials for hydrogen magnetic refrigeration and effect of magnetic field on them, IEEE Trans. Appl. Supercond. 14 (2) (2004) 1734.
[24] K.A. Gschneidner Jr., V.K. Pecharsky, A.O. Tsokol, Recent developments in magnetocaloric materials, Rep. Prog. Phys. 65 (2005) 1479.
[25] A.R. Dinesen, S. Linderoth, S. Morup, Direct and indirect measurement of the magnetocaloric effect in $La_{0.67}Ca_{0.33-x}Sr_xMnO_3$ ($x \in [0;0.33]$), J. Phys. Condens. Matter 17 (39) (2005) 6257.
[26] C.R.H. Bahl, D. Velazquez, K.K. Nielsen, K. Engelbrecht, K.B. Andersen, R. Bulatova, N. Pryds, High performance magnetocaloric perovskites for magnetic refrigeration, Appl. Phys. Lett. 100 (12) (2012) 121905.
[27] C.R.H. Bahl, T.F. Petersen, N. Pryds, A. Smith, A versatile magnetic refrigeration test device, Rev. Sci. Instrum. 79 (9) (2008) 093906.
[28] R. Bulatova, C.R.H. Bahl, K. Andersen, L.T. Kuhn, N. Pryds, Functionally graded ceramics fabricated with side-by-side tape casting for use in magnetic refrigeration, Int. J. Appl. Ceram. Technol. (2014), http://dx.doi.org/10.1111/ijac.12298 (in press).
[29] E. Ruiz-Trejo, Y. Zhou, N.P. Brandon, On the manufacture of silver-$BaCe_{0.5}Zr_{0.3}Y_{0.16}Zn_{0.04}O_{3-d}$ composites for hydrogen separation, Int. J. Hydrogen Energy 40 (11) (2015) 4146.
[30] I. Shyjumon, M. Gopinadhan, O. Ivanova, M. Quaas, H. Wulff, C.A. Helm, R. Hippler, Structural deformation, melting point and lattice parameter studies of size selected silver cluster, Eur. Phys. J. D 37 (3) (2006) 409.
[31] A. Kitanovski, J. Tušek, U. Tomc, U. Plaznik, M. Ožbolt, A. Poredoš, Active Magnetic Regeneration in Magnetocaloric Energy Conversion, Springer International Publishing, 2015. pp. 97.

A.1.5 Sensitivity study of multi-layer active magnetic regenerators using first order magnetocaloric material $La(Fe,Mn,Si)_{13}H_y$

Sensitivity study of multi-layer active magnetic regenerators using first order magnetocaloric material La(Fe,Mn,Si)$_{13}$H$_y$

Tian Lei,[1,a)] Kaspar K. Nielsen,[1] Kurt Engelbrecht,[1] Christian R. H. Bahl,[1] Henrique Neves Bez,[1] and Christian T. Veje[2]
[1]*Department of Energy Conversion and Storage, Technical University of Denmark, Frederiksborgvej 399, DK 4000 Roskilde, Denmark*
[2]*Mærsk Mc-Kinney Møller Instituttet, University of Southern Denmark, DK 5230 Odense M, Denmark*

(Received 27 February 2015; accepted 21 June 2015; published online 6 July 2015)

We present simulation results of multi-layer active magnetic regenerators using the solid-state refrigerant La(Fe,Mn,Si)$_{13}$H$_y$. This material presents a large, however quite sharp, isothermal entropy change that requires a careful choice of number of layers and working temperature for multi-layer regenerators. The impact of the number of layers and the sensitivity to the working temperature as well as the temperature span are quantified using a one dimensional numerical model. A study of the sensitivity of variation in Curie temperature through a uniform and normal distribution is also presented. The results show that the nominal cooling power is very sensitive to the Curie temperature variation in the multi-layer regenerators. A standard deviation of the Curie temperature variation for a normal distribution less than 0.6 K is suggested in order to achieve sufficient performance of a 15-layer regenerator with Curie temperature spacing of 2 K. © *2015 AIP Publishing LLC*.
[http://dx.doi.org/10.1063/1.4923356]

I. INTRODUCTION

Magnetic refrigeration is a promising technology compared to vapor-compression systems due to the use of environmentally friendly heat transfer fluids and solid-state refrigerants, as well as a potentially high efficiency. With various improvements in magnetocaloric materials (MCMs), system design, and fluid control, the magnetic refrigeration technique has recently undergone a rapid development and several kilowatt class prototypes have emerged.[1,2] MCMs exhibit a temperature rise due to adiabatic magnetization, or temperature decrease when adiabatically demagnetized. The magnetocaloric effect has a peak near the Curie temperature T_C of the MCM, and T_C is the temperature at which the transition from ferro- to paramagnetic phase takes place. With permanent magnets producing fields on the order of 1.5 T, the adiabatic temperature change of the best performing material will be about 5 K,[3] which may not be sufficient for practical applications. To achieve a large temperature span, the concepts of active magnetic regeneration (AMR)[4] and multi-layer regenerators are widely used in the design of existing machines.[2,5,6] An AMR regenerator has a similar porous structure and oscillating flow pattern as some passive regenerative heat exchangers, but uses the MCM to transfer magnetic work into the regenerator, allowing it to absorb a cooling power over a useful temperature span.

A typical AMR cycle[7] starts from the adiabatic magnetization process, which causes the solid temperature to increase. Then the heat transfer fluid flows through the porous bed from the cold to the hot end and is heated by the solid. At the hot end, the fluid rejects excess heat to the ambient. Followed by the adiabatic demagnetization and a temperature decrease of the MCM, the hot-to-cold flow will reject heat to the solid and reach a lower temperature than the initial condition. Then the fluid absorbs heat, i.e., a cooling load, at the cold end. After several cycles, a temperature gradient is achieved along the axial direction and the regenerator reaches a periodic steady state. The net enthalpy flows at the ends are the heating and cooling power (Q_h and Q_c), respectively.

The material's performance has significant effect on the cooling power and the regenerator efficiency. Recent research has presented various interesting materials with compelling performance;[2,6,8] especially, MCMs with a first-order phase transition at the Curie temperature have a large isothermal entropy change ΔS_{mag}. It is defined as

$$\Delta S_{mag}(T, H_i : H_f) \equiv S(T, H_f) - S(T, H_i), \tag{1}$$

with H and T denoting magnetic field and temperature, respectively, and the subscripts i and f denoting initial and final state, respectively. The isothermal entropy change of these first-order transition materials is often large compared to MCMs with a pure second order transition like gadolinium (Gd). La(Fe,Mn,Si)$_{13}$H$_y$ is an attractive first order material and is subject to extensive research due to the high values of ΔS_{mag}, a small hysteresis effect, adjustable T_C, relatively high thermal conductivity, and high stability.[9–11] The material was developed from La(Fe$_x$Si$_{1-x}$)$_{13}$, where the Curie temperature can be tuned by the addition of hydrogen.[12] Barcza *et al.*[10] pointed out that it is difficult to control partial hydrogenation on the industrial level with high accuracy; therefore, a method of substituting Fe with Mn[13] was used. With this method, the material is always fully hydrogenated while the Mn content tunes T_C.

Although it is anticipated that large ΔS_{mag} will improve the regenerator performance, it decreases quickly at temperatures away from its T_C. A sharp peak may prevent the

[a)]Electronic mail: tile@dtu.dk

material from working in the optimal temperature region. Multi-layer regenerators, in which each layer is aligned to make sure the T_C of each material follows the temperature gradient, can be a solution to this issue. Larger temperature spans as well as cooling capacities are expected in multi-layer regenerators using first order materials compared to single-material regenerators.

Smith *et al.*[14] pointed out that for first order materials, the peak in the specific heat will move significantly with the applied field, and in reality the ΔS_{mag} peaks also show similar shift to higher temperature in a high applied field.[11] It is implied that the best working temperature for the first order material is expected to be higher than the Curie temperature. Therefore, multi-layer regenerators could be sensitive to the working temperature and a study of how a regenerator bed should be layered is therefore presented here.

Moreover, it may be difficult to control the T_C of each material to a high accuracy when fabricating a layered regenerator. Actual regenerator beds will have some arrangements in which T_C deviates from the intended design. This paper investigates how random variations in T_C affect the AMR performance. First, the impact of the Curie temperature variation of a single layer in each position is investigated. Then a more general study is carried out, where each layer in the regenerator deviates from the desired T_C according to either a uniform distribution or a normal distribution with a set standard deviation σ.

II. ONE DIMENSIONAL NUMERICAL MODEL OF AMR

A one-dimensional transient numerical model for simulating the AMR regenerators has been developed based on the work presented by Engelbrecht *et al.*[8] The energy equations for the fluid and solid in the transient model[8,15] can be written as

$$\frac{\partial}{\partial x}\left(k_{disp}A_c\frac{\partial T_f}{\partial x}\right)-\dot{m}c_f\frac{\partial T_f}{\partial x}-\frac{Nuk_f}{d_h}a_sA_c(T_f-T_r)+\left|\frac{\partial P}{\partial x}\frac{\dot{m}}{\rho_f}\right|=\rho_fA_c\varepsilon c_f\frac{\partial T_f}{\partial t}, \quad (2)$$

$$\frac{\mathrm{Nu}k_f}{d_h}a_sA_c(T_f-T_r)+\frac{\partial}{\partial x}\left(k_{stat}A_c\frac{\partial T_r}{\partial x}\right)+(1-\varepsilon)A_c\rho_rT_r\left(\frac{\partial s_r}{\partial H}\right)_T\frac{\partial H}{\partial t}=\rho_r(1-\varepsilon)A_cc_{r,H}\frac{\partial T_r}{\partial t}, \quad (3)$$

where k, T, ρ, c, and s are the thermal conductivity, temperature, density, specific heat, and specific entropy; A_c, d_h, a_s, and ε are the cross section area, hydraulic diameter, specific area, and porosity, which reflect the geometry characteristics of a regenerator; x, t, $\dot{m}$, and H are the axial position, time, mass flow rate, and internal magnetic field. The subscripts f and r represent fluid and solid refrigerant, respectively. More details for the expressions of thermal conductivity due to fluid dispersion k_{disp}, static thermal conductivity k_{stat}, pressure drop $\frac{\partial P}{\partial x}$, and Nusselt number Nu are presented by Nielsen *et al.*[16] It should be noted that k_{disp} and k_{stat} are already scaled to fit the cross-sectional area; therefore, the porosity is not included in the conduction terms. From left to right in the fluid energy equation, the thermal dispersion, convection, heat transfer between solid and fluid, viscous dissipation, and energy storage are considered; the terms for the energy equation of the solid side are the heat transfer between solid and fluid, axial heat conduction, magnetic work, and energy storage.

In each AMR cycle, the fluid is assumed to enter the packed bed with a constant temperature T_{hot} at the hot end during the hot-to-cold blow, and T_{cold} at the cold end during cold-to-hot blow, synchronized with a periodically varying magnetic field. The temperature span is $\Delta T = T_{\mathrm{hot}} - T_{\mathrm{cold}}$ and the heating and cooling powers are

$$Q_h=\int|\dot{m}|_f(h_{f,x=0}-h_{f,T_{\mathrm{hot}}})dt \quad \text{when} \quad \dot{m}<0, \quad (4)$$

$$Q_c=\int|\dot{m}|_f(h_{f,T_{\mathrm{cold}}}-h_{f,x=L})dt \quad \text{when} \quad \dot{m}>0, \quad (5)$$

where $h_{f,x=0}$ and $h_{f,x=L}$ are the specific enthalpies of the fluid flowing out of the hot and cold end; $h_{f,T_{\mathrm{hot}}}$ and $h_{f,T_{\mathrm{cold}}}$ are the specific enthalpies of the fluid at T_{hot} and T_{cold}.

In the numerical model, the central difference and implicit time schemes are used for discretizing the partial differential equations presented above in both space and time. By solving the coupled discretized equations, the temperature gradient can be calculated after each time step given an initial condition, and the model will output the performance indices after reaching the steady state with a tolerance. The main modeling parameters are presented in Table I. The regenerator geometry is kept fixed as a packed bed, and the number of layers, the material, the averaged mass flow rate, as well as the temperature span vary in different cases.

For modeling multi-layer regenerators using $La(Fe,Mn,Si)_{13}H_y$, the magnetocaloric properties, mainly the entropy data as a function of the internal magnetic field and temperature, of numerous materials with different T_C are needed. However, existing measurements are limited. Based on the observation that $La(Fe,Mn,Si)_{13}H_y$ materials behave quite similarly under the magnetization process and the peaks of both ΔS_{mag} and specific heat c_H are similar in magnitude and shape for a range of T_C,[11] it is assumed that the properties

TABLE I. Main parameters input in the numerical model.

Parameter	Value	Unit
Maximum applied magnetic field	1.2	T
Cross sectional area	225×10^{-6}	m^2
Length	0.100	m
Frequency	2	Hz
Regenerator bed number	20	…
Bed geometry	Packed sphere bed	…
Sphere diameter	0.0003	m
Porosity	0.36	…
MCM mass	2.01	kg
MCM thermal conductivity	8	W/(mK)
MCM density	7000	kg/m^3

of the materials with different T_C other than the characterized material can be approximated by shifting one group of experimental data according to T_C. The material has a T_C of 305.0 K, and it is provided by Vacuumschmelze GmbH, Germany. The measured data of the specific heat at zero field and the absolute value of ΔS_{mag} presented in Fig. 1 are obtained from the Lake Shore 7407 Vibrating Sample Magnetometer (VSM) and a Differential Scanning Calorimeter (DSC) at the Technical University of Denmark.[17] The density of $La(Fe,Mn,Si)_{13}H_y$ is measured in a X-ray Diffraction (XRD). The thermal conductivity k_r of $La(Fe,Mn,Si)_{13}H_y$ is assumed as 8 W/(mK), which is close the measured k_r data of LaFeSi and LaFeSiH at the ambient temperature.[9]

III. RESULTS AND DISCUSSION

A. Impact of layer number and sensitivity to working temperature

Compared to second order materials, a distinguishing feature of first order materials is the shape of the ΔS_{mag} curves with respect to temperature. The sharp peak in ΔS_{mag} makes a multi-layer design necessary for regenerators using first order materials. In this section, the impact of the number of layers in the regenerator is quantitatively studied. An N_l-layer regenerator is modeled here while operating over a temperature span of 30 K, and N_l is the number of layers. The material in the n^{th} layer is assumed to have $T_{C,n} = 305 - 30(2n-1)/2n$ $(n = 1, ..., N_l)$. That is, the $T_{C,n}$ follows a linear arrangement along the temperature gradient from 305 to 275 K. Taking a 15-layer regenerator, for example, the $T_{C,n}$ $(n = 1, ..., 15)$ varies from 304 to 276 K with an interval of 2 K according to the expression above.

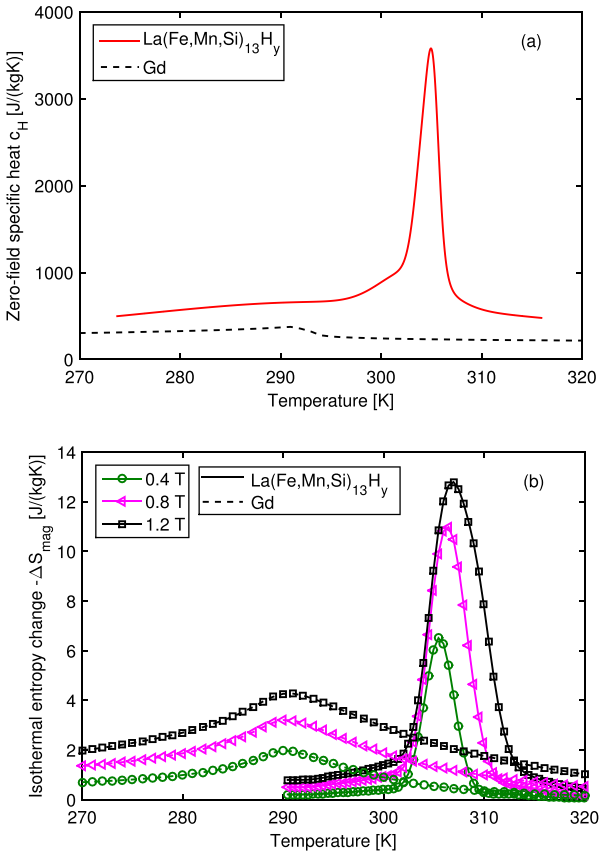

FIG. 1. The specific heat c_H at zero field (a) and the absolute value of isothermal entropy change $-\Delta S_{mag}$ (b) of $La(Fe,Mn,Si)_{13}H_y$ and Gd[18] as a function of temperature.

It is shown in Fig. 1 that the temperature, at which the peak value of ΔS_{mag} occurs, shifts to higher values as the magnetic field increases. Due to this effect, the material is predicted to perform better when the working temperature is higher than the Curie temperature. To estimate the sensitivity to the working temperature, the hot and cold end temperatures (T_{hot} and T_{cold}) are shifted at the same time by -2 to 8 K in the simulation, while the temperature span ΔT is held fixed at 30 K and $T_{C,n} = 305 - 30(2n-1)/2n$.

Fig. 2 presents the impact of the number of layers N_l and the working temperature T_w on the nominal cooling power $\eta_1 = \frac{Q_{c,T_w,N_l}}{Q_{c,T_w=307-277K,N_l=60}}$, where the denominator $Q_{c,T_w=307-277K,N_l=60}$ is the cooling power of a 60-layer regenerator under T_w of 307–277 K (also the maximum value in the figure) and Q_{c,T_w,N_l} is the cooling power of the N_l-layer regenerator working with a specific T_w. It should be noted that the averaged flow rate is optimized to get the maximum cooling power in each case.

It is shown that the nominal cooling power, η_1, increases significantly with the number of layers from 4 to 20 and approaches the maximum value when the number of layers exceeds 20 for each working temperature. The maximum number of layers in this study is 60, since a regenerator with more than 60 layers will only lead to a minimal increase in the nominal cooling power according to the results in Fig. 2. 10–15 layers may be practical considering a balance between obtaining the maximum cooling performance and the difficulty of construction. It can be observed that the performance of a multi-layer regenerator is quite sensitive to the absolute working temperature, although the temperature span is fixed. The best T_w is 307–277 K, which is 2 K higher than the

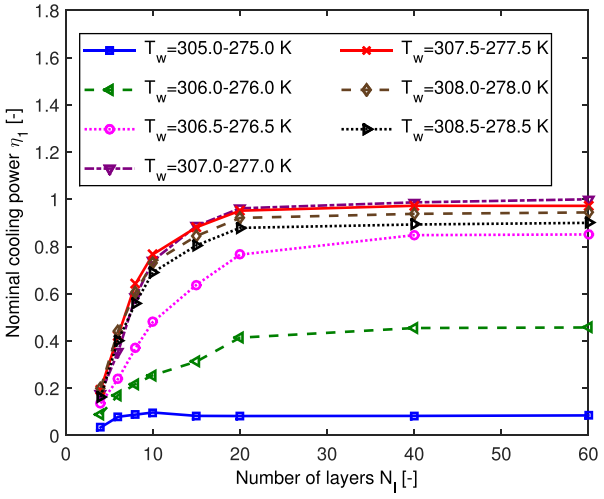

FIG. 2. Impact of number of layers N_l on nominal cooling power $\eta_1 = \frac{Q_{c,T_w,N_l}}{Q_{c,T_w=307-277K,N_l=60}}$ of N_l-layer regenerators with constant temperature span of 30 K.

initially guessed temperature span of 305–275 K. This is explained by the fact that the temperature that corresponds to the peak of ΔS_{mag} rises with increasing magnetic field. The optimal averaged mass flow rate increases with the cooling power, although the data are not presented here.

More detailed results are shown in Fig. 3, and they reveal that the multi-layer regenerators have considerable dependence on the working temperature T_w for fixed $\Delta T = 30$ K. Although both the hot and cold end temperatures are shifted, the horizontal axis only shows the hot end temperature T_{hot}. η_1 reaches the maximum value when T_w is close to 307–277 K and decreases rapidly with changes of T_w to either hot or cold region. Moreover, the nominal cooling power of the multi-layer regenerators decreases much faster when T_w is shifted lower, since the total magnetocaloric effect becomes smaller in a lower T_w region due to the shift of ΔS_{mag} curves. Flat peaks in η_1 curves are observed in the regenerators with fewer layers, which mean the sensitivity is smaller; however, much less nominal cooling power is obtained.

Fig. 4 presents the corresponding results of the coefficient of performance (COP), which is defined as $\text{COP} = \frac{Q_c}{Q_h - Q_c}$. Higher COP can be obtained in the regenerators with more layers, and the peak of the COP appears at T_w of 308.5–278.5 K, which is even higher than the guessed temperature region. The results imply that the design of the multi-layer regenerator with the first order materials is challenging, and the number of layers as well as the working temperature should be carefully chosen to achieve desired cooling power and COP.

B. Sensitivity to temperature span ΔT

Another interesting question is how multi-layer regenerators perform under different temperature spans. For the regenerators using the second order materials, the performance curves of cooling power to temperature span in the experiments[1] show a linear shape. However, with the first order materials with a narrow peak in ΔS_{mag}, the multi-layer regenerator, designed for a temperature span of 30 K, probably cannot produce more cooling power when the temperature span is decreased, because in certain layers the material may work outside its respective optimal working temperature.

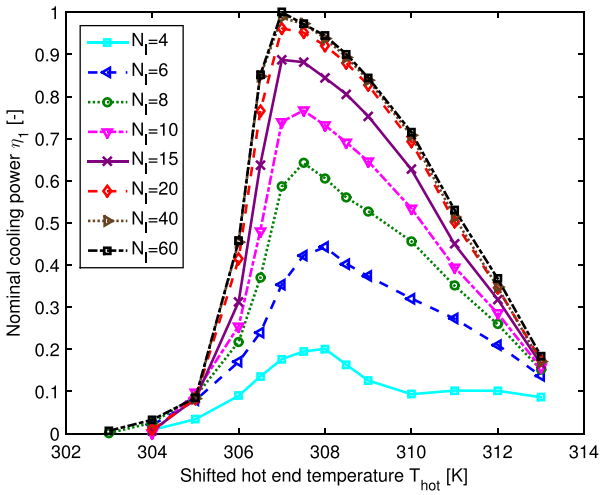

FIG. 3. Impact of working temperature T_w (from T_{hot} to $T_{\text{hot}} - 30$ K) on nominal cooling power η_1 of N_l-layer regenerators when temperature span is 30 K.

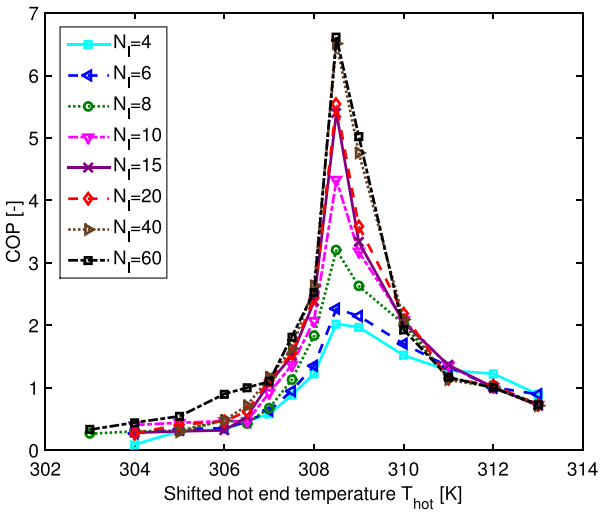

FIG. 4. Impact of working temperature T_w (from T_{hot} to $T_{\text{hot}} - 30$ K) on COP of N_l-layer regenerators when temperature span is 30 K.

To investigate this impact, the N_l-layer ($N_l = 4 - 60$) regenerators with $T_{C,n} = 305 - 30(2n-1)/2n$ K ($n = 1, \ldots, N_l$) are chosen as the simulation targets. The hot end temperature T_{hot} is fixed at 308 K, which is close to the optimal value for most cases as found in the previous study; whereas the cold end temperature T_{cold} is varied from 278 K to 298 K with an interval of 5 K, corresponding to temperature spans ΔT from 30 K to 10 K.

The results illustrated in Fig. 5 show the impact of ΔT on nominal cooling power $\eta_2 = \frac{Q_{c,\Delta T,N_l}}{Q_{c,\Delta T=10\text{K},N_l=60}}$ of the N_l-layer regenerators. Although the temperature span is decreased, the increment in the nominal cooling power η_2 is much smaller compared to the behaviors of the regenerators using

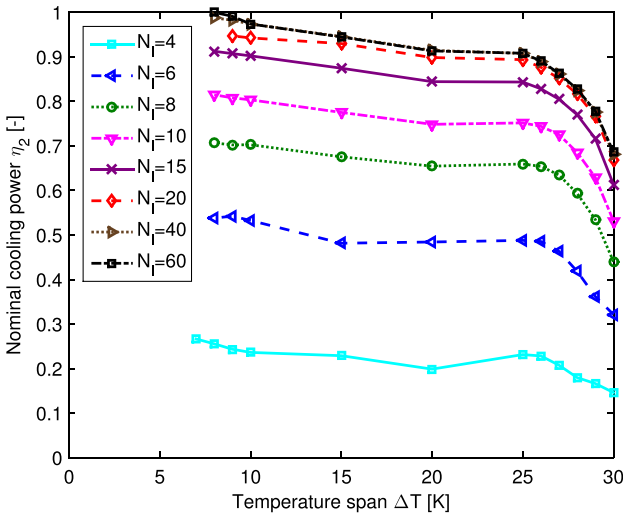

FIG. 5. Impact of temperature span ΔT on nominal cooling power $\eta_2 = \frac{Q_{c,\Delta T,N_l}}{Q_{c,\Delta T=10\text{K},N_l=60}}$ of N_l-layer regenerators with a fixed $T_{C,n}$ arrangement of $305 - 30(2n-1)/2n$.

Gd.[1] It should be noted that there is a limited temperature range for the measured material properties used in these simulations. In this case, when the temperature span falls below 7 K, the material with the lowest Curie temperature starts to operate outside of the measured property range. Here, the simulations are no longer valid and the corresponding points are not shown in Fig. 5. The results also agree well with the findings presented by Jacobs *et al.*[2] where similar performance curves can be observed for a refrigerator using a 6-layer regenerator was studied.

Moreover, to account for different temperature spans, the N_l-layer regenerators can be optimized by fitting the Curie temperature of each layer to the specific temperature span ΔT, that is, $T_{C,n} = 305 - \Delta T(2n-1)/2n$. This means that a different regenerator is modeled for each temperature span. The results of the nominal cooling power for each temperature span $\eta_3 = \frac{Q_{c,\Delta T,N_l}}{Q_{c,\Delta T,N_l=60}}$, where $Q_{c,\Delta T,N_l=60}$ is the cooling power of a 60-layer regenerator over the temperature span of ΔT, are presented in Fig. 6. The impact of the layer number is similar to the results in Fig. 2; however for a smaller temperature span, the regenerators reach the maximum cooling performance much faster, meaning fewer layers are needed to reach a cooling power near the maximum. This is because the ΔS_{mag} curves for each material have a certain width of best working temperature region and fewer layers are needed to cover a smaller temperature span.

The inset in Fig. 6 shows the number of layers when the cooling power reaches 90% of the maximum value ($\eta_3 = 0.9$) as a function of temperature span. The curve shows an approximately linear relation and gives a slope of 2.24 layers per 5 K temperature span, which can be used as a reference for choosing the number of layers when constructing layered regenerators with $La(Fe,Mn,Si)_{13}H_y$.

The results of the nominal cooling power $\eta_4 = \frac{Q_{c,\Delta T,N_l}}{Q_{c,\Delta T=5K,N_l=60}}$ produced by the multi-layer regenerators with optimized $T_{C,n}$ arrangement are presented in Fig. 7. The performance curves of the N_l-layer regenerators now behave in

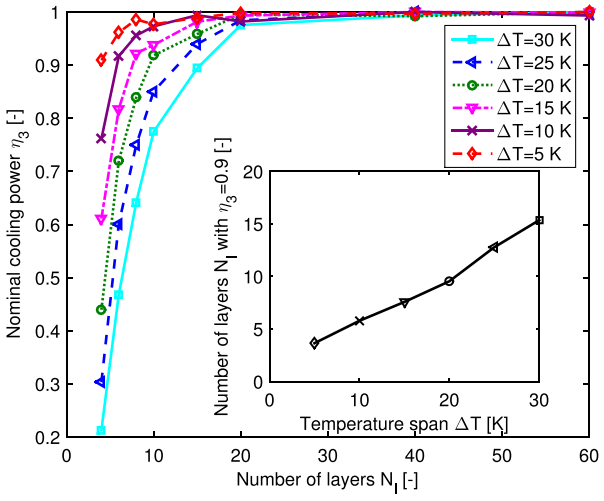

FIG. 6. Impact of number of layers N_l on nominal cooling power $\eta_3 = \frac{Q_{c,\Delta T,N_l}}{Q_{c,\Delta T,N_l=60}}$ of N_l-layer regenerators with optimized $T_{C,n}$ arrangement of $305 - \Delta T(2n-1)/2n$.

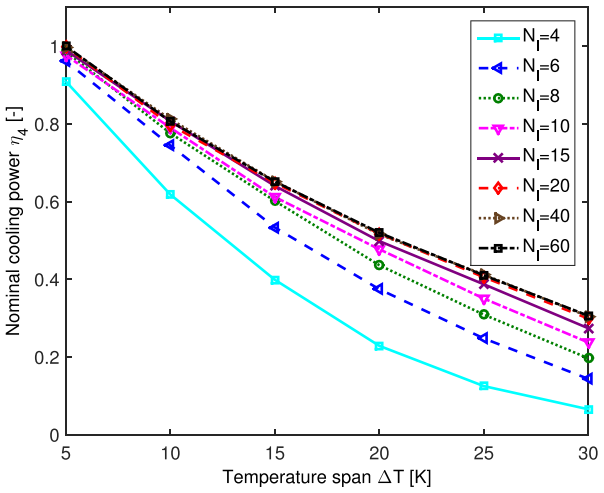

FIG. 7. Impact of temperature span ΔT on nominal cooling power $\eta_4 = \frac{Q_{c,\Delta T,N_l}}{Q_{c,\Delta T=5K,N_l=60}}$ of N_l-layer regenerators with optimized $T_{C,n}$ arrangement of $305 - \Delta T(2n-1)/2n$.

a more linear manner, which is different than those with fixed $T_{C,n}$ arrangement shown in Fig. 5. The curves split out when the temperature span becomes larger, meaning that more layers are needed to approach the maximum performance, which also reflects the conclusions drawn before.

C. Impact of Curie temperature variation in specific positions

There will always be some manufacturing variation in the Curie temperature T_C for the materials studied here, meaning the ideal T_C arrangement is quite difficult to achieve. The effect of Curie temperature variation in layered regenerators is not well understood and this will be quantified in the following study. A straightforward way to investigate this is to study the impact of the variation in the Curie temperature $\Delta T_{C,n}$, which is $T_{C,n,real} - T_{C,n,base}$ in the n^{th} layer. $T_{C,n,real}$ and $T_{C,n,base}$ are the real and base Curie temperature of every material for constructing a layered regenerator, and positive $\Delta T_{C,n}$ means shifting $T_{C,n,real}$ of the n^{th} layer to a higher temperature, and vice versa.

In the simulation, a 15-layer regenerator, in which the n^{th} layer has the Curie temperature $T_{C,n,base} = 305 - 30(2n-1)/2n$ K (n = 1…15), is used as the baseline for comparison, and in this case $\Delta T_{C,n} = 0$. Then one at a time, $T_{C,n}$ of every individual layer in the 15-layer regenerator is shifted by the variation $\Delta T_{C,n}$, which is considered to vary from −1.6 to 1.6 K with a step of 0.4 K. The temperature span is held constant at 307–277 K, and it is close to the best working temperature according to the previous study. As the number of layers and the working temperature are fixed, the optimal averaged mass flow rate for each case is close to each other, and a constant value is used in the rest of this study. The impact of $\Delta T_{C,n}$ in a single layer-n is shown in Fig. 8. The nominal cooling power η_5 is $\frac{Q_{c,\Delta T_{C,n}}}{Q_{c,\Delta T_{C,n}=0}}$, where $Q_{c,\Delta T_{C,n}=0}$ is the cooling power of the base regenerator with $\Delta T_{C,n} = 0$, meaning an even Curie temperature arrangement, and $Q_{c,\Delta T_{C,n}}$ is the cooling power of a regenerator with certain $\Delta T_{C,n}$ in the n^{th} layer. For most cases, the maximum value of η_5 is close

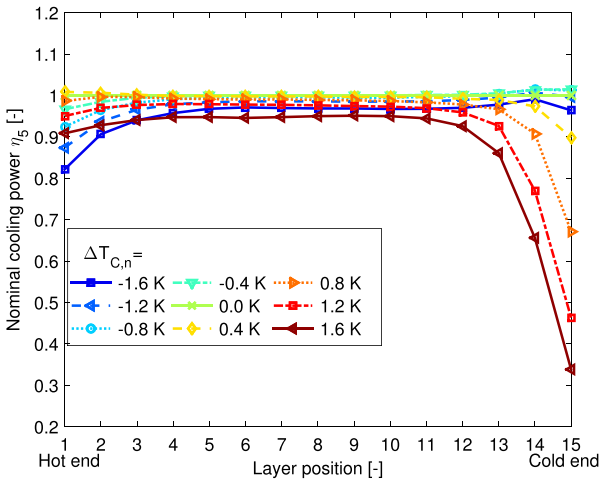

FIG. 8. Impact of Curie temperature variation $\Delta T_{C,n}$ of every individual layer on nominal cooling power $\eta_5 = \frac{Q_{c,\Delta T_{C,n}}}{Q_{c,\Delta T_{C,n}=0}}$.

to 1, which shows that the base regenerator with $\Delta T_{C,n} = 0$ is the best choice, that is, an even Curie temperature arrangement produces a cooling power close to the maximum value. It can be seen that the performance is most sensitive to $\Delta T_{C,n}$ for the cases of shifting the layers close to the hot or cold ends. Especially when shifting the layer-13, 14, and 15 to the hot region, η_5 decreases dramatically, which means that the regenerators are more sensitive to $\Delta T_{C,n}$ in the layers close to the cold end.

D. Impact of Curie temperature variations following statistical distributions

To reflect the impact of production uncertainties, it is necessary to model layered regenerators where the Curie temperature $T_{C,n}$ of each layer may vary according to a uniform distribution or a normal distribution; the latter is expected to be closer to reality. Therefore, in this section, the acceptable degree of the Curie temperature variation $\Delta T_{C,n}$ is investigated by running a batch of simulations and reflecting on the range of AMR performance that can arise from assuming $\Delta T_{C,n}$, to be a stochastic variable. The method used to generate the new regenerators assumes that the $\Delta T_{C,n}$ follows a uniform distribution first. The base regenerator is still the one presented in Sec. III C, and each layer of the new 15-layer regenerator has a random shift that is modeled in four magnitudes: ± 0.5, ± 1, ± 2, and ± 3.5 K. The uniform distribution makes sure the probability that $\Delta T_{C,n}$ of each layer appears inside the defined region is the same. For each magnitude, 200 such combinations are generated randomly and the nominal cooling powers are compared. The root mean square deviation $RMSD = \sqrt{\frac{\sum_{n=1}^{15} \Delta T_{C,n}^2}{15}}$ is utilized to present the degree of overall variation in $T_{C,n}$. *RMSD* close to 0 means near to the even $T_{C,n}$ arrangement, conversely large values mean higher average degrees of variation in $T_{C,n}$, in other words, uneven $T_{C,n}$ arrangement.

Fig. 9 shows four groups of data and the markers represent different magnitudes. Here, negative nominal cooling power is still presented for statistical purposes. It can be seen that the maximum nominal cooling power η_5 is close to 1 and η_5 decreases rapidly with the RMSD of $\Delta T_{C,n}$ in total, which means the regenerators can only tolerate relatively small $\Delta T_{C,n}$ on the order of ± 0.5 K without significant loss in cooling power. With a variation larger than ± 1 K, η_5 is away from the median value, which implies that larger variation adds considerable difficulty to realize designed cooling power of the multi-layer regenerators in the real construction.

In the following studies, we present the sensitivity of the multi-layer regenerators when $\Delta T_{C,n}$ follows a normal distribution with a mean value μ and standard deviation σ. In the simulations, $\mu = 0$ and σ is set from 0.3 K to 3 K with steps of 0.3 K. For each σ, 200 regenerators are simulated (in total 2000 cases). The results of the nominal cooling power are presented in Fig. 10. It can be seen that the impact of σ is significant. For $\sigma = 0.3$ K, the median value of the nominal cooling power is 0.960, and the 25%–75% box shows the

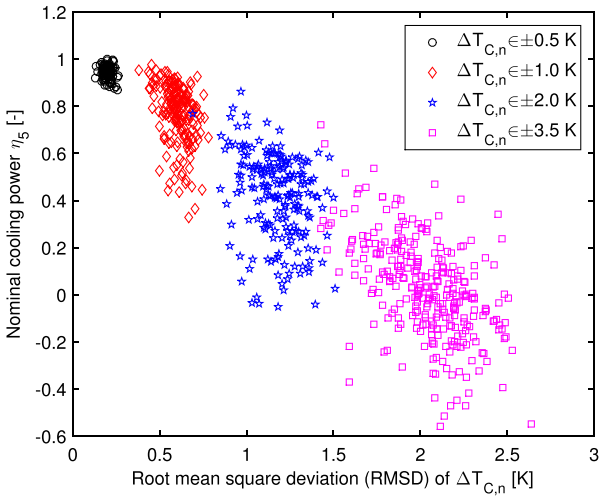

FIG. 9. Impact of *RMSD* of $\Delta T_{C,n}$ on nominal cooling power η_5 when $\Delta T_{C,n}$ follows a uniform distribution.

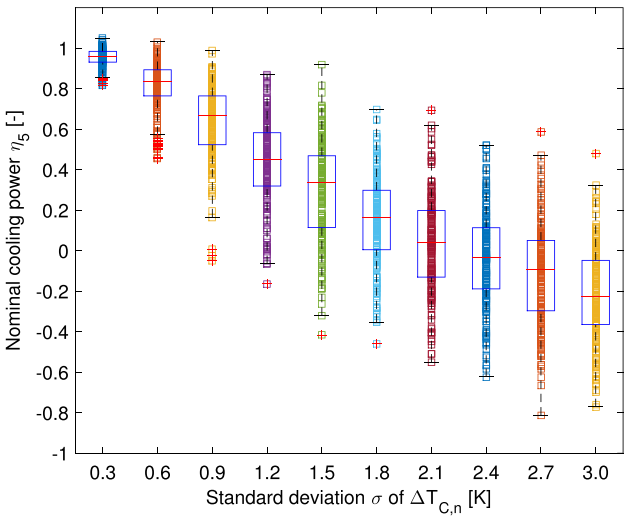

FIG. 10. Impact of standard deviation σ of $\Delta T_{C,n}$ on nominal cooling power η_5 when $\Delta T_{C,n}$ follows a normal distribution. The central mark of the 25%–75% box is the median value of η_5 for each σ, and the edges of the box are the 25th and 75th percentiles. The whiskers show the most extreme data points without outliers, and the outliers are plotted individually in red cross.

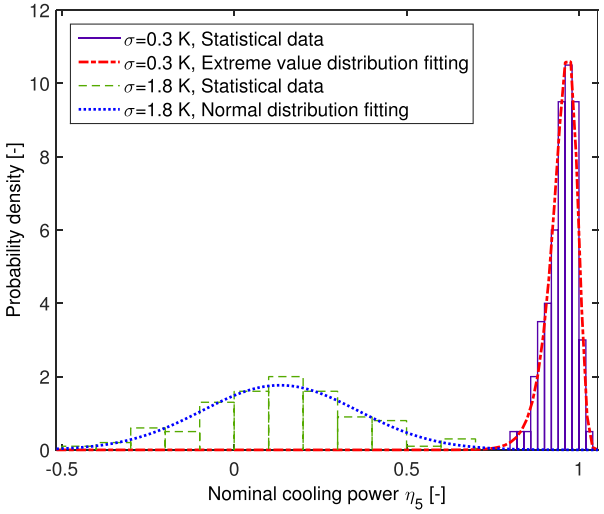

FIG. 11. Distribution fittings of statistical data of nominal cooling power η_5 when $\sigma = 0.3$ K and $\sigma = 1.8$ K. For $\sigma = 0.3$ K, the expectation and standard variation of η_5 are $\mu_{\eta_5} = 0.969$ and $\sigma_{\eta_5} = 0.034$; for $\sigma = 1.8$ K, they are $\mu_{\eta_5} = 0.133$ and $\sigma_{\eta_5} = 0.226$.

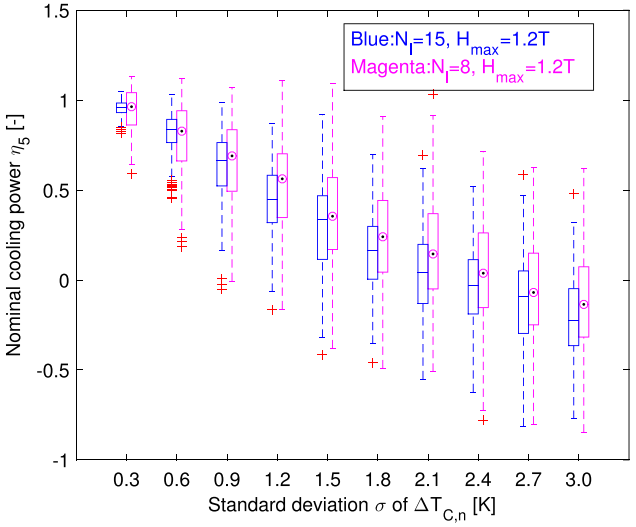

FIG. 13. Sensitivity of nominal cooling power η_5 to standard deviation σ of $\Delta T_{C,n}$ with $N_l = 15$ and $N_l = 8$. The line insides the box represents the median value of η_5 when $N_l = 15$, and the spot for $N_l = 8$.

upper limit of 0.984 and the low limit of 0.931, which implies that the regenerator performance will lie in this region with a probability of 50%. However, with increasing σ, the median value decreases dramatically and the 25%–75% box becomes bigger, meaning there is larger uncertainty in η_5. It can be seen that $\sigma > 0.6$ K will lead to at least 16.6% performance reduction in the median value and η_5 varies in quite a large range, which means a risk of getting vastly different performance from two regenerators built in the same way.

Fig. 11 presents the histogram and probability density of η_5 when $\sigma = 0.3$ K and $\sigma = 1.8$ K. It can be observed that in each case η_5 follows the extreme value distribution and the normal distribution, respectively. Besides the obvious difference in median values, the case $\sigma = 0.3$ K shows a concentrated distribution and there is a much smaller calculated

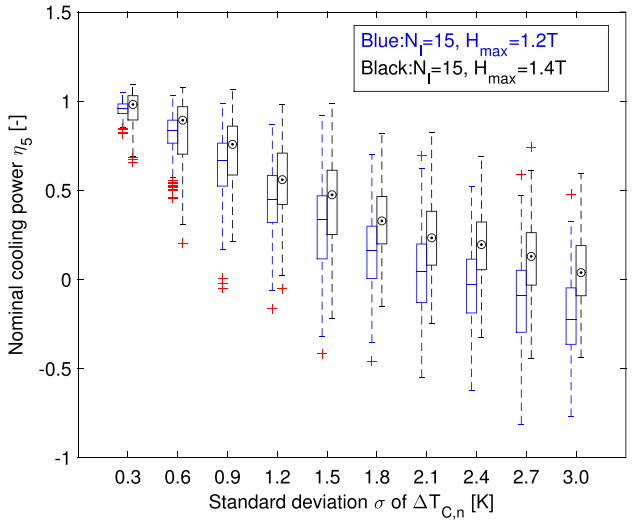

FIG. 12. Sensitivity of nominal cooling power η_5 to standard deviation σ of $\Delta T_{C,n}$ with $H_{max} = 1.2$ T and $H_{max} = 1.4$ T. The line insides the box represents the median value of η_5 when $H_{max} = 1.2$ T, and the spot for $H_{max} = 1.4$ T.

standard deviation in the nominal cooling power σ_{η_5} of 0.034, compared to $\sigma_{\eta_5} = 0.226$ of the wide distribution when $\sigma = 1.8$ K. It is also reflected in Fig. 10 in the type of wider box and region of extreme values.

As the ΔS_{mag} curve tends to be wider when the internal magnetic field increases, it is hypothesized that the multi-layer regenerators should be less sensitive to Curie temperature variation $\Delta T_{C,n}$ with a larger applied field. This is verified in Fig. 12. The results from the maximum applied field of 1.2 T and 1.4 T are compared, and it shows that not only the median cooling power is higher at larger σ but also the variation of the nominal cooling power is lower at higher applied field, that is, the regenerators become less sensitive to σ with an increase of the maximum applied field from 1.2 T to 1.4 T.

The sensitivity of an 8-layer regenerator is also investigated. Fig. 13 shows that the median value of η_5 from the 8-layer regenerator has a smaller slope with increasing σ compared to that of the 15-layer regenerators; however, the deviation in the nominal cooling power becomes larger, which indicates the regenerators with more layers are less sensitive and can reduce the risk of the performance degradation. It should be noted that, generally, the regenerators with more layers and larger maximum applied field will produce more cooling power; therefore, the base values for calculating η_5 in Figs. 12 and 13 are different.

IV. CONCLUSION

Multi-layer regenerators using the first order material series $La(Fe,Mn,Si)_{13}H_y$ were investigated. The impact of the number of layers N_l, the sensitivity to the working temperature T_w, and the sensitivity to the variations in the Curie temperature $\Delta T_{C,n}$ were presented. The results showed that the nominal cooling power increases significantly with N_l, and from a practical point, around 10 to 15 layers may be suitable for a temperature span ΔT of 30 K given an applied field of

1.2 T. Meanwhile, multi-layer regenerators are quite sensitive to T_w and the best temperature region is 307–277 K. With a non-optimized $T_{C,n}$ arrangement, the performance increases slowly with decreasing ΔT. It was also shown that fewer layers are needed for a smaller ΔT with optimized $T_{C,n}$ arrangement, and around 2.24 layers are necessary for every 5 K ΔT to get 90% of the maximum performance.

Moreover, Curie temperature variations $\Delta T_{C,n}$ in the layers close to the cold or hot end have significant impact on the system performance, which is most sensitive to $\Delta T_{C,n}$ of layers close to the cold end. Furthermore, AMR performance with $\Delta T_{C,n}$ that varies according to a uniform or normal distribution was predicted for a population of randomly generated layers. The results showed that multi-layer regenerators are considerably sensitive to RMSD of $\Delta T_{C,n}$ for a uniform distribution, and the standard deviation σ of $\Delta T_{C,n}$ for a normal distribution. In the latter case, $\sigma > 0.6$ K will cause at least 16.6% decrease in the median value of the nominal cooling power η_5 and increase in the uncertainty of η_5, which implies that there may be huge difference in the performance of two regenerators built from materials with the same accuracy in Curie temperature. It is also predicted that larger applied field and layer number will decrease the sensitivity of the multi-layer regenerator to $\Delta T_{C,n}$.

ACKNOWLEDGMENTS

This work was financed by the ENOVHEAT project which is funded by Innovation Fund Denmark (Contract No. 12-132673). The authors would like to thank Vacuumschmelze GmbH, Germany for providing the $La(Fe,Mn,Si)_{13}H_y$ material.

[1]K. Engelbrecht, D. Eriksen, C. R. H. Bahl, R. Bjørk, J. Geyti, J. A. Lozano, K. K. Nielsen, F. Saxild, A. Smith, and N. Pryds, "Experimental results for a novel rotary active magnetic regenerator," Int. J. Refrig. **35**, 1498–1505 (2012).
[2]S. Jacobs, J. Auringer, A. Boeder, J. Chell, L. Komorowski, J. Leonard, S. Russek, and C. Zimm, "The performance of a large-scale rotary magnetic refrigerator," Int. J. Refrig. **37**, 84–91 (2014).
[3]S. Y. Dan'Kov, A. Tishin, V. Pecharsky, and K. Gschneidner, "Magnetic phase transitions and the magnetothermal properties of gadolinium," Phys. Rev. B **57**, 3478–3490 (1998).
[4]J. A. Barclay, "The theory of an active magnetic regenerative refrigerator," NASA STI/Recon Technical Report No. 83 (1982), p. 34087.
[5]J. Tušek, A. Kitanovski, U. Tomc, C. Favero, and A. Poredoš, "Experimental comparison of multi-layered LaFeCoSi and single-layered Gd active magnetic regenerators for use in a room-temperature magnetic refrigerator," Int. J. Refrig. **37**, 117–126 (2014).
[6]A. Rowe and A. Tura, "Experimental investigation of a three-material layered active magnetic regenerator," Int. J. Refrig. **29**, 1286–1293 (2006).
[7]A. Rowe, "Thermodynamics of active magnetic regenerators: Part I," Cryogenics **52**, 111–118 (2012).
[8]K. Engelbrecht, K. K. Nielsen, C. R. H. Bahl, C. P. Carroll, and D. van Asten, "Material properties and modeling characteristics for $MnFeP_{1-x}As_x$ materials for application in magnetic refrigeration," J. Appl. Phys. **113**, 173510 (2013).
[9]S. Fujieda, Y. Hasegawa, A. Fujita, and K. Fukamichi, "Thermal transport properties of magnetic refrigerants $La(Fe_xSi_{1-x})_{13}$ and their hydrides, and $Gd_5Si_2Ge_2$ and MnAs," J. Appl. Phys. **95**, 2429–2431 (2004).
[10]A. Barcza, M. Katter, V. Zellmann, S. Russek, S. Jacobs, and C. Zimm, "Stability and magnetocaloric properties of sintered La(Fe, Mn, Si)H alloys," IEEE Trans. Magn. **47**, 3391–3394 (2011).
[11]K. Morrison, K. Sandeman, L. Cohen, C. Sasso, V. Basso, A. Barcza, M. Katter, J. Moore, K. Skokov, and O. Gutfleisch, "Evaluation of the reliability of the measurement of key magnetocaloric properties: A round robin study of La(Fe, Mn, Si)H conducted by the SSEEC consortium of European laboratories," Int. J. Refrig. **35**, 1528–1536 (2012).
[12]A. Fujita, S. Fujieda, Y. Hasegawa, and K. Fukamichi, "Itinerant-electron metamagnetic transition and large magnetocaloric effects in $La(Fe_xSi_{1-x})_{13}$ compounds and their hydrides," Phys. Rev. B **67**, 104416 (2003).
[13]C. Wang, Y. Long, T. Ma, B. Fu, R. Ye, Y. Chang, F. Hu, and J. Shen, "The hydrogen absorption properties and magnetocaloric effect of $La_{0.8}Ce_{0.2}(Fe_{1-x}Mn_x)_{11.5}Si_{1.5}H_y$," J. Appl. Phys. **109**, 07A910 (2011).
[14]A. Smith, C. R. H. Bahl, R. Bjørk, K. Engelbrecht, K. K. Nielsen, and N. Pryds, "Materials challenges for high performance magnetocaloric refrigeration devices," Adv. Energy Mater. **2**, 1288–1318 (2012).
[15]T. Lei, K. K. Nielsen, and K. Engelbrecht, "Modelling and simulation of regenerators with complex flow arrangements for active magnetocaloric refrigeration," in *ASME 12th Biennial Conference on Engineering Systems Design and Analysis* (2014), Vol. 3, p. V003T12A007.
[16]K. K. Nielsen, G. Nellis, and S. Klein, "Numerical modeling of the impact of regenerator housing on the determination of Nusselt numbers," Int. J. Heat Mass Transfer **65**, 552–560 (2013).
[17]S. Jeppesen, S. Linderoth, N. Pryds, L. T. Kuhn, and J. B. Jensen, "Indirect measurement of the magnetocaloric effect using a novel differential scanning calorimeter with magnetic field," Rev. Sci. Instrum. **79**, 083901 (2008).
[18]R. Bjørk, C. R. H. Bahl, and M. Katter, "Magnetocaloric properties of $LaFe_{13-x-y}Co_xSi_y$ and commercial grade Gd," J. Magn. Magn. Mater. **322**, 3882–3888 (2010).

A.1.6 Strain development during the phase transition of $La(Fe,Mn,Si)_{13}H_z$ (under review in *Applied Physics Letters*)

Strain development during phase transition of La(Fe,Mn,Si)$_{13}$H$_z$

Henrique N. Bez,[1, a)] Kaspar K. Nielsen,[1] Anders Smith,[1] Poul Norby,[1] Kenny Ståhl,[2] and Christian R. H. Bahl[1]
[1)] *Department of Energy Conversion and Storage, Technical University of Denmark - Frederiksborgvej 399, DK-4000 Roskilde - Denmark*
[2)] *Department of Chemistry, Technical University of Denmark - Anker Engelunds Vej, DK-2800 Lyngby - Denmark*

(Dated: 26 April 2016)

We use the powder X-ray diffraction (XRD) to evaluate the temperature dependence of the crystalline properties during the magnetic phase transition of La(Fe,Mn,Si)$_{13}$H$_z$ as a function of Fe/Mn/Si ratio. Both the paramagnetic and ferromagnetic phases were observed as peak overlaps in the patterns around the Curie temperature, and it occurred continuously in a temperature range of about 5 K. Using the Williamson-Hall method we evaluate the strain developing in the crystallites during the transition and find that it is associated with the growth of the ferromagnetic phase as the transition occurred. Based on our measurements and microstructure analyses, we propose that cracking during the phase transition is due to or aggravated by the small content a La-rich phase.

Keywords: Magnetocaloric, phase transition, strain, XRD,Williamson-Hall

Magnetocaloric materials present a thermal response close to the Curie temperature of their magnetic phase transition when an external magnetic field is varied[1]. These materials are generally classified in two groups: (i) first order phase transition (FOPT) materials, which exhibit latent heat during the transition and where the transition usually involves structural and/or volume change; (ii) second order phase transition (SOPT) materials, which does not have latent heat associated with the transition, nor structural or volume change is involved.

One of the material series that may have a FOPT is La(Fe,Mn,Si)$_{13}$H$_z$, where the Curie temperature, T_C, can be controlled by the proportion of Fe/Mn/Si. Recently we have shown via X-ray diffraction (XRD) measurements, that for the stoichiometries with $T_C > 300$ K the materials present a volume change above 0.8 % [2], without changing the type of crystal structure. Even though this material presents a FOPT, the transition develops during a temperature range, rather than discontinuously as a FOPT is expected to. We have shown using magnetization measurements and applying the Bean-Rodbell model[3], that this behavior is due to chemical inhomogeneities, which effectively lead to a spread of T_C throughout the sample.

Due to the volume change during the phase transition, one may expect development of internal stresses. It has been shown[4,5] that samples may break apart during the phase transition, due to the so called *virgin effect*. Moreover, Lovell et al.[6] showed that the magnetic coupling between fragments of La(Fe,Si)$_{13}$ may vary with local demagnetization effects, which then further leads to a more distributed transition as the fragments are further apart from each other due to a weaker magnetic coupling and a slower kinetics of nucleation and growth of domains.

To investigate these questions in greater detail we used X-ray diffraction (XRD) measurements in combination with the Williamson-Hall method to calculate the strain in both the paramagnetic (PM) and ferromagnetic (FM) phases across the phase transition. Williamson and Hall[7] showed that the peak broadening, β, from an XRD pattern is related to the strain and particle size as given by:

$$\beta(\theta)\cos\theta = \frac{k\lambda}{D} + 4\epsilon\sin\theta, \quad (1)$$

where k is a constant, λ is the wavelength of the incident radiation, D is the particle size, ϵ is the strain and θ is the scattering angle.

The material used in this investigation is particulate $LaFe_{13-x-y}Mn_xSi_yH_{1.65}$ where $x = 0.25, 0.22$ and 0.06; $y = 1.28, 1.23$ and 1.18, respectively. This material was synthesized by power mettalurgical process described elsewhere[8]. Scanning electron microscopy (SEM) backscattered images were taken in a Hitachi TM3000 microscope equipped with a Bruker Quantax EDS detector. The XRD measurements were performed as explained elsewhere[2]. Rietveld refinement was done in order to extract the peak broadening for each sample and each temperature. To evaluate the effect of the interstitial hydrogen in the strain of the material, a dehydrogenation process was additionally performed on the material with $x = 0.06$. This was done as follows: the powder material was heated to 773 K at 5 K/min under high vacuum, where the temperature was held for one hour then slowly cooled to room temperature in the furnace. The dehydrogenated sample did not show extra peaks in the XRD, confirming that no oxide phase was formed during the dehydrogenation process.

Figure 1 shows a SEM backscattered image of a particle which has undergone XRD measurements. The grain sizes are in the range of 15 to 30 μm, and $\alpha-$Fe is present as a secondary phase together with minor content of La-rich phase (the white spots in the image). The crack propagation in this particle shows the brittle behavior of the main phase, La(Fe,Mn,Si)$_{13}$H$_z$. One of the cracks is

[a)] Electronic mail: hnbe@dtu.dk

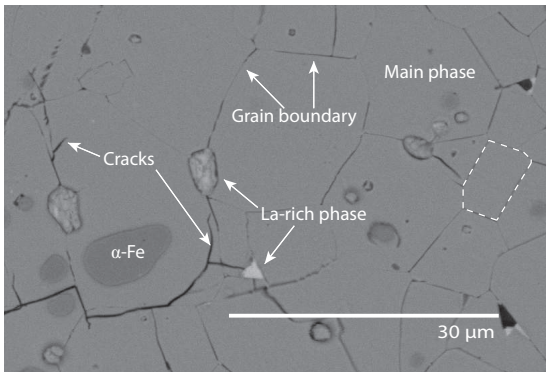

FIG. 1. Particle of $LaFe_{13-x-y}Mn_xSi_yH_{1.65}$ where x=0.06. One may notice the crystallites with sizes between 15 and 30 μm, cracks, and small contents of secondary phases, i.e. α-Fe and La-rich phase.

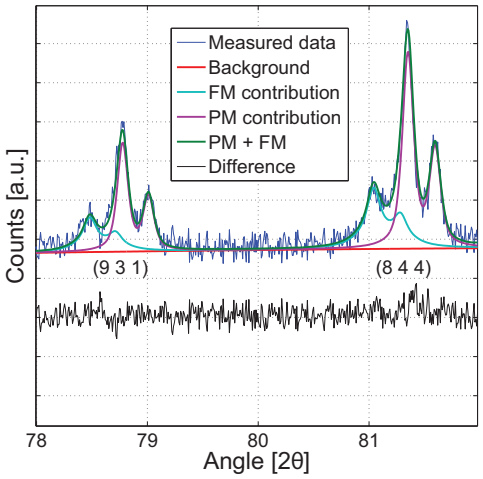

FIG. 2. (Color online) Zoom in the peaks (9 3 1) and (8 4 4) of the XRD pattern (at 340 K) of $LaFe_{13-x-y}Mn_xSi_yH_{1.65}$ where x=0.06, showing the measured data, the fittings and the difference between the measured and the total fitting.

pointed out in the image starting on the La-rich phase, and it may be seen that contours the grain containing α-Fe, a ductile phase, and continues to propagate transgranularly in the main phase. This is the usual crack propagation behavior of a brittle material[9], as a transgranular fracture tends to happen when the crystal is more brittle than the grain boundary itself. This is the case for the main phase, while not for the ductile secondary phase. It should be noted that the crack did not necessarily develop during the XRD measurements, but could be a consequence of the grinding of the particles done prior the measurement.

The Rietveld refinement measurements show a continuous phase transition with respect to temperature, developing over a temperature range of about 5 K, as reported elsewhere[2]. This points to a region of co-existence of the FM and PM phases. Figure 2 shows two peaks of the main phase at 340 K for $x = 0.06$. As pure phases, these peaks would be in pairs (due to Kα_1 and Kα_2 radiation); however, due to the lattice parameter difference between the FM and PM phase, and the co-existence of both phases, groups of three peaks are observed. In Figure 2, one may see the FM and PM contribution in the peaks; lower angle peaks means that the lattice parameter of the FM phase is larger than the PM phase.

Usually, the peak broadening β is determined by fitting each peak individually. However, in this case such an approach cannot be used as during the phase transition of La(Fe,Mn,Si)$_{13}$H$_z$ each peak will be the result of an overlap of the two phases. Therefore it is necessary to apply the Rietveld refinement full width at half maximum fitting parameters for the analysis. From the refinement one may express β as a function of the angle as given by the Caglioti equation[10]:

$$\beta(\theta) = (u\tan^2\theta + v\tan\theta + w)^{1/2}, \qquad (2)$$

where u, v and w are fitting parameters. Once β is extracted from the refinement, one has to correct for the instrumental broadening that is implicit in every measurement. The broadening can be corrected through a Gaussian summation of two contributions:

$$\beta^2 = \beta(\theta)^2_{\text{measured}} - \beta(\theta)^2_{\text{instrumental}}, \qquad (3)$$

where the $\beta_{\text{instrumental}}$ was extracted from a strain free standard LaB_6 sample, measured under the same conditions. Figure 3 shows the Williamson-Hall plot for the FM phase of $LaFe_{13-x-y}Mn_xSi_yH_{1.65}$ where $x = 0.06$, for $335 \leq T \leq 341$ K. Equation 1 shows that the slope of this linear function is in fact the average strain in that phase. One may see that all the slopes are positive, which would mean positive strain, i.e. the material is under tensile stress. However, this method of strain calculation does not allow determining the type of stress. The broadening of the full width at half maximum does not relate differently for the different types of strain or stress. The implicit principle of broadening as an outcome of strain is related to the non-uniform distances between atoms in the crystal structure, and both a compressive or a tensile non-uniform strain will give a broadening of the peak. Therefore, we consider the different effects before, during and after the transition to decide whether the strain is positive or negative.

Figure 4(a) shows the strain and (b) the volume as a function of temperature for $x = 0.06$. The error bars represent the error propagated from the different fittings – Rietveld refinement fitting of the La(Fe,Mn,Si)$_{13}$H$_z$ material, the reference material LaB_6 and the linear fitting in Figure 3. The pure phases present some degree of non-uniform strain. This is expected as the material is not perfect – it contains some dislocation concentration, grain boundaries, etc. Moreover, as shown before[2], the material tends to exhibit some chemical inhomogeneity that by itself could generate a

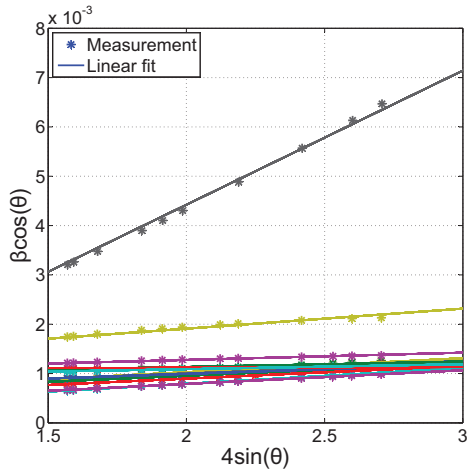

FIG. 3. (Color online) Williamson-Hall plot of the ferromagnetic phase of $x = 0.06$ for different temperatures.

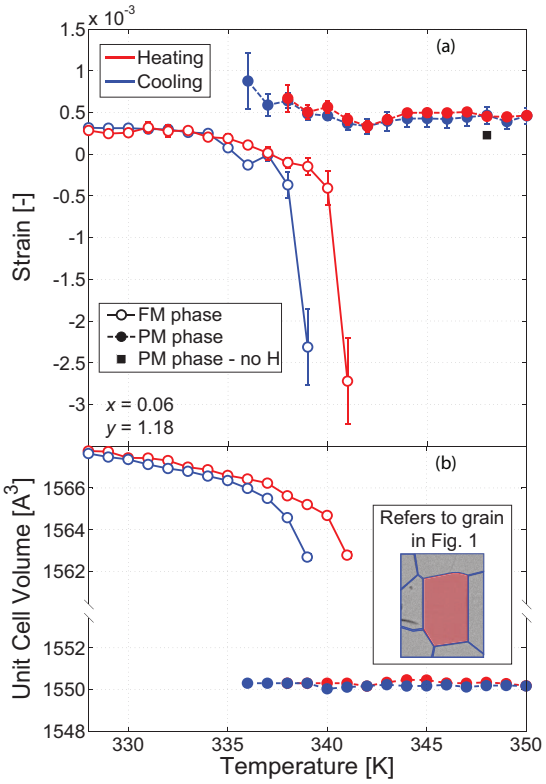

FIG. 4. (Color online) (a) Strain and (b) volume as a function of the temperature. The inset shows a schematic micrograph of the material for explanation of the strain development during the transition.

non-uniform strain. In fact, the H-desorbed sample exhibits half of the strain of the hydrogenated sample, as Figure 4 shows. As the H is inserted interstitially in the structure and resulting in an increase of the unit cell, it is expected to generate positive strain on the pure phases, i.e. a tensile strain.

The strain in the FM phase decreases to zero just below the T_C. This can be caused by the softening of the lattice induced by the magnetic interactions closer to the transition[11]. As explained before, via the Williamson-Hall method one cannot predict if the strain is negative or positive, therefore there are two possibilities for the FM phase during the transition, positive or negative. However, as one may see in Figure 4(b) the FM volume decreases continuously with temperature. Therefore the most likely strain development is compressive strain being developed during the transition. Accordingly in Figures 4 and 5 the strain during the transition is shown with negative values. Figure 5 shows the strain development of two other FOPT La(Fe,Mn,Si)$_{13}$H$_z$ compositions, showing a similar behavior, confirming what is observed for $x = 0.06$.

The FM and PM phases present different strain behavior. This can be related to the differing behavior of the bulk modulus of each phase, as observed in other magnetocaloric materials with a volume change at T_C[12]. A schematic drawing of the expected behavior of the bulk moduli is shown in Figure 6. The larger volume of the FM phase is attributed to the magneto-elastic coupling present in this material. As Gruner et al.[11] have shown, close to the transition there is a softening of the lattice induced by the magnetic interactions. This will lead to a decrease of the bulk modulus of the FM phase, making this phase more susceptible to stresses through deformation. The same softening is not expected for the PM phase, where the magnetic moments are uncoupled; thus the bulk modulus of this phase will be more or less constant close to the transition, as schematically shown in Figure 6.

The fact that the transition occurs gradually as a function of the temperature can be explained by a compositional distribution where neighbouring grains have slightly different transition temperatures. The inset in Figure 4(b) shows a grain of the main phase (highlighted in Figure 1). As the temperature increases, more and more FM grains become isolated and completely surrounded by the PM phase. The PM phase, being smaller, will then compress the FM phase, and the FM phase being susceptible to compressive forces will respond with a large strain. On top of this behavior, the material is polycrystalline and even if there were no chemical inhomogeneity, strain development could be expected as the different crystallites have different orientation[13].

As a multi-phase material (La(Fe,Mn,Si)$_{13}$H$_z$, α-Fe and La-rich phase), the fracture mechanics is dependent on the microstructure as well. It has been reported[14], and also observed in the present investigation, that α-Fe crystallites are imbedded within the crystallites of the main phase, while La-rich phases are located at the grain boundaries of the main phase. The latter, even if only present in such small amounts as not to be found by XRD, may play an important role in the cracking mechanism.

One can think of the cracking mechanism in analogy

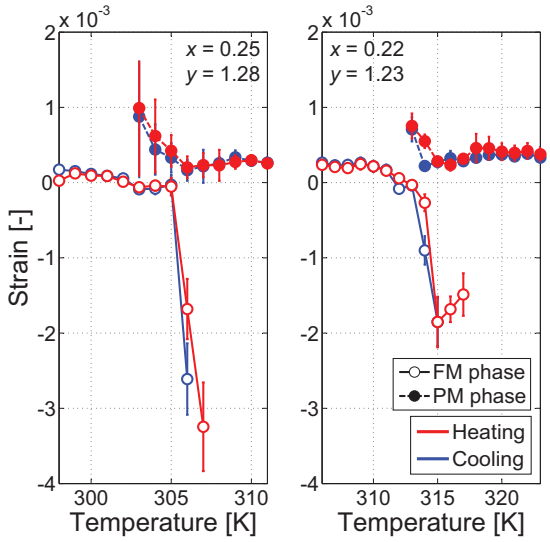

FIG. 5. (Color online) Strain as function of temperature for x= 0.25 and 0.22, during heating and cooling.

with the hydrogen-decrepitation observed in several rare-earth alloys[15–17]. During the decrepitation process, hydrogen diffuses first in the rare-earth rich phase, expanding it and generating cracks. Upon further hydrogenation, the hydrogen also diffuses through the main phase (e.g. for Nd-magnets, $Nd_2Fe_{14}B$), which also breaks apart. The whole mechanism of hydrogen-decrepitation, i.e. powderization of bulk material, is given by volume expansion of different phases. In the case investigated here, an analogous process occurs; however, instead of being chemically driven, it is thermally/magnetically driven. Still, in this case we observe that the FM phase is much more susceptible to strain than the PM phase due to the softening of the magnetic interactions. Therefore, it seems that the cracking must start in the rare-earth-rich phase, which is also the only brittle phase without volume change, and then propagate throughout the sample; one can observe this behavior in Figure 1. Thus we propose that a way to make the material more mechanically stable is to find a method to remove the La-rich secondary phase.

In conclusion, we have investigated the phase transition of La(Fe,Mn,Si)$_{13}$H$_z$ by careful XRD measurements and refinement. We observed an asymmetric development of strain, which differs from the FM to the PM phase. The strain development is related to three main features: (i) chemical inhomogeneity, (ii) different bulk moduli change and (iii) polycrystalline samples. The interplay between these three leads to the strain development observed, and are intrinsically related to the cracking during phase transition. We point out that a better understanding of the mechanical properties of such magnetocaloric materials with first order phase transition is crucial for designing the materials for magnetic cooling applications, and that decreasing the amount of La-rich phase could lead to a more mechanically stable material.

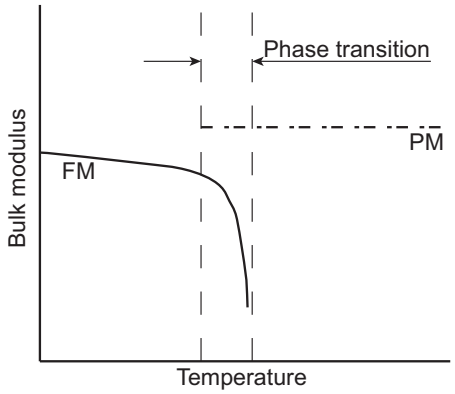

FIG. 6. (Color online) Schematic drawing of the bulk moduli behavior of the ferromagnetic and paramagnetic phase.

This work was financed by the ENOVHEAT project which is funded by Innovation Fund Denmark (contract no 12-132673). The authors are grateful to Vacuumschmelze GmbH for providing the samples.

[1] A. Smith, C. R. H. Bahl, R. Bjø rk, K. Engelbrecht, K. K. Nielsen, and N. Pryds, Adv. Energy Mater. **2**, 1288–1318 (2012).
[2] H. N. Bez, K. K. Nielsen, P. Norby, A. Smith, and C. R. H. Bahl, AIP Adv. **6**, 056217 (2016).
[3] C. P. Bean and D. S. Rodbell, Phys. Rev. **126**, 104–115 (1962).
[4] J. Lyubina, R. Schäfer, N. Martin, L. Schultz, and O. Gutfleisch, Adv. Mater. **22**, 3735–9 (2010).
[5] A. Waske, L. Giebeler, B. Weise, A. Funk, M. Hinterstein, M. Herklotz, K. Skokov, S. Fähler, O. Gutfleisch, and J. Eckert, Phys. Status Solidi RRL **9**, 136–140 (2015).
[6] E. Lovell, A. M. Pereira, a. D. Caplin, J. Lyubina, and L. F. Cohen, Adv. Energy Mater. **5**, 1401639 (2015).
[7] G. K. Williamson and W. H. Hall, Acta Metall. **1**, 22–31 (1953).
[8] A. Barcza, M. Katter, V. Zellmann, S. Russek, S. Jacobs, and C. Zimm, "Stability and Magnetocaloric Properties of Sintered La(Fe, Mn, Si)$_{13}$H$_z$ Alloys," IEEE Transactions on Magnetics **47**, 3391–3394 (2011).
[9] M. André Meyers and K. K. Chawla, 2nd ed. (Cambridge University Press, 2009) p. 882.
[10] G. Caglioti, A. Paoletti, and F. P. Ricci, Nucl. Instrum. Methods **3**, 223 (1958).
[11] M. E. Gruner, W. Keune, B. Roldan Cuenya, C. Weis, J. Landers, S. I. Makarov, D. Klar, M. Y. Hu, E. E. Alp, J. Zhao, M. Krautz, O. Gutfleisch, and H. Wende, Phys. Rev. Lett. **114**, 057202 (2015).
[12] C. Zhu, R. Zheng, J. Su, and J. He, Appl. Phys. Lett. **74**, 3504–3506 (1999).
[13] R. E. A. McKnight, T. Moxon, A. Buckley, P. A. Taylor, T. W. Darling, and M. A. Carpenter, Journal of Physics: Condensed Matter **20**, 075229 (2008).
[14] J. Liu, M. Krautz, K. Skokov, T. G. Woodcock, and O. Gutfleisch, Acta Mater. **59**, 3602–3611 (2011).
[15] I. R. Harris, C. Noble, and T. Bailey, J. Less-Common Met. **106**, L1–L4 (1985).
[16] M. Ragg, G. Keegan, H. Nagel, and I. R. Harris, Int. J. Hydrogen Energy **22**, 333–342 (1997).
[17] H. N. Bez, C. S. Teixeira, B. G. F. Eggert, J. A. Lozano, M. S. Capovilla, J. R. B. Jr., and P. A. P. Wendhausen, IEEE Transactions on Magnetics **49**, 4626–4629 (2013).

A.1.7 Non-universal scaling of the magnetocaloric effect as an insight into spin-lattice interactions in manganites (accepted in *Physical Review B*)

Non-universal scaling of the magnetocaloric effect as an insight into spin-lattice interactions in manganites

Anders Smith, Kaspar K. Nielsen, Henrique N. Bez, and Christian R.H. Bahl

Department for Energy Conversion and Storage,

Technical University of Denmark, Risø Campus,

Frederiksborgvej 399, DK-4000 Roskilde, Denmark

(Dated: October 13, 2015)

Abstract

We measure the magnetocaloric effect of the manganite series $La_{0.67}Ca_{0.33-x}Sr_xMnO_3$ by determining the isothermal entropy change upon magnetization, using variable field calorimetry. The results demonstrate that the field dependence of the magnetocaloric effect close to the critical temperature is not given uniquely by the critical exponents of the ferromagnetic-paramagnetic phase transition, i.e. the scaling is non-universal. A theoretical description based on the Bean-Rodbell model and taking into account compositional inhomogeneities is shown to be able to account for the observed field dependence. In this way the determination of the non-universal field dependence of the magnetocaloric effect close to a phase transition can be used as a novel method to gain insight into the strength of the spin-lattice interactions of magnetic materials. The approach is shown also to be applicable to first order transitions.

PACS numbers: 75.30.Sg, 64.60.F-,75.40.Cx

For the past several decades manganites have been a rich field of study for their many fascinating properties, including colossal magnetoresistance, multiferroic effects, charge and orbital ordering including novel inhomogenous phases such as stripes.[1–3] In recent years several manganites have also been studied for their magnetocaloric properties, both in bulk[4, 5] and in thin films, where it was shown that the effect of substrate strain can increase the magnetocaloric effect significantly.[6] This has been motivated by their possible application in near-room-temperature magnetic refrigeration.[7] However, measurements of the magnetocaloric effect can also give important information on the intrinsic magnetic properties of materials, as has been realised since the very discovery of the effect by Weiss and Piccard.[8, 9] Of particular interest is the field dependence of the magnetocaloric quantities which has been discussed extensively in recent literature. It has been claimed that the field dependence close to the critical temperature of the ferromagnetic-to-paramagnetic transition is universal and determined by the critical exponents of the system in question.[10, 11] Recently we showed theoretically that the scaling of the magnetocaloric quantities is not universal: Models in the same universality class differ in their scaling exponents at finite fields.[12] Here we show that this lack of universality is in fact observable experimentally and can be used to gain insight into the strength of the spin-lattice interactions which ultimately are responsible for the appearance of the magnetocaloric effect.

The rare earth manganites are in many ways an ideal system to study the field dependence of the magnetocaloric quantities, due to the ability of changing the critical temperature of the sample by only slight variations in the composition. The parent composition is the perovskite structure $AMnO_3$ where A is a rare earth such as La. By substituting alkali metal or alkaline earth metal cations on the A-site one obtains ferromagnetic compounds with a critical temperature which varies strongly with composition. Here we study the series $La_{0.67}Ca_{0.33-x}Sr_xMnO_3$. When x is varied from 0 to 0.33, the critical temperature of the compound varies from 267 K to 369 K.[13] The universality class of these compounds have been investigated by a number of authors. Their findings are not in total agreement. Thus, several authors have found that one end member of the series, $La_{0.67}Ca_{0.33}MnO_3$, has a first order transition,[14–16] but this has been questioned by detailed examination of the latent heat associated with the transition.[17] For the other end member, $La_{0.67}Sr_{0.33}MnO_3$, there is agreement that the transition is second order, but the critical exponents have variously been determined as being those of the 3D Ising model[18, 19] and those of the 3D Heisenberg

model.[20, 21] For the series as a whole no general studies of the universality class exist. Starting with $La_{0.67}Sr_{0.33}MnO_3$ the main effect of substituting Ca for Sr is to change the Mn-O-Mn bond angle from $\sim 170°$ to $\sim 162°$, which changes the hopping integrals between the orbitals e_g(Mn)–p_σ(O)–e_g(Mn), causing a change in the coupling between the Mn-spins.[22, 23] The consensus seems to be that all the materials of the series except possibly close to $La_{0.67}Ca_{0.33}MnO_3$ (i.e. small x) are in fact second order and of the same universality class. Even though the series has not been investigated extensively enough to rule out a cross-over from one universality class to another (e.g., from 3D Heisenberg to 3D Ising) as x is varied, it can be safely assumed that the critical exponents do not vary continuously with x.

The identification of the universality class is often done by determining the critical exponents β and γ (associated, respectively, with the scaling of the magnetization M below T_c and the scaling of the inverse susceptibility χ^{-1} above T_c) from magnetization data. A widely used procedure is that of Kaul:[24, 25] From a starting guess of the critical exponents β and γ the modified Arrott plot of M^β as a function of $(H/M)^{1/\gamma}$ is constructed; here H is the internal field (i.e. the applied field corrected for demagnetization). From the intersection of the curves (suitably extrapolated) with the coordinate axes, $M(T, H = 0)$ and $\chi^{-1}(T, H = 0)$ are extracted and new exponents β' and γ' calculated. The procedure is then repeated until convergence; T_c is determined as the temperature corresponding to the M^β vs. $(H/M)^{1/\gamma}$ curve which intersects $(0, 0)$ when extrapolated. Although in principle rather straightforward, in practice this procedure requires a temperature resolution of the magnetization which is often not available: If, as is usual, magnetization curves are only recorded with a temperature step of 2–3 K the number of curves which actually fall within the critical region is very limited. With a T_c near room temperature a critical region of the order of $|t| \lesssim 10^{-2}$[24] (where $t = (T - T_c)/T_c$ is the reduced temperature) corresponds to a temperature interval of 5–10 K. This means that only 4–5 Arrott curves fall within the critical region. To use these curves to extract three parameters (β, γ, T_c) is clearly associated with considerable uncertainty. And since the critical exponents of, e.g., the 3D Heisenberg and 3D Ising models are in fact rather close, assigning a definite universality class on the basis of this procedure is often not warranted.

The analysis is further hampered by the fact that these systems have a marked tendency to form magnetically inhomogeneous states, even in single crystals.[26] For polycrystalline samples the compositional variations will be at least as pronounced. This means that the

magnetic transition becomes spread out over a range of critical temperatures assumed to depend on the local composition, $T_c = T_c(\mathbf{r})$. If the spread in critical temperatures is comparable to the size of the critical region, it becomes difficult to assign definite critical exponents to the system. This is also true if one tries to determine the universality from the critical behaviour of the specific heat, which some have suggested as a better alternative.[27] Here we will show that direct measurements of the isothermal entropy change not only allows for a reliable determination of the critical temperature but also gives insight into the spin-lattice coupling of the system. The isothermal entropy change, ΔS, is defined as the change in entropy as the magnetic field is changed from 0 to H at a fixed temperature T: $\Delta S(T, H) = S(T, H) - S(T, 0)$. In most systems, including the manganites, it is negative, since the effect of the external field is to order the magnetic moments. The field dependence of ΔS is characterized by an approximately power law behaviour. Thus, one can define a scaling exponent b through $\Delta S \sim aH^b$. The scaling exponent will in general be a function of both T and H, making its introduction more a matter of convenience than of profound theoretical justification. Considered as a function of T, b will have a minimum both at T_c and at the temperature at which $-\Delta S$ peaks.[28] These two temperatures are in general close together and as $H \to 0$ they coincide. This means that the critical temperature can be experimentally determined as the temperature for which the scaling exponent is a minimum for low fields.

Six samples with a nominal composition of $La_{0.67}Ca_{0.33-x}Sr_xMn_{1.05}O_3$ (with x varying from 0.0375 to 0.0750 in steps of 0.0075) were produced in the form of irregularly shaped pieces of thin plates (thickness 0.3 mm) by tapecasting the powder suspended in a slurry, followed by sintering (for details, see ref. 29). The slight over-stoichiometry of Mn was chosen to improve the sintering properties of the plates; this does not change the structure or critical temperature.[30] An additional seventh sample with a composition of $La_{0.67}Ca_{0.33}MnO_3$ was prepared by the solid state route. X-ray diffraction shows single phase samples, and lattice parameters are consistent with those found in the literature. The isothermal entropy change ΔS was measured using a custom built differential scanning calorimeter (DSC) equipped with a permanent magnet array allowing the field to be varied.[31, 32] This way of determining the isothermal entropy change ΔS at a fixed temperature, instead of the conventional method of integrating magnetization data,[33] allows for a much better temperature resolution of the data, critical for the results presented here. The samples were mounted in

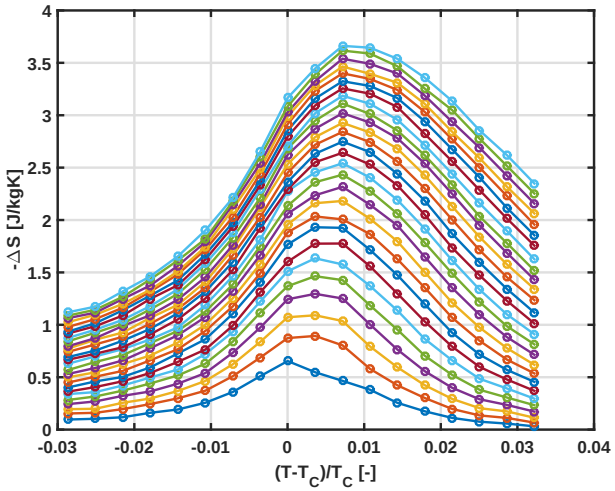

FIG. 1. (Color online) The isothermal entropy change of $La_{0.67}Ca_{0.33-x}Sr_xMn_{1.05}O_3$ for $x = 0.0375$ for a field change of $0.05 - 1.5$ T, as measured by in-field calorimetry. The relative uncertainty on each data point is approximately 5%.

such a way as to minimize the geometrical demagnetization. In addition, the measurements were corrected for demagnetization using magnetization data taken in a Lake Shore 7407 vibrating sample magnetometer (VSM) and the geometrical demagnetization correction for a prism.[34] For each sample the isothermal entropy change was measured starting from zero field for applied magnetic fields in the range of $\mu_0 H = 0.05$ T to 1.5 T with a field step of 0.05 T and a temperature step of 1 K. A representative set of measurements is shown in Fig. 1. To extract a (temperature-dependent) scaling exponent b, the results were fitted to a power law function of the form aH^b.

The (mean) critical temperature of each sample, found as the position of the minimum of the scaling exponent b, shows a dependence on nominal composition consistent with that previously found in the literature,[14] see Fig. 2, confirming the accuracy of the nominal compositions of the samples.

In Fig. 3 we show the scaling exponent at the critical temperature of each sample. A clear trend is visible, showing b decreasing continuously from a value close to 2/3, which is that expected for a pure mean field model, as the Sr content x is decreased. All of the LCSM samples are second order, and the continuous dependence of the scaling exponent on x demonstrates the non-universal nature of the field dependence of the isothermal entropy change. It can also be seen that the scaling of $La_{0.67}Ca_{0.33}MnO_3$ is markedly different; this

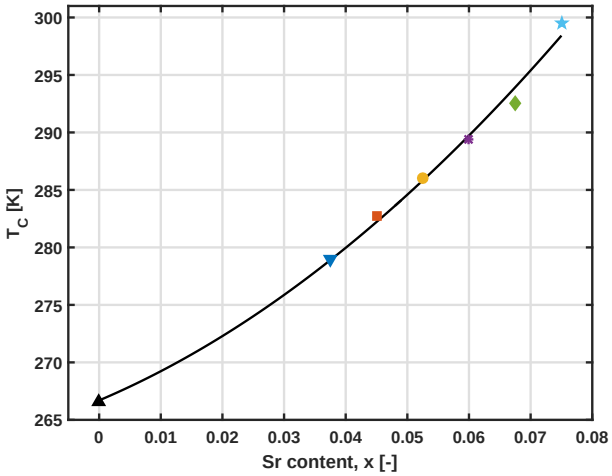

FIG. 2. (Color online) Critical temperatures of the seven samples as a function of strontium content. The critical temperature was determined as the position of the minimum of the scaling exponent associated with the isothermal entropy change for low fields. The line is a guide to the eye.

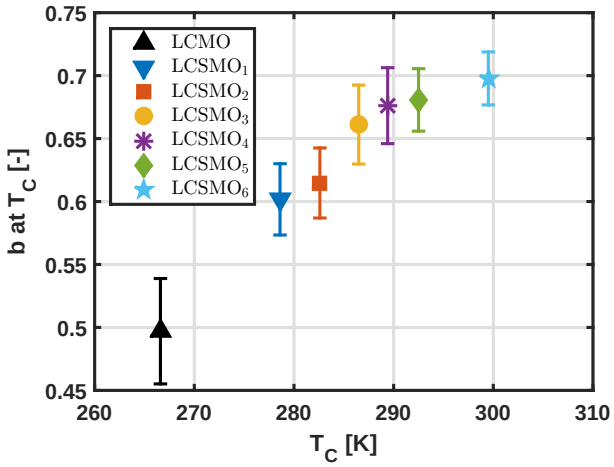

FIG. 3. (Color online) Experimentally determined scaling exponent of the isothermal entropy change at the critical temperature of each sample and a field change of 1.5 T. For a pure mean field model with no spin-lattice coupling, a scaling exponent close to 2/3 is expected.

is a signature of a more first-order-like phase transition, as will be discussed below.

To interpret these results we use a mean field approach. Previous theoretical work has been based on a Landau expansion of the free energy in which a distribution of T_c has been introduced.[35, 36]. However, the Landau expansion is only valid for small applied fields H and close to T_c (being a series expansion in M); in particular, it does not account for the

approach to saturation. It is preferable to consider a microscopic model which accounts for saturation and which gives physically reasonable results for any T and H. Here we use the Bean-Rodbell model, which is basically a mean-field model in which the exchange constant depends on the lattice spacing.[37] It is well known that the critical exponents of the Bean-Rodbell model (for the range of parameters where the transition is second order) are those of mean field theory. However, the model is not identical to Landau theory outside the critical region (small reduced temperature and small field). While the Bean-Rodbell model like all mean field models predicts the wrong critical exponents for the manganites, the spread in T_c combined with the limited temperature resolution of most magnetization measurements make it questionable whether the critical region is in fact accessed experimentally. Outside the critical region (but still close to T_c), it is well accepted that the Bean-Rodbell model accounts qualitatively and to some extent also quantitatively for the behavior of many magnetocaloric materials, in particular the manganites.[38] As we show below, the field behaviour of the isothermal entropy change can in fact be modelled rather satisfactorily by the Bean-Rodbell model. This allows information on the spin-lattice interactions to be extracted.

The Bean-Rodbell model is a mean field model in which the exchange coupling λ is assumed to depend linearly on the inter-spin distance: $\lambda = \lambda_0(1 + \beta\frac{V-V_0}{V_0})$, where V is the actual volume, V_0 the volume in the absence of exchange interactions, and β a parameter which controls the strength of the spin-lattice coupling. The behavior of the model can conveniently be classified by another parameter η, given by

$$\eta = 40\frac{N_s}{V}\kappa(k_B T_0)\beta^2\frac{(J(J+1))^2}{(2J+1)^4 - 1}. \quad (1)$$

Here J is the magnitude of the spins (in units of $\hbar$), N_s the number of spins, κ the isothermal compressibility, and T_0 the transition temperature for $\beta = 0$; k_B is Boltzmann's constant. The order of the phase transition described by the Bean-Rodbell model is determined by η: $\eta > 1$ correspond to a first order transition. For $\eta < 1$ the Bean-Rodbell model describes a second order phase transition with the same critical exponents as the standard mean field model but with different behavior at finite fields. This leads to a scaling behaviour of ΔS which depends on η, as shown recently.[12] To account for compositional variations we introduce a statistical spread in T_0, i.e. we assume T_0 to be normally distributed around its average with a standard deviation of σ_{T_c}. We do a least-squares fit of the field dependence

of ΔS at $T = T_c$ for each sample, using η and σ_{T_c} as the fitting parameters. This results in the values of η (and thus of the magnitude of the spin-lattice interaction β) and σ_{T_c} shown in Figs. 4 and 5; the error bars in the plots reflect a 10% increase in the residual of the fitting.

The five LCSM samples all have approximately the same spread, independent of x, consistent with the fact that they are produced by the same route which presumably introduces similar amounts of compositional variation. The spread in critical temperature is in all cases of the order of 1–1.5 K, while the spread in T_c for the LCM sample is slightly higher. The value of η increases as x decreases, i.e. addition of strontium increases the magnitude of the spin-lattice coupling. For the LCM sample we find a value of 1.2 for η, meaning that the transition in LCM is of first order. This is consistent with several other reports in the literature. Our finding that the magnitude of the spin-lattice interaction increases monotonously with decreasing x quantifies the often-stated assertion that the LCSM materials become more first-order-like as $x = 0$ is approached. The fact that η is significantly larger than 1 for $x = 0$ suggests that the first order transition may extend to finite, but small x (certainly smaller than $x = 0.0375$ which we unequivocally identify as second order). We see that even though there are no critical exponents associated with a first order transition, our approach looking at the full field dependence of ΔS allows us to identify the order of the transition.

In conclusion we have demonstrated experimentally that the finite-field scaling of the magnetocaloric effect close to a second order phase transition is not universally determined by the critical exponents of the transition. Further, we have argued that compositional variations in many cases lead to a spread in T_c of a magnitude which preclude direct access to the critical region. Nevertheless, a careful determination of the field dependence of the isothermal entropy change close to the average transition temperature allowed us to determine the variation of the effective spin-lattice coupling as a function of the strontium content of lanthanum calcium strontium manganite. It will be of interest to apply this analysis to different series of magnetocaloric compositions.

This work was in part financed by the ENOVHEAT project which is funded by Innovation Fund Denmark (contract no. 12-132673). The assistance of Kjeld Bøhm Andersen in the tapecasting of the samples is gratefully acknowledged.

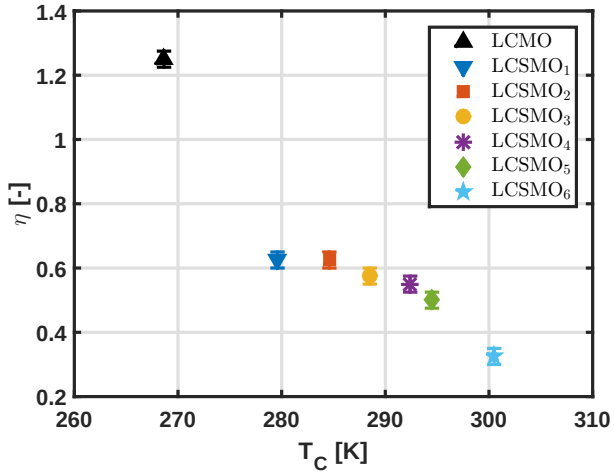

FIG. 4. (Color online) Bean-Rodbell parameter η extracted from the experimental field dependence of ΔS by fitting to the Bean-Rodbell model with a spread in critical temperatures. The increase in η as the strontium content decreases is equivalent to an increase in the spin-lattice coupling. A value $\eta > 1$ corresponds to a first order transition.

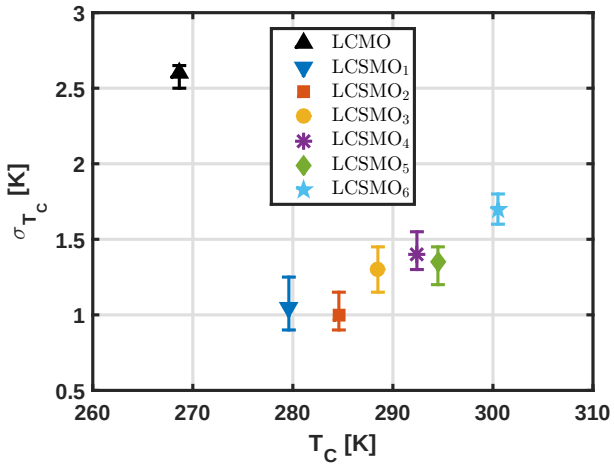

FIG. 5. (Color online) The spread in critical temperature as measured by the standard deviation σ_T, calculated from a fit of the model to the experimental field dependence of ΔS at T_c.

[1] J. Coey, M. Viret, and S. von Molnar, Adv. Phys. **48**, 167 (1999).

[2] M. B. Salamon and M. Jaime, Rev. Mod. Phys. **73**, 583 (2001).

[3] N. Mathur and P. Littlewood, Phys. Today **56**, 25 (2003).

[4] M. H. Phan and S. C. Yu, J. Magn. Magn. Mater. **308**, 325 (2007).

[5] L. I. Koroleva, D. M. Zashchirinskii, A. S. Morozov, and R. Szymczak, J. Exp. Theor. Phys. **115**, 653 (2012).

[6] X. Moya, C. Ducati, L. Phillips, M. Ghidini, M. Vickers, E. Defay, N. Mathur, L. Hueso, O. Hovorka, A. Berger, L. Hueso, F. Maccherozzi, S. Dhesi, A. Tovstolytkin, D. Podyalovskii, M. Ghidini, and E. Defay, Nat. Mater. **12**, 52 (2013).

[7] A. Smith, C. R. H. Bahl, R. Bjørk, K. Engelbrecht, K. K. Nielsen, and N. Pryds, Adv. Energy Mater. **2**, 1288 (2012).

[8] P. Weiss and A. Piccard, J. Phys. (Paris), 5th Ser. **7**, 103 (1917).

[9] A. Smith, Eur. Phys. J. H **38**, 507 (2013).

[10] V. Franco and A. Conde, Int. J. Refrig. **33**, 465 (2010).

[11] V. Franco, A. Conde, J. M. Romero-Enrique, Y. I. Spichkin, V. I. Zverev, and A. M. Tishin, J. Appl. Phys. **106**, 103911 (2009).

[12] A. Smith, K. K. Nielsen, and C. R. H. Bahl, Phys. Rev. B **90**, 104422 (2014).

[13] A. R. Dinesen, S. Linderoth, and S. Mørup, J. Phys.: Condens. Matter **17**, 6257 (2005).

[14] J. Mira, J. Rivas, F. Rivadulla, C. Vázquez-Vázquez, and M. A. López-Quintela, Phys. Rev. B **60**, 2998 (1999).

[15] J. Mira, J. Rivas, F. Rivadulla, and M. Quintela, Physica B - Cond. Mat. **320**, 23 (2002).

[16] V. Amaral, J. Araujo, Y. Pogorelov, J. Sousa, P. Tavares, J. Vieira, P. Algarabel, and M. Ibarra, J. Appl. Phys. **93**, 7646 (2003).

[17] K. Morrison, A. Berenov, and L. Cohen, Mater. Res. Soc. Symp. Proc. **1310**, 31 (2011).

[18] A. Oleaga, A. Salazar, D. Prabhakaran, and A. T. Boothroyd, J. Appl. Phys. **95**, 7366 (2004).

[19] A. Oleaga, A. Salazar, D. Prabhakaran, and A. T. Boothroyd, Phys. Rev. B **70**, 184402 (2004).

[20] M. Nasri, M. Triki, E. Dhahri, and E. K. Hlil, J. Alloys Compd. **546**, 84 (2013).

[21] M. H. Phan, V. Franco, N. S. Bingham, H. Srikanth, N. H. Hur, and S. C. Yu, J. Alloys Compd. **508**, 238 (2010).

[22] J. L. García-Muñoz, J. Fontcuberta, M. Suaaidi, and X. Obradors, J. Phys.: Condens. Matter **8**, L787 (1996).

[23] A. R. Dinesen, *Magnetocaloric and magnetoresistive properties of* $La_{0.67}Ca_{0.33-x}Sr_xMnO_3$, Ph.D. thesis, Technical University of Denmark (2004).

[24] S. Kaul, J. Magn. Magn. Mater. **53**, 5 (1985).

[25] M. H. Phan, G. T. Woods, A. Chaturvedi, S. Stefanoski, G. S. Nolas, and H. Srikanth, Applied Physics Letters **93**, 252505 (2008).

[26] N. G. Bebenin, R. I. Zainullina, and V. V. Ustinov, J. Magn. Magn. Mater. **322**, 963 (2010).

[27] A. Gamzatov, A. Aliev, K. Khizriev, I. Kamilov, and A. Mankevich, J. Alloys Compd. **509**, 8295 (2011).

[28] V. Franco, A. Conde, M. D. Kuz'min, and J. M. Romero-Enrique, J. Appl. Phys. **105**, 07A917 (2009).

[29] R. Bulatova, C. R. H. Bahl, K. Andersen, L. T. Kuhn, and N. Pryds, Int. J. Appl. Ceram. Tec. **12**, 891 (2015).

[30] I. Biering, M. Menon, and N. Pryds, Ceram. Trans. **205**, 71 (2009).

[31] K. K. Nielsen, H. N. Bez, L. von Moos, R. Bjørk, D. Eriksen, and C. R. H. Bahl, submitted to Rev. Sci. Instrum. (2015).

[32] R. Bjørk, C. R. H. Bahl, A. Smith, and N. Pryds, J. Magn. Magn. Mater. **322**, 3664 (2010).

[33] V. K. Pecharsky and K. A. Gschneidner Jr., J. Appl. Phys. **86**, 565 (1999).

[34] A. Aharoni, J. Appl. Phys. **83**, 3432 (1998).

[35] J. Lyubina, M. D. Kuz'min, K. Nenkov, O. Gutfleisch, M. Richter, D. L. Schlagel, T. A. Lograsso, and K. A. Gschneidner, Phys. Rev. B **83**, 012403 (2011).

[36] N. G. Bebenin, R. I. Zainullina, and V. V. Ustinov, J. Appl. Phys. **113**, 073907 (2013).

[37] C. P. Bean and D. S. Rodbell, Phys. Rev. **126**, 104 (1962).

[38] J. A. Turcaud, A. M. Pereira, K. G. Sandeman, J. S. Amaral, K. Morrison, A. Berenov, A. Daoud-Aladine, and L. F. Cohen, Phys. Rev. B **90**, 024410 (2014).

A.1.8 Resin bonded magnetocaloric plates tested in a refrigeration device (*submitted to the International Journal of Refrigeration*)

Resin bonded magnetocaloric plates tested in a refrigeration device.

Christian R.H. Bahl, Kristina Navickaitė, Henrique Neves Bez, Tian Lei, Kurt Engelbrecht, Rasmus Bjørk

Department of Energy Conversion and Storage, Technical University of Denmark, Frederiksborgvej 399, DK-4000 Roskilde, Denmark

Ke Li, Zhenxin Li, Jun Shen, Wei Dai

Technical Institute of Physics and Chemistry, Chinese Academy of Sciences, Beijing 100190, China

Jichen Jia, Yuanyuan Wu, Yi Long

University of Science and Technology Beijing, Beijing 100083, China

Fengxia Hu, Baogen Shen

Institute of Physics, Chinese Academy of Sciences, Beijing 100190, China

Abstract

Bonded plates made by hot pressing $La_{0.85}Ce_{0.15}Fe_{11.25}Mn_{0.25}Si_{1.5}H_y$ particles and resin have been tested as active magnetic regenerators in a small scale magnetocaloric device. Firstly the plates were carefully characterised magnetically and thermally. The plates were prepared with 5 wt% resin, and from density measurements it was found that the volume ratio of the magnetocaloric material was 0.53, due to the resin and porosity. The best operating conditions for the plate regenerator were determined at which a temperature span of 6.4 K was measured along the plates.

Keywords: Magnetocaloric, Magnetic refrigerator, Regenerator, Resin bonding

1. Introduction

For the past decade significant progress has been made in bringing magnetic refrigeration towards commercialisation. New magnetocaloric materials have been developed and magnetocaloric demonstration devices become ever more powerful and efficient (Kitanovski et al., 2015). Most of these devices have employed the so called active magnetic regenerator (AMR) cycle as a method of utilising the magnetocaloric effect in a device. Here the temperature of a porous regenerator structure is increased and decreased by applying and removing a magnetic field, while a heat transfer fluid is reciprocated back and forth in order to build up a temperature gradient. Keys to utilising the AMR concept are firstly to have a magnetocaloric material, or a cascade of such, with high magnetocaloric effect, and secondly, to shape this material in a way that there is good thermal contact between solid and fluid, allowing an effective heat transfer.

Many magnetocaloric materials have been studied and considered for application in devices (Smith et al., 2012). Recently a lot of research has been done on materials that undergo a first order magnetic phase transition, so-called first order materials, as they have a very high magnetic entropy change ΔS_{M} around the phase transition. An important example of this class of materials is the intermetallic $\mathrm{La(Fe,Si)_{13}H}_y$, which has been studied with a number of different elements doped into the Fe and Si sites (Zhang et al., 2013). In general this material series has a high magnetocaloric effect, a tunable Curie temperature and only a small amount of undesirable thermal hysteresis. The disadvantage of these materials is the lack of structural stability due to the volume change at the phase transition (Lyubina et al., 2010).

Recently, different strategies for shaping these and similar magnetocaloric materials into the desired shapes have been proposed and tested. Polymer bonding and pressing to plates has been demonstrated for first order materials (Skokov et al., 2014; Radulov et al., 2015) and second order materials of the same type (Pulko et al., 2015). Other methods of producing structures have also been presented, such as injection moulding (Lanzarini et al., 2015), hot pressing with Cu (Liu et al., 2015) and extrusion into monoliths Pryds et al. (2011). Actual AMR performance in a test device has only been reported for the second order bonded plates (Pulko et al., 2015). However, porous particle based regenerators where the particles are bonded for stability have been presented, most notably by Jacobs et al. (2014) using

$La(Fe,Si)_{13}H_y$.

Here we demonstrate in a small versatile AMR device the performance of plates of first order materials bonded with resin and cured during pressing.

2. Experimental

A $La_{0.85}Ce_{0.15}Fe_{11.25}Mn_{0.25}Si_{1.5}$ ingot was prepared in an induction furnace. The purity of the raw materials was at least 99.9 wt%. The annealed ingots were crushed into particles less than 0.35 mm in size for the hydrogenation process. These were annealed in a high purity hydrogen atmosphere until saturation. The structure of the hydrides was confirmed by x-ray powder diffraction. The hydrogen concentration y of $La_{0.85}Ce_{0.15}Fe_{11.25}Mn_{0.25}Si_{1.5}H_y$ (referred to as LaFeSiH in the following) was estimated to be 2.0 wt% by the inert gas pulse infrared absorption method. When vacuum annealing under 350 °C for 2 hours a sharp decrease of the Curie temperature was observed due to the escape of H.

2.1. Processing the plates

The resulting powder was mixed with a phenolic resin system in a mass ratio of 20:1. The mixed powders were pressed into plate shape under pressure of 20 MPa and then solidified at 150 °C for 10 minutes, as shown in Figure 1. The plates were prepared in the size 25 mm by 40 mm, in order to fit into the regenerator test device, with a thickness of 0.5 mm. Measuring the specific heat shows that the Curie temperature does not change during the resin curing process, indicating that the LaFeSiH is unaffected by this treatment.

2.2. Characterisation of the plates

Thermal conductivity was measured at 300 K using a Thermal Transport Option (TTO) on a Quantum Design physical property measurement system (PPMS). The density of the plates was measured using AccuPyc 1340 helium pycnometer repeating each measurement 10 times, and the density of the resin was measured with a Pentapyc5200e Auto Density Analyzer. The magnetic properties were analysed in a LakeShore vibrating sample magnetometer (VSM) 7407. The sample was measured in the temperature range 270 K - 306 K at applied fields up to 1.5 T. The specific heat of the sample was measured using a custom built differential scanning calorimeter (DSC),

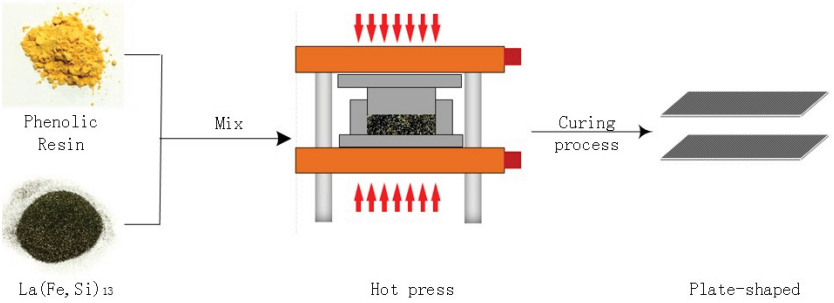

Fig. 1: Illustration of the fabrication process, showing the mixing of powder with resin, hot pressing and the final plates.

allowing the applied field to be varied in the range 0-1.6 T at a fixed orientation relative to the sample (Jeppesen et al., 2008). An scanning electron microscope (SEM) (Hitachi TM3000, equipped with a Bruker Quantax EDS detector) was used to analyse the microstructure of a piece of one of the plates.

3. Results

3.1. Physical properties of the plates

Figure 2 shows the structure of a plate. It consists of irregular particles of LaFeSiH with a broad size range. There is a significant porosity between the particles. Using EDS mapping we can probe the presence of the resin by isolating the carbon signal, as this will be unique to the resin. As shown in Figure 3 the resin covers large areas binding together the particles, but there are still significant volumes of porosity between particles. So the system can be considered as a mixture of three phases, LaFeSiH, resin and pores.

A representative density value of 5721 ± 3 kgm^{-3} was measured based on pieces of plates weighing in total 2.3947 g. The mass fraction of magnetocaloric material is 0.95 and the mass fraction of resin is 0.05. Based on the structural symmetry and lattice parameters the density of the LaFeSiH, ρ_{LaFeSiH}, is 7207 kgm^{-3} and the density of the resin, ρ_{resin}, is 1166 kgm^{-3} found by crushing down a sample of pure resin into a powder and measuring the density. Assuming that there are no pores closed to helium penetration, the weighted average density of the LaFeSiH and the resin is 5724 kgm^{-3}, very close to the measured value.

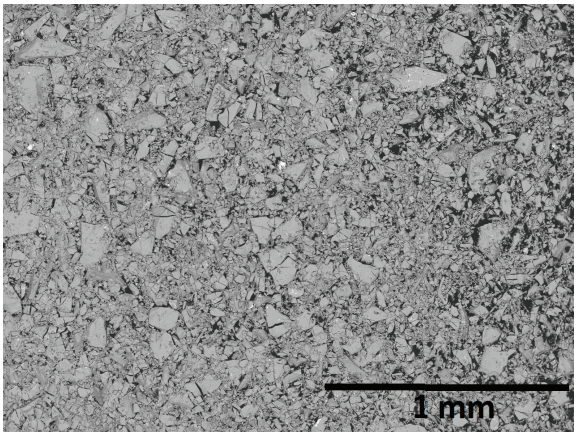

Fig. 2: Backscattered SEM image of an area of a plate. The image shows the surface of the plate as prepared.

Geometrically measuring and weighing a plate gave a density of approximately 4000 kgm^{-3}, which includes all pores. From this we can calculate the porosity of the plates as 0.30. Thus the volume fractions of LaFeSiH, resin and pores are approximately 0.53, 0.17 and 0.30, respectively.

Based on the mass fractions of LaFeSiH and resin the reduction in effective adiabatic temperature change due to the presence of resin is quite limited. The actual temperature change $\Delta T_{\mathrm{effective}}$ will be given by:

$$\Delta T_{\mathrm{effective}} = \frac{\Delta T_{\mathrm{ad}} c_{\mathrm{H,MCM}}}{0.95 c_{\mathrm{H,MCM}} + 0.05 c_{\mathrm{H,resin}}} \approx 0.94 \Delta T_{\mathrm{ad}}, \tag{1}$$

where $\mathrm{c_{H,MCM}}$ and $\mathrm{c_{H,resin}}$ are the specific heats of LaFeSiH (500 $\mathrm{Jkg^{-1}K^{-1}}$) and resin (1200 $\mathrm{Jkg^{-1}K^{-1}}$), respectively. As the peak of specific heat in LaFeSiH is very narrow and field dependent we use the background value away from the peak. Closer to the peak $\Delta T_{\mathrm{effective}}$ will be even closer to ΔT_{ad}.

Magnetisation measurements were used to calculate the magnetic entropy change, ΔS_{M}, in the conventional way described by Pecharsky and Gschneidner Jr. (1999b). A 11.76 mg piece of one of the plates was used. This piece seemed free of resin, but there may be a little resin included. This would slightly change the level reached by the peak, but not the profile shape. The data was corrected for demagnetisation approximating the sample to a prism and using the expression by Aharoni (1998).

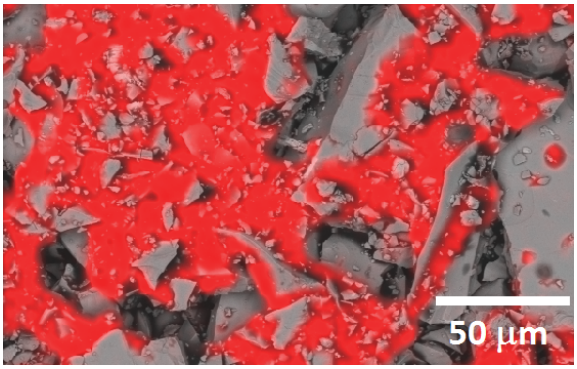

Fig. 3: EDS filtered to show carbon. The resin is observed to bind together the particles, but there is also a significant porosity remaining as discussed in the text.

To probe for the presence of hysteresis the magnetic entropy was measured both during cooling and during heating. Between each measurement the sample was 'reset' at an equilibrium temperature far above or below the measurement range, for cooling and heating, respectively (Caron et al., 2009). The ΔS_{M} values are consistent with those found in literature (Zhang et al., 2013). Figure 4 shows that the hysteresis at the phase transition is very low. In order to further probe the presence of hysteresis the specific heat of the sample was measured during heating and cooling at different temperature ramp rates in the range 1 Kmin^{-1} to 5 Kmin^{-1}. By applying a linear regression of the peak temperatures with respect to the temperature rates, the hysteresis is found to be 0.4 ± 0.2 K, consistent with the magnetisation data, as shown in Figure 5.

When applying a magnetic field the temperature of the peaks of the specific heat increase at a rate of about 4.3 KT^{-1}. Also, the peak goes from being very sharp to becoming more broad, as shown in Figure 6, consistent with the results reported by Basso et al. (2015). Due to the very low value of the hysteresis and the errors on the lines fitted to the peak temperatures, determining the critical field at which the hysteresis vanishes cannot be done with confidence.

3.2. Regenerator testing

A stack of 25 plates was tested as an AMR in a small scale test device at DTU. The stack was prepared as described in Engelbrecht et al. (2011) by layering the plates with ø0.25 mm metal wire as spacers. The sides were then sealed with epoxy before removing the metal wire. This resulted in a

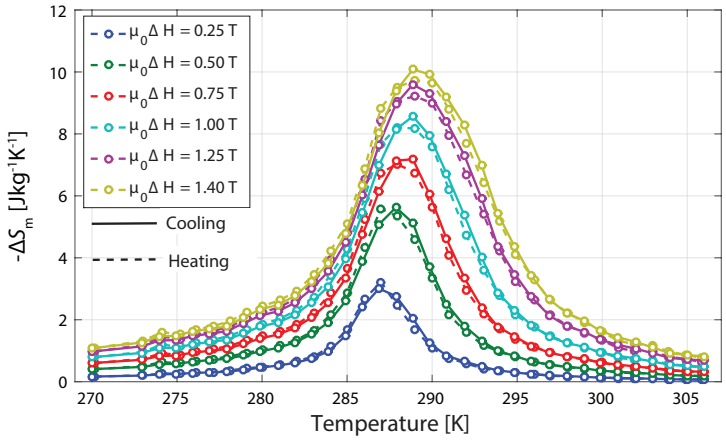

Fig. 4: Measured entropy change of a sample of one of the plates. Both the heating and cooling curves are shown, and the hysteresis is observed to be small.

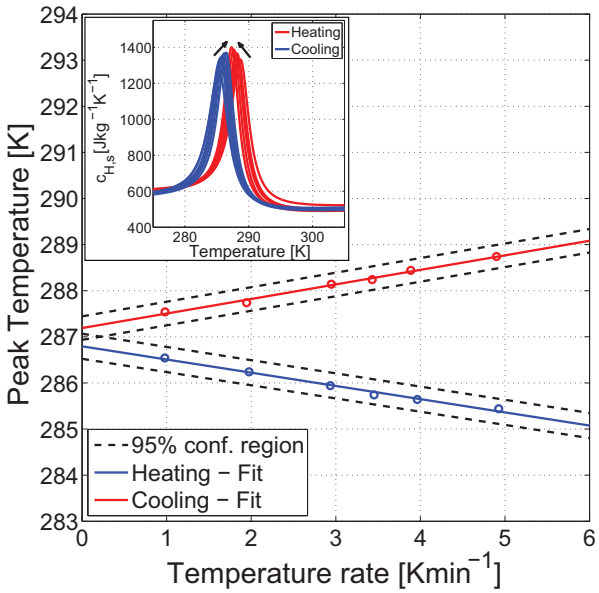

Fig. 5: The peak temperature of the specific heat measured at different ramp rates in the DSC. Both the heating peak and the cooling peak have been measured, as shown in the inset. Extrapolating to zero ramp rate gives a measure of the hysteresis.

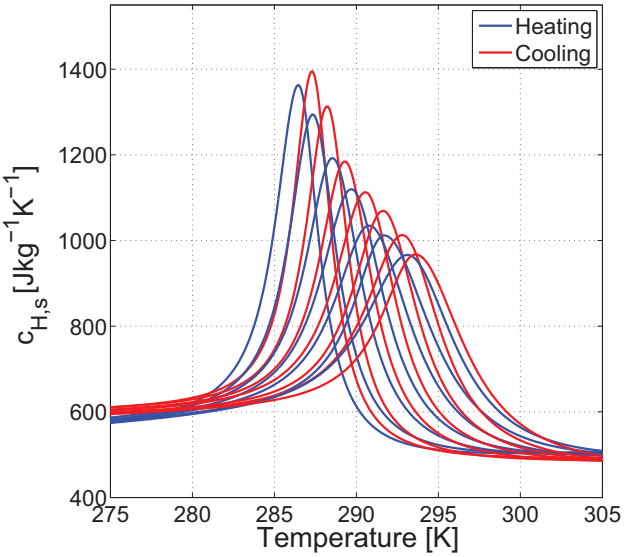

Fig. 6: Field dependence of the peak in specific heat, for cooling and heating. Applied fields of 0, 0.25, 0.50, 0.75, 1.00, 1.25 and 1.50 T are shown, with the peak moving up in temperature and broadening as the field increases.

20.5 mm tall stack, 25 mm wide and 40 mm long, which was then mounted in a cylindrical regenerator housing using silicone around the border of the stack. The mass of each plate was approximately 2 g, so the mass of the regenerator was 50 g.

The glued stack, before being mounted in the regenerator housing, is shown in Figure 7. The channels between the plates are clearly seen, but close inspection reveals that with the chosen plate spacing the unevenness of the plates becomes significant. Thus the actual channel height varies significantly across the regenerator. The effect of this will be discussed later.

Testing of the regenerator was done in the versatile test device described previously (Bahl et al., 2008; Engelbrecht et al., 2011). Here the cylindrical regenerator housing moves in and out of the bore of a 1.1 T permanent magnet Halbach cylinder. A ø18 mm reciprocating piston forces the heat transfer fluid through the regenerator to perform the well known four steps of the AMR cycle (Pecharsky and Gschneidner Jr., 1999a). Demineralised water, mixed with 2 vol% of ENTEK FNE corrosion inhibitor, as recommended for a similar material by Velazquez et al. (2014), was used as the heat transfer fluid.

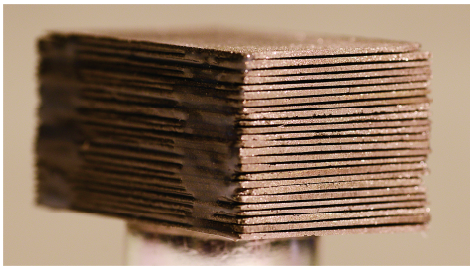

Fig. 7: The stack of plates used in the regenerator before being mounted in the cylindrical regenrator housing.

Three parameters were varied in the testing of the regenerator, the fluid velocity, the length the piston is moved, and the ambient temperature. A heat exchanger at the hot end of the regenerator keeps the temperature of this close to that of the temperature controlled cabinet, in which the device is mounted. The length the piston moves is conventionally expressed as the utilisation, ϕ, defined as

$$\phi = \frac{m_{\mathrm{f}} c_{\mathrm{f}}}{m_{\mathrm{s}} c_{\mathrm{H,s}}} \tag{2}$$

where m_{f} is the mass of the fluid pushed through the regenerator in one blow, c_{f} is the specific heat of the fluid, m_{s} is the mass of the solid regenerator and $c_{\mathrm{H,s}}$ is the specific heat of the bonded plates. m_{f} is found from the movement of the ø18 mm piston, c_{f} is set as the textbook value of 4200 $\mathrm{Jkg^{-1}K^{-1}}$, ignoring the small amount of corrosion inhibitor, m_{s} is 50 g and for $c_{\mathrm{H,s}}$ the background value of 600 $\mathrm{Jkg^{-1}K^{-1}}$ is used, as found from Figure 6, including the resin.

Starting at an ambient temperature of 290 K and a utilisation of 0.23, the AMR cycle is repeated until the temperature difference between the cold end and the hot end, known as the temperature span, ΔT_{span}, reached a constant value. Different values of the fluid velocity were tested recording the achieved ΔT_{span}, as shown in Figure 8. Note that the fluid velocity reported is the velocity in the channels, not the piston velocity. It is observed that the highest values of the span are found in a broad optimum around about 7 $\mathrm{mms^{-1}}$, which is consistent with that previously found for plates of a similar material (Engelbrecht et al., 2011). The plates in Engelbrecht et al. (2011) were somewhat thicker and cut from blocks made of different $\mathrm{La(Fe,Co,Si)_{13}}$ compounds, all with a second order phase transition. Using this fluid velocity of 7 $\mathrm{mms^{-1}}$ and staying at an ambient temperature of 290 K the utilisation

was varied to find the best performance, as shown in Figure 9. Again a broad peak of ΔT_{span} is observed, the utilisation giving the highest values being about 0.23, similar to Engelbrecht et al. (2011); Bahl et al. (2012). Due to the change in the distance and velocity of the piston movement the cycle time varies in the range of 5 to 24 s in Figure 8 and in the range 5.5 - 12 s in Figure 9.

The magnetocaloric effect in materials with a first order magnetic phase transition occurs over a narrow range of temperatures, as shown in Figure 4. Thus it is very important when utilising these materials in a device that the span of the device is across the peak in magnetocaloric effect. Figure 10 shows the achieved span of the device as the hot end temperature is changed, while keeping a utilisation of 0.23 and a fluid velocity of 7 mms^{-1}. The cycle time remains constant at about 9 s. We observe a relatively narrow peak that drops off sharply at 293 K, which is a few degrees above the peak temperature of ΔS_{M} in a 1 T field. The maximum ΔT_{span} was 6.4 K, which is around double the maximum adiabatic temperature change of such a material in this applied field, see e.g. Basso et al. (2015), demonstrating the AMR cycle in the regenerator. The maximum span is lower than the 10.2 K span achieved using plates of the benchmark material Gd (Engelbrecht et al., 2011), but comparable to the spans achieved using plates of a single second order LaFeCoSi material or the single perovskite type material $\text{La}_{0.67}\text{Ca}_{0.26}\text{Sr}_{0.07}\text{Mn}_{1.05}\text{O}_3$ (Pulko et al., 2015; Engelbrecht et al., 2011). When grading the regenerator to two similar materials with Curie temperatures close to each other the span can be significantly increased for both the LaFeCoSi type materials (Engelbrecht et al., 2011) and the perovskite type materials (Bahl et al., 2012). Layering materials is key to the success of first order materials, due to the narrow peaks of the magnetocaloric effect, so it is clearly expected that if a regenerator were constructed with a number of different Curie temperatures along the flow direction significantly higher performance could be reached. However, as shown recently it is extremely important to have the correct spacing of the Curie temperatures, as the performance can easily be significantly reduced if this is not the case (Lei et al., 2015).

4. Discussion

The measured maximum temperature span of 6.4 K is relatively low compared to other reported spans from this and similar devices. But when using

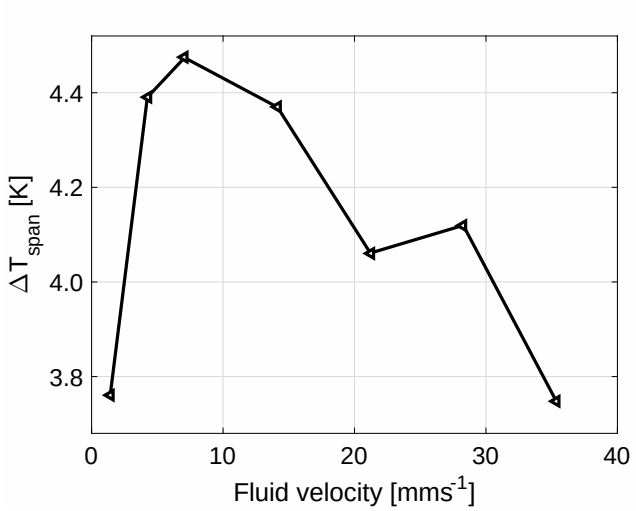

Fig. 8: The steady state temperature span between the hot and the cold end as a function of the velocity of the fluid being pushed between the plates.

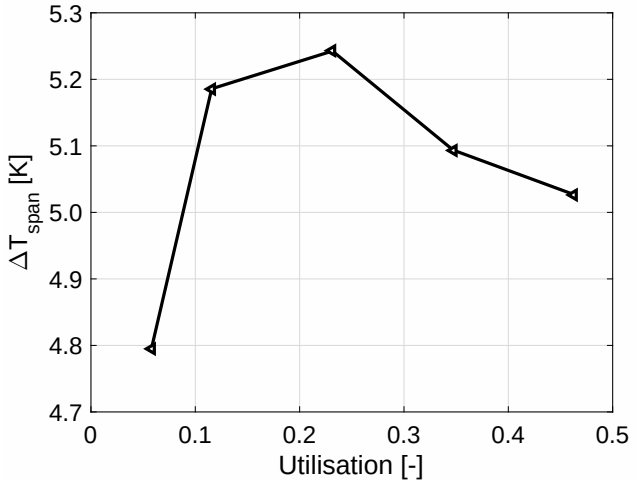

Fig. 9: The steady state temperature span between the hot and the cold end as a function of the utilisation.

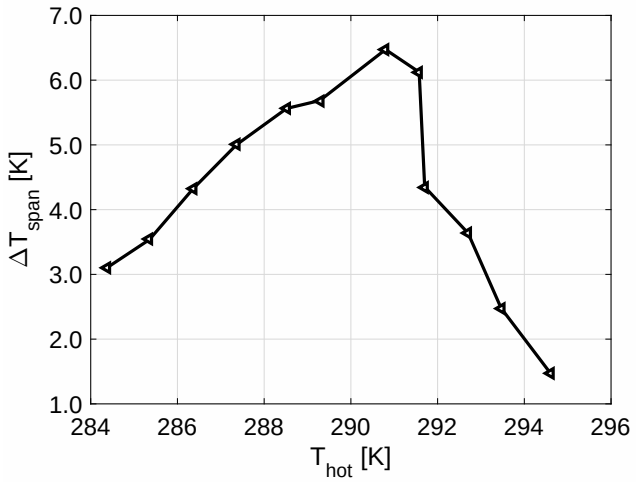

Fig. 10: The steady state temperature span between the hot and the cold end as a function of the constant hot end temperature.

just a single first order material, there is a natural limit to the achievable span, due to the very narrow ΔS_{M} peak. This span may be expanded by layering materials with slightly different Curie temperatures, as done by Jacobs et al. (2014). Previously it has been shown how thin plates consisting of a number of magnetocaloric materials have been produced by tape casting (Bulatova et al., 2015). A similar production technique could be imagined for hot-pressing single plates consisting of multiple materials.

Regenerator performance is heavily influenced by the morphology of the regenerator. In the present study flat parallel plates were chosen, giving a regenerator with a significantly reduced pressure drop compared to an equivalent packed bed one. Lower pressure drop leads to higher efficiency, although this is not measured in the device used here. The disadvantage of plates is the demand for thin very parallel plates with small plate spacing, which is often hard to realise. The increase of the Biot number for thicker plates will result in a slower heat transfer to the surrounding fluid, preventing fast operation and high performance. A higher thermal conductivity will allow for the use of thicker plates. The thermal conductivity of the plates tested here has been measured to be 3.13 $\mathrm{Wm^{-1}K^{-1}}$, reduced from the generally accepted value of about 9 $\mathrm{Wm^{-1}K^{-1}}$ for this type of material (Fujieda et al., 2004), due to porosity and the presence of resin in the plates. In order to realise the full potential of plates with this relatively low thermal conductivity the

thickness would have to be significantly reduced, and the channel thicknesses be reduced accordingly.

In addition to the challenges of producing significantly thinner plates the flatness requirement of such plates will also become more critical. The reduction in regenerator performance due to a maldistribution of the plate spacings has been shown both by modelling and experimentally (Nielsen et al., 2012; Engelbrecht et al., 2013). Even seemingly insignificant variation in the channel thicknesses can have a large impact. With sub-millimeter plates a requirement of less than 10% variation in spacing, in accordance with the general recommendation in Nielsen et al. (2012), will necessitate very accurate production techniques.

Although the addition of the low mass fraction resin hardly influences ΔS_{M} per unit mass, the volumetric ΔS_{M} decreases from about 70 $\mathrm{mJcm^{-3}K^{-1}}$ to about 40 $\mathrm{mJcm^{-3}K^{-1}}$ due to the porous structure of the bonded material under a changing magnetic field of 1.4T. From a practical point of view, the volumetric ΔS_{M} is of more importance (Gschneidner Jr. et al., 2005), since the magnetic system is the most expensive part and the magnetic field volume is thus limited. This is a challenge when making bonded plates and reducing the amount of resin to the minimum amount that will still maintain the structural integrity of the plates should be considered. Also, the 0.30 volume fraction of pores could possibly be reduced by improving the processing route.

5. Conclusion

We have shown that it is possible to use resin bonded plates of the magnetocaloric material $\mathrm{La_{0.85}Ce_{0.15}Fe_{11.25}Mn_{0.25}Si_{1.5}H_{\mathit{y}}}$ as regenerators in a small scale magnetocaloric testing device. The plates were characterised thermally and magnetically to determine the magnetic entropy change, the heat capacity and the hysteresis. The maximum achieved temperature span was 6.4 K. Increasing this span may be achieved by layering materials, reducing the amount of resin and pores or by manufacturing thinner and flatter plates.

Acknowledgements

The authors acknowledge the International Network Programme: Rare-earth/transition-metal oxides and compounds for environment friendly energy science and technology (grant no 4070-00047) from The Danish Agency

for Science, Technology and Innovation. This work is supported by National Natural Science Foundation of China (51322605, 51571018, 51531008) and also partly financed by the ENOVHEAT project which is funded by Innovation Fund Denmark (contract no 12-132673).

Aharoni, A., 1998. Demagnetizing factors for rectangular ferromagnetic prisms. J. Appl. Phys. 83, 3432.

Bahl, C. R. H., Petersen, T. F., Pryds, N., Smith, A., 2008. A versatile magnetic refrigeration test device. Rev. Sci. Instrum. 79, 093906.

Bahl, C. R. H., Velazquez, D., Nielsen, K., Engelbrecht, K., Andersen, K., Bulatova, R., Pryds, N., 2012. High performance magnetocaloric perovskites for magnetic refrigeration. Appl. Phys. Lett. 100, 121905.

Basso, V., Küpferling, M., Curcio, C., Bennati, C., Barzca, A., Katter, M., Bratko, M., Lovell, E., Turcaud, J., Cohen, L., 2015. Specific heat and entropy change at the first order phase transition of La(Fe-Mn-Si)$_{13}$-H compounds. J. Appl. Phys 118, 053907.

Bulatova, R., Bahl, C. R. H., Andersen, K. B., Theil Kuhn, L., Pryds, N., 2015. Functionally graded ceramics fabricated with side-by-side tape casting for use in magnetic refrigeration. Int. J. Appl. Ceram. Technol 12, 891898.

Caron, L., Ou, Z., Nguyen, T., Thanh, D. C., Tegus, O., Brück., E., 2009. On the determination of the magnetic entropy change in materials with firstorder transitions. J. Magn. Magn. Mater. 321, 35593566.

Engelbrecht, K., Bahl, C., Nielsen, K., 2011. Experimental results for a magnetic refrigerator using three different types of magnetocaloric material regenerators. International Journal of Refrigeration 34, 1132–1140.

Engelbrecht, K., Tusek, J., Nielsen, K., Kitanovski, A., Bahl, C., Poredos, A., 2013. Improved modelling of a parallel plate active magnetic regenerator. J. Phys. D.: Appl. Phys 46, 255002.

Fujieda, S., Hasegawa, Y., Fujita, A., 2004. Thermal transport properties of magnetic refrigerants La(Fe$_x$Si$_{1-x}$)$_{13}$ and their hydrides, and Gd$_5$Si$_2$Ge2 and MnAs. J. Appl. Phys. 95, 24292431.

Gschneidner Jr., K. A., Pecharsky, V. K., Tsokol, A. O., 2005. Recent developements in magnetocaloric materials. Rep. Prog. Phys. 68, 1479.

Jacobs, S., Auringer, J., Boeder, A., Chell, J., Komorowski, L., Leonard, J., Russek, S., Zimm, C., 2014. The performance of a large-scale rotary magnetic refrigerator. Int. J. Refrigeration 37, 84–91.

Jeppesen, S., Linderoth, S., Pryds, N., Kuhn, L. T., Jensen, J. B., 2008. Indirect measurement of the magnetocaloric effect using a novel differential scanning calorimeter with magnetic field. Review of Scientific Instruments 79 (8), 083901.

Kitanovski, A., Tusek, J., Tomc, U., Plaznik, U., Ozbolt, M., Poredos, A., 2015. Magnetocaloric Energy Conversion: From Theory to Applications. Springer International Publishing, New York.

Lanzarini, J., Barriere, T., Sahli, M., Gelin, J., Dubrez, A., C.Mayer, Pierronnet, M., Vikner, P., 2015. Thermoplastic filled with magnetocaloric powder. Materials and Design 87, 1022–1029.

Lei, T., Nielsen, K., Engelbrecht, K., Bahl, C., Bez, H. N., Veje, C., 2015. Sensitivity study of multi-layer active magnetic regenerators using first order magnetocaloric material La(Fe,Mn,Si)$_{13}$H$_y$. J. Appl. Phys 118, 014903.

Liu, J., Zhang, M., Shao, Y., Yan, A., 2015. LaFe$_{11.6}$ Si$_{1.4}$/Cu Magnetocaloric Composites Prepared by Hot Pressing. IEEE Trans. Magn. 51, 2501502.

Lyubina, J., Schäfer, R., Martin, N., Schultz, L., Gutfleisch, O., 2010. Novel Design of La(Fe,Si)$_{13}$ Alloys Towards High Magnetic Refrigeration Performance. Advanced Materials 22, 3735–3739.

Nielsen, K., Engelbrecht, K., Christensen, D., Jensen, J., Smith, A., Bahl, C., 2012. Degradation of the performance of microchannel heat exchangers due to flow maldistribution. Appl. Therm. Engineer 40, 236.

Pecharsky, V. K., Gschneidner Jr., K. A., 1999a. Magnetocaloric affect and magnetic refrigeration. J. Magn. Magn. Mater. 200, 44.

Pecharsky, V. K., Gschneidner Jr., K. A., 1999b. Magnetocaloric effect from indirect measurements: Magnetization and heat capacity. J. Appl. Phys. 86, 565–575.

Pryds, N., Clemens, F., Menon, M., Nielsen, P. H., Brodersen, K., Bjørk, R., Bahl, C. R. H., Engelbrecht, K., Nielsen, K. K., Smith, A., 2011. A monolithic perovskite structure for use as a magnetic regenerator. Journal of the American Ceramic Society 94, 2549–2555.

Pulko, B., Tusekek, J., J.D.Moore, Weise, B., Skokov, K., Mityashkin, O., Kitanovski, A., Favero, C., Fajfar, P., Gutfleisch, O., Waske, A., Poredos, A., 2015. Epoxy-bondedlafecosi magnetocaloricplates. J. Magn. Magn 375, 65–73.

Radulov, I., Skokov, K., nad T. Braun, D. K., Gutfleisch, O., 2015. Polymer-Bonded La(Fe,Mn,Si)$_{13}$H$_x$ Plates for Heat Exchangers. IEEE Trans. Magn. 51, 2501204.

Skokov, K. P., Karpenkov, D., Kuzmin, M. D., Radulov, I., Gottschall, T., Kaeswurm, B., Fries, M., Gutfleisch, O., 2014. Heat exchangers made of polymer-bonded La(Fe,Si)$_{13}$. J. Appl. Phys 115, 17A941.

Smith, A., Bahl, C., Bjørk, R., Engelbrecht, K., Nielsen, K., Pryds, N., 2012. Materials challenges for high performance magnetocaloric refrigeration devices. Advanced Energy Materials 2, 1288–1318.

Velazquez, D., Castro, M., Palacios, E., Burriel, R., 2014. Practical properties of lafecosi materials to be used in magnetic cooling regerators. Proceedings 6th IIF-IIR International Conference on Magnetic Refrigeration, Victoria, BC, 7-10 September 2014.

Zhang, H., Hu, F., Sun, J., Shen, B., 2013. Effects of interstitial H and/or C atoms on the magnetic and magnetocaloric properties of La(Fe, Si)$_{13}$-based compounds. Science China Physics, Mechanics and Astronomy 56, 2302–2311.

A.2 Publications in conference proceedings

A.2.1 Epoxy-bonded $La(Fe,Mn,Si)_{13}H_z$ as a multi layered active magnetic regenerator

EPOXY-BONDED La(Fe,Mn,Si)$_{13}$H$_z$ AS A MULTI LAYERED ACTIVE MAGNETIC REGENERATOR

Henrique Neves Bez[(a)], Kristina Navickaitė [(a)], Tian Lei[(a)], Kurt Engelbrecht[(a)], Alexander Barcza[(b)], Christian R. H. Bahl[(a)*]

[(a)] *Department of Energy Conversion and Storage – Technical University of Denmark, Frederiksborgvej 399, Roskilde, Denmark*

[(b)] *Vacuumschmelze GmbH & Co. KG, D-63450 Hanau, Germany*

[*]Corresponding author. E-mail: chrb@dtu.dk

ABSTRACT

The high magnetocaloric effect and tunability of the Curie temperature over a broad range makes La(Fe,Mn,Si)$_{13}$H$_z$ a promising magnetocaloric material for applications. Due to a volume change across the transition and the brittleness of the material as well as erosion due to fluid flow, the particles of the material may break apart during operation. In this context, we studied epoxy-bonded La(Fe,Mn,Si)$_{13}$H$_z$ regenerators, in a small versatile active magnetic regeneration (AMR) test device with a 1.1 T permanent magnet source. The magnetocaloric material was in the form of packed irregular particles (250-500 µm), which were mechanically held in place by an epoxy matrix connecting the particles, improving the mechanical integrity, while allowing a continuous porosity for the fluid flow. Water with 2 wt% ENTEK FNE as anti-corrosion additive was used as the heat transfer fluid for the epoxy-bonded regenerators. A series of AMRs was evaluated by varying the epoxy content in the range 1-4 wt%.

Keywords: Magnetocaloric, refrigeration, epoxy-bonded, layered regenerator, AMR.

1. INTRODUCTION

Since the discovery of a material with a giant magnetocaloric effect two decades ago[1] there has been a desire to translate the very high entropy change observed into an increased performance in a magnetocaloric device. Since the first room temperature device presented by Brown in 1976[2] most magnetocaloric devices have used materials with a second order phase transition (SOPT). In these materials the transition between the ferromagnetic and the paramagnetic phase results in a smooth entropy change across a broad temperature range. Contrary to this, the discontinuous transition in materials with a first order phase transition (FOPT) results in a very sharp and narrow entropy change. However, the peak values of the entropy change are in general several times higher than those found in SOPT materials.

In order to improve performance, first order magnetic phase transition magnetocaloric materials may be used in the AMR. One of the most promising FOPT materials' series is La(Fe,Mn,Si)$_{13}$H$_z$[3]. This material has the Curie temperature, T_C, near room temperature, while it can be finely tuned by the Fe/Mn/Si ratio. Still, using FOPT materials instead of SOPT ones is not trivial and further considerations must be taken. Firstly, FOPT materials exhibit hysteresis [4], although it has been shown that for the La(Fe,Mn,Si)$_{13}$H$_z$ series it is rather small and in the range of 1 K [5]. Additionally, by definition FOPT materials exhibit a discontinuous phase transition over temperature and field, which is the reason that they exhibit large magnetocaloric effect. Nevertheless, the temperature range where there is a significant magnetocaloric effect is much narrower for FOPT materials. For example, the full width at half maximum of the Δs peak of Gd is about 30 K [6] for a field change of 1 T, while for La(Fe,Mn,Si)$_{13}$H$_z$ it can be as low as 7 K [5]. This brings forth the necessity of layering the regenerator with La(Fe,Mn,Si)$_{13}$H$_z$ with slightly different compositions along the direction of the temperature span, in such a way that the working temperature of each layer is optimized. This engineering is not straightforward and many complications have been shown elsewhere [7]. Furthermore, due to the necessity of interstitial H in order to bring the T_C to near room temperature without significant changes of the magnetocaloric properties, the shapeability of the material is compromised, as the hydrogenation process must be performed while the material is in the powder form and further sintering options remain limited [8].

Moreover, this material undergoes a volume change of ~0.9 vol% during the magnetic phase transition [8,9]. Given the brittleness of the material, microstructure and secondary phases, the volume change may lead to

cracking [10,11]. A method proposed to avoid cracking and erosion of the material under application is to bond the particles of the magnetocaloric material with epoxy, increasing the mechanical stability of the regenerator while still maintaining a continuous porosity [12].

In this context, we evaluate the performance of $La(Fe,Mn,Si)_{13}H_z$ epoxy-bonded double layer AMRs. The factors investigated here are: the effect of epoxy content; the heat transfer fluid; the effect of layering; and the utilization.

2. EXPERIMENTAL PROCEDURE

Fine particles of five slightly different compositions of $La(Fe,Mn,Si)_{13}H_{1.65}$ were used to make regenerators. The materials were produced by the same processing route[3] and will in the following be identified by their Curie temperature, measured by magnetometry.

Two types of regenerators were made: one with loose particles, held in place mechanically with a mesh at either end and a second where the particles were bonded together by a small amount of epoxy. In both cases the regenerators were cylindrical and made to fit into the versatile test device described previously[13,14]. The regenerator moves in and out of the 40 mm diameter bore of a 1.1 T permanent magnet Halbach cylinder. The device is placed in a temperature controlled cabinet, and the hot end temperature, T_{hot}, is fixed by a heat exchanger to be slightly above the ambient temperature in the cabinet, T_{amb}.

A table listing the regenerators tested is given below. The particle sizes were in a range of 250-500 µm and the regenerators had a porosity of 55%. The relatively high porosity is due to the relatively high irregularity of the shape of the particles, leading to a low packing density. The epoxy bonded regenerators were all fixed in 40 mm long pieces of Perspex tube, as shown in Fig. 1 all with masses of 95 g. The non-bonded regenerators were held in a custom container allowing filling with different amounts of material. Additionally, the viscosity and density of the transfer fluids were evaluated in an Anton Paar Lovis 2000 M/ME viscometer.

Name	**Description**	T_C	**Mass**
Single	Single layer regenerator with no epoxy	23.3 ºC	48 g
Double	Double layer regenerator with no epoxy	19.2 and 23.3 ºC	25 g each
Single4wt%	Single layer regenerator with 4 wt.% epoxy	22 ºC	95 g
Double1wt%	Double layer regenerator with 1 wt.% epoxy	23 and 26.6 ºC	95 g
Double2wt%	Double layer regenerator with 2 wt.% epoxy	23 and 26.6 ºC	95 g
Double4wt%	Double layer regenerator with 4 wt.% epoxy	23 and 26.6 ºC	95 g

Table 1: Description and properties of the regenerators for each given name.

Fig. 1 : Photo of an epoxy bonded regenerator, pen top for scale.

3. RESULTS AND DISCUSSION

For the regenerator tests we used two different corrosion protection additives, which have previously been shown to be effective for $La(Fe,Mn,Si)_{13}H_z$ type material, namely ethylene glycol based automotive antifreeze (EG) and Entek FNE (NT) [15]. Viscosity and density of water with different amounts of these additives were measured and compared to pure water, as shown in Fig. 2. The measurements were done at 20 ºC, which is close to the range the regenerators are tested in. Previous experience has shown that a concentration of around 15% of EG is needed for good corrosion protection, while concentrations in the order of 1-2% are sufficient when using NT. It is observed in Fig. 2 that the effect of the additive on the density and viscosity is much less for NT than for EG, presumably due to the much smaller concentrations. It can be noted that the change in viscosity per percent of additive is approximately the same while the effect on density is higher per percent of EG than NT. Also, while there is a significant change in the absolute viscosity of about 50% for EG and 20% for NT, the difference in density is only of the order of 3% for EG and less than 1% for NT.

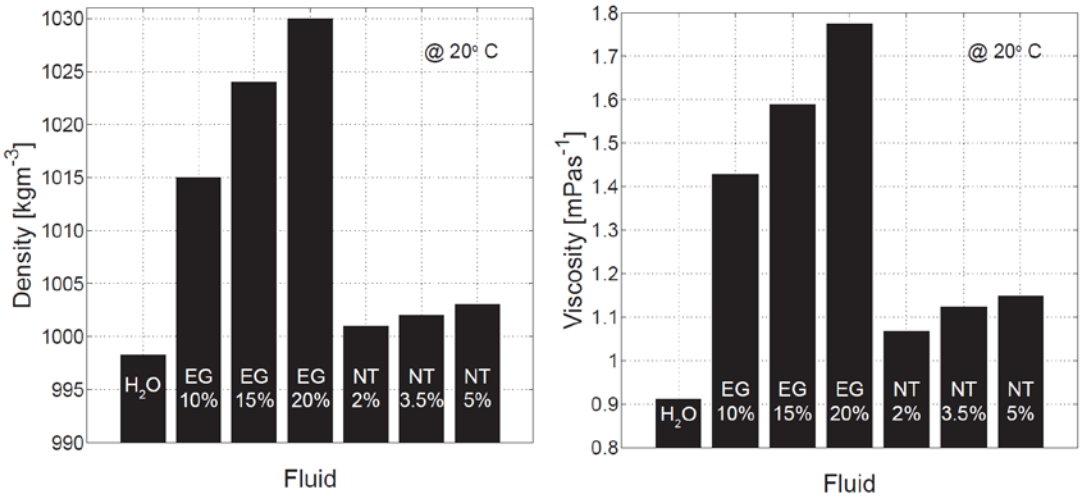

Fig. 2 : (a) The density and (b) the viscosity of the different fluids.

The apparent mechanical strength of the regenerators is generally good. However, during the regenerative tests the *Double1wt%* regenerator with just 1 wt.% of epoxy could not withstand the forces during operation and the regenerator broke apart.

We initiate the investigation of the regenerative performances by evaluating the influence of the utilization at a T_{hot} in the region of the maximum temperature span. The utilization, ϕ, is defined as

$$\phi = \frac{m_f c_f}{m_s c_s} \quad (1)$$

where m_f is the mass of the fluid pushed through the regenerator in one direction, c_f is the specific heat of the fluid, m_s is the mass of the solid regenerator and c_s is the specific heat of the regenerator material. The values used for c_s and c_f are 480 [5] and 4200 $Jkg^{-1}K^{-1}$, respectively.

Since the utilization is linearly proportional to the blown fluid mass, m_f, in Fig. 3 ΔT_{span} is shown as a function of the blown fluid mass. One can see that the trend of the span versus the m_f is approximately the same for the two regenerators without epoxy, independent of the number of layers and amount of material. The epoxy bonded regenerators have the peak at the same blown fluid mass as the ones without epoxy. Nonetheless, the mass of the solid regenerator is basically double of the ones without epoxy, and as we can see in equation (1) the effect will be to decrease the utilization by half.

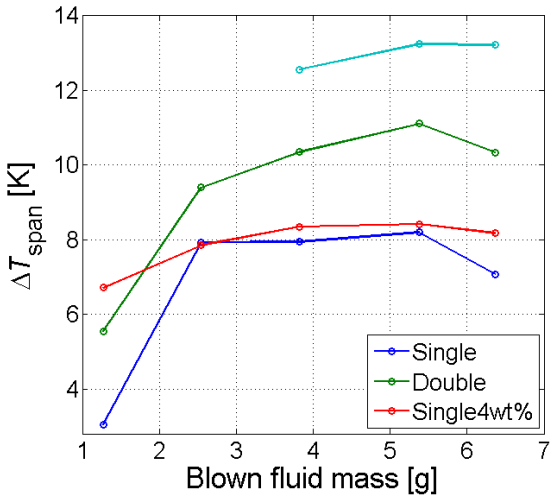

Fig. 3 : Temperature span as a function the blown fluid mass for three different regenerator at the region of maximum temperature span.

The temperature span as a function of the hot end temperature is shown in Fig. 4, where the left graph shows the results of the material without epoxy, while the right shows the results of the material with epoxy. It should be noted that the results of the regenerators without epoxy were done with water and 15 vol.% EG as the heat transfer fluid, while for the epoxy containing ones the fluid was changed to water with 2 vol.% NT. As discussed above these additives do change the viscosity, but only have a weak impact on the density. Due to the low frequency (0.13 Hz) the viscous dissipation is small when pushing the fluid through the regenerator, so even for the EG this will not have a large influence on the results. The regenerators were operated with the best resulting m_f, 5.4 g, which due to the difference of mass in the regenerators lead to different utilizations: 0.5 for the epoxy-bonded regenerators while those without epoxy were operated at a utilization of 0.9, in accordance with the results found in Fig. 3.

A feature common in all the results is a steady increase of temperature span with increasing T_{hot} up to a maximum at a temperature about 3-5 K above the highest T_C, then the span sharply decreases at higher hot end temperatures[7]. Additionally, it is observed that increasing the number of layers, from one to two, significantly increases the span, as expected. The measured temperature spans in the regenerators were not affected much by the epoxy-bonding. In fact they increased a little, as the dashed lines in Fig. 4 suggest. This, however, could be a combined effect of the different heat transfer fluids, differences in the mass of magnetocaloric materials and effects related to the epoxy itself. Additionally, the T_C spacing of the double layer regenerator without epoxy and the ones epoxy-bonded is slightly different. As it is shown in the literature[7], the temperature span can be heavily influenced by this spacing.

Although good performance was observed in the regenerators without epoxy, these regenerators were not mechanically stable. After three weeks of measurements, the regenerators started to release some very fine particles to the heat transfer fluid. These fine particles are believed to be the corners of the irregular particles, which are more susceptible to cracking. We believe that erosion during the fluid blow periods, coupled with the ~0.9% volume change that the material experiences at the transition [9, 11] result in breaking apart of the particles. Additionally, once this breaking apart starts, the packing of the regenerators is lost, and the particles are free to move inside the regenerator housing leading to further degradation of the regenerators. Indeed, this is what was observed. Shortly after the first fine particles were observed the number of particles in the fluid increased until the whole regenerators broke apart.

The reason for introducing the epoxy into the regenerator matrix was to enhance the mechanical stability and prevent breaking apart of the regenerators. As expected, the mechanical stability of the regenerators was increased significantly by epoxy bonding the particles. No degradation related to particles breaking was observed, even after 5 weeks of testing. By comparing the temperature span of regenerators *Double2wt%* and *Double4wt%* in Fig. 4 it is observed that increasing the amount of epoxy was detrimental to the span. So when epoxy bonding it is important to find the minimum amount of epoxy that can be used while still

maintaining the structural integrity of the regenerator. As discussed above the regenerator *Double1wt%* broke apart during initial testing, so the minimum amount of epoxy to avoid this seems to be 2 vol.%.

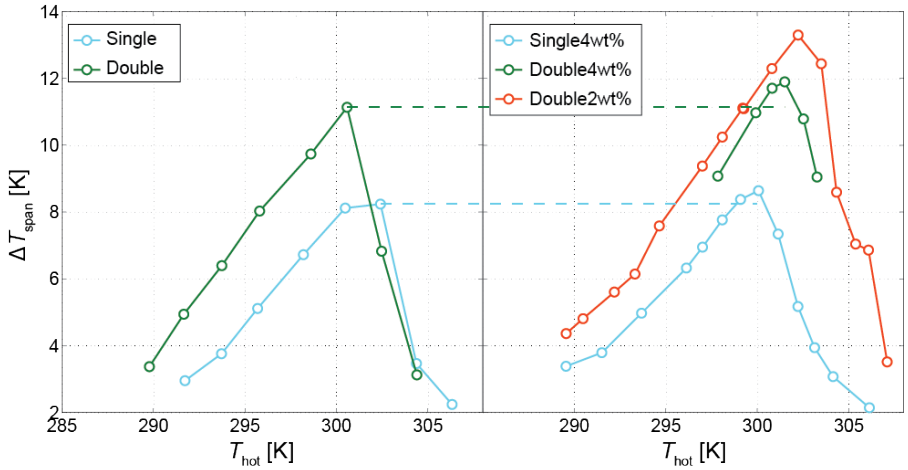

Fig. 4 : Temperature span as a function of the hot end temperature for different regenerators. The Dashed line is a guide to the eye.

4. CONCLUSIONS

The performance of $La(Fe,Mn,Si)_{13}H_z$ as an active magnetic regenerator is evaluated in a custom-built device. The results show that irregular particles of $La(Fe,Mn,Si)_{13}H_z$ deteriorate during application which would limit the use of this material as an AMR. By epoxy bonding the particles, the mechanical stability of the regenerators increased significantly and no deterioration due to particles breaking was observed. The temperature span reached by the epoxy-bonded regenerators suggest that 2 wt.% of epoxy maximizes the span, while still maintaining the mechanical integrity. The characterization of the transfer fluid showed that the Entek solutions have a lower viscosity and density then the ethylene glycol ones. Although the effect of a lower viscosity does not influence of the tests here done since the frequency is relatively low, this might play a very important role under high frequency operations.

ACKNOWLEDGMENTS

This work was financed by the ENOVHEAT project which is funded by Innovation Fund Denmark (contract no 12-132673). The authors are grateful to Vacuumschmelze GmbH for providing the samples.

REFERENCES

[1] V. K. Pecharsky and K. A. Gschneidner, Jr., "Giant Magnetocaloric Effect in $Gd_5Si_2Ge_2$," *Phys. Rev. Lett.*, vol. **78**, no. 23, pp. 4494–4497, 1997.

[2] G. V. Brown, "Magnetic heat pumping near room temperature," *J. Appl. Phys.*, vol. **47**, no. 8, p. 3673, 1976.

[3] A. Barcza, M. Katter, V. Zellmann, S. Russek, S. Jacobs, C. Zimm, "Stability and Magnetocaloric Properties of Sintered $La(Fe, Mn, Si)_{13}H_z$ Alloys," *IEEE Trans. Magn.*, vol. **47**, no. 10, pp. 3391–3394, 2011.

[4] L. von Moos, C. R. H. Bahl, K. K. Nielsen, and K. Engelbrecht, "The influence of hysteresis on the determination of the magnetocaloric effect in $Gd_5Si_2Ge_2$," *J. Phys. D. Appl. Phys.*, vol. **48**, no. 2, p. 025005, 2015.

[5] V. Basso, M. Küpferling, C. Curcio, C. Bennati, A. Barzca, M. Katter, M. Bratko, E. Lovell, J. Turcaud, and L. F. Cohen, "Specific heat and entropy change at the first order phase transition of $La(Fe-Mn-Si)_{13}$-H compounds," *J. Appl. Phys.*, vol. **118**, no. 5, p. 053907, 2015.

[6] K. K. Nielsen, H. N. Bez, L. von Moos, R. Bjørk, D. Eriksen, and C. R. H. Bahl, "Direct measurements of the magnetic entropy change," *Rev. Sci. Instrum.*, vol. **86**, no. 10, p. 103903, 2015.

[7] T. Lei, K. K. Nielsen, K. Engelbrecht, C. R. H. Bahl, H. Neves Bez, and C. T. Veje, "Sensitivity study of multi-layer active magnetic regenerators using first order magnetocaloric material

$La(Fe,Mn,Si)_{13}H_y$," *J. Appl. Phys.*, vol. **118**, no. 1, p. 014903, 2015.

[8] S. Fujieda, a. Fujita, K. Fukamichi, Y. Yamazaki, and Y. Iijima, "Giant isotropic magnetostriction of itinerant-electron metamagnetic $La(Fe_{0.88}Si_{0.12})_{13}H_y$ compounds," *Appl. Phys. Lett.*, vol. **79**, no. 5, p. 653, 2001.

[9] H. N. Bez, K. K. Nielsen, P. Norby, A. Smith, and C. R. H. Bahl, "Magneto-elastic coupling in $La(Fe, Mn, Si)_{13}H_y$ within the Bean-Rodbell model," *AIP Adv.*, vol. **6**, no. 5, p. 056217, 2016.

[10] J. Lyubina, R. Schäfer, N. Martin, L. Schultz, and O. Gutfleisch, "Novel design of $La(Fe,Si)_{13}$ alloys towards high magnetic refrigeration performance.," *Adv. Mater.*, vol. **22**, no. 33, pp. 3735–9, 2010.

[11] A. Waske, L. Giebeler, B. Weise, A. Funk, M. Hinterstein, M. Herklotz, K. Skokov, S. Fähler, O. Gutfleisch, and J. Eckert, "Asymmetric first-order transition and interlocked particle state in magnetocaloric $La(Fe,Si)_{13}$," *Phys. status solidi - Rapid Res. Lett.*, vol. **9**, no. 2, pp. 136–140, 2015.

[12] J. Lanzarini, T. Barriere, M. Sahli, J. C. Gelin, A. Dubrez, C. Mayer, M. Pierronnet, and P. Vikner, "Thermoplastic filled with magnetocaloric powder," *Mater. Des.*, vol. **87**, pp. 1022–1029, 2015.

[13] K. Engelbrecht, K. K. Nielsen, and N. Pryds, "An experimental study of passive regenerator geometries," *Int. J. Refrig.*, vol. **34**, pp. 1817–1822, 2011.

[14] C. R. H. Bahl, T. F. Petersen, N. Pryds, and a Smith, "A versatile magnetic refrigeration test device.," *Rev. Sci. Instrum.*, vol. **79**, no. 9, p. 093906, 2008.

[15] D. Velázquez, M. Castro, E. Palacios, and R. Burriel, "Pratical Properties of LaFeCoSi Materials to Be Used in Magnetic Cooling Applications," in *Proceedings of Thermag VI*, 2014, pp. 133–134.